A STUDY OF A LONG BASELINE

GRAVITATIONAL WAVE ANTENNA SYSTEM

Prepared for the National Science Foundation
under NSF Grant PHY-8109581
to the Massachusetts Institute of Technology

Prepared By:

Paul Linsay	MIT
Peter Saulson	MIT
Rainer Weiss	MIT

With Contributions By:

Stan Whitcomb	CalTech

Industrial Consultants:

Arthur D. Little Corporation	Cambridge, Massachusetts
Stone & Webster Engineering Corporation	Boston, Massachusetts

OCTOBER 1983

ACKNOWLEDGEMENTS

AT MIT

Cindy Kaplan

AT ARTHUR D. LITTLE

R. Warren Breckenridge
Marianne Brissette
Arthur Fowle
Thomas E. Hoffmann
Harry Lambe
Robert Lucas
Francis Mallahan
Peter von Thuna
William A. Vachon
Richard Wells

AT STONE AND WEBSTER

Hemendra Acharya
Vincent Amato, Jr.
Robert DeLuca
Anthony Furia
Donald Guild
William Martin
Janice McCoy
Alireza Moazed
Les Tyrala
Denise Wilton

TABLE OF CONTENTS

		Page
I.	INTRODUCTION	
	Introduction	I-1
	History & Overview	I-3
	Introduction to the Concept of an Electromagnetically Coupled Antenna	I-11
II.	SOURCES OF GRAVITATIONAL RADIATION	II-1
III.	PHYSICS AND DETECTION	
	Response of a Free Mass Interferometric Antenna to Gravitational Wave Excitation	III-1
	Multiple Antennas and Signal Detection	III-17
IV.	PROTOTYPES AND OPTICAL CONCEPTS	
	Prototypes	IV-1
	Classification of the Optical Concepts	IV-14
	Optical Delay Lines	IV-20
	Considerations in a Fabry-Perot (S. Whitcomb)	IV-30
V.	NOISE SOURCES	
	Transducer Noise	V-2
	Light Propagation Fluctuations due to Pressure Fluctuations	V-13
	Mechanical Thermal Noise	V-20
	Vibration Isolation	V-32
	Electromagnetic Fields	V-62
	Noise due to Cosmic Rays	V-66
	Noise Summary	V-69
VI.	VACUUM SYSTEM	
	Arthur D. Little Study of Long Baseline Antenna Vacuum System and Costs	VI-1
VII.	SITE SURVEY	
	Stone and Webster Study of Above and Below Ground Sites	VII-1
VIII.	CONSTRUCTION	
	Stone and Webster Study of Construction and Costs	VIII-1

TABLE OF CONTENTS (page 2)

Page

IX. PROPOSED DESIGN

X. APPENDICES

A. Acoustic and Electromagnetically Coupled Antennae in the Naive Quantum Limit X-1

B. Why a Fiber Optic Antenna Will Not Suffice X-9

Introduction

This document is the result of a study of the sensitivity, design and costs for a gravitational wave detection system based on interferometric long baseline antennas. The study was initiated by the MIT Gravitational Research Group who engaged the engineering firms of Arthur D. Little of Cambridge and Stone and Webster of Boston. Arthur D. Little studied the vacuum system design and costs while Stone and Webster made an evaluation of sites and studied various construction concepts and their costs. The spirit of the costing exercise was to fix on a design but at the same time to establish the cost scaling laws applicable to other designs.

In later phases of the study, the advice and criticism of the Cal Tech Gravitational Research Group were sought. Parts of this study have benefited from this interaction, however the tyranny of the schedule to complete this document have left substantial parts of it without their constructive review.

The principal conclusion of this study is that it is timely and feasible to construct a gravitational wave detection system based on at least two long baseline interferometric antennas. The development could open a new field of astrophysics--gravitational astronomy--with its own unique sources and insights into the universe and gravitation. The technical ability exists now to extend the search for gravitational radiation into new frequency bands and to gain a million fold increase in energy sensitivity over present detection systems.

Furthermore, there is substantial margin for further improvement in the sensitivity with technical advances as the fundamental limits for these systems are still many orders of magnitude below the projected sensitivities.

The positive conclusion of this study may have been anticipated. It could have been otherwise: the basic concept could have been flawed, the technology could have been inadequate, the costs could have been beyond reasons. None of these appears to be the case.

The concept that gravitation along with all other interactions in nature propagates with finite speed originates with Einstein and special relativity in 1905. The formulation of relativistic theories of gravitation began after the discovery of special relativity and continues to this day. A central feature of all of these theories is gravitational radiation.

The choice made in this report and in most but not all prior attempts at detection of gravitational radiation has been to focus on the tensor waves predicted by Einstein in 1918 as one of the theoretical results of general relativity. These waves are expected to be transverse with two polarization states and propagate at the velocity of light. General relativity, by virtue of its simplicity and elegance, has been the favored relativistic gravitational theory since its formulation in 1916. However, the experimental basis for its acceptance has not been strong. Experiments and observations performed terrestrially and in the solar system during the past twenty years have established that in the low velocity, weak field limit general relativity is a proper description of nature. The discovery of PSR 1913+16, a binary system consisting of a pulsar orbiting a neutron star, has been an important element in improving the experimental basis for general relativity. This system is found to obey all the dynamical predictions of general relativity at weak fields and in addition appears to be decreasing its orbital period--

shedding energy-- at just the rate required by gravitational radiation damping as expected by general relativity. This is the first experimental evidence for gravitational radiation and a strong indicator that the Einstein tensor waves are the right ones to look for.

The actual detection and the experimental verification of the wave properties has not been accomplished. This alone is sufficient motivation to carry out the search. One might imagine that an experimental program similar to the Hertzian experiments with electromagnetic waves, where the source and receiver are under the experimenter's control, would be the appropriate method for such a study. Unfortunately it is just here that the extreme weakness of the gravitational interaction strikes hardest. The gravitational strain amplitudes, the measurable in the Einsteinian tensor waves, are always of the order

$$h \sim \left(\frac{GM}{Rc^2}\right) \frac{v^2}{c^2} \qquad (1)$$

where h is the strain, G the Newtonian gravitational constant, R is the distance to the radiating mass, M, which is moving with velocity, v. c is the velocity of light. In order to separate radiation from induction the observer must be in the wave zone at a distance of the order of the wavelength. For an oscillating system then, one would estimate the largest wave strains as

$$h \sim \frac{GM\omega^3 a^2}{c^5} \qquad (2)$$

where a is the oscillation amplitude of the radiating source at frequency ω. The reader can readily show that the G/c^5 factor is devastating when coupled to the masses, amplitudes and oscillation frequencies one might contemplate in a laboratory experiment.

Astrophysical phenomena involving the coherent motions of large masses at relativistic speeds are the sources most likely to give terrestrially measurable gravitational radiation strains and permit a study of the wave properties. It is, moreover, just these extreme phenomena that, if they can be made observable, will allow us to test relativistic gravitation in the strong field--high velocity limit. A view held by many is that this is the most important reason to engage the search for gravitational radiation. Implicit in this view is that signatures in the gravitational radiation may well be the most definitive means to establish the existence and study the interactions of black holes with their surroundings.

A review of the astrophysical sources that have been contemplated is given in this study and the interested reader is invited to turn to that section of the report. The theoretical predictions indicate that detection of gravitational waves by the proposed system is entirely plausible, but by no means guaranteed. In these introductory remarks it is worth highlighting a more speculative viewpoint which borders on a truism but is really at the heart of the matter. Should one succeed in observing gravitational radiation, the chances are excellent that specific and fundamental issues in gravitation will be settled. In

addition the search itself, as it offers a new probe of the universe, may uncover totally unexpected phenomena. Both are exciting prospects and in our opinion make the search one of the most interesting scientific opportunities of this epoch.

None of the foregoing is intrinsically new except for the spectacular discovery of PSR 1913+16. Much of this was on the mind of Joseph Weber when he initiated the search for gravitational radiation using acoustic (bar) detectors[1] in the mid 1960s. Setting aside the controversy raised by the first experiments, it became clear, after a world wide effort, that nature was not as generous as might have been indicated in the early experiments. In a broad sense this realization was the beginning of the search in earnest; the arguments for carrying out the search remained persuasive, the sources were just not that strong nor, in hindsight, was it reasonable to expect that they could have been.

Impressive progress has been made in improving the sensitivity of acoustic antennas since the pioneering experiments. By lowering the operating temperature, choosing antenna materials with higher internal Q and the development of better position transducers coupled

[1]Acoustic detectors are usually longitudinal mechanical resonators coupled to motion transducers. The gravitational wave induces time dependent longitudinal stresses in the device which then responds as a harmonic oscillator to a time dependent external force.

to lower noise amplifiers, the strain sensitivity has been increased by a factor close to a thousand over the last decade. At the present (Fall 1983) one cannot make a sharp judgment that these improvements have not uncovered gravitational radiation sources. The best present system is operating at an rms strain sensitivity of approximately 10^{-18} near 1 KHz. Although conventional wisdom holds that it is unlikely to find sources at this level, the fact is that there has been no opportunity to run two such antennas in coincidence to find out for sure.

The hope is that acoustic detectors can be improved by approximately another two orders of magnitude in strain sensitivity before they may be limited by quantum fluctuations. Considerable theoretical effort has gone into analysing whether the quantum fluctuations do indeed impose a hard limit. The consensus is that in principle they do not but there is argument whether a practical scheme to circumvent the quantum fluctuations can be implemented and, if it can be, what improvements in sensitivity might result.

Our assessment is that acoustic bar antennas are the most sensitive devices with which to carry out the search at present and they will remain so for the next several years.

"Free" mass electromagnetically coupled antennas[2], the central

[2]Electromagnetically coupled antennas measure the gravitational wave induced modulation of the travel time of light between masses that label points in space. The masses are free at frequencies above their suspension resonance. The concept is described in detail in the section of this report on the antenna response functions.

subject of this study, were first considered in the early 1970s both at MIT and the Hughes Research Laboratories independently. Although more complex and expensive than acoustic detectors, especially the low sensitivity room temperature bar detectors of the early experiments, it was recognized from the start that electromagnetically coupled antennas have several desirable properties when constructed on a large enough scale. The strain sensitivity is in principle better than that of an acoustic detector by the ratio of the velocity of light to the velocity of sound in solids. As there is no reliance on resonance to match the position transducer to the mechanical system, they are broad band and therefore useful in the search for all classes of gravitational radiation sources--periodic impulsive or stochastic. Furthermore if sources were ever to be uncovered with sufficient signal to noise, electromagnetically coupled antennas could follow the time dependent wave shapes of the gravitational wave metric perturbations with fidelity and be a powerful diagnostic tool in determining the radiative processes in the source. Finally, the practical realization of an antenna system designed to meet the sensitivities presumed to be astrophysically interesting, did not require more than the thoughtful application of even then current technology if the systems were made large enough. One might ask why no large project was started? The answer, simply stated, is that in the early 1970s the time wasn't right.

In the mid 1970s the Office of Space Science at NASA encouraged research in exploring the properties of electromagnetically coupled antennas deployed in space, using optical techniques to avoid the index fluctuations of the interplanetary plasma. It was realized that antennas in space would be able to measure gravitational radiation at long periods, minutes to hours. This region is inaccessible on the ground, but is interesting astrophysically; especially since this band includes the expected radiation from stellar binaries. The study of optical long baseline low frequency antennas is being carried on at JILA (University of Colorado) and at JPL and hopefully will be incorporated into the long range plans of the NASA Space Sciences Program.

By the mid 1970s the concept began to interest other research groups, especially in Europe. In 1974 the Gravitational Research Group at the Max Planck Institute in Munich, who had carried out the search for gravitational radiation with room temperature acoustic detectors, began developing an electromagnetically coupled antenna. The group then directed by Prof. H. Billing has constructed a 3 meter long prototype using multi pass delay line optics in a Michelson interferometer configuration similar in concept to the design at MIT. In the course of their experimental program they discovered and solved many of the technical difficulties in the practical implementation of the idea. To date, they have demonstrated the best performance of a prototype electromagnetically coupled antenna; their instrument is operating at an rms strain sensitivity of approximately 10^{-16} near 1 KHz. They are now developing a 30 meter version of this system and hope to go on to longer systems.

In the later 1970s the Gravitational Research Group at Glasgow University directed by Prof. R. Drever, who also had been involved in the search for gravitational radiation with acoustic antennas, began the development of electromagnetically coupled antennas. The Glasgow group chose to use Fabry-Perot cavities as the antenna elements after preliminary experiments with multi-pass White cells mounted on a split bar acoustic detector. In the course of these early studies they discovered the problems associated with scattering of light which had not been adequately recognized earlier.

In the late 1970s Cal Tech made the decision to begin a program in experimental gravitation, the central focus of which has become the search for gravitational radiation using electromagnetically coupled antennas. Professors R. Drever and S. Whitcomb direct this effort. The Cal Tech prototype is a 40 meter Fabry-Perot system which has begun to function this year. The optical design is similar to the Glasgow instrument. The Cal Tech instrument is at present the largest prototype to come into operation.

We have learned recently that a group is being formed by A. Brillet at the Laboratoire de l'Horloge Atomique at Paris-Sud to develop a prototype electromagnetically coupled antenna, the state of this project is not known to us.

INTRODUCTION TO THE CONCEPT OF AN ELECTROMAGNETICALLY COUPLED ANTENNA

The basic concepts of an electromagnetically coupled antenna are presented in this section without mathematical encumbrance; these are left for more detailed presentations later in this document.

The fundamental idea is straightforward. The travel time of light between two objects in free fall,--travelling along geodesics of the four dimensional geometry of space and time--is modulated by a gravitational wave. The measurable quantities are the changes in the travel time. Except for geometric factors, the change in travel time is equal to the integral of h taken over the travel time. Since the gravitational wave strain amplitudes are expected to be small and there are as yet no time standards of the requisite stability, the difference in travel time of light propagating in two orthogonal directions is measured. This technique applies specifically to the polarization states of the Einstein tensor waves which have strains of opposite sign in orthogonal directions transverse to the direction of wave propagation. The relation between the measured time difference and h is primarily a function of the total time the light spends in the gravitational wave, this time is referred to as the storage time. And, except for subtleties, a single long light path is equivalent to the sum of many shorter ones. In simple geometries nothing is gained if the storage time is larger

than 1/2 the gravitational wave period. As pointed out by Drever, this need not be a limit if the gravitational wave is periodic, for it is then possible to accumulate time differences for storage times larger than the gravitational wave period providing that one arranges the light beam to oscillate between the two orthogonal directions in synchronism with the gravitational wave period.

In practice, the time difference is not measured directly but rather the difference in phase of two light beams having traversed the orthogonal paths is measured interferometrically. The condition that the system be insensitive to clock instability is satisfied by making the optical paths in the two orthogonal directions equal.

The smallest gravitational wave strain measurable is determined by a host of perturbing effects which are broadly organized in two groups; those that limit the ability to measure the time (or phase) differences and those that compromise the assumption that the masses are truly free and unperturbed. A few of the effects are fundamental and others can be reduced by sound engineering practice. The influence of all effects that perturb the masses is reduced by increasing the physical length of the antenna.

A fundamental limit is imposed by quantum fluctuations which effect both the ability to measure the time differences and cause a perturbation on the masses. The limit can be analyzed heuristically much like the Heisenberg microscope but with many photons and macro-

scopic masses. It can also be viewed as an intrinsic quantum diffusion process. The limit is reduced by increasing the mass and the physical length of the antenna. As with the quantum limit for acoustic detectors, there is speculation that the quantum limit is not really fundamental but in the case of electromagnetically coupled antennas this argument is at present more academic both because the strain limits are so much lower than for acoustic detectors and that, in the first generation of large baseline electromagnetically coupled antennas, the other perturbing effects are expected to be larger than the quantum limit.

Time dependent gravitational gradients from distant sources, induction fields rather than radiation, are indistinguishable from gravitational waves in only one antenna and could be considered as imposing a fundamental limit. These are estimated to be very small in the frequency bands open for the search on the ground.

Less fundamental but at present more influential noise sources are thermal excitations of internal modes in the masses at high frequencies and low frequency motions in the suspension system that support the masses. These are reduced by using low loss (high Q) materials and could be further reduced by cryogenic operation in future refinements of long baseline antennas. Thermal noise does not play the same crucial role in determining the limit of electro-

magnetic antennas as in the acoustic types because one does not work on the resonances and the noise is reduced by increasing the antenna length.

Ground noise (seismicity) and acoustic vibrations communicate forces to the masses through the suspension. The noise becomes more influential at low frequencies because the excitation spectrum grows at low frequencies and vibration isolation systems become more difficult to implement at low frequencies. The reduction of this noise source requires more subtle engineering in electromagnetic than acoustic antennas primarily because of the intent to extend the search to lower frequencies. The influence of this noise term also reduces with antenna length.

A list of less significant perturbations on the masses includes the influence of time varying electric and magnetic fields, the momenta imparted to the masses by cosmic ray impacts, thermal gradient driven gas pressure forces, radiation pressure variations due to amplitude fluctuations of the light source, made evident by optical or mechanical unbalance in the system. All of the above phenomena are discussed in later sections of this report. And all are reduced by increasing the length.

Noise terms that limit the measurement of the time (phase) differences, the equivalent of the system transducer noise, are also divisible into fundamental terms and those that are reduced by

technical improvements.

The ability to measure a small time difference (phase shift) is determined by the photon counting statistics at the photo detectors--the shot or Poisson noise--. The gravitational strain limit imposed by this noise is reduced by increasing the circulating light power and the light storage time in the antenna, in effect increasing the transducer gain.--the change of intensity at the photo detector per change of phase difference. When the power and storage time are increased to the point where the uncorrelated light pressure fluctuations on the masses become measurable, one has attained the quantum limit. At present and in the prospects for the first long baseline system, the light powers are sufficiently low that the Poisson noise is expected to dominate at high frequencies. The Poisson term in the low power limit does not depend explicitly on the antenna length but rather on the storage time, so that it is possible to reduce its effect by multiple reflection. One should bear in mind, however, that to gain a long storage time in a small antenna requires many beam transits which impacts on the complexity and quality requirements of the optics.

Other noise terms effecting the ability to measure small phase (time) differences include: laser frequency and amplitude fluctuations, the effect of light scattering, the interaction of antenna

misalignments with laser beam position and angle fluctuations. None of these effects are fundamental and their importance is a strong function of the specific optical design. Different designs deal with these terms in varying ways as will become clearer in the section describing the prototype antennas.

A factor common to all designs is the necessity of a vacuum system. This requirement is driven by both classes of perturbing effects. A vacuum is needed around the masses to: reduce acoustic noise coupling, eliminate thermal gradient forces driven by gas pressure and to reduce gas damping which introduces thermal noise. A vacuum is also required along the light paths to reduce index of refraction fluctuations due to acoustic excitation and the fundamental thermally driven statistical column density fluctuations of a gas at equilibrium.

SOURCES OF GRAVITATIONAL RADIATION

1.0 Introduction

In this section of the report we present a review of the possible sources of gravitational radiation and of the nature of the signals they would produce. We will express the strength of the signal in terms of h (=2 $\Delta\ell/\ell$), the value of the metric perturbation (strain) at the antenna.

Gravitational radiation is produced by the time-varying gravitational field of a massive system. Monopole radiation is forbidden by the conservation of energy, while dipole radiation is forbidden by the conservation of momentum and angular momentum. Thus the lowest order of gravitational radiation allowed is quadrupole radiation. For most systems, this order dominates the gravitational luminosity, in which case the luminosity is given approximately by

$$L = \frac{G}{c^5} \langle \dddot{Q}^2 \rangle$$

where $\dddot{Q}$ is the third time derivative of the reduced quadrupole moment of the mass distribution. The flux at a distant point is given by

$$F = f(\theta,\phi) \frac{L}{4\pi D^2}$$

where D is the distance to the source and $f(\theta,\phi)$ is the radiation pattern (of order unity). The metric perturbation h is related to the flux by

$$F = \frac{c^3}{16\pi G} \langle \dot{h}_+^2 + \dot{h}_x^2 \rangle .$$

The chain of reasoning in making predictions about possible gravitational wave signals takes the following form: The astrophysicist considers a kind of source, and from a study of its dynamics is able to calculate the strength and temporal or spectral character of the gravitational radiation which it emits. (Often it is the case that the difficulty of this task lies less in the subtleties of general relativity than in the complexity of astronomical systems.) In addition, it is necessary to estimate the rate of occurrence (or density) of such sources in some fiducial volume, say a galaxy. For impulsive sources, one calculates a maximum likely signal strength by assuming that the source is located on the surface of a sphere (centered on the antenna) large enough to contain one event per month (or year, or however long an experimenter is able to wait). For periodic sources, one assumes the source is approximately $n^{-1/3}$ away from the antenna where n is the number density of sources. Of course, for known individual objects one uses the true distance away. The duration and frequency content (i.e. characteristic frequency, bandwidth) determine to some extent the experimenter's design of his apparatus and data analysis strategy. The expected signal strength, when compared with instrument noise levels, indicates whether it is likely that a successful detection can be made. Unfortunately the uncertainties in all of the dimensions of these predictions are large, so only very general guidance can be drawn from them.

2.0 Neutron Star Binaries

Binary stars are the commonest astronomical systems. Calculation of their gravitational radiation is almost trivial. Every known binary, however, has such a long period that the gravitational wave signal is far outside the passband of any terrestrial antenna. Among the shortest periods are Am CVn at 18 minutes and WZ Sge at 81 minutes. Sources such as these could only be observed by an antenna in space, free of the seismic disturbances of the terrestrial environment. It is unfortunate that these sources will remain beyond our reach for some time, since by their very simplicity they allow the cleanest possible test of the general relativistic prediction of the strength and polarization of gravitational radiation.

There is one particularly noteworthy binary system, PSR1913+16. This is the famous binary pulsar consisting of two 1.4 $M_\odot$ objects, one certainly a neutron star and the other almost certainly one. Although not as strong a radiator as the binaries named above, the high quality clock provided by the pulsar allowed Taylor and his coworkers (see Taylor and Weisberg 1982) to demonstrate the decay of the orbit due to gravitational radiation reaction forces. This is the first and only time that the existence of gravitational radiation has been demonstrated empirically, a fact which puts the entire field of research on a much sounder basis than it was only a few years ago.

For the purposes of this discussion, however, PSR1913+16 plays the humbler role of prototype of a source of high frequency gravi-

tational waves, the rapid final decay of a double compact binary due to strong gravitational radiation reaction forces (PSR1913+16 itself will not suffer this fate for another 10^8 years). The burst of gravitational radiation from a pair of neutron stars was studied in detail by Clark and Eardley (1977). Depending on the parameters of the system (chiefly the masses of the two neutron stars) the system may either suffer immediate tidal disruption of the lighter neutron star, or may undergo a brief (around 1 sec) period of stable mass exchange from the lighter to the heavier star before ultimate disruption. In either case the signal is a "chirp", with rising frequency and strongly increasing amplitude for a few tens of milliseconds until the system reaches minimum separation, followed by rapidly decreasing amplitude and frequency. The typical maximum frequency for neutron stars near 1 $M_\odot$ is below 1 kHz. The maximum amplitude is of order $h=10^{-21}$ for a distance of 15 Mpc (distance to the Virgo Cluster). This corresponds to several percent of the rest mass radiated away, a rather high efficiency. The decay should yield a detectable signal even earlier than the final 10 msec, even though the amplitude of the emitted wave is lower. This is because the extra integration time available earlier outweighs the lower amplitude (which scales as $t^{-1/4}$, where t is the remaining lifetime). Thus, the highest signal to noise ratio is available at the lowest observationally feasible frequencies.

The question of the rate of such decays was addressed by Clark, van den Heuvel, and Sutantyo (1979). Their argument is simple and

rather crude. Some fraction of order unity of all supernova events lead to pulsars, and of 315 known pulsars (in 1979) one was a binary pulsar. They use Tammann's (1977) value of 1 supernova per 11 years in the Galaxy (thought by most workers to be around a factor of two too frequent) to arrive at a rate of formation (equal to rate of decay) of $2.9*10^{-4}$/yr in the Galaxy, within a few factors of two. For the total number of events within a sphere of radius D>10Mpc they give $r=3.2*10^{-3}(D/10Mpc)^{3}$/yr, where a Hubble constant H_o=100 km/sec-Mpc was assumed. To see around 10 events per year we must see to distance of 150 Mpc, where maximum amplitudes are around $h=10^{-22}$.

3.0 Supernovae

In many respects the most popular prospective source of gravitational waves has been the collapse of a neutron star in a Type II supernova. It was the prediction that as much as 1% of the rest energy of the resulting neutron star would be liberated as a 1 msec pulse of gravitational radiation that encouraged much of the work on bar detectors in the past decade or so. Theoretical estimates of the efficiency of gravitational wave production have shrunk, some estimates dramatically so. The problem is that the physics of the supernova event is extremely complicated, so that it is difficult to make firm predictions about the relevant quantities such as the size of the quadrupole moment and its time derivatives. The most detailed numerical

calculations of the course of a supernova event even explicitly make the assumption of spherical symmetry for economy of computation. Saenz and Shapiro (1981 and references therein) have pursued a different approach, studying the collapse of a homogeneous ellipsoid which is endowed by hand with the physical properties to agree with the detailed spherical models. The mechanism for gravitational radiation from a supernova may be summarized as follows: A massive star produces a core of roughly 1 $M_\odot$ which has burned to iron. Above a density of $4*10^9 gm/cm^3$ the electron pressure which has supported the core is reduced abruptly as the core becomes partially neutronized. The collapse which is thus initiated is reversed in a sudden "bounce" once the core has collapsed to nuclear densities, around $3*10^{14} gm/cm^3$. If the collapse is not spherically symmetric, then the bounce is responsible for a large value of $\dddot{Q}$ and hence a burst of gravitational radiation. Depending on the degree of damping the first bounce may be followed by several others.

If the departure from spherical symmetry is due to rotational flattening, then the output of gravitational radiation depends on the angular momentum of the collapsing core. For the energy released in the first bounce, Saenz and Shapiro find $dE \propto J^4$, with a peak $dE=10^{-4}Mc^2$ at $J=3*10^{48}$ erg-sec. (For higher J, see discussion below). The Crab pulsar has $J=2*10^{47}$ erg-sec, although its angular momentum may have been much higher at birth. In the lower J region, however, Saenz and Shapiro find that the eccentricity grows during succeeding bounces at

such a rate that when all bounces are included the gravitational wave output has been substantially enhanced. For the $J=10^{48}$ erg-sec cores, the damping is strong enough so that the effect is negligible. A core with the Crab's present angular momentum would radiate more than $3*10^{-6}$ of its rest mass away gravitationally. This corresponds to a peak value of $h=10^{-22}$ at the distance of the Virgo Cluster. Muller (1981) reports on another set of calculations which treat rotational flattening non-perturbatively, which gives energy efficiences roughly an order of magnitude lower than this (*3 lower in h). These models treat the microphysics in more detail than Saenz and Shapiro. It is not clear whether the difference is due to this sophistication, or merely due to different choices for the poorly known nuclear density equation of state.

The case for $J>10^{49}$ erg-sec suffers from a nearly total lack of consensus on even the qualitative features of the collapse. The recent discovery of PSR1937+214 with a frequency of 642 Hz and $J=5*10^{48}$ erg-sec has given new life to the dispute. Saenz and Shapiro argued that above $J=10^{49}$ erg-sec centrifugal forces would resist gravitational collapse, preventing the star from reaching the high density state where gravitational radiation is strong. Clark and Eardley (1977) raised the possibility that such strong centrigual forces would cause the core to break up, perhaps only into two pieces, in which case their calculation for the decay of a neutron star binary would predict gravitational radiation efficiency around 10^{-2}. Endal and Sofia (1977)

performed stellar evolution calculations which indicated that the core would have retained enough of the angular momentum from its value on the main sequence to cause either fission or a strong non-axisymmetric distortion. In the latter case also, gravitational radiation efficiencies approach 10^{-2} (Miller 1974). On the other hand, Hardorp (1974) uses evidence from the observed rotation of white dwarfs and neutron stars to argue that some more efficient mechanism for angular momentum loss than was considered by Endal and Sofia must exist. Thus the question of whether to expect efficiencies nearer 10^{-2} or 10^{-6} remains in dispute. Still, it should be borne in mind that $J=10^{49}$erg-sec is a very small fraction of the angular momentum of the parent star, so that unless the angular momentum transfer mechanism is highly efficient (on the short time scale of the collapse), then the most reasonable expectation is that rapid rotation of collapsing cores is the rule, rather than the exception.

The supernova event rate in a galaxy comparable to the Milky Way is believed to be around 3 to $4*10^{-2}$/yr, approximately equal to the estimated pulsar birthrate. (This agreement is somewhat surprising since Type II supernovae make up only half of the supernovae, and it is believed that gravitational collapse is not a result of Type I events. Perhaps the discrepancy can be reconciled if pulsars can also be made by the collapse of "bare cores" which don't produce a bright flash of light. See the review by Trimble (1982) for a discussion of these points). A heliocentric sphere which includes the

Virgo Cluster must be searched to find more than one event per year. For efficiencies in the range 10^{-2} to 10^{-4}, this yields h=10^{-21} to 10^{-22}.

Another mechanism has been proposed for radiation from collapsing supernova cores, namely radiation from the anisotropic emission of neutrinos during collapse. Epstein (1978) estimated the strength of such radiation, which should have a charateristic frequency of 100 Hz or below. For the case of low eccentricity he gives an efficiency estimate more than eight orders of magnitude lower than Saenz and Shapiro. If the eccentricity of the neutrinosphere is comparable to the eccentricity of the core, then the gravitation radiation flux due to the neutrinos may become comparable to that due to the bouncing core itself. However, it is likely that the eccentricity has been damped to a low level by the time of neutrino emission (Thorne in Epstein and Clark 1979).

4.0 Pulsars

The pulsars which are the product of supernovae have themselves been considered as possible sources of gravitational radiation. The signal would consist of line radiation due to the rotation of the (presumably) non-axisymmetric neutron star. Thus, although the origin of the radiation is also ultimately due to stellar collape, the signature of the signal is radically different.

A simple model of a pulsar is a 1.4 M_o neutron star of radius 10 km, and moment of inertia $I=10^{45}$ gm-cm^2 rotating with frequency f. The pulsar is slightly deformed from axisymmetry. The gravitational radiation luminosity of the pulsar can be shown to be

$$L = \frac{288}{45}\frac{G}{c^5}\ \varepsilon_e^2 I^2 (2\pi f)^6$$

where ε_e is the equatorial ellipticity. (See Ostriker and Gunn 1969). It is this last parameter that is poorly known. A reasonable minimum value is the distortion due to the dipole magnetic field. This can be estimated using the relation

$$\varepsilon = \frac{E_{magnetic}}{E_{gravitational}} = \frac{B^2R^4}{GM^2} = 10^{-12}$$

if $B=10^{12}$ gauss (typical of most pulsars). Then $L=10^{30}$ergs/sec(f/1kHz)6. The equivalent value of $h=3*10^{-31}(f/1kHz)^2(10kpc/D)$. If pulsars are born rapidly rotating then there should be several of the most recent pulsars with such an amplitude present in the galaxy at any time. This rapid rotation question is exactly the same one involved in the argument about the strength of the gravitational wave burst from a supernova. If slow rotation is the norm the signals will be substantially weaker, due to the f^2 dependence of h.

Note that the one known fast pulsar, PSR1937+214, apparently has an anomalously low magnetic field (10^8 gauss) as determined by its period derivative. If its distortion is due to magnetic stresses, its gravitational luminosity is probably nearer 10^{14}ergs/sec, for a value

of $h=10^{-39}$. It has been proposed that the rapid rotation of this pulsar is due to its having been spun up as it consumed a low mass companion star (Alpar et al. 1982). So the debate about the initial angular momentum of collapsing stellar cores rages unabated).

In the model discussed above, the gravitational radiation is monochromatic with a frequency 2f, since a prolate spheroid rotating about a short axis has the same appearance (= quadrupole moment) every half cycle of rotation. Zimmerman and Szedenits (1979) studied slightly different models which yield more complicated signals. They imagine that the pulsar is a rigid body whose shape is not necessarily determined by the stress due to the currently measured B-field, but may be a "fossil". One simple shape is an oblate spheroid rotating about an axis inclined by an angle θ to the principal axis with the largest moment of inertia. If $\theta=0$, the gravitational radiation is zero, but if $\theta \neq 0$ the body precesses (or wobbles) about the angular momentum vector. Then, in addition to radiation at frequency 2f, there is radiation at the fundamental frequency f, which is dominant if θ is small. Zimmerman and Szedenits also consider a more general triaxial body, which produces radiation at 2f and at two frequencies $f\pm = (1\pm e)f$, where e is a measure of the equatorial ellipticity. Thus there is potentially a fair degree of complexity (or interest) to the signal from a pulsar.

The most important aspect of the "rigid body" pulsar models is that they can lead in a natural way to much stronger gravitational

radiation than is predicted in the magnetic stress models. Consider a neutron star spinning at frequency f. If it were fluid, it would assume the figure of an oblate spheroid, with an oblateness given by

$$\frac{I_3 - I_1}{I_1} = \varepsilon = \frac{15}{16\pi} \frac{(2\pi f)^2}{G\rho}$$

where I_1 is the equatorial moment of inertia, and I_3 is the polar moment of inertia (Goldreich 1970). The equilibrium figure of the solid neutron star is this shape. Now imagine that a small torque on the neutron star causes the angular momentum to shift by an angleθ from the polar axis of the rigid figure. Zimmerman (1978) gives the amplitude of the gravitational wave emitted by such a star as

$$h = \frac{G}{c^4} \frac{2I_1 \varepsilon (2\pi f)^2 \sin\theta}{r}$$

The amplitude scales as f^4, because of the frequency dependence of the oblateness. The oblateness of the Crab pulsar (f=30Hz) is $2*10^{-4}$. The gravitational wave amplitude at the Earth should be $2.5*10^{-25}\sin\theta$, which is substantially larger than the signal due to the magnetic distortion, unless the angular momentum is very precisely aligned with the principal axis of the star. Observation of the constancy of the pulse shape rules out $\sin\theta>0.1$, but $\sin\theta=0.01$ is probably allowed.

For the fast rotator PSR1937+214, the oblateness equals 0.23, implying a gravitational wave amplitude of $h=5*10^{-20}\sin\theta$. The other rapidly rotating pulsar, PSR1953+29, with f=160Hz (Boriakoff et al. 1983),

should have an amplitude $h=1*10^{-22}\sin\theta$. Unfortunately, it is unlikely that these short period pulsars will be seen radiating by this mechanism. The gravitational radiation reaction force acts in such a way as to cause $\sin\theta$ to vanish, without affecting the angular velocity about the principal axis (Eardley 1982). The ratio of the gravitational luminosity to the kinetic energy reduction due to alignment gives a characteristic time, which is independent of $\sin\theta$, but which is proportional to f^{-8}. For f=1kHz, this time is approximately 40 msec, while for f=100Hz the damping time is about 1 month. Thus unless these pulsars are being continually perturbed, they ought to be nearly perfectly aligned, and hence invisible. For the Crab, the damping time is $1.5*10^{3}$ yr, about equal to its age.

A real neutron star may in fact be triaxial. It is difficult to predict how strongly it may be distorted, although in principle an upper limit could be set by requiring that the internal stresses in the rotating star be smaller than the (poorly known) yield stress of the stellar material. Lacking an argument along these lines, one notes that in this case, as in the case of the prolate magnetic distortion, the emission of gravitational radiation will cause an observable slowdown in the rate of arrival of radio pulses. For the case of the fast pulsar, PSR1937+214, the limit on the period derivative yields an upper limit to the strain amplitude of $h=3*10^{-27}$, assuming negligible braking due to the emission of electromagnetic radiation.

Wagoner (1983) has described a mechanism for gravitational radiation from a low magnetic field neutron star (like PSR1937+214) which is in the process of being spun-up by accretion from a companion star. As the neutron star acquires angular momentum it reaches a point where it becomes unstable to the emission of gravitational radiation. That is, gravitational radiation reaction forces drive a non-axisymmetric distortion which in turn enhances the gravitational radiation. This instability is damped by viscosity in the neutron star, so that a steady-state is attained. For the magnitude of viscosity believed to characterize neutron stars, it is an m = 3 or 4 distortion (rather than the m=2 quadrupole) which is most likely to be excited. The gravitational radiation will be emitted at f=500± 300Hz, with an amplitude given by

$$h = 3\times10^{-27}\left(\frac{1\text{kpc}}{D}\right)\left(\frac{1\text{kHz}}{mf}\right)^{\frac{1}{2}}\left(\frac{L_\gamma}{10^{-8}\text{ergscm}^{-2}\text{sec}^{-1}}\right)^{\frac{1}{2}},$$

where L_γ is the X-ray flux (proportional to accretion rate). $L_\gamma=10^{-8}$ ergs/cm^2-sec is characteristic of galactic X-ray sources which are believed to be powered by accretion onto a compact object.

5.0 Black Holes

A potentially strong source of gravitational radiation is the birth of a black hole by gravitational collapse, or the collision of two black holes already formed. The difficulty with predicting signals from this kind of source is that there is no equivalent of PSR1913+16

to serve as a prototype. There are two known objects, Cygnus X-1 and LMC X-3 (Cowley et al. 1983), which are considered candidate black holes, because they seem too heavy (around 10 $M_\odot$) to be anything else as dim. Much less secure arguments are advanced for the existence of a 10^9 $M_\odot$ black hole in the center of the giant elliptical galaxy M87 (Young et al. 1978). Indeed, the violent motions of ionized gas clouds in the center of our Galaxy are believed by several workers to be due to a 10^6 $M_\odot$ black hole, although recent detailed modelling has called this interpretation into question (Lacy et al. 1982)

From the theorist's point of view, massive black holes would provide a natural explanation for many of the properties of active galactic nuclei (Blandford 1979). Indeed, Rees (1978) considered the possible evolutionary paths for the dense central regions of galaxies, and found many ways to form black holes, only a few ways to avoid forming them. But many skeptics remains unconvinced that black holes exist. Certainly there is no reason for confidence in any prediction of the rate of black hole events.

The collision of a pair of black holes is a kind of source which is a cousin of the neutron star binaries. Detweiler and Szedenits (1979) used perturbation theory to study the gravitational radiation from a test particle falling into a Schwarzschild black hole. They find that the amount of rest energy converted into gravitational

waves is roughly $dE=A(M_1/M_2)M_1$ where M_1 is the mass of the test particle, M_2 is the mass of the black hole, and A is a constant of proportionality which depends on the orbital angular momentum. For J=0, A is of order 10^{-2}, while for $J>M_1M_2G/c$, A can exceed 10^{-1}. Smarr (1979) finds that a similar formula applies in the limit that $M_1=M_2$.

Thorne (1978) describes the sort of signal produced by a generic black hole event (birth or collision). The signal probably consists of a burst caused by the initial collapse or approach, followed by damped normal-mode ringing of the resulting black hole. The characteristic frequency is $11kHz(M/M_\odot)^{-1}$, and the ringing probably persists for several periods. If the efficiency dE/Mc^2 is around 0.1, then the amplitude of the signal is $h=2*10^{-20}(1Mpc/D)(M/M_\odot)$.

The remaining facts needed to make a prediction of signal strengths are the densities of the populations of black holes of various masses. It is here that our knowledge of astrophysics fails us. It is certainly not possible to rule out zero density for all masses. The models which are considered most plausible at any given time are subject to the whims of astrophysical fashion (which is not to say that our current beliefs are necessarily wrong). A popular model for globular cluster X-ray bursters used to be a 10^3 $M_\odot$ black hole sitting at the cluster center accreting stars. The formation of one such black hole per globular cluster per Hubble time gives around one event per year in the nearest

500Mpc (Thorne, in Epstein and Clark 1979), with h=several*10^{-20}. Current models of bursters invoke neutron star binaries instead of black holes (see the review by Joss and Rapaport 1983), so there is no longer a strong justification for this estimate of the rate of black hole events. But that does not mean that there can not be such events, if there exists a similar number of black holes hidden elsewhere. Such black holes may exist, for example, in the non-luminous halos of galaxies which dominate the mass of the universe, or in the cores of galaxies. Our ignorance on this subject is too vast to make confident predictions, yet the opportunities for a far-reaching discovery are nowhere greater than in the case of black holes.

4.0 Stochastic Backgrounds

One can imagine searching for a stochastic background of gravitational waves in addition to impulsive signals and periodic signals. Operationally, a stochastic signal has roughly constant amplitude (not impulsive) and a broad continuous spectrum (not periodic). Predictions of the possible strength of stochastic gravitational waves are even less secure than predictions of the strengths of other kinds of signals. Certainly one way to make a stochastic background is to superpose the signals from enough sources so that they overlap, either in time if they are bursts, or in frequency is they are periodic. For the sorts of sources considered previously, the signals become stochastic only at very low valuesof h.

One possible source which appears interesting is the superposition of the signals from the collapse of the purported supermassive Population III stars which may make up the "missing mass". Carr (1980) considers several scenarios in which short-lived stars of mass up to $10^3 M_\odot$ are created, subsequently dying by strongly asymmetrical collapse to form black holes. Depending on the time of formation and the mass distribution, the characteristic frequency of the resulting gravitational waves can vary throughout (or even beyond) the range 1Hz to 1kHz. The energy density allowed in the resulting gravitational wave background may range from 10^{-4} all the way up to 10^{-1} times the closure density of the universe. The corresponding values of h_{rms} vary from $3*10^{-23}$ to 10^{-21} near 1kHz, or 10 times larger if the characteristic frequency is 100 Hz. The likelihood that the missing mass is in supermassive black holes is, at the moment, a question to be answered only by personal inclination. Put more positively, the search for a stochastic gravitational background provides a unique means to search for a possible component of the universe which would be otherwise invisible.

Another source of stochastic gravitational waves could be strong anistropy in the initial conditions of the Big Bang, or quantum gravitational processes which occurred at the Planck time (10^{-43} sec afterwards). Our understanding of the physics involved is so poor that prediction of the strength is futile. Carr (1980) points out that the energy density in such a primordial background is constrained by the

success of cosmic nucleosynthesis calculations. In order not to spoil this success, the energy density in primordial gravitational waves must be small compared to the energy density in the cosmic (microwave) background radiation, around 10^{-4} times the closure density.

7.0 Discussion

The review given above has addressed quite a few individual source models, with some attention given to technical issues which limit our confidence in our understanding of the sources. Several points need to be stressed, independently of any particular model.

1. Although the predictions have large uncertainties, reflecting our ignorance of important aspects of astrophysical processes, there are many reasonable arguments which do predict detectable amounts of gravitational radiation. Indeed, one might consider the uncertainty as a virtue, for it shows how much there is to learn from the study of gravitational radiation. Actually making the gravitational wave measurements is the best way to learn about stellar collapse, for example.

2. The models considered by most theorists span only a narrow range of the space of possible sources. Note that the three best studied sources (supernovae, pulsars, and compact binaries) all involve, either directly or as an immediate antecedent, the gravitational collapse of 1 $M_\odot$ to a neutron star. It is not that this is the only chain of

events that can lead to production of gravitational waves. It is just the only well-known process.

3. When gravitational waves are finally detected, it will open a whole new window on the universe. To use a phrase of Thorne's (1982), the information carried by gravitational radiation is nearly "orthogonal" to that carried by electromagnetic radiation. This is true in the sense that electromagnetic radiation is usually generated as the superposition of a multitude of atomic processes, while gravitational radiation can only be produced in large amounts by coherent motions of large masses. Furthermore, the collapsing core of a supernova is obscured by the envelope of the star which has a great optical depth. The collision of two black holes may take place in the absence of sufficient gas to generate substantial amounts of light. Thus, we can expect not only to see more clearly into processes we already know about (such as stellar collapse), but also to be made aware of phenomena heretofore completely hidden.

4. The surest way to make new discoveries is to employ radically new means of looking at the universe. The early days of radio astronomy and X-ray astronomy were so exciting at least in part because the application of new technology revealed phenomena whose existence had barely been dreamt of. (This has been discussed recently by Harwit 1981). The next generation of gravitational wave detectors will achieve more than five orders of magnitude improvement of sensitivity (in energy)

over the best presently operating detectors. In addition, the search will be extended from a few extremely narrow frequency channels to the entire band from 30Hz to several kiloHertz. This is not merely incremental progress, but a brand new opportunity for discovery.

5. The detection of gravitational waves remains the single most important task of experimental relativity. The existence and nature of gravitational radiation is a prediction of Einstein's which has remained unconfirmed for over half a century. As Eardley (1982) has pointed out, the current state of this field of research is analogous to the state of particle physics between the demonstration of the necessity that the neutrino exist (the analog of Taylor's important work) and the actual physical detection of the neutrino itself. We cannot claim to understand gravity until we have detected gravitational waves.

Summary of Predicted Gravitational Wave Signals

The following three diagrams show the expected signals from the models of sources which we described in the text.

Figure 1, Impulsive Sources: The range of expected signal strengths from a supernova event in the Virgo Cluster is represented by the crossed error bars just above 1 kHz. The center is the "standard model" of Saenz and Shapiro (1981). The high J, high efficiency models give results near the top of the vertical bar in the case of a non-axisymmetric distortion of the core, or near the corner marked "binary fission". An upper bound on the signal due to the expanding cloud of neutrinos in the explosion is marked near 50 Hz (see Epstein 1978). The evolving signal from the destruction of a pair of neutron stars, following Clark and Eardley (1977), is labelled "1 $M_\odot$ Compact Binary." The binary is assumed to be 150 Mpc away, sufficient for 1 event per month. The point marked "$\tau = 0$" represents the final 10 msec burst of radiation, while the amplitude and frequency of the signal at earlier times are marked "$\tau = 1$ sec", "$\tau = 1$ min", and "$\tau = 1$ hr". Note that better signal to noise is available at the earlier stages due to the longer integration times. Finally, the signals from black hole formation events are plotted, based on the work of Thorne (1978). In the mass range 10^2 $M_\odot$ to 10^4 $M_\odot$ the distance assumed is 500 Mpc, while in the range 10^5 $M_\odot$ to 10^7 $M_\odot$ the strength is plotted as if the black holes formed at the epoch of peak quasar

activity, z =2.5.

Figure 2, Periodic Sources: In the bottom right hand corner of the diagram are plotted the expected signal strengths from four well-known pulsars and one hypothetical one, under the assumption that the only departure from spherical symmetry is that due to the stress of the dipole magnetic field. The stronger estimate of Zimmermann (1978) for the Vela and Crab pulsars is labelled "Wobbling." Wagoner's (1983) prediction of the signal from a neutron star spun up by accretion to the point of instability is plotted near 500 Hz. At f=0.2 Hz appears the signal from a binary pair of neutron stars one year before collision (Clark and Eardley 1977). Finally, at low frequencies are plotted the signals from several well-known binary star systems, including the radiation (in several harmonics) from the highly eccentric orbit of the binary pulsar 1913+16 (tabulated by Douglass and Braginsky in Hawking and Israel, Einstein Centenary Volume, 1979).

Figure 3, Stochastic Background: The graph shows the amplitude of a stochastic background with an energy density of either 10^{-1} or 10^{-4} times the closure density of the universe. The quantity plotted is the amplitude at a given frequency, under the assumption that all the energy is concentrated in a bandwidth equal to the frequency. The value of $\Omega = 10^{-4}$ is the limit on primordial backgrounds set by the success of nucleosynthesis calculations. Non-primordial

backgrounds may contain up to 1/10 of the closure density, according to Carr (1980).

Figure 1: Impulsive Sources

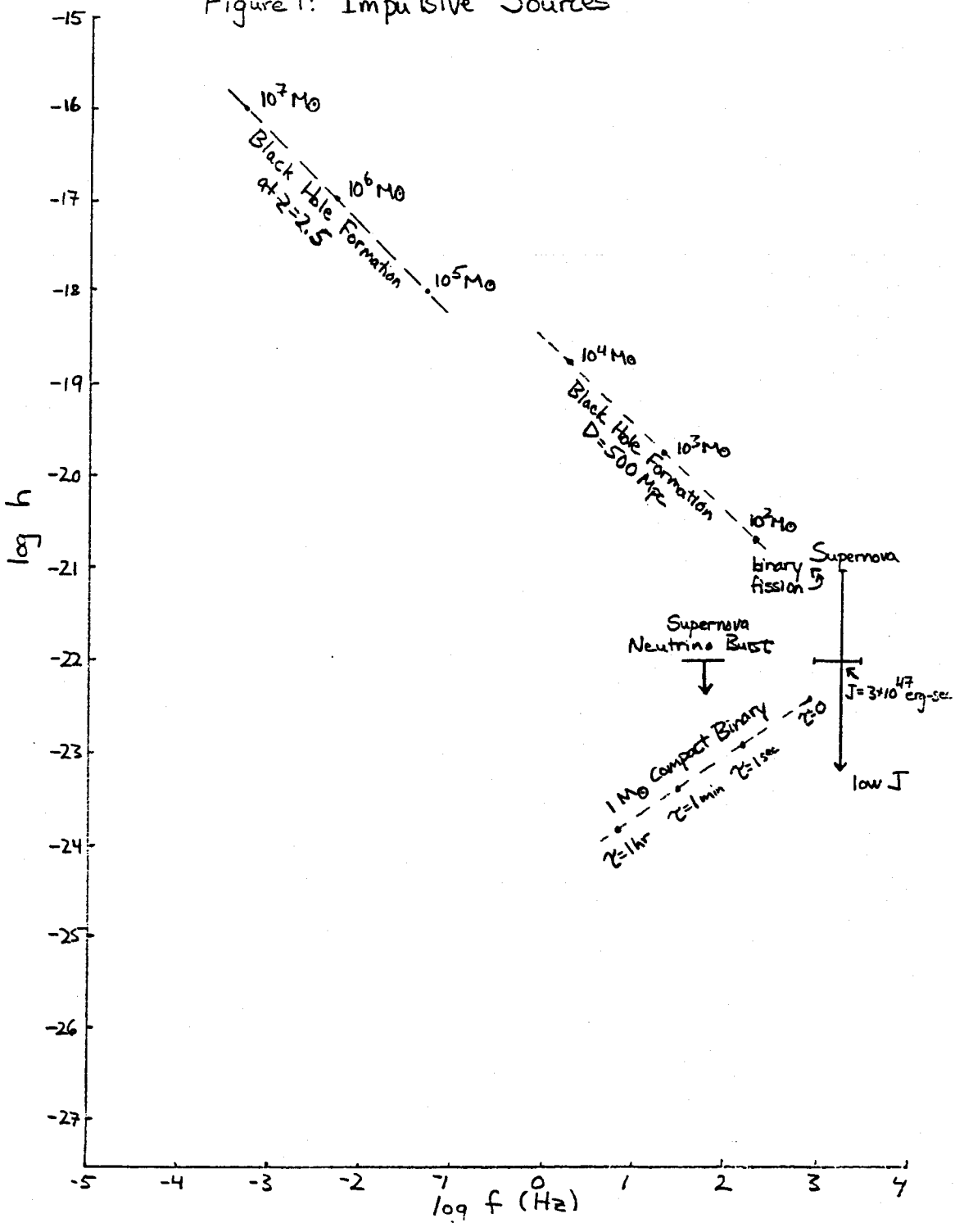

Figure 2: Periodic Sources

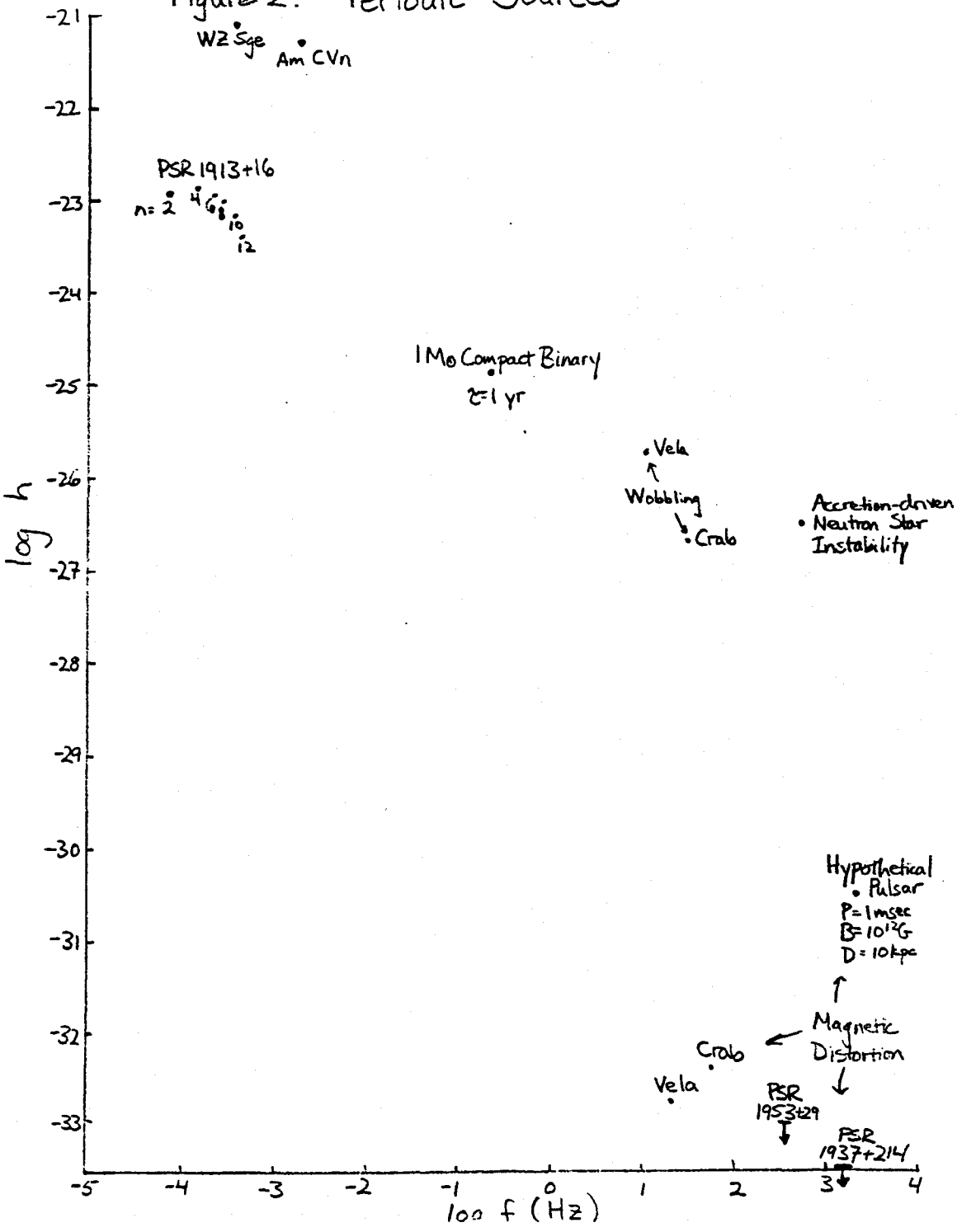

Figure 3: Stochastic Background

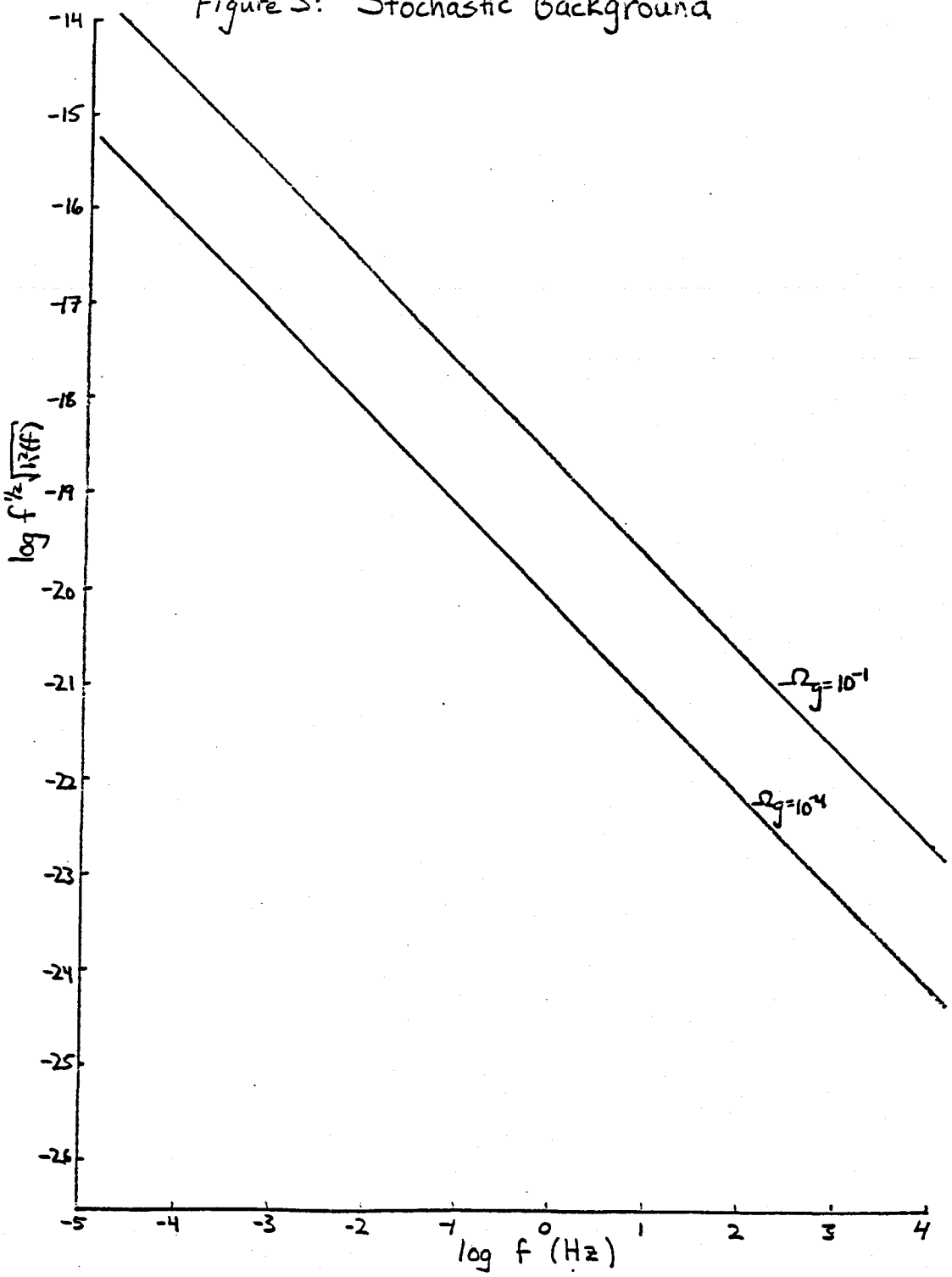

REFERENCES

Alpar, M.A., Cheng, A.F., Ruderman, M.A., and Shaham, J., Nature 300, 728 (1982)

Blandford, R.D., in Sources of Gravitational Radiation, ed. L. Smarr, Cambridge University Press. (1979)

Boriakoff, V., Buccheri, R., and Fauci, F., Nature 304, 417 (1983)

Carr, B.J., Astron. Astrophys.89, 6 (1980)

Clark, J.P.A., and Eardley, D.M., Ap. J. 215, 311 (1977)

Cowley, A.P., Crampton, D., Hutchings, J.B., Remillard, R., and Penfold, J.E., Ap. J. 272, 118 (1983)

Detweiler, S.L. and Szedenits, E., Jr., Ap. J. 231, 211 (1979)

Eardley, D.M. in Gravitational Radiation, ed. N. Deruelle and T. Piran, North-Holland (1982)

Endal, A.S. and Sofia S.,Phys. Rev. Letters 39, 1429 (1977)

Epstein, R., Ap. J. 223, 1037 (1978)

Epstein, R. and Clark, J.P.A., in Sources of Gravitational Radiation, ed. L. Smarr, Cambridge University Press (1979)

Goldreich, P.,Ap. J. Letters, 160, L11

Hardorp, J. , Astron. Astrophys. 32, 133 (1974)

Harwit , M. Cosmic Discovery, Basic Books (1981)

Joss, P.C., and Rappaport, S.A., preprint (to appear in Annual Reviews of Astron. and Astrophysics)

Lacy, J.H., Townes, C.H., and Hollenbach, D.J., Ap. J. 262, 120 (1982)

Miller, B.D., Ap. J. 187, 609 (1974)

Müller, E.,in Supernovae, ed. M.J. Rees and R.J. Stoneham, Reidel (1981)

Ostriker, J.P.,and Gunn, J.E., Ap. J. 157, 1395 (1969)

Rees, M.J. in Structure and Properties of Nearby Galaxies, ed. Berkhuijsen and Wiekbinskii, Reidel, (1978)

Saenz, R.A., and Shapiro, S.L., Ap. J. 244, 1033 (1981)

Smarr, L., in Sources of Gravitational Radiation, ed. L. Smarr, Cambridge University Press (1979)

Tammann, G.A. in Ann. NY. Acad.Sci., 302, ed. M.D. Papagianns, (1977)

Taylor, J.H., and Weisberg, J.M. Ap. J. 253, 908 (1982)

Thorne, K.T., in Theoretical Principles in Astrophysics and Relativity, ed. N.R. Lebovitz, W.H. Reid, and P.O. Vandervoort, Univ. of Chicago Press (1978)

Thorne, K.T., in Gravitational Radiation, ed. N. Deruelle and T. Piran, North-Holland (1982)

Trimble, V., Rev. Mod. Phys. 54, 1183 (1982)

Wagoner, R.V. preprint (paper presented at GR10, Padua, 1983)

Young, P.J., Westphal, J.A., Kristian, J., Wilson, C.P., and Landauer, F.P., Ap. J. 221, 721 (1978)

Zimmerman, M., Nature 271, 524 (1978)

Zimmerman, M., and Szedenits, E., Jr., Phys. Rev. D. 20, 351 (1979)

RESPONSE OF A FREE MASS INTERFEROMETRIC ANTENNA TO GRAVITATIONAL WAVE EXCITATION

The approach taken here is purely kinematic, the antenna masses are assumed to be free following unconstrained geodesics. In the gravitational wave metric perturbation, the measurable is the travel time of light between the masses. For simplicity of the algebra, the gravity antenna arms are laid out along the x and y axes in the antenna reference frame. The central mass is at the origin. A plane gravitational wave propagates through the antenna structure at a polar angle θ and azimuthal angle ϕ measured in the antenna frame. The gravitational wave polarization is defined in the wave frame, the primed frame, as

$$h'_{\text{Perturbation}} = \begin{pmatrix} 0 & 0 & 0 & 0 \\ 0 & h(z',ct) & 0 & 0 \\ 0 & 0 & -h(z',ct) & 0 \\ 0 & 0 & 0 & 0 \end{pmatrix}$$

A general polarization state is specified by rotation Ω about the wave propagation direction, z'.

The perturbation metric in the antenna frame is a symmetric tensor with the following independent components:

$$h_{11} = h(\hat{\gamma},ct) \quad [\cos 2\Omega \, (\cos^2\phi - \sin^2\phi \cos^2\theta) - \sin 2\Omega \sin 2\phi \cos\theta]$$

$$h_{22} = h(\hat{\gamma},ct) \quad [\cos 2\Omega \, (\sin^2\phi - \cos^2\phi \cos^2\theta) + \sin 2\Omega \sin 2\phi \cos\theta]$$

$$h_{33} = -h(\hat{\gamma},ct) \quad [\sin^2\theta \cos 2\Omega]$$

$$h_{21} = h_{12} = h(\hat{\gamma},ct) \quad [\cos 2\Omega \sin 2\phi + \cos 2\phi \sin 2\Omega \cos\theta]$$

$$h_{23} = h_{32} = h(\hat{\gamma},ct) \sin\theta \, [\sin 2\Omega \sin\phi - \cos 2\Omega \cos\phi \cos\theta]$$

$\hat{\gamma}$ is the transformed propagation vector with components

$$\hat{\gamma} = \sin\theta\sin\phi\hat{x} - \sin\theta\cos\phi\hat{y} + \cos\theta\hat{z}$$

Note that in this formulation coordinate time and proper time are the same and furthermore that the velocity of light as well as gravitational waves is c. With the gravity antenna arms along the x and y axes, the only components of the perturbation metric that will concern us are h_{11} and h_{22}.

The total metric in the antenna frame is $g_{ij} = \eta_{ij} + h_{ij}$. η_{ij} is the local inertial Minkowski metric with the convention that the time term is negative. The antenna masses are located at $(0,\ell,0)$, $(\ell,0,0)$ and $(0,0,0)$ where ℓ is the distance between masses when $h_{ij} = 0$, no gravity wave. At time t_0 light waves leave the central mass $(0,0,0)$ in the direction down the arms. At time t_x the light arrives at the mass $(\ell,0,0)$ and at time t_y the light arrives at the mass $(0, \ell,0)$. The masses are fixed at these spatial coordinate values as, in this view of the interaction, there are no forces on the antenna end points. The interval between the receipt and transmission of the light in one antenna arm is given by

$$\int_{E_1}^{E_2} ds^2 = 0 = \int_{E_1}^{E_2} g_{ij} dx_i dx_j \qquad (1)$$

As the interval is always zero (light propagation) and furthermore since the antenna arms lie along the coordinate axes, the integrals

of equation (1) are straightforward and of the type

$$\int_{E_1}^{E_2} cdt = \int_{E_1}^{E_2} \pm \left(1 + h_{ij}(\gamma, t)\right)^{1/2} dx_i \qquad (2)$$

The + and - signs are needed to account for the direction of light propagation in the arms in subsequent calculations: positive for propagation in increasing coordinate and negative for the return trip.

In the type of antennas being considered, the measurement will always consist of the difference in the times taken by the light to traverse the two arms, this difference being taken at the origin. The natural interval is therefore,a complete back and forth transit of the light in an arm.

As a specific example, let us assume a sinusoidal wave. All components of the gravitational wave metric will be given by

$$h\ (\hat{\gamma},ct)\quad h_{ij}(\Omega,\theta,\phi) =$$

$$h_{ij}(\Omega,\theta,\phi)\ e^{i(\sin\theta\sin\phi x\ -\ \sin\theta\cos\phi y\ +\ \cos\theta z)k}\ e^{-i\omega t}$$

where $k = 2\pi/\lambda$, λ being the gravity wave wavelength and ω the wave angular frequency.

Consider the x arm of the antenna first. Since we will always assume that $h<<1$, it is a good approximation to write for the trajectory of the light in the interferometer arm

$$x=c(t-t_0)$$

for the outbound trip, and

$$x=l-c(t-t_0-t_{trans})$$

for the return trip.

Here t_0 is the time of the transmission of the light, and t_{trans} is equal to the nominal one-way transit time, ℓ/c. Using the relation $k=\omega/c$, we can write for the metric on the outbound trip

$$c\ dt = (1+\frac{1}{2}h_{11}e^{-i\omega t_0 \sin\theta\sin\phi}e^{i(\sin\theta\sin\phi-1)\omega t})\ dx \qquad (3)$$

We can rearrange this expression, remembering that the second term in the parentheses is small, to give the integral expression for the interval along the outbound trip as

$$\frac{1}{t_{trans}}\int_{t_0}^{t_{x1}}(1-\frac{1}{2}h_{11}e^{-i\omega t_0\sin\theta\sin\phi}e^{i(\sin\theta\sin\phi-1)\omega t})\,dt=l$$

where t_{x1} is the time of receipt of the light. Similarly, for the return trip we can write

$$\frac{1}{t_{trans}}\int_{t_{x1}}^{t_{x2}}(1-\frac{1}{2}h_{11}e^{i\omega(t_0+2t_{trans})\sin\theta\sin\phi}e^{-i(\sin\theta\sin\phi+1)\omega t})\,dt=l.$$

Here t_{x2} is the time of return of the light at the origin.

The analysis proceeds in a similar manner for the y leg, except that $h_{22}(\Omega,\theta,\phi)$ replaces $h_{11}(\Omega,\theta,\phi)$ and the spatial propagation term in the exponential becomes $-i\sin\theta\cos\phi ky$ rather than $i\sin\theta\sin\phi kx$.

The measurable is the difference in arrival times at the origin

$$\Delta t = t_{x_2} - t_{y_2}$$

This difference is a small quantity of order $h_{ij} * t_{trans}$, therefore in those parts of the time integrations that involve h_{ij}, the second terms in the argument of time integrations, the limit t_{x_1} and t_{y_1} are replaced by $t_{trans} + t_0$ and subsequently t_{x_2} and t_{y_2} by $2t_{trans} + t_0$. With these quite justified approximations, the time difference is given by

$$\begin{aligned}\frac{\Delta t}{t_{trans}} = \frac{1}{2} e^{-i\omega(t_0+t_{trans})} [h_{11}(&\mathrm{sinc}(\tfrac{\omega t_{trans}}{2}(1-\sin\theta\sin\phi))e^{\frac{i\omega t_{trans}}{2}(1+\sin\theta\sin\phi)} \\ &+\mathrm{sinc}(\tfrac{\omega t_{trans}}{2}(1+\sin\theta\sin\phi))e^{\frac{-i\omega t_{trans}}{2}(1-\sin\theta\sin\phi)} \\ &-h_{22}(\mathrm{sinc}(\tfrac{\omega t_{trans}}{2}(1+\sin\theta\cos\phi))e^{\frac{i\omega t_{trans}}{2}(1-\sin\theta\cos\phi)} \\ &+\mathrm{sinc}(\tfrac{\omega t_{trans}}{2}(1-\sin\theta\cos\phi))e^{\frac{-i\omega t_{trans}}{2}(1+\sin\theta\cos\phi)})]\end{aligned} \tag{4}$$

For convenience we have defined

$$\text{sinc}\ (x) = \sin x/x.$$

Before discussing the implications of equation (4) it is worth noting the further modifications that are made in it if the light waves execute b traversals of the arms before their time difference is measured. This is the case in a delay line interferometric antenna. The phase shifts per pass in a Fabry-Perot interferometer are described by equation (4) but the overall response is different.

The time difference for a multi-pass delay-line system is

$$\frac{\Delta t}{t_{stor}} = \frac{1}{2b} e^{-i\left(t_0 + \frac{t_{stor}}{2}\right)} \frac{\sin \frac{t_{stor}}{2}}{\sin t_{trans}} \left[h_{11}\left(\text{sinc}\left(\frac{\omega t_{trans}}{2}(1-\sin\theta\sin\phi)\right)e^{\frac{i\omega t_{trans}}{2}(1+\sin\theta\sin\phi}\right.\right.$$

$$+\text{sinc}\left(\frac{\omega t_{trans}}{2}(1+\sin\theta\sin\phi)\right)e^{\frac{-i\omega t_{trans}}{2}(1-\sin\theta\sin\phi)}\Big)$$

$$-h_{22}\left(\text{sinc}\left(\frac{\omega t_{trans}}{2}(1+\sin\theta\cos\phi)\right)e^{\frac{i\omega t_{trans}}{2}(1-\sin\theta\cos\phi)}\right. \qquad (5)$$

$$\left.\left.+\text{sinc}\left(\frac{\omega t_{trans}}{2}(1-\sin\theta\cos\phi)\right)e^{\frac{-i\omega t_{trans}}{2}(1+\sin\theta\cos\phi)}\right)\right]$$

t_{stor} is the time the light wave spends in the antenna arms and is equal to $b * t_{trans}$.

The simplest case to understand is if the gravitational wave is normally incident on the antenna and polarized along the antenna arms. ϕ, θ, and Ω are then all zero and the antenna transfer function is simply

$$\frac{\Delta t(\omega)}{h(\omega)} = t_{stor}\,\mathrm{sinc}\left(\frac{\omega t_{stor}}{2}\right)e^{-i\omega\frac{t_{stor}}{2}} \qquad (6)$$

The magnitude as a function of gravitational wave frequency in units of $1/t_{trans}$ is shown in figure 1. The antenna has its primary response to gravity waves with frequencies less than $1/t_{stor}$ but secondary lobes exist at higher frequencies.

In this simple case with no gravity wave retardation across the antenna, the time response of the antenna is the convolution of the antenna Green's function, which is a box function of length t_{stor}, with the gravity wave signal

$$\Delta t(t') = \int_{-\infty}^{t'} h(t' - \tau)\; G(\tau)\,d\tau \qquad (7)$$

$$G(\tau) = 1 \qquad 0 \leq \tau \leq t_{stor}$$

$$= 0 \qquad \text{otherwise}$$

In effect the gravity antenna output signal is the integral of the metric perturbation taken over a storage time. The antenna faithfully reproduces pulses having time structures longer than the storage

time. It responds to shorter pulses but with reduced sensitivity and distortion.

The general case is more difficult to interpret, the transfer function in the low frequency limit when both ωt_{trans} and ωt_{stor} are much less than 1 is

$$\left|\frac{\Delta t}{t_{stor}}(0)\right| = \frac{h_{11}(\phi,\theta,\Omega) - h_{22}(\phi,\theta,\Omega)}{2} =$$

$$\frac{h}{2}[2\sin 2\Omega \sin 2\phi \cos\theta - \cos 2\Omega \cos 2\phi (1 + \cos^2\theta)] \qquad (8)$$

Phase = 0

Equation 8 shows that the antenna is sensitive to gravity waves of all polarizations coming from all directions and exhibits the symmetries in ϕ and θ associated with a pair of orthogonal quadrupolar antenna patterns. It is clear without knowledge of the polarization, Ω, a single two legged antenna will leave ambiguities in establishing the direction of the wave.

The transfer function for the medium frequency case, $\omega t_{trans} < 1$,

$$\left|\frac{\Delta t}{t_{stor}}(\omega)\right| = \text{sinc}\left(\frac{\omega t_{stor}}{2}\right)\left|\frac{\Delta t}{t_{stor}}(0)\right| \qquad (9)$$

$$\text{Phase} = \frac{-\omega t_{stor}}{2} \pm g(\phi,\Omega,\theta)\omega t_{trans}$$

which is not very illuminating but indicates that the first order effects of the wave retardation across the antenna cause phase shifts

in the antenna response. These, if there is ever a source discovered with sufficient signal to noise, would allow a measurement of the velocity of gravitational wave propagation in a single antenna.

The exact transfer functions and Green's functions for several cases are shown in figures 1 through 6. The interesting cases are those for which transfer function approaches 0 at low frequencies. The wave retardation is then the only source of response.

An interesting variant to the antenna structure discussed above has been proposed by Drever. In this scheme the light waves after having spent a time t_{stor} in each arm are interchanged between the arms. The process is repeated 2N times before their time differences are measured. The scheme results in an enhancement of the antenna amplitude sensitivity by a factor of approximately N to periodic sources with period $2t_{stor}$, but at the expense of antenna bandwidth.

The analysis that follows is for a delay line structure and is carried out for normal incidence of a gravity wave of optimum polarization, $\Omega = 0$.

The algebra is most compact if one works in the time domain using the Green's function of equation 7. Since $h_{11} = -h_{22}$ when $\Omega = 0$, the interchanges between arms cause the new Green's function to be a series of 2N unit amplitude box functions each of length t_{stor} but alternating in sign. All odd values of N being positive and even values negative.

The transfer function is the Fourier transform of the Green's function and is given by

$$\frac{\Delta t}{t_{stor}}(\omega) = 2 \sum_{\substack{m=1 \\ m \text{ odd}}}^{2N-1} \frac{e^{imx}}{ix} - 2 \sum_{\substack{m=2 \\ m \text{ even}}}^{2N-2} \frac{e^{imx}}{ix} - \frac{(e^{i2Nx} + 1)}{ix}$$

$$x = \omega t_{stor}$$

Figures 7 through 9 show the transfer functions for N = 3, 10 and 100. Each figure also shows the transfer function of a non-alternating antenna for comparison.

The analysis for a Fabry-Perot has been performed by Whitcomb (whom we also thank for having pointed out an error in a previous version of the derivation given above.) The frequency response contains an extra factor which accounts for the gradual leakage of light out of the Fabry-Perot cavities (in contrast to the discrete storage time of a multi-pass delay line). He finds that at low frequencies the Fabry-Perot system has a signal-to-noise ratio better than a delay line by a factor of e/2, while at higher frequencies the two systems have equal SNRs. Full details will be published elsewhere.

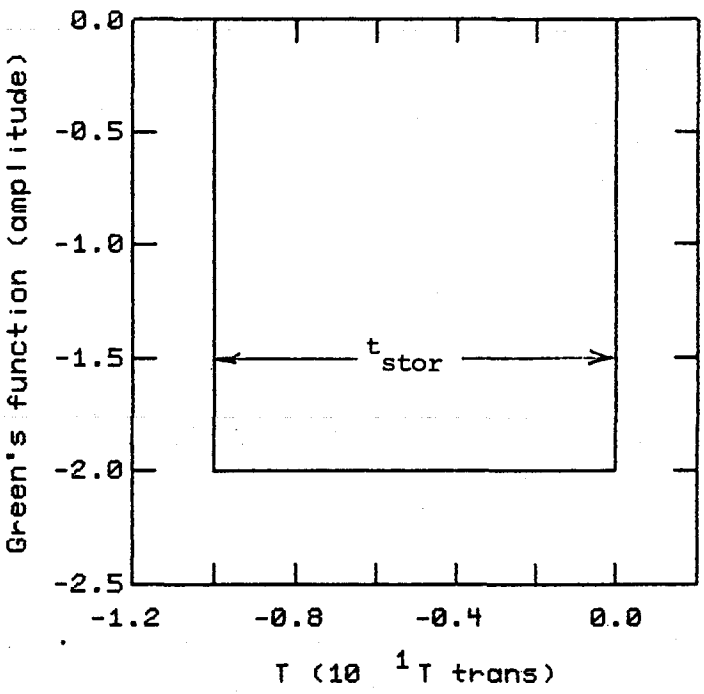

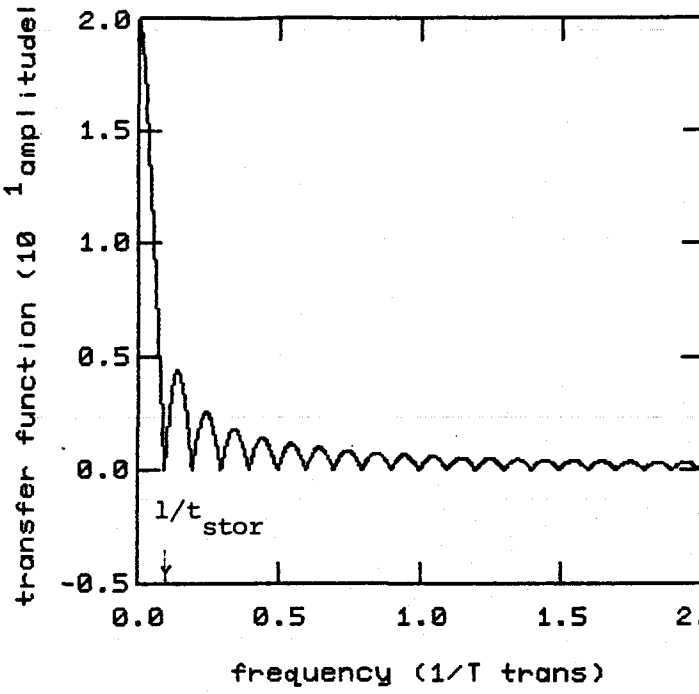

omega= 0.00 theta= 0.00 phi= 0.00 b= 10

Figure 1

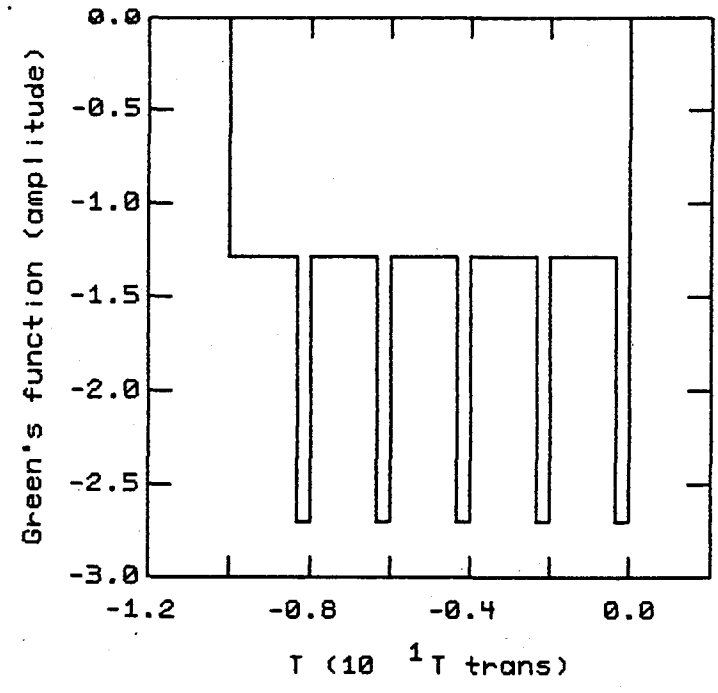

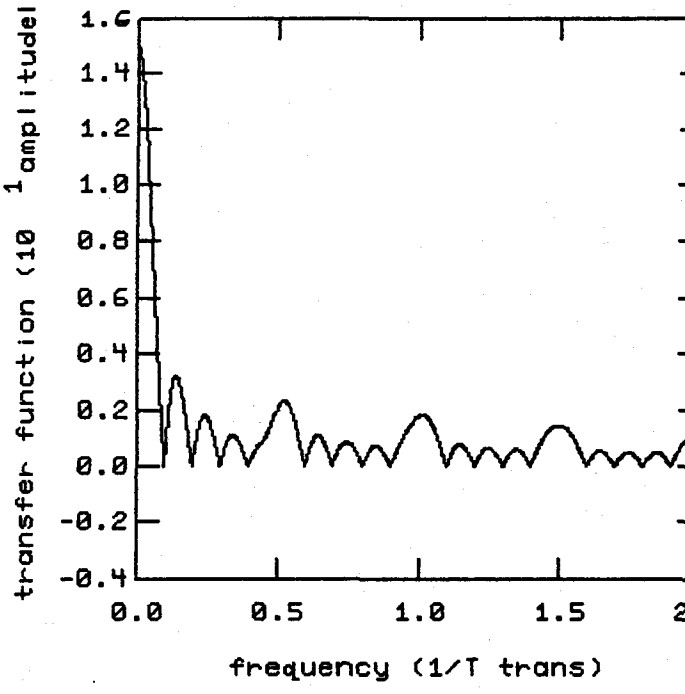

omega= 0.00 theta= 45.00 phi= 90.00 b= 10

Figure 2

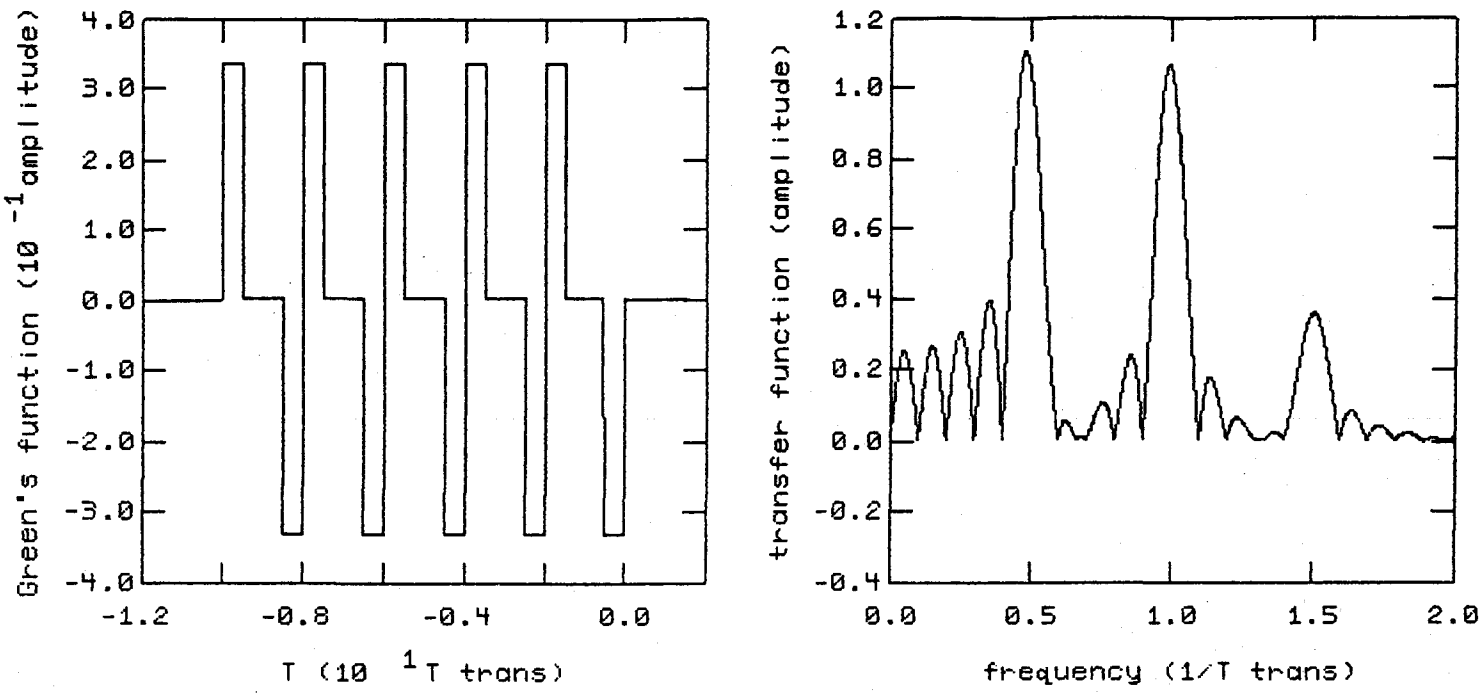

omega= 0.00 theta= 45.00 phi= 225.00 b= 10

Figure 3

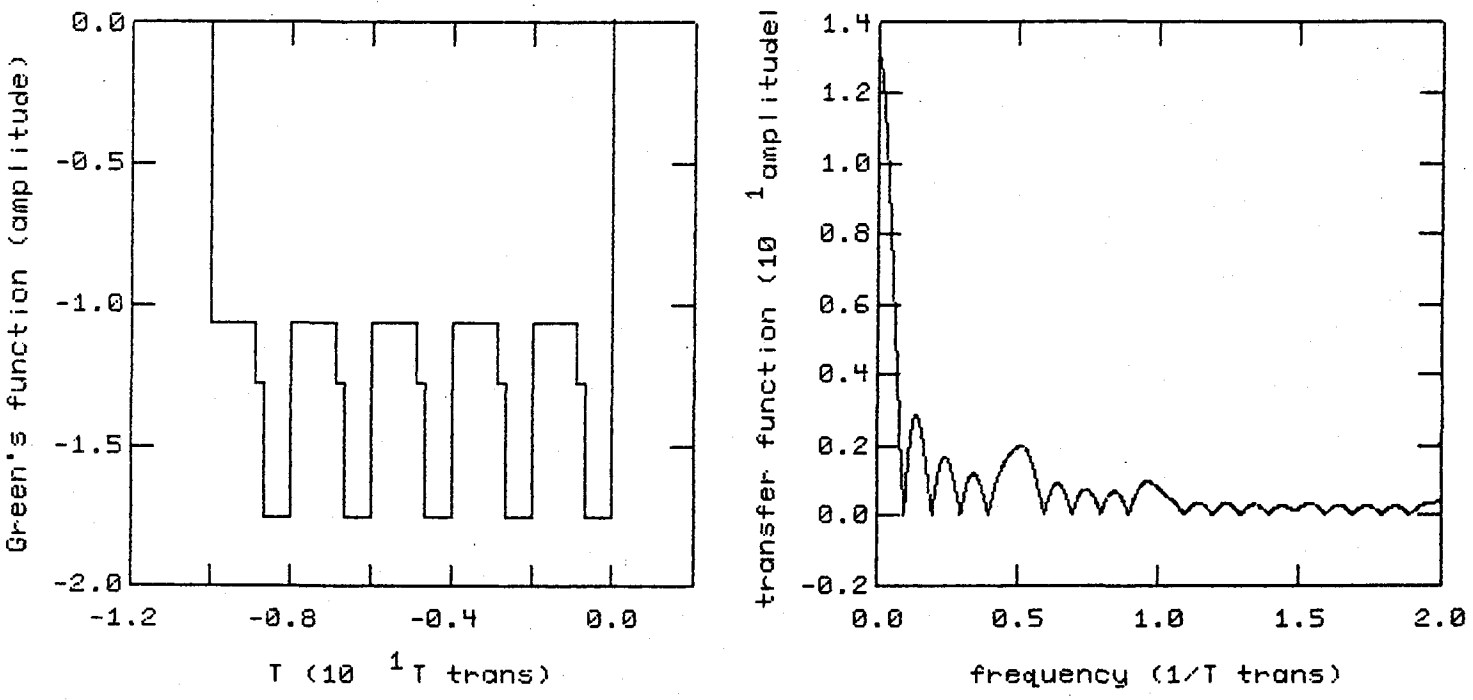

omega= 0.00 theta= 22.50 phi= 112.50 b= 10

Figure 4

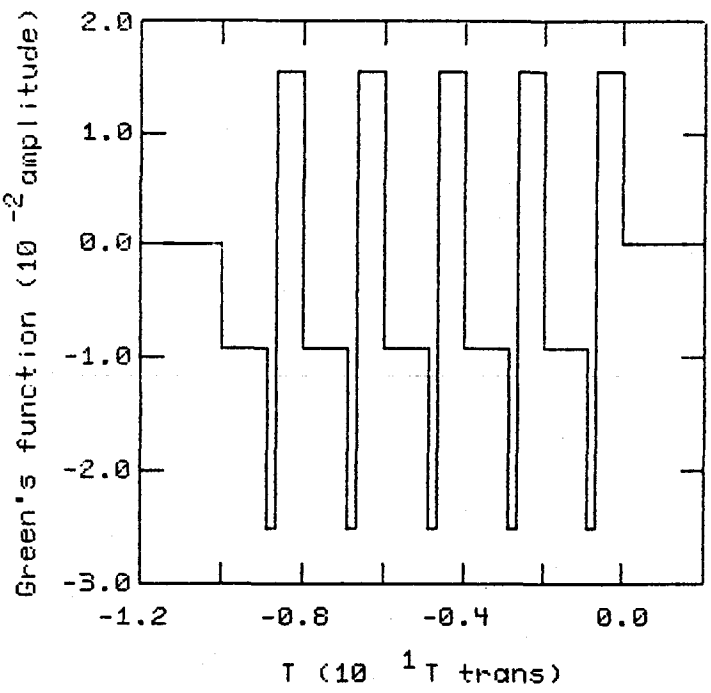

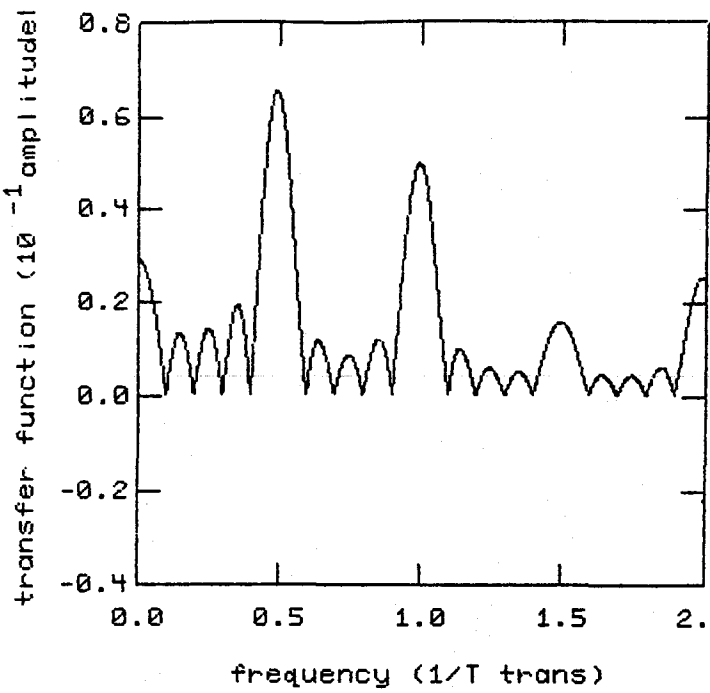

omega= 22.50 theta= 22.50 phi= 112.50 b= 10

Figure 5

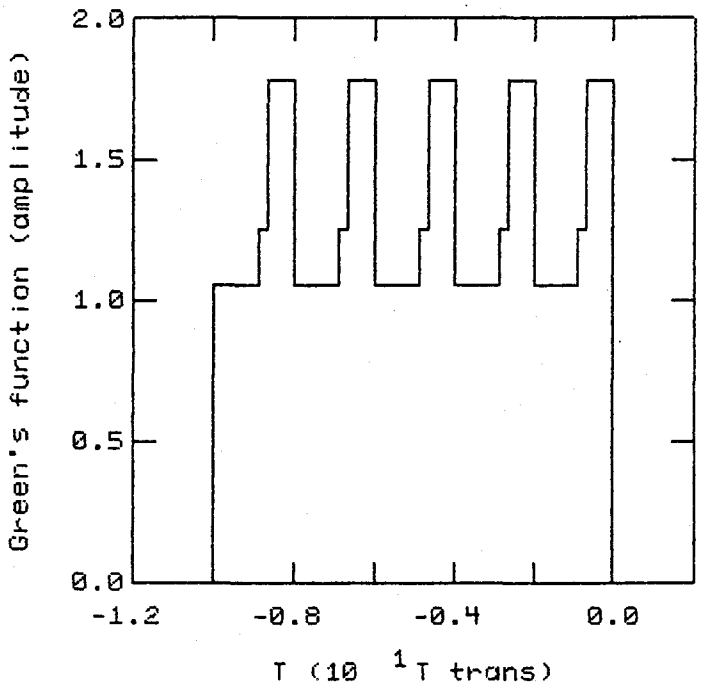

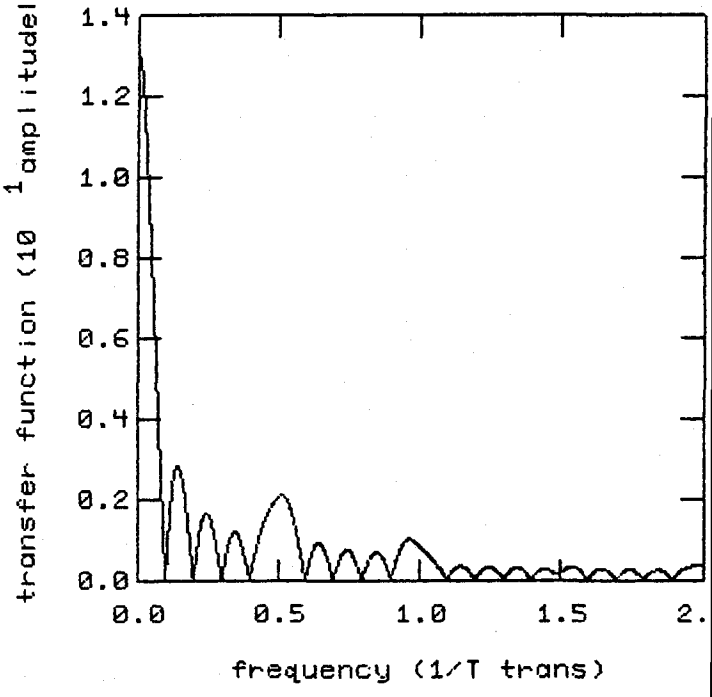

omega= 45.00 theta= 22.50 phi= 112.50 b= 10

Figure 6

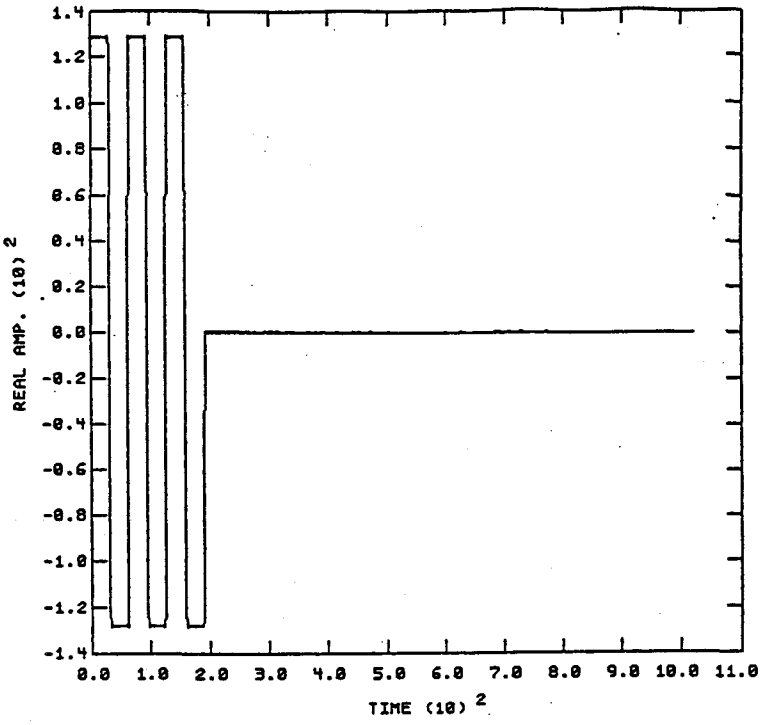

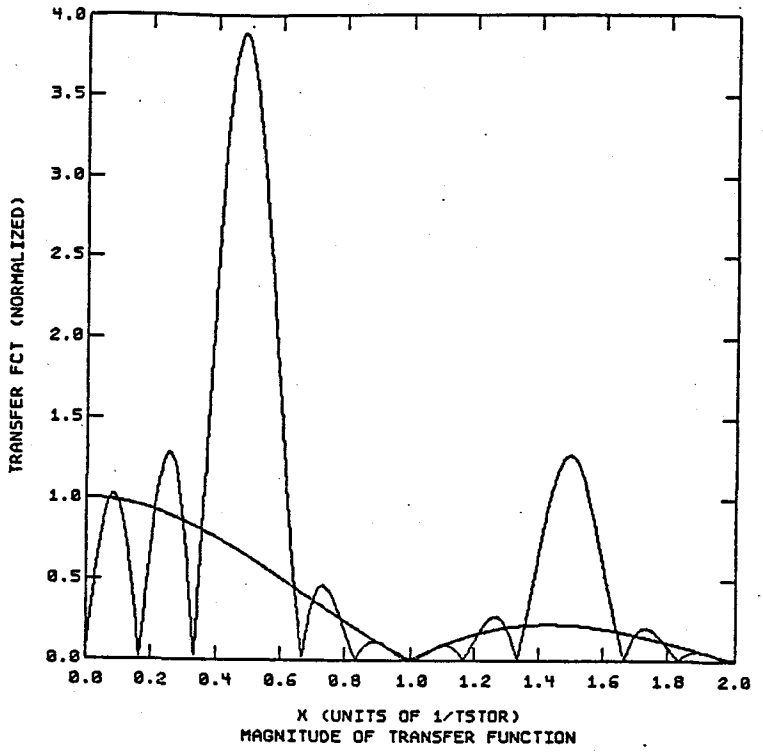

$\Omega = 0$
$\theta = 0$
$\phi = 0$
$N = 3$
$t_{stor} = 32.0$

Figure 7

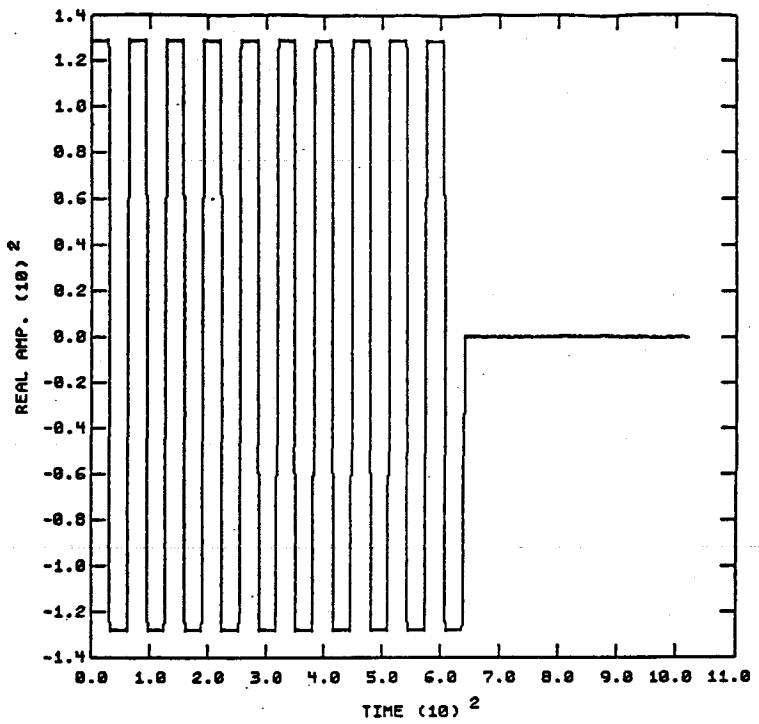

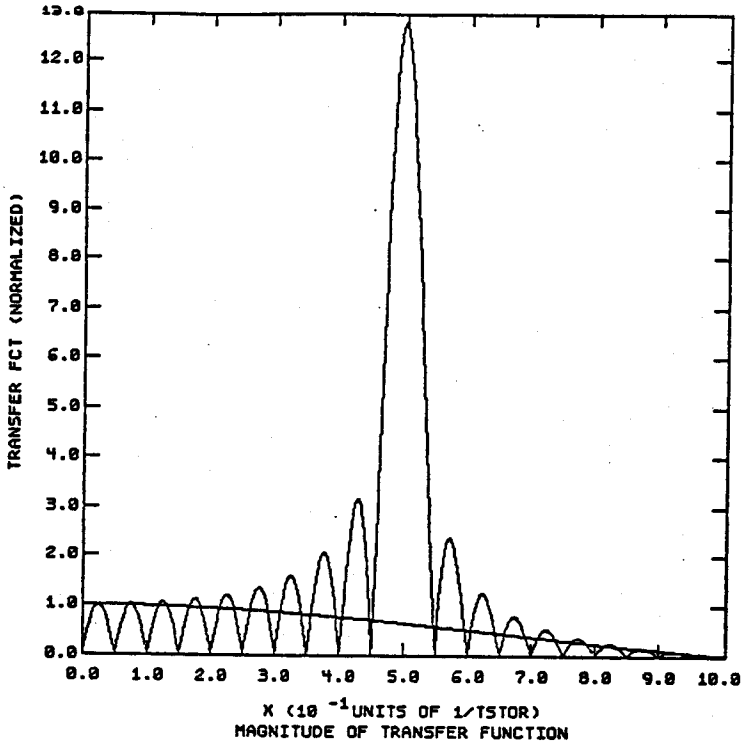

$\Omega = 0$
$\theta = 0$
$\phi = 0$
$N = 10$
$t_{stor} = 32.0$

Figure 8

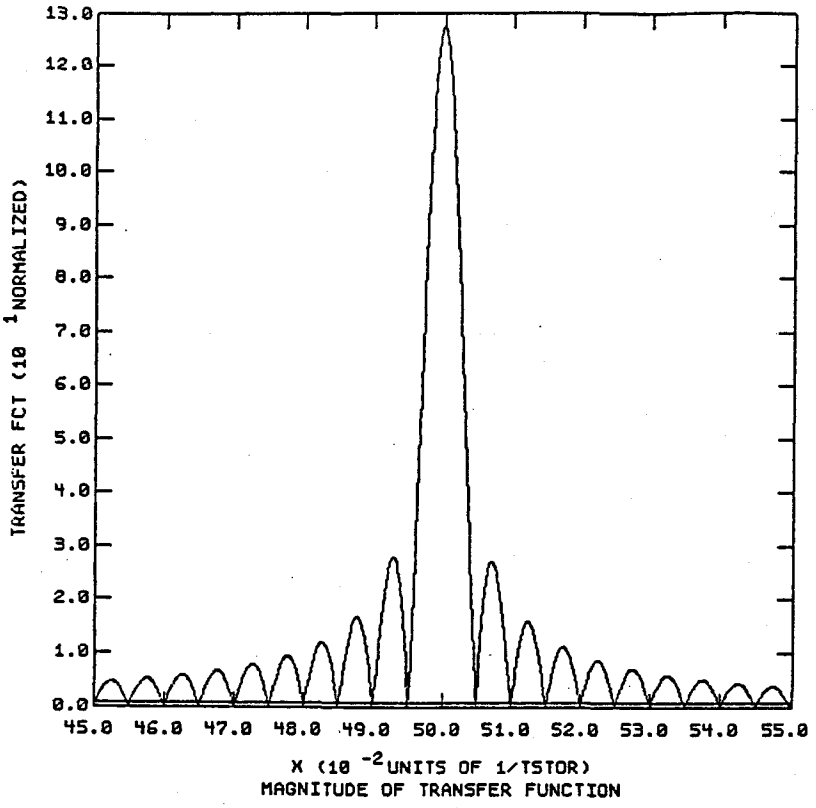

$\Omega = 0$
$\theta = 0$
$\phi = 0$
$N = 100$

Figure 9

MULTIPLE ANTENNAS AND SIGNAL DETECTION

Pulses:

Pulses are the most difficult signals to detect with a gravity antenna. This is unfortunate since some of the most interesting sources produce only short bursts of gravitational radiation. A perturbed black hole of 10 Mo is expected to produce a 1 KHz decaying sine wave which dies out after three or four cycles to give a signal lasting only a few milliseconds. The final infall of a binary system of compact stars may produce a "chirp" of increasing frequency that lasts minutes to seconds. (These and other impulsive sources are discussed more fully in the section on sources). Since these signals are so short lived one cannot improve the signal to noise by integrating for long periods of time as is possible with a stable periodic source. There are two ways to improve the signal to noise: first reduce the system noise to the minimum possible; second, use multiple antennas and coincidence techniques. Having reduced the system noise to the minimum possible the use of multiple antennas allows identification of low signal to noise sources with improved confidence.

In general we do not know the distribution of sources but do know the probability density of the noise spectrum. This information is sufficient for estimates of the false alarm rate, P_{fa}, and our ability to find a signal in an otherwise noisy spectrum. If the noise time series is a stationary Gaussian process, then the probability that its

amplitude, r, exceeds some threshold value, x, is given by

$$P(r>x) = \frac{2}{\sigma\sqrt{2\pi}} \int_{x}^{\infty} \exp(-t^2/2\sigma^2)\,dt$$

where the root mean square noise amplitude equals σ. As every experimenter knows, very few noise processes are actually Gaussian beyond three or four standard deviations. Generally the distribution develops long tails due to rare events which cannot be modelled by a normal distribution. We can separate true signals from local noise by applying coincidence techniques to these extraneous pulses. In order to get some idea of the ability of multiple antennas to reduce these long tails we choose an exponential noise distribution (which is analytically tractable). In this case, where the time series is a stationary exponential process, the probability that the noise amplitude, r, exceeds some threshold value, x, is given by

$$P(r>x) = \exp(-x/\sigma)$$

These cumulative distributions are shown in figure 1.

These curves plus a few simple assumptions allow us to calculate the improvement we get in using a pair of antennas over a single antenna and the size of signal needed to be certain that we are not fooling ourselves. For example, if we assume that we have a three millisecond time resolution, and require no more than one false alarm

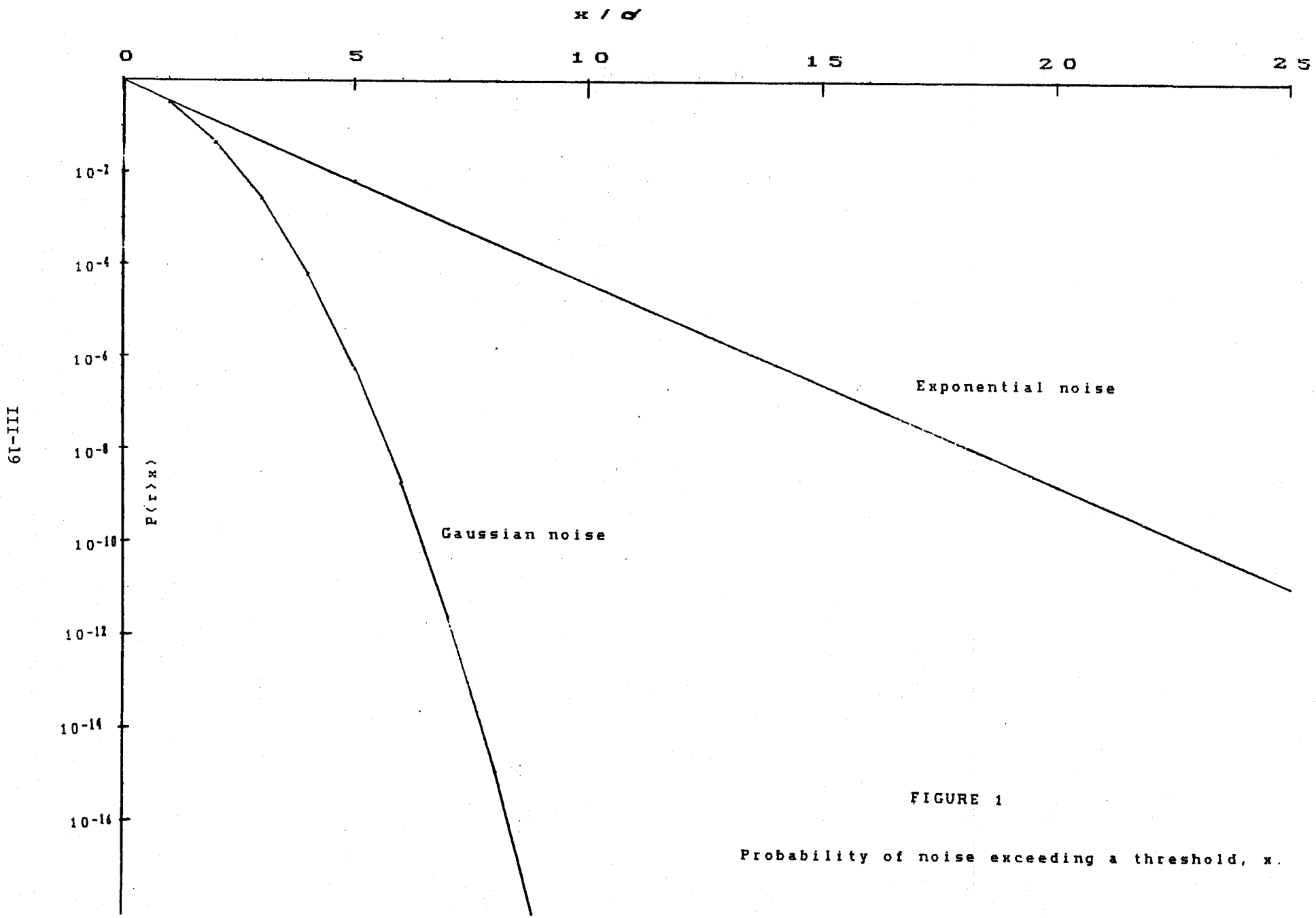

FIGURE 1

Probability of noise exceeding a threshold, x.

every 10 years, then the threshold must be set to give

$$P(r>x) < 10^{-11}$$

if only a single antenna is in operation. In the case of Gaussian noise the threshold must be 6.8 σ and for the case of exponential noise cutoff is at 25 σ. If we run a pair of antennas in coincidence the threshold of each antenna only needs to be set to give

$$P(r>x) < 10^{-5.5}$$

for each antenna. This probability is achieved for a Gaussian process if the signal threshold in the Fourier spectrum is set to 4.8 σ and for the exponential process at a level of 12.5 σ. This is made more dramatic in fig. 2 which shows the rate per day of false threshold crossings for a single antenna and for a pair of antennas in coincidence when the noise process is Gaussian. At a setting of 4.8 σ the antennas in coincidence only produce a false signal once every ten years whereas each antenna alone crosses threshold 100 times a day or nearly once every 15 minutes. The same holds true for an exponential noise process (Fig 3) but at the higher threshold level of 12.5 because of the long tail. We learn two things from this calculation: a pair of antennas allows us to reduce our threshold for detecting signals while simultaneously keeping spurious signals at a manageable level, and; if the noise process responsible for false alarms has a long tail, as in the case of the exponential, coincidence detection of a signal allows a

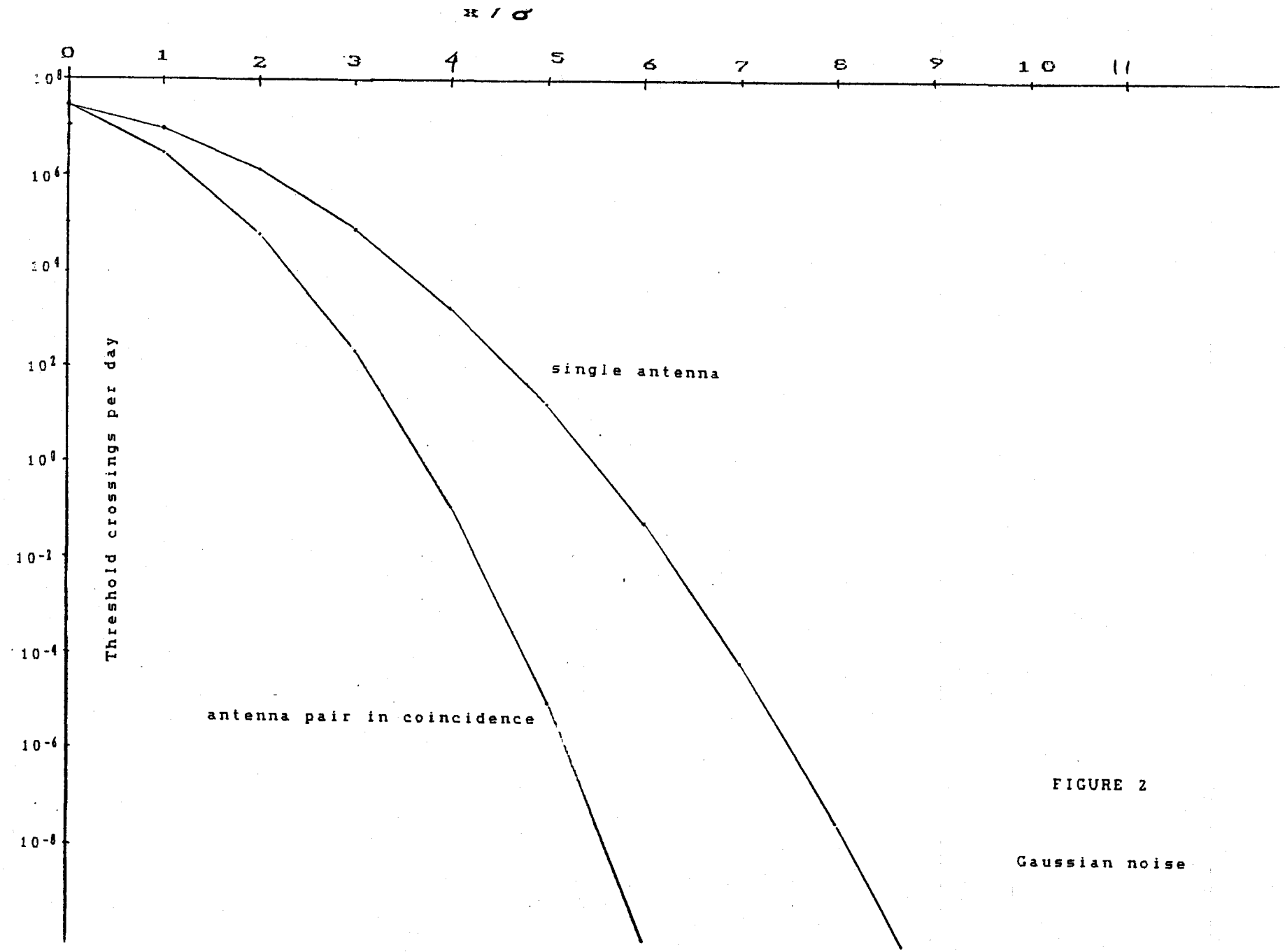

FIGURE 2

Gaussian noise

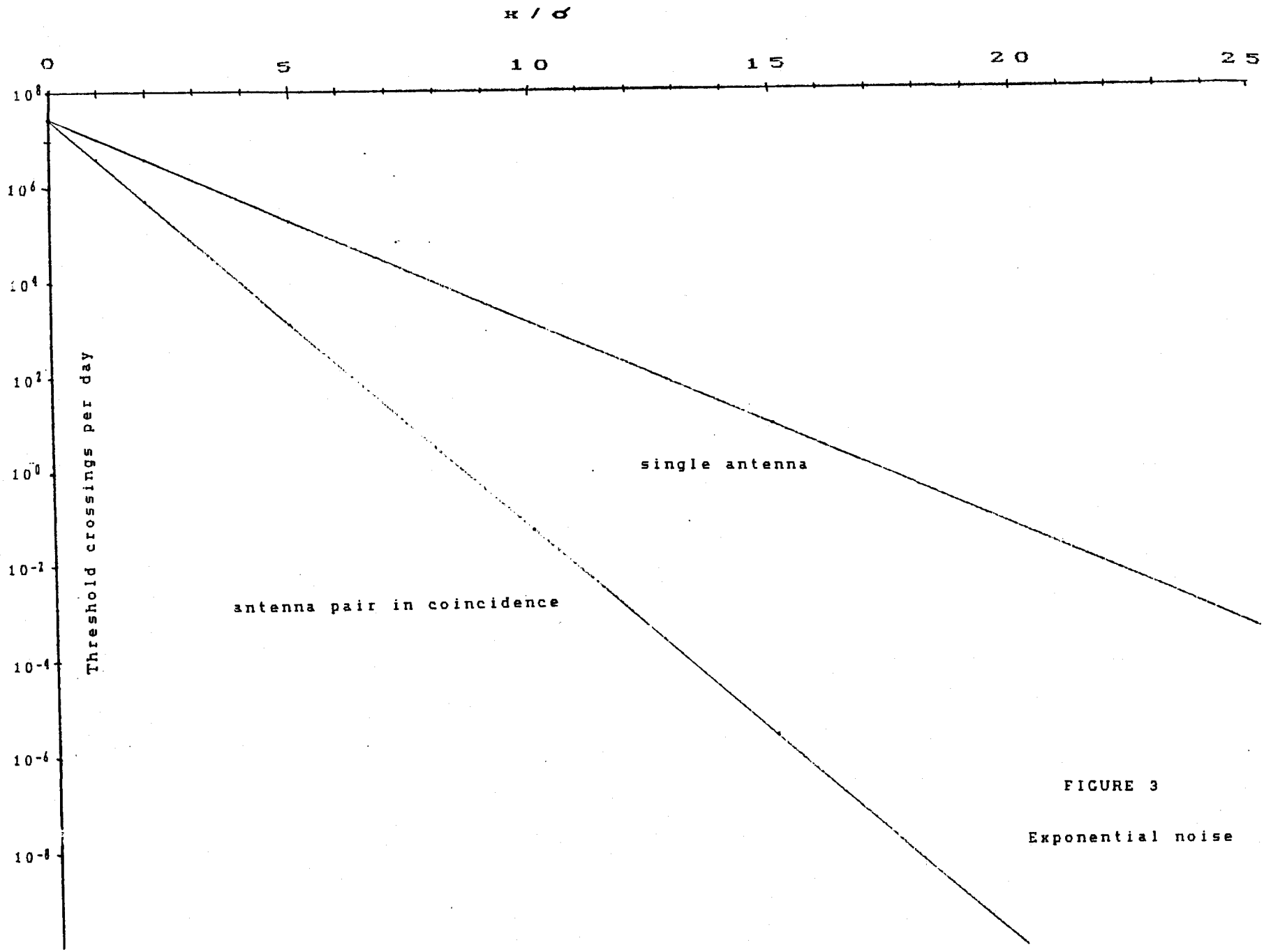

FIGURE 3

Exponential noise

dramatic reduction of the signal threshold relative to the use of a single antenna.

We can now proceed further and use these values to estimate our sensitivity to a particular source. The black hole signal described above is a damped sine wave,

$$h(t) = h_o \exp(-at) \sin(wt) \qquad t>0.$$

From Detweiler's results one finds that the signal damps out after four or five cycles independent of the mass (hence frequency) of the black hole and as a consequence the peak strain field is about $0.8\ h_o$.

We know from statistical communications theory that if a noise process has a frequency dependent power spectral density, $h(f)$, and if the system transfer function is $T(f)$, then the mean square noise function within a frequency band is

$$h^2_{rms} = \int_{f_0}^{f_1} h^2(f) |T(f)|^2 \, df.$$

For the simple case of a constant noise density and a unity transfer function

$$h_{rms} = h(f)(\Delta f)^{\frac{1}{2}}$$

If the antenna noise is $2\text{x}10^{-23}/\text{Hz}^{1/2}$ then the r.m.s. noise fluctuation due to the assumed 333 Hz bandwidth is $3.5\text{x}10^{-22}$. A pair of antennas in coincidence which had Gaussian noise could detect a signal with a strain of $2\text{x}10^{-21}$ with certainty whereas a single antenna with an exponential background noise process would only be able to see signals with a strain greater than $1\text{x}10^{-20}$. Optimum filters can be used to improve these limits.

Periodic Sources

The detection of periodic sources presents a different problem in signal analysis from finding pulsed gravity wave signals. In principle the method is quite straightforward with a broadband antenna: one takes a time series of length T and takes the Fourier transform. A perfect sine wave source will appear as a peak at a single frequency. Since the system is broadband all signals of sufficient amplitude and within our bandwidth can be searched for simultaneously.

The true frequency resolution of a single frequency bin is 1/T so that noise with a power spectral density of h(f) produces a noise amplitude $h(f)/T^{\frac{1}{2}}$ in a frequency bin centered on f. The longer a time series one can take and invert the better the frequency resolution and the smaller the noise amplitude in each frequency bin. For example if we can take an uninterrupted time series that is one month long, that is, 2.6×10^{6} seconds long and if our system noise is $2 \times 10^{-23}/Hz^{\frac{1}{2}}$ the frequency resolution will be 3.9×10^{-7} Hz and we will be able to see periodic sources with strains greater than 1.2×10^{-26} at a signal to noise ratio of one. (The detection criteria described above for pulsed sources must be applied to periodic sources as well.) A pair of antennas can be used to improve sensitivity and to reject local periodic sources such as internal resonances of the equipment, rotating machinery, and so forth which will not be the same at both antennas (signals associated with the 60 Hz line frequency are an exception to this). There are major computational difficulties to be overcome here. If the incoming signal is sampled at the rate of 5 KHz for a month we will have to perform a Fourier transform on 1.3×10^{10} points in order to achieve full sensitivity. Any algorithm to search for periodic sources is further com-

plicated by the fact that the antenna response to a fixed source in the sky varies with the daily rotation of the earth and the yearly rotation of the earth around the sun. The frequency of the signal is also modulated by the Doppler shifts caused by the earth's rotation ($v/c \sim 1.6 \times 10^{-6}$) and by the annual motion ($v/c \sim 1.0 \times 10^{-4}$). For example, a 1 KHz signal must be corrected for the daily 10^{-3} Hz and annual 10^{-1} Hz Doppler shifts to achieve the full frequency resolution available in the long integration times we anticipate.

Stochastic sources

Stochastic sources can only be found with multiple antennas since the signal is by definition the noise in the external "bath" of gravitational radiation and must be measured by cross correlating the noise in two or more antennas. The requirements for measuring the stochastic background are in conflict with those for pulse detection. Pulse detection requires a large separation between antennas so that local sources cannot produce spurious coincidences between the antennas. However a large separation between antennas produces a high frequency sensitivity cutoff to the stochastic background that is inversely proportional to the antenna separation. This cutoff does not apply to a point source of gravitational noise. In that case one can recover the correlation between antenna signals by introducing an appropriate time delay. In either case it can be shown that the estimate of the noise spectrum improves with the square-root of the integration time.

References:

Detweiler, S., Ap. J. 239, 292 (1980)

OPTICAL CONCEPTS AND THE PROTOTYPE DESIGNS

The intent of this section is to discuss the choices for the optical design of an electromagnetically coupled antenna. The fact that there are choices is in good measure due to the inventiveness of the various research groups and their differences in taste. No specific design is at present obviously superior to the others in concept or ease of implementation and all of the concepts would function in a long baseline system. We begin by describing the various prototype antennas and at the end of the section attempt to summarize by classifying the differences in the approaches and discuss their implications for a large baseline system.

We start with the prototype at MIT, not that it is necessarily better than the others, but it is the most familiar to us. A schematic diagram of the apparatus is shown in Figure 1. The device is a Michelson interferometer in a vacuum with the mirrors mounted on masses suspended by single rods as pendula. Light entering from outside the vacuum system is split, then enters the interferometer arms through holes cut in the mirrors. The light traverses each arm 60 times (eventually 200 times) and reemerges through the same hole by which it entered, but at a different angle than on entering. The multipass geometry is an optical delay line and is formed by two spherical mirrors, the number of transits is determined by the radii of the mirrors and their separation. When the input and output beams pass through the same point, the configuration is called reentrant. In this condition the beam appears to be reflected by the back spherical

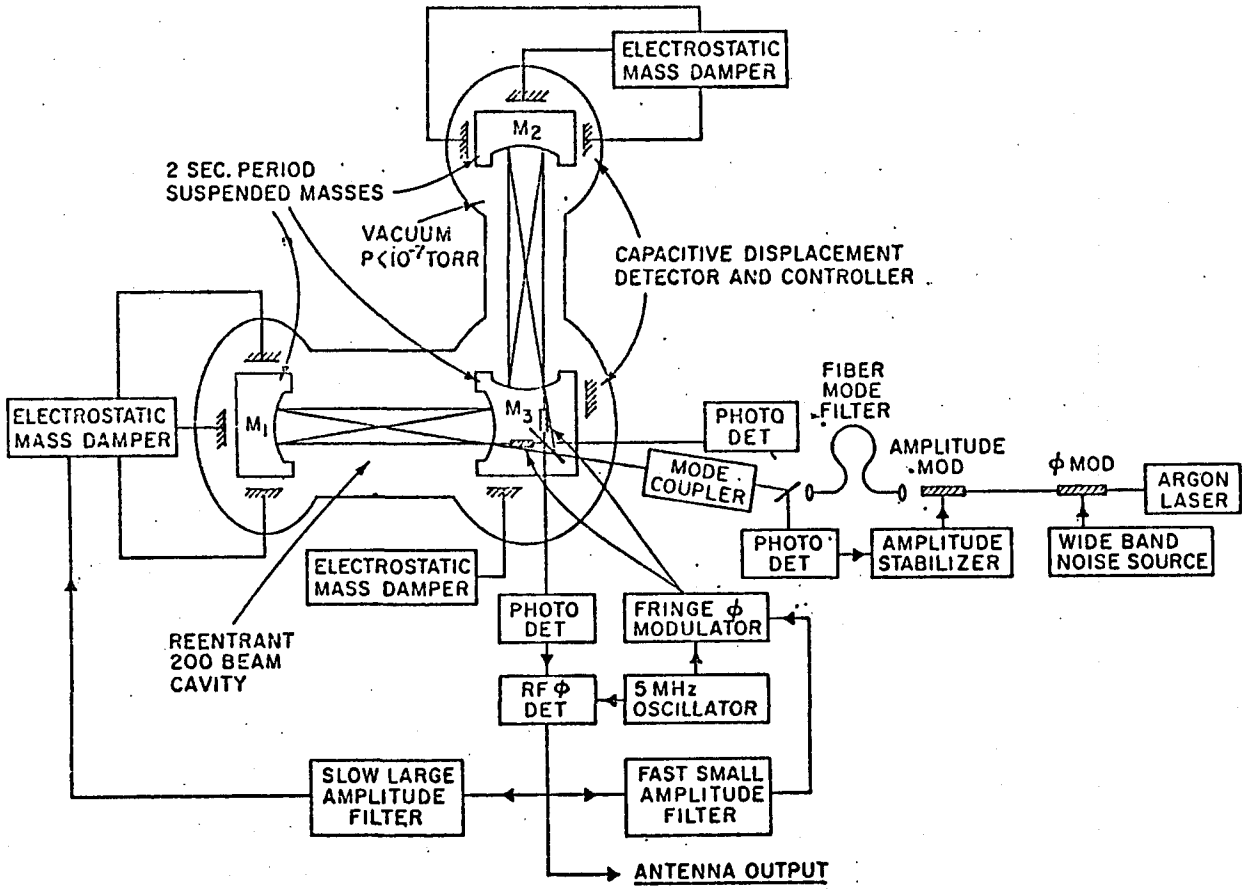

Figure 1 The Prototype Antenna at MIT

surface of the input mirror and the position and angle of the output beam become independent of the position of the other mirror. The reentrant geometry has several alignment insensitive properties. In each arm of the interferometer the light next passes through an electro-optic phase modulator (Pockel's cell) after which it is recombined. Both the sum and difference outputs are measured at photodetectors.

In order to measure the fringe motion, a 5 MHz phase modulation is impressed on the beams in each arm by the electro-optic modulators. As a consequence, the photodetector output voltage will contain signals at 5 MHz and its harmonics. The amplitude of the 5 MHz signal is proportional to the distance a fringe has moved from a symmetry point and the phase gives the direction of the motion. These signals are demodulated and returned to the Pockel's cells after filtering to hold the interferometer on a symmetry point of the fringe. This is the first of many feedback systems in the device. The speed of the electrooptic device is high but the dynamic range is limited, so that to hold the interferometer on a fixed fringe, for low frequency but large amplitude excursions one of the masses is moved by electrostatic controllers driven by the demodulated photodetector output. The gravitational wave signal is then measured as the voltages required to maintain the interferometer on a fixed fringe. The advantages of this seemingly complicated arrangement are many. By high frequency modulation, the fringe signals are

placed at frequencies where the laser, photodetectors and amplifier are free of 1/f noise. By holding the fringe in this null servo technique, gain variations are suppressed, the extrinsic amplitude fluctuations of the light become less important and one can maintain the unique zero path length difference fringe (white light fringe) which is needed to reduce the noise from frequency fluctuations of the input light.

The remainder of the optical system serves to control another set of noise sources. The light source is a ½W Argon ion laser used at a wavelength of 5145A°. The light first enters an electrooptic phase modulator driven by wide band noise which serves to spoil the temporal coherence of the light by converting the laser's narrow line into a Lorentzian with an an instantaneous line width of approximately 3 GHz.

The frequency broadening is useful in suppressing the interference modulation of the main beam by scattered light in the interferometer. As the scattered light will have experienced different relative delay times than the main beam, this interference modulation will be washed out if the relative delay times are longer than the reciprocal of the instantaneous line width.

Following the phase modulator is an amplitude modulator used in a servo loop to remove low frequency amplitude noise in the laser output. The photodiode that samples the light to control the ampli-

tude fluctuations is placed after the light has passed through a single mode polarization preserving optical fiber. This fiber, a few meters long, serves two functions. First it permits the laser, which is a mechanical noise source due to its water cooling, to be placed at a distance from the antenna. More important, because the fiber propagates only one mode and is lossy for all others, the end of the fiber fixed to the antenna becomes a light source invariant in beam profile and phase front to the injection conditions at the other end. This is significant since it is never possible to align an interferometer so well that the phase difference of the beams traversing the two arms is totally insensitive to the input injection conditions. The mode filtering by the fiber is sufficiently wavelength independent to accomodate the frequency broadening of the laser light due to the phase noise modulator. The fiber may introduce additional amplitude fluctuations of the light which are removed by the amplitude modulator.

The final element in the optical train is a spatial mode coupler which matches the output of the fiber to the spatial modes of the optical delay line. In the present prototype the fiber and mode coupler are external to the vacuum. In the next refinement of the prototype the mode coupler and the output end of the fiber will be mounted on M_3, the central mass.

The final components of the apparatus are a set of 18 servo systems that capacitatively sense and electrostatically control motions

of the masses. The principal function of these servos is to independently damp the oscillations of each of the 6 degrees of freedom of the 3 masses hanging on their suspensions. The damping reduces the Q of the modes electronically and adds little additional noise in the gravitational wave band at higher frequencies. By reducing the Q of the modes the rms motions of the masses driven by ground noise are made small enough so that the fringe servo system can maintain a lock on one fringe without exceeding the dynamic range of the controllers. Not all modes of motion are equally important in producing a fringe shift, in fact when the interferometer is properly aligned all motions that do not have a net component along the arm when integrated over all the beams produce fringe shifts proportional to second order in those motions. The servo systems also provide a means of positioning the masses and the servo output signals are used to determine the ground noise excitation spectrum.

Although all the individual elements of the system have been tested over the past several years, the complete integration of the apparatus took place in the summer of 1983. At this time (Fall 1983) in the process of progressively testing the integrated device, the position sensitivity with the masses not floating has been determined. In the frequency band above 4KHz the position noise is 10^{-14} cm/Hz$^{\frac{1}{2}}$ and limited by the shot noise in the photo current.

A schematic diagram of the prototype at the Max Planck Institute

near Munich is shown in figure 2. The instrument is an evacuated Michelson interferometer using delay line optics with arms 3 meters in length. The beam executes 138 passes in the arms. The fringe interrogation scheme is similar to that in the MIT prototype but only one phase modulator is used which impresses phase modulation in one arm but on both beam entry and exit. The system is used as a null servo on a fringe by feedback to the phase modulator and at low frequencies to control the position of one of the masses. No special effort is made to operate on the white light fringe.

The external optics are different than in the MIT device. An important difference is that the laser frequency is actively stabilized by locking the laser to an external high Q Fabry-Perot cavity which serves as a short term frequency reference. The technique employs an electrooptic phase modulator in the laser optical cavity as an optical path length modulator to control small amplitude high frequency laser frequency fluctuations and a Piezo electric translator on one of the laser mirrors to control lower frequency large amplitude frequency excursions. With this technique they have achieved short term laser frequency noise amplitude densities of 10^{-1} Hz/Hz$^{\frac{1}{2}}$. In a side experiment not shown in fig. 2, they have further improved the frequency stability by another factor of 10 by using the entire Michelson interferometer as a reference cavity.

The frequency stabilized light beam after leaving the laser is passed through a high Q mode apodizing cavity. The cavity is a Fabry-Perot interferometer designed to have high transmission losses for

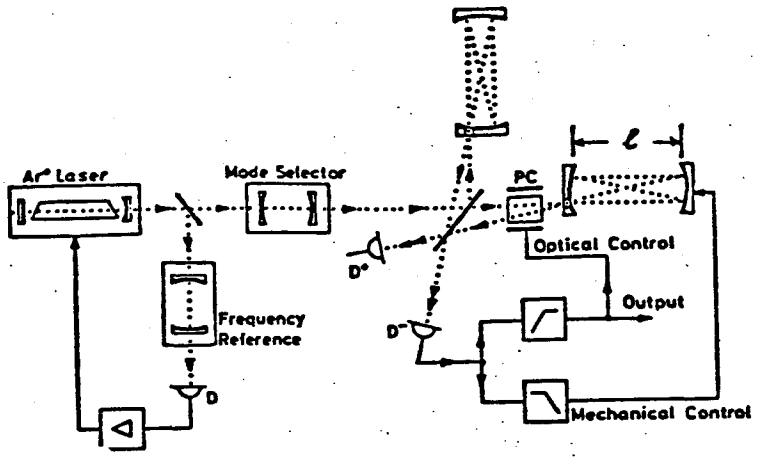

Fig. 2 The Prototype at the Max Planck Institute

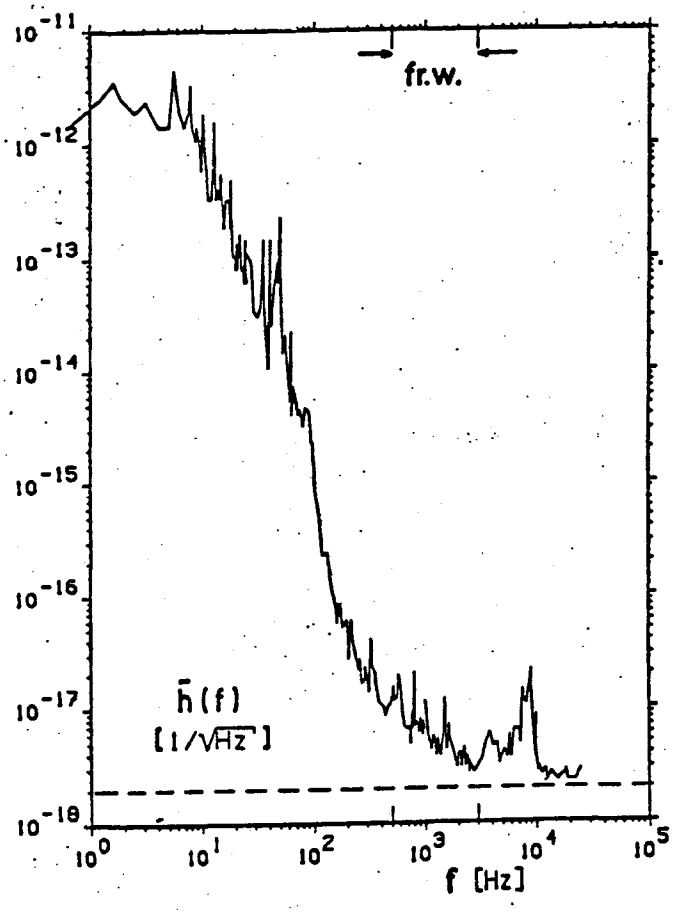

Fig. 3
Noise spectrum in Munich 3-m interferometer, expressed as apparent strain $\tilde{h}(f)$. Data taken September, 1982. Dotted line represents shot noise limit for ηP = 25 mW

all spatial modes but the lowest order Gaussian mode. This cavity serves to suppress the laser beam angle and position fluctuations before the beam enters the interferometer.

Laser frequency stabilization is used in this system for several reasons. The primary function is to reduce the interferometric noise due to scattered light. The philosophy being to accept the interferometric terms in the scattering with different delay times but to reduce the noise contribution in the overall interference by fixing their phases. The assumption being that the individual scattering sources are themselves physically stationary. The second purpose of frequency stabilization is to relax the condition on the equality of paths in the two interferometer arms as it lays demands on the equality of the mirror radii to simultaneously achieve the white light fringe and the reentrant beam geometry-- a problem that is possibly more difficult to handle in a short antenna than a long one. Finally, the mode apodizing cavity requires a narrow laser line to function.

The masses are isolated from ground noise by pendulum suspensions. Each mass has separate optical sensors to determine rotation and translation locally. The output of these sensors is used to damp the suspension modes by applying magnetic forces from air core coils fixed to the ground on a set of permanent magnets mounted on the masses. Furthermore the same controllers are used for pointing the mirrors

in a separate optical system which senses the relative orientations of the masses.

The noise spectra of the instrument are shown in figure 3. They at present represent the best performance of any prototype in operation. The data is plotted as the equivalent strain noise amplitude density. Aside from what is now believed to be a low Q noise peak from a poor mirror mount near 8 KHz, the displacement noise above 1 KHz is close to $1 \times 10^{-15} cm/Hz^{\frac{1}{2}}$.

The instrument in operation at Glasgow is shown in figure 4. It is the first version of an evolving design using Fabry-Perot cavities rather than multipass delay lines as the antenna arms. The CalTech prototype, figure 5, is quite similar in concept and in the ensuing presentation they will be described together indicating only where the instruments differ. The Glasgow antenna has a length of 10 meters while the CalTech system is 40 meters long. This is the largest system now in operation. In both prototypes the two Fabry-Perot cavities are used as independent interferometers. One arm is used as a reference cavity in an elegant laser frequency stabilization scheme similar in concept to the Pound stabilizer for microwave oscillators. In this scheme the laser light is compared in frequency with the frequency filtered light stored in the cavity. A frequency discriminant is derived by phase modulation of the laser output with an electrooptic phase modulator that impresses radio

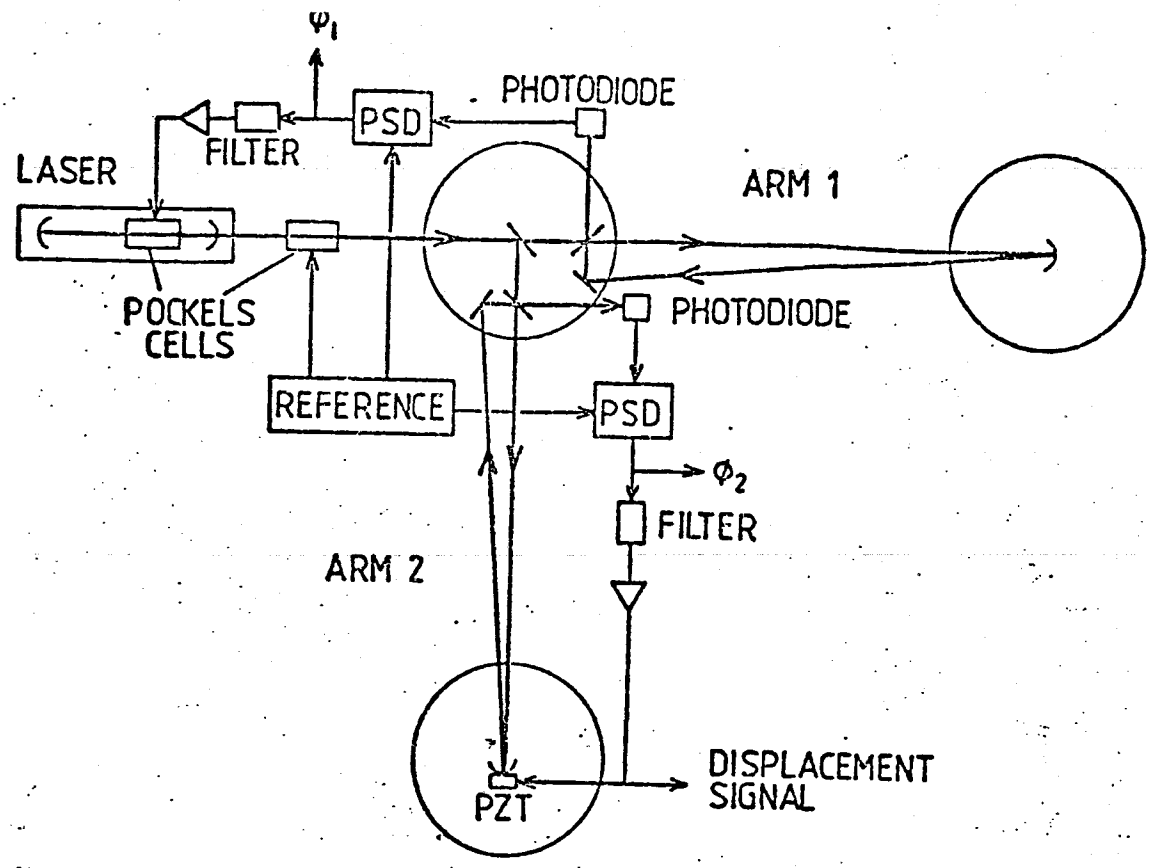

Fig. 4 Schematic diagram of the optical cavity interferometer being tested in Glasgow.

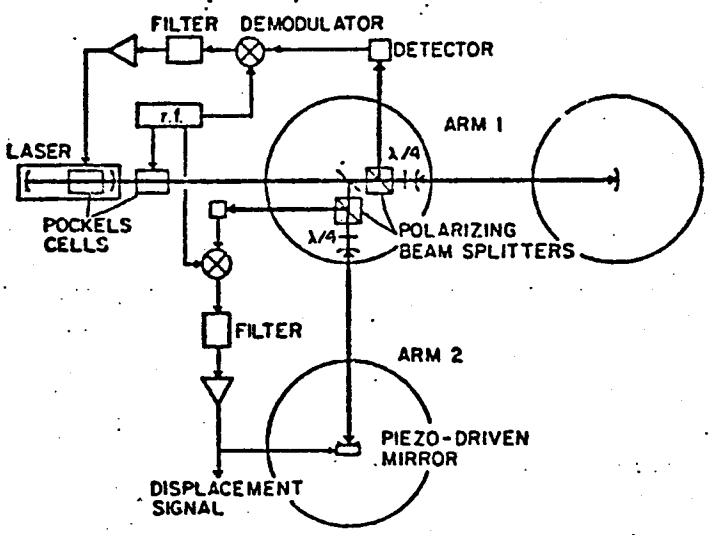

Schematic diagram of optical cavity interferometer currently in use at Caltech.

Fig. 5

frequency side bands on the light outside the acceptance band of the cavity. The phase and amplitude of the interference at the side band frequencies contains the information required to derive an error signal proportional to the amplitude and sign of the frequency difference of the instantaneous laser frequency and the cavity resonance frequency. The important feature of the stabilizing system is that it is not limited in bandwidth by the cavity storage time. The error signal is used to control a Pockel's cell phase modulator within the laser cavity to control the laser frequency.

With the laser frequency locked to the length of one arm, the same phase modulated light is impressed on the second arm. The reflection of this second cavity is measured in the same manner but on a different photodetector. The error signal derived in this system is a measure of the length of the second arm. The error signal is used to adjust the length of the arm by a Piezo electric translator mounted on one of the mirrors in a null servo. This error signal includes the gravitational wave signal.

The optical implementation at Glasgow uses a triangular cavity to avoid reflections back to the laser, while the Cal-Tech system employs two mirrors (hence smaller cavity losses) and nonreciprocal polarization isolators to avoid these reflections.

In near future developments of the prototypes the reflections from the two arms will be combined interferometrically before photo-

detection to further reduce the sensitivity to laser frequency fluctuations providing the cavities are well matched.

Laser beam jitter may be a noise source and both Glasgow and CalTech are incorporating mode apodizing cavities in their prototypes.

The masses are supported by pendulum suspensions but with multiple wires to allow for orientation and positioning. In this scheme the controlling forces are applied to the support points of the suspension rather than to the masses directly, which affords some measure of isolation from the high frequency noise forces that may originate in the positioning servo systems. The positioning error signals, which damp and orient the masses, are derived, as in the Munich system, by auxiliary optical levers locally and with optical levers between the masses to gain fine position and orientation control.

Frequency stabilization of the laser is a central requirement of the Fabry-Perot scheme, by matching the cavity storage times it is anticipated the demands on the precision of the stabilization can be reduced. The effect of light scattering by the mirrors (but not by other components in the system) may be less influential in a Fabry-Perot than in the delay line geometries. Finally the Fabry-Perot offers similar rotation and transverse translation independence as the delay line if the radial modes other than the principle Gaussian mode are suppressed.

At present the two Fabry Perot systems are exhibiting comparable position amplitude spectral densities of 10^{-14} cm/Hz$^{\frac{1}{2}}$ at frequencies

above 5 KHz. Cal Tech has operated its system continuously for periods of several weeks.

Classification of the Optical Concepts

The long range goal for the optical design is to bring the measurements of the time (phase) differences to a level where the antenna strain sensitivity is limited by the stochastic forces on the masses. In the limit when the stochastic forces due to the quantum pressure fluctuations are the only ones remaining, the system has attained the quantum limit. This is not a hope in the near future at high gravitational wave frequencies but may become a serious consideration in long baseline antennas at lower frequencies in this decade.

The short term goal for the optical design is to achieve Poisson (shot) noise limited performance with the largest circulating optical power in the antenna for long storage times. Clearly this goal can not be viewed in isolation from the entire system performance which will require a parallel effort to reduce the stochastic forces, but at high frequencies the dominant noise contribution is expected, at present, to be imposed by the Poisson noise limit.

The prototypes are a convenient vehicle with which to highlight the various approaches toward achieving the short term goal. In all

cases, however, the choices are driven by the assessment of technical feasibility rather than any fundamental issues because the limiting sensitivity of all the schemes is the same.

One branch point is the choice to use broad band or narrow band light. Broad band light systems will be less vulnerable to the perturbations of scattered light from all sources and since they impose fewer demands on the laser frequency stability there is a good chance that they will be able to operate with high laser power. They appear less complex than the narrow band light systems. A broad band light system precludes the use of a Fabry-Perot or any other interferometric design which relies on the superposition of multiple beams to gain fringe phase sensitivity. Broad band schemes are therefore limited to those techniques where the interference takes place at the end of the storage time and they require near equality of the optical paths. The narrow band light systems require unprecedented but not impossible frequency stability. They handle the scattering problem by fixing the phase in the scattering paths from stationary scattering sources. There is less constraint on the equality of optical paths and they permit the use of Fabry-Perot cavities. The narrow band light systems will most likely not extract as much light from the laser but this may be offset by a scheme proposed by Drever to incorporate the entire interferometer into a resonant cavity and thereby increase the

circulating optical power. The concept schematized in fig. 6 is applicable to narrow band light interferometers of either the delay line or Fabry-Perot design.

The concept is to hold the interferometer at a minimum output from the antisymmetric port sensed by photodetector P1. If the losses are small within the interferometer arms, most of the input light will emerge from the symmetric port, where in this scheme it is returned to the input and combined with the incident laser light by a beam splitter. If the phase relation of the laser light and the returned light is adjusted by the electrooptic phase modulator P4 to null the light to photodetector D2, the internal circulating power in the interferometer is increased by a factor close to the reciprocal of the interferometer loss coefficient. The scheme has not been tried as yet. It appears promising, but requires close matching of phase fronts and rigorous frequency stabilization to be effective.

The choice of cavity configuration involves several considerations. The Fabry-Perot having spatially superposed beams will be able to use smaller diameter mirrors than a delay line in which the beams are spatially separated.At high gravitational wave frequencies in a long baseline system involving few (20) beam transits, the difference is not very important, however, at lower frequencies it could become a design discriminant.

If mirror size becomes a real constraint and should it prove

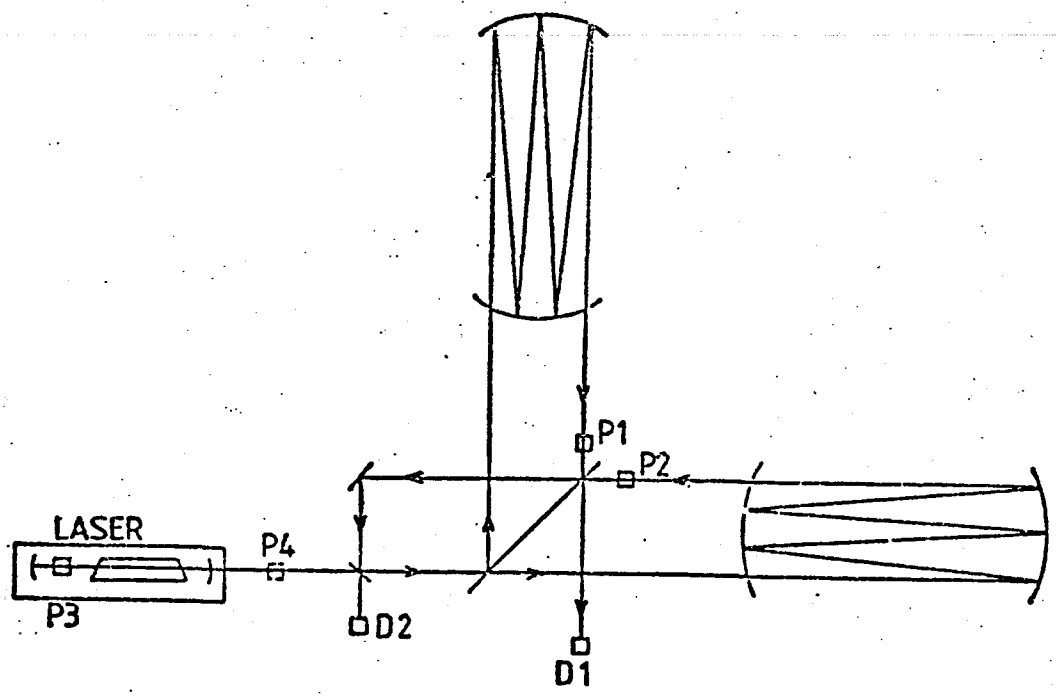

Fig. 6
Proposed scheme for enhancing performance of a Michelson interferometer by incorporating it within a resonant cavity.

advantageous in the refinement of a long baseline antenna to retain the delay line concept, it is possible, though at present untried, to spatially superpose the beams but give them separate identities by making their frequencies different. One scheme for doing this is to use a Fabry-Perot etalon with transmission maxima at frequency intervals Δf as the input mirror of a delay line. With each transit of the beam through the arm the frequency of the light is shifted by an amount δf either by moving the mirror at the other end of the arm at constant velocity or, more practically, by shifting the frequency in a travelling wave phase modulator. The returned beam is shifted off the transmission resonance of the etalon and trapped by reflection until after n transits, $n = \Delta f/\delta f$, the beam reemerges from the delay line to interfere with the beam in the other arm which has been treated in the same manner. The scheme automatically reduces scattering perturbations and does not require precision frequency stabilization. The storage time of the arms can be made variable by changing the etalon spacing. Although it seems to have several attractive features, the scheme is more complex than needed at present and is not a candidate for the first optical system to be installed in a long baseline antenna.

Still other factors to be weighed in the choice of a cavity configuration are the alignment sensitivity and perturbation of the interfering wave fronts by mirror vibration. As the length of the

cavity increases the radial spatial modes of the Fabry-Perot become more closely spaced in frequency and the fringe phase sensitivity to beam misalignment grows.

It is clear from the discussion that it is not possible to make a recommendation for a specific optical design. We consider it a poor scientific strategy to delay the development of a long baseline antenna system until an optimal configuration is demonstrated. The rationale for this view is given by the following: First, as stated in the beginning, all of the present designs will function and, when applied to large baseline systems, will make a substantial improvement over the sensitivity of present systems. Second, the refinement and upgrading of the optical system in a long baseline antenna will continue as the technology develops and the optimal concept may well change. Third, many of the experimental problems encountered in developing a short baseline system are not the same as in a long baseline system and finally, the optics is not a cost driver of the capital costs of this project.

Optical Delay Lines

In order to achieve the highest sensitivity possible a gravity antenna interferometer must have very long optical paths. This can be done by folding the optical path between two mirrors that are close together. One such scheme, first described by Herriot (1964), is the optical delay line. In this technique a light beam injected into a cavity formed by a pair of spherical mirrors bounces off the mirrors several times and then exits at its point of injection.

A delay line made of two spherical mirrors with radius of curvature, R, and separated by a distance, d, is shown in figure 1. The z axis of the coordinate system is along the line joining the centers of curvature, the mirror separation, d, is measured along this axis from the surface of one mirror to the surface of the other, and the x axis is perpendicular to the z axis and passes through the injection hole at X_o on mirror 1 (mirror 2 has no hole bored in it). Since a mirror of radius, R, acts like a lens of focal length f = R/2 it is straightforward to calculate the position and angle of a light beam as it bounces around inside the cavity. The x, y position of the nth spot is given by

$$X_n = X_o \cos(n\theta) + \frac{X_o + R\,X'_o}{(2R/d - 1)^{1/2}} \sin(n\theta)$$

$$= X_o \cos(n\theta) + X_* \sin(n\theta)$$

$$Y_n = Y_o \cos(n\theta) + \frac{Y_o + R\,Y'_o}{(2R/d - 1)^{1/2}} \sin(n\theta)$$

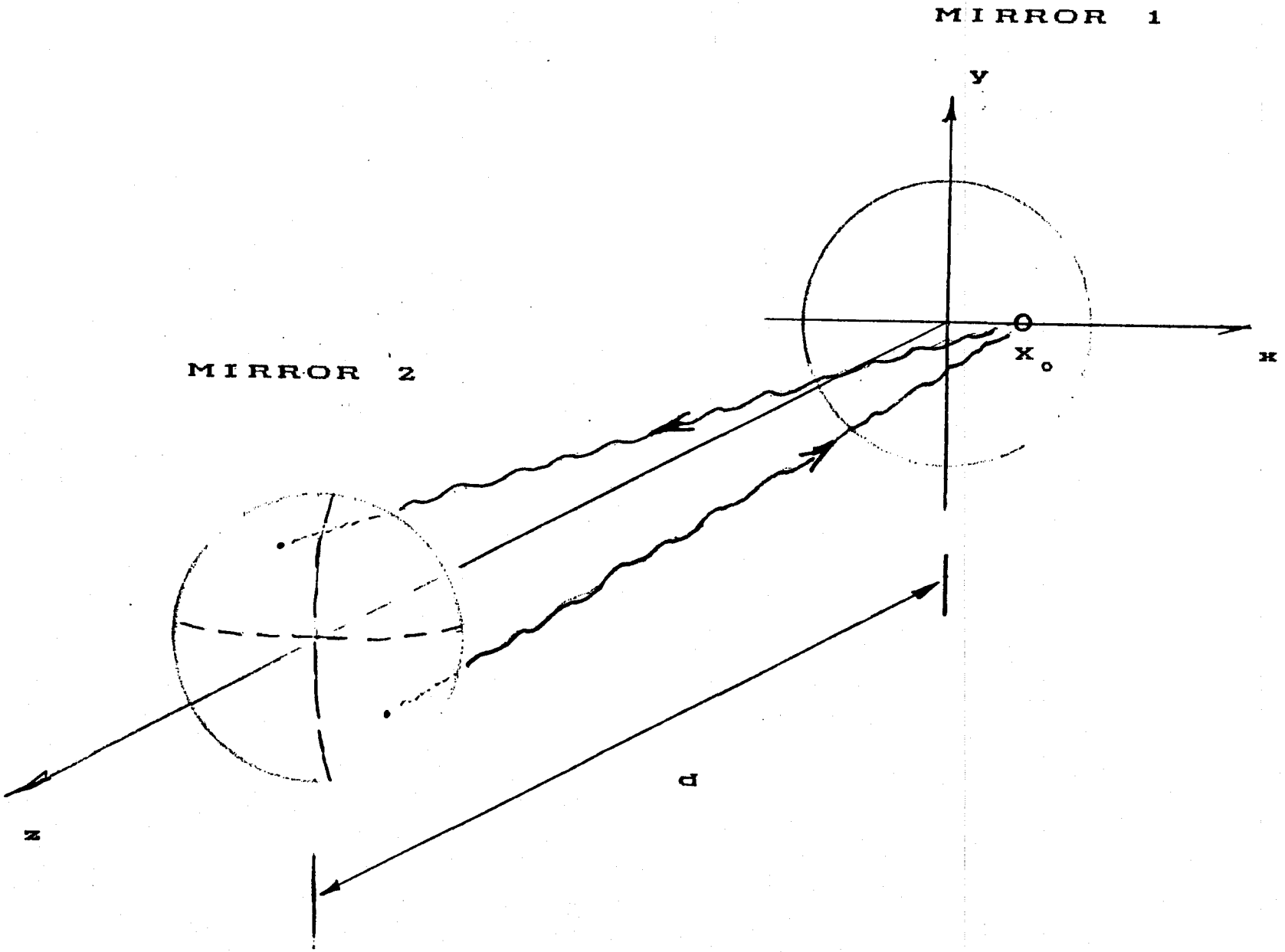

FIGURE 1

$$= Y_o \cos(n\theta) + Y_* \sin(n\theta)$$

$$\cos(\theta) = 1 - d/R$$

where X'_o and Y'_o are the tangents of the injection angle in the xz and yz planes repsectively. The even numbered spots appear on mirror 1 and the odd numbered spots on mirror 2. If the raio d/R is chosen so that

$$N\theta = 2\pi K$$

and if N and K are relatively prime then the cavity becomes re-entrant, i.e.,

$$X_N = X_o$$

$$Y_N = Y_o$$

and the beam leaves the cavity through the injection hole after exactly N bounces on the mirrors. In general the spot pattern the beam makes will be oval. By choosing the input conditions to be

$$X'_o = -X_o/R \text{ i.e. } X_* = 0$$

$$Y'_o = \frac{X_o}{R}(2R/d - 1)^{\frac{1}{2}} \quad \text{i.e. } Y_* = X_o$$

the spots will lie on a circle and their position will be

$$X_n = X_o \cos(n\theta)$$

$$Y_n = Y_o \sin(n\theta)$$

and after each bounce the beam rotates through an angle $\theta = 2\pi K/N$.

A mode chart relating the number of bounces, N, and the ratio, d/R, is given in figure 2. The curves which begin at the right side

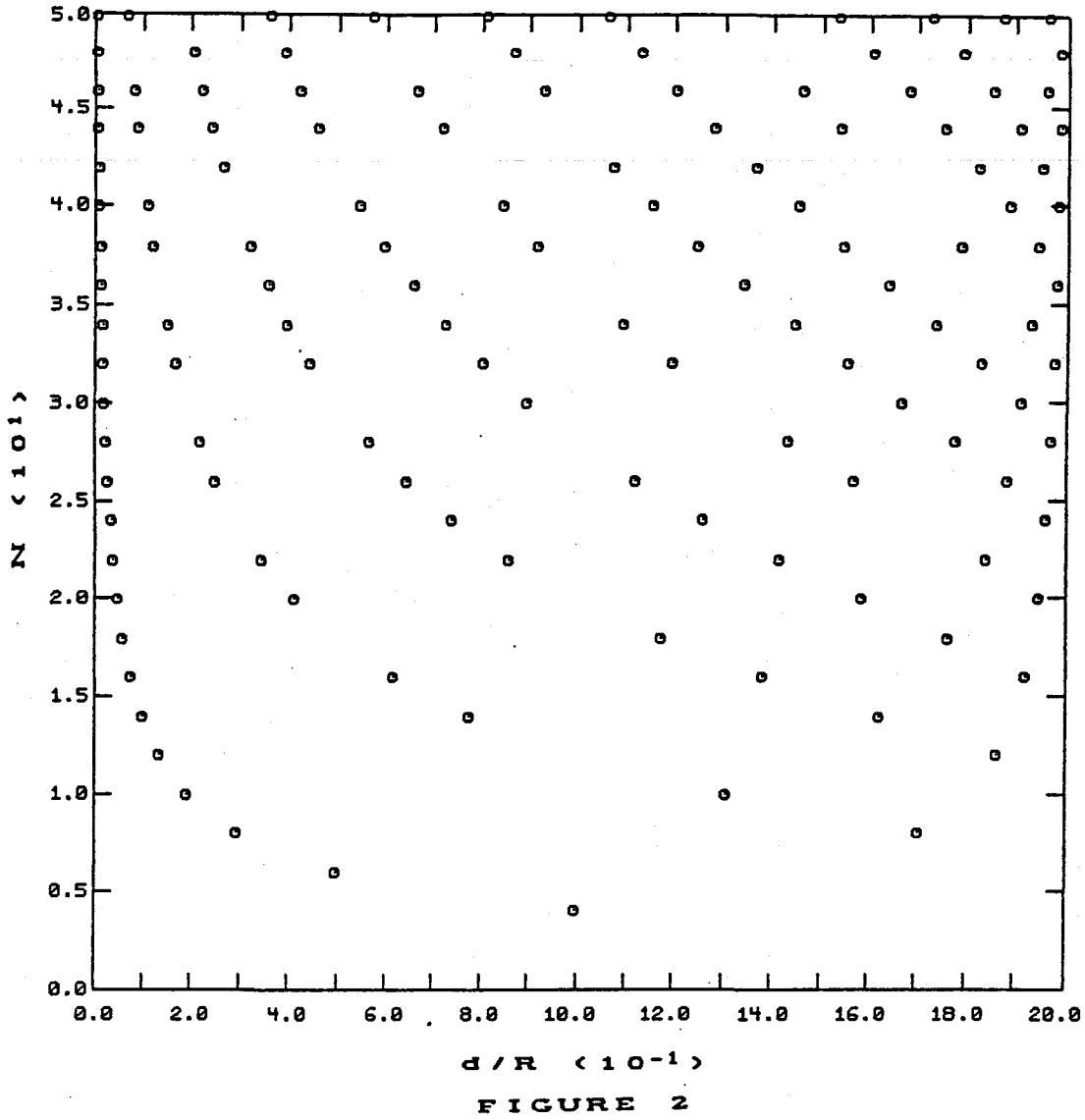
5.0
4.5
4.0
3.5
3.0
2.5
2.0
1.5
1.0
0.5
0.0
N (10⁴)
0.0
2.0
4.0
6.0
8.0
10.0
12.0
14.0
16.0
18.0
20.0
d/R (10⁻¹)

FIGURE 2

of the plot and curve to the top left correspond to K = 1,3,5,...with K = 1 having the smallest values of d/R.

The angle of the beam after reflection on the nth bounce is

$$X'_n = X'_o \cos(n\theta) - \frac{X'_o + 2\,X_o/d}{(2\,R/d - 1)^{1/2}} \sin(n\theta)$$

$$Y'_n = Y'_o \cos(n\theta) - \frac{Y'_o + 2\,Y_o/d}{(2\,R/d - 1)^{1/2}} \sin(n\theta)$$

It is obvious from these formulas that if the cavity is re-entrant the beam direction after the Nth reflection would be equal to the initial direction. However, there is no Nth reflection since the beam exits through the injection hole. Thus, if the cavity is re-entrant the exiting beam appears to be the initial beam reflected off the surface of a spherical mirror. This geometric property is convenient for alignment of an interferometer since the return mirrors (mirror 2) can be ignored once the cavities are made re-entrant.

If the beam is actually injected through a hole in the mirror, Gaussian optics determines the size of the hole. The optimum spot radius which minimizes diffraction losses of the beam inside the cavity is (Yariv, 1975)

$$r_n = \left(\frac{\lambda d}{2\pi}\right)^{1/2} \left(\frac{2}{d/R(1 - d/2R)}\right)^{1/4}$$

(For a 10 kilometer cavity with λ= 514nm and d/R = 1.3 i.e. N = 10 K = 3 then r_n = 4 cm)

The radius of the injection hole also limits the number of bounces

of the beam. If too many bounces are required some spot will prematurely overlap the injection hole and leave the cavity before the full number of bounces is taken.

The difference between the actual mirror separation and the ideal re-entrant separation is also limited by the size of the injection hole. We can estimate this by calculating the position derivative of the Nth beam spot with respect to mirror separation at the re-entrant condition,

$$\frac{\delta Y_n}{\delta d} = \frac{-NY_*}{R \sin(\theta)}$$

Thus is the hole radius is r_n the beam exits properly if we require

$$r_n > \Delta Y_N \simeq \Delta d \frac{NY_*}{R \sin(\theta)}$$

or

$$\Delta d < \frac{r_n R \sin(n\theta)}{NY_*}$$

If we take r_n= 5cm, R = 10km, N = 10, Y_* = 50cm, cos(θ) = -.03, then d < 1km a very weak restriction, unlike an antenna with short arms where this restriction can be severe if N is large and r_n small.

Sensitivity to Transverse Motions and Rotations

The travel time of a light beam stored in a delay line cavity is principally affected by motions of the mirrors along the optic axis.

NOISE SOURCES

In this section of the study we present an analysis of the various sources of noise that limit the strain sensitivity of a long baseline antenna. The order of the presentation is to begin with noise sources in the measurement of the time (phase) differences; the transducer noise and the noise incurred by the propagation of the light in an imperfect vacuum. The effect of stochastic forces on the masses follows. The section on vibration isolation includes the analysis of a scheme to reduce the effects of ground noise in a large baseline antenna.

The section ends with a graphical summary of all the noise sources that have been considered and displays the limiting antenna performance as a function of gravitational wave frequency for a range of antenna lengths.

The sample parameters used in the calculations and in the final graphs have values we consider technically feasible in a first generation long baseline antenna system. In these projections of antenna performance none of the noise terms are set at limits which are fundamental in the sense that they cannot be reduced by improvements in the technology or by a new concept.

TRANSDUCER NOISE

In this section in contrast with the section that developed the response of an electromagnetically coupled antenna to a gravitational wave, we adopt the viewpoint of the interferometer as a motion transducer. We first determine the gain of the motion transducer and then look at the noise terms that limit its performance. This more conventional approach applies both to interferometric systems that make phase comparisons at the end of a storage time like delay lines and those that gain phase sensitivity by multiple superposition of beams like the Fabry-Perot.

In the analysis we assume that the optical components are lossless except for scattering and wavefront distortion. In a small antenna this is a poor assumption, but in a first generation long baseline system it is applicable because of the smaller number of beam transits or finesse required to achieve optimal storage times and because of the advances being made in mirror reflectivities, which are approaching (1-R) of a few 10^{-4}.

The optical output power of a Michelson interferometer in which the optical phase is electrooptically modulated and in which the beam makes b transits in each arm is given by

$$P(t) = \left(\frac{P_o - P_B}{2}\right)(1 + \cos(kb\, x(t) - \theta + \Omega(t)) + P_B \qquad (1)$$

In this expression P_o is the input power, P_B is the unmodulated output power due to imperfections such as scattering and wave

front distortion, $k = 2\pi/\lambda$. $\Omega(t)$ is the phase modulation signal assumed to be a square wave with amplitude Ω_o, and θ is either 0 if the beam emerges from the symmetric port or π if from the antisymmetric one. $x(t)$ is the differential motion of the mirrors that define the two arms.

The transducer gain is the change in output power with respect to change in the differential position taken at a symmetry point of the fringe, where $kb\,x(t)$ is close to zero. With the output observed at the antisymmetric port, the gain is given by

$$\frac{\Delta P}{\Delta x} = (P_o - P_B)\,\frac{2\pi b}{\lambda}\,\sin\Omega_o \qquad (2)$$

In a Michelson arrangement where the multipass cavities are Fabry-Perot cavities used in reflection, the transducer gain is

$$\frac{\Delta P}{\Delta x} = (P_o - P_B)\,\frac{2F}{\lambda}\,\sin\,\Omega_o \qquad (3)$$

where F is the finesse of the cavity given by

$$F = \pi/(1-R).$$

(1-R) is the transmission of the input mirror assuming that the reflectivity of the other mirror in the cavity is unity.

The light storage time in the delay line is $t_{st} = b\ell/c$ while in the Fabry-Perot it is $F\ell/\pi c$. ℓ is the separation of the mirrors

The transducer noise is analysed for both systems as the fluctuations in power incident on the photodetector. There are two main sources: the Poisson (shot) noise which can only be reduced by increasing the optical power circulating in the interferometer for a fixed quantum efficiency in the photodetector, and power fluctuations at the detector due to frequency or phase instabilities in the light source which can be reduced to small values by making the storage times in the two arms close to equal. The displacement noise spectral density is then related to the spectral density of the power fluctuations by

$$x^2(f) = P^2(f)/(\Delta P/\Delta x)^2 \qquad (4)$$

The Poisson noise is given by

$$P^2(f) = \frac{2hc}{\eta\lambda} \langle P_D \rangle \qquad \text{Watts}^2/\text{Hz} \qquad (5)$$

where η is the quantum efficiency of the photodetector and $\langle P_D \rangle$ is the average power incident on the photodetector. The average power from the antisymmetric port is

$$\langle P_D \rangle = \frac{(P_o - P_B)}{2} (1-\cos\Omega_o) + P_B \qquad (6)$$

In the best case the Poisson noise dominates and the displacement power spectral density becomes

$$x^2(f) = \left(\frac{hc\lambda}{4\pi^2 b^2 \eta P_o}\right)\left[\frac{(1-\cos\Omega_o) + 2B/(1-B)}{(1-B)\sin^2\Omega_o}\right] \qquad (7)$$

Here B is the ratio of the unmodulated to the total incident power. The quantity in the square brackets determines the optimum phase modulation amplitude for a given value of B. For small values of B it is close to 1/2, at B = 0.1, an interferometer with 90% fringe contrast, it has grown to 1.0 and B = 0.2 it has become 1.6.

The Poisson limit for small values of B is

$$x^2(f) = \left(\frac{hc\lambda}{8\pi^2 b^2 \eta P_o}\right) \qquad cm^2/Hz \qquad (8)$$

for b = 60, η = 1/2, P_o = 100 watts, λ = 5145A°, $x(f) \sim 8.5 \times 10^{-18} cm/Hz^{\frac{1}{2}}$. To apply equations 7 and 8 to the Fabry-Perot cavity replace b by F/π.

The fluctuating output power in the interferometer due to frequency instability has been analyzed by Armstrong (J. Opt. Soc. Am. 56, 1024, 1966) for a Michelson interferometer illuminated by light with Gaussian phase noise. The light source is characterized by a Lorentzian frequency width δ . In the limit where the frequency of the power fluctuations is less than δ and the difference in storage time in the two arms, τ, is such that $\delta\tau << 1$, the output power fluctuations are given by

$$P^2(f) = \frac{2}{3} P_o^2 \left(\frac{\delta\tau}{\delta}\right)^3 \qquad (9)$$

The condition that the Poisson noise dominates sets a limit on τ. δ is not a free parameter since the frequency width of the light source will be determined, in some of the interferometer designs, by requirements on the suppression of the noise from scattered light.

In a Fabry-Perot configuration as the multipass element in a Michelson interferometer, the output power fluctuations due to frequency instabilities are given by

$$P^2(f) = [P_o \left(\frac{\Delta F}{F} + \frac{\Delta \ell}{\ell}\right) 4\pi t_{st}]^2 \upsilon^2(f) \qquad (10)$$

ΔF and $\Delta \ell$ are the differences in finesse and length of the two cavities and $\upsilon^2(f)$ is the power spectral density of the light source frequency fluctuations in units of Hz^2/Hz. Equations 8 and 10 are only valid for the Fabry-Perot if $\delta t_{st} < 1$ which sets an independent condition on δ.

From equations 5, 6 and 10 the condition that Poisson noise dominates sets the following condition on the cavity matching and the power spectral density of the frequency fluctuations in a high contrast Fabry-Perot-Michelson system

$$\left(\frac{\Delta F}{F} + \frac{\Delta \ell}{\ell}\right) \upsilon(f) < \frac{1}{4\pi t_{st}} \left(\frac{hc}{2\eta\lambda P_o}\right)^{1/2} \qquad (11)$$

For an instrument with 95% contrast, $P_o = 100$ watts, $\eta = 1/2$, $t_{st} = 1$ msec, $\lambda = 5145\ A^o$. The product on the left hand side of Eq. 11 must be less than $5 \times 10^{-9}\ Hz/Hz^{1/2}$.

It is useful to reexpress the Poisson noise limit Eq. 8 in terms of the minimum detectable gravitational strain amplitude density, this is

$$h(f)_{gw} > \frac{1}{\sqrt{8\pi}\, t_{st} c} \left(\frac{hc\lambda}{\eta P_o}\right)^{1/2} \frac{1}{\text{sinc}\ (\omega t_{st}/2)} \qquad (12)$$

where it is assumed that the gravitational wave is normally incident on the antenna in the most favorable polarization. Refer to the section on the antenna response function, for the more general case.

In an antenna illuminated by 100 watts and 1 msec storage time

$$h(f)_{gw} > \frac{1.7 \times 10^{-23}}{\text{sinc}\,(\omega t_{st/2})} \quad \text{strain/Hz}^{1/2} \tag{13}$$

The effect of amplitude fluctuations of the light other than the intrinsic Poisson photodetection noise can be suppressed by proper design. The fringe interrogation schemes described in the section on the prototypes are specifically designed to put the fringe motion signal at a carrier frequency well above the frequencies where lasers have extrinsic amplitude noise. Furthermore, the null servo system designs which hold the fringe at a symmetry point, with sufficient loop gain will further suppress extrinsic amplitude noise. If need be the amplitude noise is also measurable directly in the fringe output independently of the fringe phase. In other words, there are many lines of defense and this noise source is not considered a problem.

Extrinsic amplitude noise of the light source with frequency components in the gravitational wave detection band must however be considered but in a different context. If there is an unbalance in the power circulating in the two interferometer arms or if the masses are not matched, the relative displacements of the arms will depend on the extrinsic amplitude fluctuations through radiation pressure fluctuations.

To estimate the importance of this effect assume that the input power fluctuations are proportional to the power

$$\Delta P_{rms} = \alpha P . \tag{14}$$

and for ease of calculation that the power fluctuation spectrum is uniform over a band width Δf. The power spectral density of power fluctuations is

$$P^2(f) = \frac{\alpha^2 P_o^2}{\Delta f} \tag{15}$$

which by the radiation pressure produces a fluctuating force described by the force power spectral density

$$F^2(f) = \frac{4b^2 P^2(f)}{c^2} \tag{16}$$

The antenna masses respond as "free" above the suspension resonances. A single mass will therefore move with a displacement power spectral density of

$$x^2(f) = \frac{b^2 \alpha^2 P_o^2}{m^2 \omega^4 c^2 \Delta f} \tag{17}$$

where m is the mass and it is assumed that the input power has been split close to equally. Let there be a power or mass unbalance parameterized by γ which is zero if the system is balanced and one if totally unbalanced. The strain sensitivity of the system to this effect is given by

$$h(f) \sim \frac{\gamma \alpha t_{st} P_o}{2\pi^2 m f^2 \Delta f^{1/2} \ell^2} = \frac{\gamma \alpha P_o}{2\pi^2 m f^3 \Delta f^{1/2} \ell^2} \tag{18}$$

$$t_{st} = 1/f$$

In a 5 km antenna having $t_{st} = 1/f$, a mass 10^6 gm, $P_o = 100$ W, and $\Delta f = 1$ KHz

$$h(f) \sim \frac{10^{-11}\, \alpha\, \gamma}{f^3}$$

At best one might expect to balance the system to 1% so that it will become important, especially at low gravitational wave frequencies, to reduce α by actively controlling the light source amplitude fluctuations. This will not be a consideration in first generation antennas of sufficient length but cannot be neglected in future improvements.

There are also intrinsic and fundamental pressure fluctuations of the light pressure which are not correlated at the masses due to quantum fluctuations in the radiation field itself. These are discussed more extensively in Appendix A on the "naive" quantum limit of an antenna. Here for sake of completeness and comparison, we quote the strain limits imposed by them, which are

$$h(f) = \frac{\sqrt{8}\, t_{st}}{(2\pi)^2\, \ell^2\, m f^2} \left(\frac{h P_o c}{\lambda} \right)^{1/2} = \frac{\sqrt{8}}{(2\pi)^2\, \ell^2\, m f^3} \left(\frac{h P_o c}{\lambda} \right)^{1/2} \qquad (19)$$

$$t_{st} = \frac{1}{f}$$

Evaluating Eq. (19) for the same parameters as above

$$h(f) \sim \frac{1.8 \times 10^{-20}}{f^3}$$

Another noise source that is related to the light power is the so called radiometer effect because it is responsible for the rotation of the poorly evacuated radiometers seen in jeweler's windows. In a structure with temperature gradients, gas atoms that accommodate and then are reemitted by the hotter surfaces impart larger recoil momenta to the surface than those reemitted by colder parts. In an interferometric gravitational antenna the surfaces illuminated by the light will be hotter than the other parts and there will be net forces and torques on the masses due to the radiometer effect. The fluctuations in these forces can arise from laser power fluctuations coupled to a system unbalance or pressure fluctuations in the vicinity of the masses.

The fluctuations of the surface temperature of a mirror when illuminated by a light source with varying intensity is given by

$$T(f) = \frac{I_{abs}(f)}{(\pi\, c\, k_t\, \rho)^{1/2}\, f^{1/2}} \qquad (20)$$

ρ is the density of the material, k_t the thermal conductivity, c the specific heat and $I_{abs}(f)$ is the fluctuating intensity that is absorbed by the surface. Eq. 20 assumes that the temperature of the entire structure remains constant and that only the surface temperature fluctuates, and furthermore that radiative transport is less important than thermal diffusion.

The change in force on the surface due to a change in temperature is

$$\Delta F = \frac{n\, k_B\, \Delta T\, A}{4} \tag{21}$$

where n is the number density of gas atoms k_B, Boltzmann's constant, A, the surface area and ΔT the temperature change. Eq. 21 assumes complete accommodation of the emitted atoms to the surface temperature. Combining Eqs. 20 and 21 and reexpressing them in terms of spectral densities, yields a force amplitude density

$$F(f) = \frac{n\, k_B\, P\,(f)\, \beta}{4\,(\pi\, c\, k_t\, \rho)^{1/2}\, f^{1/2}} \tag{22}$$

where P (f) is the amplitude spectral density of the total power fluctuations and β is the fraction of the power absorbed by the surface. Using Eq. 15 as a model for the extrinsic power fluctuations and analyzing the motion of a free mass driven by the force density of Eq. 22 yields a strain spectral density of

$$h(f) \sim \frac{\alpha\, n\, \beta\, k_B\, P}{8\pi^2\, \ell\, m\, (\pi\, c\, k_t\, \rho)^{1/2}\, f^{5/2} \Delta f^{1/2}} \tag{23}$$

Here it is assumed that the pressure is most likely to be the unbalanced quantity. If the pressure is low enough this noise is of little consequence. Using the same sample parameters as above and in addition that $(\pi\, c\, k_t\, \rho)^{1/2} \sim 4 \times 10^6$ (cgs units) for fused quartz

gives

$$h(f) \sim \frac{6 \times 10^{-19}}{f^{5/2}} \alpha \beta$$

at a pressure of 1×10^{-6} mm Hg.

The noise due to the pressure fluctuations of gas atoms interacting with surfaces at different but constant temperatures is handled in the same manner as the thermal noise discussed in a later section of this report. The thermal noise makes more stringent requirements on the quality of the vacuum than the radiometer effect.

Light propagation fluctuations due to pressure fluctuations

Residual gas molecules in the evacuated arms of the interferometer cause phase fluctuations of the laser light as it propagates back and forth between the mirrors. The magnitude of the resultant phase fluctuation noise is a function of the path length traversed by the light so this noise source is one of the few that tend to increase as the length of the interferometer arms is increased.

Although, in principle, there could be intermittent large fluctuations in gas density due to outgassing bursts, this does not appear to be an important problem in a clean vacuum system. Very little information on this subject is available in the literature. An experiment is now in progress to set a limit on this hypothetical phenomena. However, current informed opinion of those familiar with the large vacuum systems used in accelerator storage rings indicates that outgassing bursts, if they occur at all, certainly are extremely rare. (Ref: H.J. Halama, Brookhaven, private communication)

The phase fluctuations with which we are concerned are attributable to random fluctuations in the index of refraction of the propagating medium that arise because the number of molecules or atoms in a column of gas fluctuates randomly about some average or equilibrium value. This process is thermally driven and can be treated as having a stationary distribution.

The purpose of the calculations in this section, therefore, is to estimate the quality of the vacuum that is required to ensure that the magnitude of the noise which results from column density fluctuations is smaller than the magnitude of the other noises in the system. This re-

quirement is crucial because the minimization of the phase fluctuation noise is the prime justification for the vacuum system that is one of the most expensive components of the interferometric gravity wave antenna.

We have to consider two cases; interferometers where the multi-pass beams are spatially separated, as in the present versions of delay line systems, and those in which the beams coincide as in a Fabry Perot or delay line with spatially coincident but frequency tagged beams. The cases differ in the degree of correl ation of the phase noise due to column density fluctuations. As will be shown, the vacuum required by the two cases depends identically on several parameters but depends differently on the length of the interferometer arms.

The case of spatially separated beams.

We consider first a delay line interferometer in which the light beams that are reflected back and forth between the mirrors do not overlap anywhere.

To show that this idealization is physically realistic, we evaluate first the diameter of a light beam and the diameter of the spot size on the reflecting surfaces. Assume a symmetric cavity with spherical mirrors of radius of curvature, R, close to but not exactly equal to the interferometer arm length ℓ. The minimum beam diameter for a Gaussian beam, defined as 1/e intensity point, occurs at the cavity midpoint and is given by

$$D = \left(\frac{2\lambda\ell}{\pi}\right)^{\frac{1}{2}} \simeq 2\omega_0 \qquad (1)$$

λ is the light wavelength. The beam diameter at the mirrors is $\sqrt{2}D$. For example, in a 5km arm antenna using 5145A laser light, the beam diameter at the mirrors is 5.7 cm.

Now, if the light beam is reflected to make b transits of the interferometer arm, the equilibrium value for the number of atoms<N> in the total gas column is

$$\langle N \rangle = \rho \ \ell \ b \ \ (\pi \ D^2/4) \qquad (2)$$

where ρ is the average number of atoms per unit volume. The rms fluctuations about the equilibrium value, is

$$\Delta N^2 = \langle N \rangle \qquad (3)$$

The average column density of atoms is

$$\sigma = \frac{\langle N \rangle}{(\pi \ D^2/4)} \qquad (4)$$

While the fluctuation of column density is given by

$$\Delta\sigma^2 = \frac{\Delta N^2}{(\pi \ D^2/4)^2} = \frac{\rho \ \ell \ b}{(\pi \ D^2/4)} \qquad (5)$$

The index of refraction n of the gas column is

$$n = 1 + \alpha\rho \qquad (6)$$

where α is the effective molecular polarizability at λ . α for nitrogen $= 9.7 \times 10^{-24} cm^3/atom$. The rms phase fluctuation of the laser light that is caused by column density fluctuations is then given by

$$\Delta\phi^2 = \left[\frac{2\pi}{\lambda}\,\alpha\right]^2 \Delta\sigma^2 = \left[\frac{2\,\pi\,\alpha}{\lambda}\right]^2 \left[\frac{\rho\,\ell\,b}{\pi\,D^2/4}\right] \qquad (7)$$

A phase change causes an inferred change of the separation between the end masses according to

$$\Delta x = \left[\frac{\lambda}{2\pi b}\right] \Delta\phi \qquad (8)$$

so the fluctuation in the inferred length corresponding to the phase fluctuations, and hence to the column density fluctuations, is

$$\Delta x^2 = \left[\frac{\lambda}{2\pi b}\right]^2 \Delta\phi^2 = \frac{4\alpha^2\rho\ell}{b\pi D^2} \qquad (9)$$

To convert this to a power spectral density, we note that the relevant time scale of the fluctuations is the time that an atom resides in the light beam. This residence time t_r is approximately

$$t_r = \frac{D}{V_t} \qquad (10)$$

where V_t is the thermal velocity of the atom.

So, for frequencies less than $(1/t_r)$, the power spectral density of the inferred length fluctuations is

$$x^2(f) = t_r\ \Delta x^2 = \frac{4\alpha^2\rho\ell}{b\pi DV_t} \qquad (11)$$

A more useful formulation is to reexpress this noise in terms of the equivalent strain spectral density using the arm storage time, t_s, defined by

$$t_{\mathcal{S}} = b\ell/c \qquad (12)$$

and the beam diameter of Equation 1. The equivalent strain spectral density is then

$$h^2_{uncor}(f) = \frac{2\alpha^2\rho}{t_s c v_t (\pi\lambda\ell)^{\frac{1}{2}}} \qquad f < 1/t_r \qquad (13)$$

The Spatially Correlated Case

We consider next an interferometer in which all the light is reflected back and forth through the same gas column. The light storage time t_s is greater than the residence time t_r of a thermally driven atom in the beam, and the residence time in turn is greater than the light transit time t_t $(=\ell/c)$ along the interferometer arm.

As before, the phase fluctuation introduced during one transit of the interferometer arm, $\Delta\phi_t$, is given by Equation 7. However, now, the phase fluctuations for a time equal to the atom residence time are correlated. The beam makes t_r/t_t transits through the same gas column fluctuation and on the average the beam samples t_s/t_r independent fluctuations in the arm during a storage time. The rms phase fluctuation becomes

$$\Delta\phi^2 = \left(\frac{t_r}{t_t}\right)^2 \Delta\phi_t{}^2 \quad \frac{t_s}{t_r} = \frac{t_r \; t_s}{t_t{}^2} \Delta\phi_t{}^2 \qquad (14)$$

Following the same steps as before the strain spectral density is given by

$$h^2_{cor}(f) = \frac{4\alpha^2\rho}{\pi V_t^2 \; t_s \ell} \qquad (15)$$

Equations 13 and 15 are the results of this section. Instead of, as in other sections of this report, evaluating the requirements of the system to meet a specified h(f), it is more useful here to look at the break points in vacuum technology. Broadly speaking low vacuum technology using roughing pumps and elastometer seals allows system pressures of at best 10^{-3}mm Hg. This pressure is too high for antenna lengths considered economically feasible. The next level of vacuum technology employing additional pumps, diffusion, ion, or sorption pumps in addition to roughing pumps has a break at pressures of about 10^{-6} mm Hg. Vacuum system with pressures less than 10^{-6}mm Hg; the ultra high vacuum region, require further refinements such as metal to metal seals and the ability to be heated for outgassing while evacuated. As indicated in the Arthur D. Little study, we have chosen to price a vacuum system which is able to maintain 10^{-6}mm Hg in the light paths but which can be improved at some additional expense for operation at lower pressures if the need arises in a second generation development of the antenna system.

With a pressure of 10^{-6}mm Hg, consisting of N_2 at room temperature and a light wave length λ of 5145A°, the strain amplitude spectral noise due to vacuum fluctuations is given for the two cases as

$$h(f)_{uncor} = \frac{5.2\times10^{-25}}{t_s^{\frac{1}{2}}\,\ell^{\frac{1}{4}}} \qquad h(f)_{cor} = \frac{3.5\times10^{-23}}{t_s^{\frac{1}{2}}\,\ell^{\frac{1}{2}}}$$

in a 5km antenna with a 10^{-3} sec storage time the noises are

$h_{uncor}(f) = 6 \times 10^{-25}$ strain/$Hz^{\frac{1}{2}}$ $\quad$ $h_{cor}(f) = 1.6 \times 10^{-24}$ strain/$Hz^{\frac{1}{2}}$

Some of the other parameters interesting to note in this example are

$t_{transit} = 1.7 \times 10^{-5}$ sec

$t_{residence} \simeq 1 \times 10^{-4}$ sec

$\langle \phi \rangle = 1.1$ radians

$\langle \phi \rangle$ is the average phase shift of the light due to the gas in traversing an interferometer arm for t_{stor}.

MECHANICAL THERMAL NOISE

Mechanical thermal noise can become a factor in the noise budget of long baseline interferometric antennas, especially at the low frequency end of the band, for the sensitivities being projected. The influence of mechanical thermal noise, as well as all other stochastic forces that are uncorrelated at the antenna end points, is reduced by increasing the antenna length.

There are two classes of thermally driven motions in the antenna. The first are translations and rotations in the final stage of the vibration isolation suspension which produce noise at low frequencies and the second are excitation of internal vibrational modes of the end masses, mirrors and associated optics which should occur at high frequencies. Not all motions of the antenna masses are equally perturbative. Due to the symmetry of the interferometer optical design and the isotropy of the light intensity distribution about the optic axis, the effect of all rotations and translations perpendicular to the optic axis can be reduced to second order in these motions. The critical motions are those which have a net component along the optic axis when integrated over a gravity wave period.

The standard method of calculating thermal noise follows the prescription of Langevin and Nyquist which is consistent with equipartition and the fluctuation-dissipation theorem. However the method must be used with care. The thermal noise is modelled by a stochastic driving force given by the power spectral density (Nyquist noise)

$$F^2(f) = 4kT\,\alpha \qquad \text{Dynes}^2/\text{Hz} \qquad (1)$$

where k is Boltzmann's constant, T the temperature of the damping medium and α the damping coefficient of this medium. For a mechanical system with a single degree of freedom (one normal mode) and in which the damping coefficient is frequency independent, it is useful to re-express the Nyquist noise in terms of the system Q as

$$F^2(f) = \frac{4kTm\omega_o}{Q} \qquad (2)$$

where m is the moving mass of the oscillator and ω_o the resonant frequency. The response of the oscillator to the Nyquist noise force is calculated using the harmonic oscillator transfer function and given by

$$x^2(f) = \frac{4kT\omega_o}{mQ[(\omega_o^2 - \omega^2)^2 + (\frac{\omega_o\omega}{Q})^2]} \quad cm^2/Hz \qquad (3)$$

The rms motion of the oscillator, the integral of $x^2(f)$ over all frequencies, is the equipartition value

$$x^2_{rms} = \frac{2KT}{m\omega_o^2} = \int_o^\infty x^2(f)df \qquad (4)$$

In the gravity antenna design we endeavour to avoid mechanical resonances at frequencies in the gravitational wave band. The high and low frequency limits of Equation 3 become the relevant relations. These are given by

$$x^2(f)_{\omega>>\omega_o} = \frac{4kT\omega_o}{mQ\omega^4} \qquad (5)$$

$$x^2(f)_{\omega<<\omega_o} = \frac{4kT}{mQ\omega_o^3} \qquad (6)$$

The net displacement spectral noise density is the incoherent sum of the contributions from all independent normal modes.

The thermal noise produced by gas damping (Doppler friction) is the classic example of a damping mechanism which is described by the model. The coherent part of the damping is due to the average momentum imparted to the gas while the noisy part comes from the fluctuations in the number of atoms hitting the oscillator. In this case the impulses of the atomic collisions imparted to the oscillator obey a Poisson distribution and therefore have a frequency independent power spectrum at frequencies lower than the average rate of atomic collisions with the oscillator. That other damping mechanisms, such as the various mechanisms of internal dissipation in solids, can really be modelled by a frequency independent stochastic force is at this time only a conjecture. The fact one is sure of is that the frequency integral of the stochastic force does give the equipartition value. The bar gravity antennas have demonstrated this beautifully.

There are situations where a blithe application of the model would give the wrong results. Two cases which occur in present interferometric antenna designs are good examples: the case of coupled oscillators and schemes employing active servo feedback damping. The vibration isolation systems at the end points of an interferometric gravity antenna are high Q pendulum suspensions which are attached

to compliant and lossier structures to achieve additional seismic isolation. Motions of the pendulum feed power to the support structure where it is dissipated. The Q of the pendulum is lowered by this, however the Nyquist force on the pendulum bob is not given by Eq. 2 but rather by Eq. 2 multiplied by the frequency dependent isolation transfer function of the pendulum. A proper calculation of the normal mode excitations of the coupled system with each normal mode driven by its own Nyquist force gives this result. The thermal motion of the pendulum is a superposition of the normal mode excitations.

Servo feedback damping is employed to reduce the rms amplitude and ringing time of the pendulum motion. In these schemes a signal proportional to the velocity of the pendulum is derived from a transducer (an interferometer, capacitance or inductance bridge). After filtering the signal is fed to a controller, which depending on the design exerts electrostatic or magnetic forces on the pendulum. Leaving aside for the moment, the additional noise that is generated by the transducer, which is small in practice but nevertheless imposes a fundamental limit in the technique, the damping of the pendulum has been altered without an increase in the Nyquist noise force. The power spectral density of the displacement noise is still given by equations 5 and 6 where the appropriate Q is the value with the servo system turned off. The rms displacement on the other hand is smaller and given by

$$x_{rms}^2 = \frac{2kT}{m\omega_o^2} \frac{Q_{servo}}{Q_o} \qquad (7)$$

where Q_{servo} is the actively damped Q. Typically, $Q_{servo}/Q_o << 1$ and one can loosely say the oscillator has been refrigerated to an effective temperature

$$T_{eff} = T \frac{Q_{servo}}{Q_o} \qquad (8)$$

which is true for the integral but unfortunately not in calculating the thermal noise at frequencies far from resonance.

With the above provisos in mind, we make an analysis of the magnitude of the thermal noise in the interferometric antenna.

a) Thermal noise at low frequencies.

The fundamental resonance frequency of the suspension is chosen to be smaller than the lowest gravitational wave frequency, so that limit of Equation 5 applies. Three sources of thermal noise important at low frequencies are considered: dissipation in the flexure of the pendulum support, residual gas damping and eddy current damping by unshielded magnetic fields.

In the presently conceived design, the thermal noise arising from the dissipation in the flexure of the pendulum suspension makes the largest contribution at low frequencies. Although the major part of the restoring force in a pendulum is gravitational and non-dissipative, a small portion is provided by the flexure of the suspension. Some of the elastic energy stored in the flexure is dissipated. The overall Q of the pendulum is given by

$$Q = Q_{mat} \left(\frac{E_{grav} + E_{elastic}}{E_{elastic}}\right) \sim Q_{mat} \frac{E_{grav}}{E_{elastic}} \qquad (9)$$

where Q_{mat} is the internal Q of the suspension material in flexure, generally 1/10 of the Q in pure compression, E_{grav} the energy stored as gravitational potential energy and $E_{elastic}$ the energy stored in flexure which is usually much smaller than E_{grav}.

Clearly to achieve a high Q one would like to make $E_{elastic}$ as small as possible which implies thin support members. However, the Q_{mat} is a strong inverse function of the internal stresses of the material beyond a critical stress, σ_{max}, so that an optimization must be performed. The magnitude of the suspended mass, an important parameter in the optimization, is however not only a function of this noise term and must be chosen by an overall minimization of the antenna noise budget.

If the mass is supported by a single cylindrical fiber, the overall pendulum Q is given by

$$Q = Q_{mat}\ (\sigma_{max})\ \frac{4\sqrt{\pi}L\sigma_{max}}{(Ymg)^{\frac{1}{2}}} = Q_{mat}(\sigma_{max})\ \frac{4L}{a^2\sqrt{\pi}}\ \left(\frac{mg}{Y}\right)^{\frac{1}{2}} \qquad (10)$$

where L is the length of the pendulum, m the supported mass, a the fiber radius and Y is Young's modulus for the material. If N fibers are used, each stressed to σ_{max}, the overall Q improves as $N^{\frac{1}{2}}$. For example, the ratio of the Q for a rectangular ribbon of thickness 2a and width w to that of a cylindrical fiber of radius a is $\left(\frac{3w}{8\pi a}\right)^{\frac{1}{2}}$.

Typical sample parameters for a 4 fiber quartz suspension at 300°K are $L = 10^2$ cm (2 second pendulum), $m = 10^6$ grams, $Y = 7\times10^{11}$ dynes/cm^2, $\sigma_{max} = 10^{-2}\,Y$ and $Q_{mat}(\sigma_{max}) = 10^4$ in flexure. The overall pendulum

Q is 3×10^6. The diameter of each fiber is close to 2mm. Sapphire might be a better material but less is known about its internal losses in flexure.

The spectral density of thermal displacement noise at frequencies above the suspension resonance is given by Eq. 5. Using the above sample parameters it amounts to

$$x(f) \sim \frac{1 \times 10^{-14}}{f^2} \quad \text{cm/Hz}^{\frac{1}{2}}$$

at 300°K. The strain amplitude noise is

$$h(f) = \frac{2x(f)}{\ell} = \frac{2}{\sqrt{2}\pi^{3/2}} \left(\frac{kT}{mQ\tau_o}\right)^{\frac{1}{2}} \frac{1}{\ell f^2} \qquad (11)$$

where ℓ is the antenna baseline. The 2 comes from the fact that the thermal motions of all the antenna masses must be included. For a 5km long antenna, the low frequency thermal noise limit due to this cause varies as

$$h(f) = 4.2 \times 10^{-20}/f^2 \quad \text{strain/Hz}^{\frac{1}{2}} .$$

In second generation improvements on a large baseline gravitational antenna, electromagnetic field support suspensions or cryogenic operations could be contemplated to reduce this noise term but at present the added complexity is not warranted.

Damping due to Doppler friction by the residual gas is reduced by operating the pendulum in high vacuum. The Q due to gas damping is given by

$$Q_{gas} = \frac{\rho_m a w_o}{2\sqrt{3}(m_a kT)^{\frac{1}{2}} n} \qquad (12)$$

Here ρ_m is the density of the pendulum mass, a the length of a side of the mass if cubical, m_a the average mass of the residual gas atoms and n the number of atoms per cubic centimeter. ω_o is the pendulum resonance frequency. Eq. 11 applies in the limit where the mean free path of atoms in the residual gas is larger than a. Using the sample parameters T = 300°K, m = 10^6gm, a = 50 cm, τ_o = 2 sec pendulum period, a residual gas at 10^{-6} mm Hg composed primarily of N_2 yields a Q limited by gas damping of 5×10^9.

Eddy current damping in the unshielded earth's magnetic field can be a thermal noise source. At low frequencies where the skin depth is comparable and larger than the linear dimensions of the pendulum mass, the thermally driven electrical currents in a conducting mass produce fluctuating magnetic forces on the pendulum. This is another example of a "colored" Nyquist force. The Q due to this mechanism is independent of the volume and given by

$$Q_{eddy} = \frac{\rho a \omega_o c^2}{\sigma B^2} \qquad (13)$$

where B is the magnetic field at the mass, σ is the conductivity of the mass in cgs units and c the velocity of light. Using the same parameters as above, $\sigma \sim 5 \times 10^{17}$ sec^{-1}, typical of good conductors, and a field of 1/2 Gauss yields a $Q \sim 8 \times 10^4$. Modest magnetic shielding and/or the use of non-conducting masses, coated by a thin layer of conductor to avoid electric changing, reduces this damping mechanism, below the level

of the others discussed so far.

b) Thermal noise at high frequencies.

The thermal excitation of the normal modes of the masses, mirrors, mirror mounts and optical components in the phase sensitive portions of the interferometer contribute high frequency noise. Thermal noise from this source is now being observed in all the prototype interferometric antennas and is not unexpected given their unoptimized mechanical designs.

The reduction of this high frequency thermal noise requires that the lowest oscillatory mode frequencies lie above the gravity wave frequency, that the modes have a high Q and that there be as few modes as possible. These requirements argue for simplicity of the design and monolithic construction of the masses and their associated optical components. The critical modes are those at the lowest frequency, as indicated by Eq. 6.

In a good design the low frequency longitudinal modes having components of motion along the optic axis, should dominate. Assuming that the mirrors are integral with the masses (monolithic construction), the low frequencies of the compressional modes are determined by the longitudinal sound speed and the linear dimension of the mass along the optic axis. The oscillation frequencies of these modes are given by

$$f_n = \frac{n}{2}\frac{c_L}{a} = \frac{m}{2a}\left(\frac{Y}{\rho}\right)^{\frac{1}{2}} \qquad (14)$$

n odd

where c_L is the longitudinal sound speed, a the thickness of the mass along the optic axis, Y the Young's modulus and ρ the density of

the material. The moving mass in these modes is 1/2m. The thermal noise displacement density is calculated by using Eq. 6. Summing over the modes gives

$$x^2(f) = \frac{8k\,Ta^2\rho^{\frac{1}{2}}}{\pi^3 Q A\, Y^{3/2}} \sum_{\substack{n=1 \\ \text{odd}}}^{\infty} \frac{1}{n^3} \qquad f < f_1 \qquad (15)$$

A is the cross section of the mass, Q is the value appropriate to the dissipation of the material in compression.

As an example consider a quartz (fused silica) mass of 10^6 grams having a cylindrical shape with length equal to the radius of 50cm. The Q for the compressional modes, if not compromised by the support, is 10^5 at room temperature. The lowest longitudinal mode frequency for this mass is 6KHz. The amplitude spectrum at frequencies less than 6KHz, given by Eq. 15, is $x(f) \sim 3\times10^{-19}$ cm/Hz$^{\frac{1}{2}}$. The limiting strain sensitivity in a 5km baseline from this noise source alone would be $h(f) \sim 6\times10^{-25}$ strain/Hz$^{\frac{1}{2}}$.

The modes involving pure shear (no internal volume changes) have both lower frequencies and lower Q. However in a symmetric and isotropic optical design, the fringe sensitivity to these modes can be reduced to second order in their amplitudes.

In the lowest frequency pure shear mode, the neutral plane of the oscillation bisects the largest dimension of the mass. The frequency of the mode is

$$f_{sh} = \frac{2}{\pi t}\, c_{sh} = \frac{\sqrt{2}}{\pi t} \left(\frac{Y}{2(1+\sigma)\,\rho}\right)^{\frac{1}{2}} \qquad (16)$$

t is the largest dimension, 2a in the above example, and c_{sh} is the transverse or shear sound velocity in the materials. σ is the Poisson ratio. The moving mass is the total mass. For sake of comparison using the same sample parameters as above; adding that the Poisson ratio for quartz, σ, is 0.17, one finds from Eq. 16, the lowest shear mode at 1.7KHz. Assuming a Q in shear of 10^4, the average amplitude density of thermal motions of the surface below 1.7 KHz, due to this mode alone is approximately, $x(f) = 1.8 \times 10^{-18} cm/Hz^{\frac{1}{2}}$. The strain limit imposed by this type of oscillation depends critically on the optical design, as already mentioned.

The final class of motions considered, flexural vibrations, involve both shear and compression. A good example of such a mode is the oscillation, perpendicular to the surface, of a thin mirror clamped at its edges. These are troublesome in current prototype interferometer designs, and their suppression indicates monolithic construction. The normal mode frequencies have been calculated in the theory of the oscillation of plates. For a circular plate with a clamped outer edge the normal mode frequencies are given by

$$f_{nm} = \frac{\pi t}{a^2} \left(\frac{Y}{3\rho(1-\sigma^2)}\right)^{\frac{1}{2}} \beta_{nm}^2$$

Here t is the plate thickness and a the radius. The indices n and m indicate the number of radial and azimuthal nodes of the oscillation. β is a constant dependent on the mode, for the lowest order mode having one radial node and no azimuthal dependence, $B_{10} = 1.015$. The next mode n = 1, m = 1, has a frequency 2.09 times higher. The

lowest frequency flexural mode for the sample dimensions given above is 22 KHz and therefore not important.

In summary, the most important thermal noise term that figures in the gravity antenna performance is the suspension noise at low frequencies and this is not a severe constraint in a first generation large baseline antenna of sufficient length. The improved performance in a second generation system may require modification in suspension and mass design.

VIBRATION ISOLATION

1.0 Introduction

Two different mechanical noise sources will be considered here: seismic noise, and gravity gradient noise. By seismic noise is meant mechanical coupling of the test masses, through their supporting structures, to the low level vibration of the earth. Gravity gradient noise is motion due to the fluctuating gravitational forces on the test masses caused by acoustic density fluctuations in the material media (earth and atmosphere) surrounding the antenna, or due to the motion of massive bodies in the vicinity of the antenna.

A recent compilation of earth motion spectra is given by Fix (1972). Between 0.1 Hz and 10 Hz, the spectrum is approximately proportional to $(f/1\ \text{Hz})^{-2}$, where the constant of proportionality varies from 10^{-5} to $3*10^{-8}$ $\text{cm/Hz}^{\frac{1}{2}}$. If the spectra continued to fall with the same slope, even at the quietest places the earth motion exceeds the expected shot noise floor at all frequencies below 20 kHz. Thus the test masses must not have a rigid mechanical connection to the earth, but must instead be mechanically isolated. A simple form of isolation is a pendulum suspension of high Q, whose transmission is equal to $((f_0/f)^2$, where f_0 is the resonant frequency. A 1 Hz suspension would reduce the seismic noise to below 10^{-17} $\text{cm/Hz}^{\frac{1}{2}}$ above 250 Hz at the quietest locations, above 1 kHz at a noisy site.

The fluctuating gravitational force from density variations in

the earth due to seismic motion has been evaluated by Saulson (1983a). The spectrum of test mass motion calculated there is $x = B*(1Hz/f)^4$, where B runs from 10^{-15} $cm/Hz^{1/2}$ at a quiet site to $3*10^{-13} cm/Hz^{1/2}$ at a noisy site. Thus this noise term is larger than $10^{-17} cm/Hz^{1/2}$ at frequencies below 3 to 13 Hz. The gravitational coupling of seismic noise to the test masses is, then, weaker than direct mechanical coupling. Yet, unlike mechanical coupling, the gravitational force can not be shielded, so this lacter term represents a true noise floor. (In principle, a regression scheme could remove some of this noise from the output of the antenna by recognizing the signature of a local tidal force on the antenna. However, the gravitational forces on the test masses are only strongly correlated at frequencies where the acoustic wavelength of the disturbance is large compared to the separation between the test masses. In the proposed system of 5 km baseline, this is only true at extremely low frequencies, especially if there is a non-negligible contribution due to atmospheric infrasound.)

This study has shown that the most serious mechanical noise source for the antenna is seismic vibration, followed in importance by Brownian motion of the test masses. In the rest of this section we will describe the conceptual design of a feasible test mass suspension which should reduce mechanical noise to below $10^{-17} cm/Hz^{\frac{1}{2}}$ at all frequencies above 70 Hz, with appreciable reductions as well at lower frequencies. Few aspects of the design are dictated explicitly by the specifications, but we have tried to make reasonable choices.

In our proposed design, we have elected to avoid the headaches associated with cooling the test masses, but are left instead with the headache of large masses. A second important feature of this design is to make a cascade of several stages of isolation, rather than lowering the resonant frequency of a single stage. Even at the quietest site, an ideal suspension would have to have a period of 20 sec (for a pendulum, this would mean a length of 90 meters!) This simple calculation neglects internal resonances in the suspension's structural members, which make it difficult to achieve the theoretical isolation over more than two decades in frequency. A third aspect of the design is to make use of active vibration isolation in addition to passive isolation. This is especially valuable for frequencies near and below 30 Hz, less so above 30 Hz. Active isolation is included because a fairly elaborate servo control system will probably be required for DC alignment and low-noise damping of the high Q resonance, so using the sensors and actuators for broad band vibration reduction comes almost "for free."

2.0 THEORETICAL ANALYSIS

2.1 Equations of Motion

A schematic diagram of the sort of system we are considering is given in Figure 1. At this level of analysis we treat all the motions as one-dimensional, parallel to the x-axis. M_3 is the test mass itself, while k_3 and f_3 represent the spring constant and damping

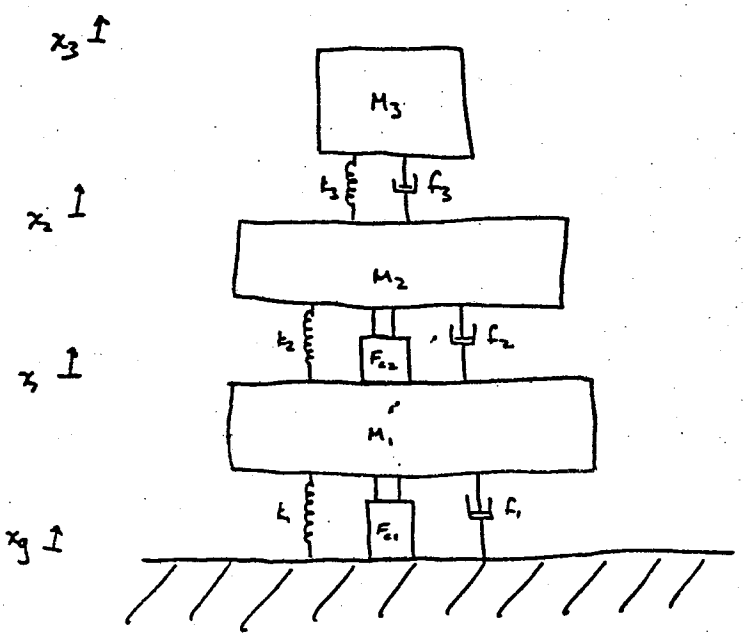

Figure 1: Schematic Diagram of Vibration Isolation System

coefficient of the suspension of the test mass, most likely a pendulum. M_3 is suspended from a second mass, M_2, which is in turn suspended from M_1. The whole system is, finally, suspended from a frame fixed to the ground. In addition, two linear actuators are installed, one between the ground and M_1, the second between M_1 and M_2.

The equations of motion for the system are:

$$M_1\ddot{x}_1 = -k_1(x_1-x_g) - f_1(\dot{x}_1-\dot{x}_g) - k_2(x_1-x_2) - f_2(\dot{x}_1-\dot{x}_2) + F_{c1} - F_{c2}$$

$$M_2\ddot{x}_2 = -k_2(x_2-x_1) - f_2(\dot{x}_2-\dot{x}_1) - k_3(x_2-x_3) - f_3(\dot{x}_2-\dot{x}_3) + F_{c2} \qquad (1)$$

$$M_3\ddot{x}_3 = -k_3(x_3-x_2) - f_3(\dot{x}_3-\dot{x}_2)$$

These equations are simplified as follows. First, for brevity of notation, define $\mu_{21} = M_2/M_1$ and $\mu_{32}=M_3/M_2$. Also, define $\omega_{01}^2=k_1/M_1$, $Q_1=M_1\omega_{01}/f_1$, and the analogous quantities for suspensions 2 and 3. We consider only the steady-state solutions, so we can make the ansatz $x = x(\omega)e^{i\omega t}$. Then $\dot{x} = i\omega x$, $\ddot{x} = -\omega^2 x$, and the system of equations becomes a set of simultaneous linear equations in the coordinates of the masses. Further, if we are only interested in the response of the system to forces from the motion of the ground (ignoring Nyquist force on M_3, for example), then we can express $x_3 - x_2$ as some transfer function times x_2:

$$x_3 - x_2 = \frac{\omega^2}{\omega_0^2-\omega^2+\frac{i\omega\omega_{03}}{Q_3}}\, x_2 \equiv T_3 x_2 \qquad (2)$$

so that only the coordinates x_1 and x_2 remain. With these simplifications the equations (1) reduce to the 2 by 2 matrix equation

$$\begin{bmatrix} T_{11} & T_{12} \\ T_{21} & T_{22} \end{bmatrix} \begin{bmatrix} x_1 \\ x_2 \end{bmatrix} = \begin{bmatrix} T_g x_g \\ 0 \end{bmatrix} \tag{3}$$

where

$$T_{11} = \frac{1}{\mu_{21}\mu_{32}}\left(-\omega^2+\omega_{01}^2 + \frac{i\omega\omega_{01}}{Q_1} + \omega_{02}^2\mu_{21} + \frac{i\omega\omega_{02}}{Q_2} - \frac{T_{c1}}{M_1}\right),$$

$$T_{12} = \frac{1}{\mu_{32}}\left(-\omega_{02}^2 - \frac{i\omega\omega_{02}}{Q_2} + \frac{T_{c2}}{M_2}\right),$$

$$T_{21} = \frac{1}{\mu_{32}}\left(-\omega_{02}^2 - \frac{i\omega\omega_{02}}{Q_2}\right),$$

$$T_{22} = \frac{1}{\mu_{32}}\left(-\omega^2+\omega_{02}^2 + \frac{i\omega\omega_{02}}{Q_2} - \frac{T_{c2}}{M_2} - \omega_{03}^2\mu_{32}T_3 - \frac{i\omega\omega_{03}}{Q_3}\mu_{32}T_3\right)$$

$$T_g = \frac{1}{\mu_{21}\mu_{32}}\left(\omega_{01}^2 + \frac{i\omega\omega_{01}}{Q_1}\right).$$

In these equations T_{c1} represents the transfer function F_{c1}/x_1 and similarly $T_{c2} = F_{c2}/x_2$. Solving the system of equations gives the following transfer functions:

$$\frac{x_1}{x_g} = \frac{T_g T_{22}}{T_{11}T_{22}-T_{12}T_{21}}$$

$$\frac{x_2}{x_g} = \frac{-T_g T_{21}}{T_{11}T_{22}-T_{12}T_{21}} \tag{4}$$

$$\frac{x_3}{x_g} = \frac{-T_g T_{21}(T_3+1)}{T_{11}T_{22}-T_{12}T_{21}}.$$

To obtain concrete results we have to choose the values of 8 parameters: the three resonant frequencies, the 3 quality factors, and two mass ratios. (The overall mass scale does not affect the transfer functions.) We know that Q_3 must be around 10^6. Q_2 and Q_1 need not be as high, since there is isolation between them and M_3. We somewhat arbitrarily set $Q_2=10^3$ and $Q_1=10$. Inspection of elements T_{11} and T_{22} indicates that the cross-coupling terms have the form $\omega_{02}^2\mu_{21}$ (in T_{11}) and $\omega_{03}^2\mu_{32}$ (in T_{22}). If M_3 is as large as 1 ton, it would be a great advantage not to have to have $M_1>>M_2>>M_3$ to make the outer stages sufficiently stiff for proper operation of the servo loops. We obtained satisfactory results with $\mu_{21}=\mu_{32}=1$, but with progressively stiffer springs moving outward from M_3. We show the results for $\omega_{01}=2\pi*10$ Hz, $\omega_{02}=2\pi*3$ Hz, and $\omega_{03}=2\pi*1$ Hz.

Figure 2 shows the passive isolation of the system, obtained by solving for the transfer function x_3/x_g with the feedback terms T_{c1} and T_{c2} set equal to zero. This transfer function is given by equation (4), above. The form of the transfer function is easy to understand. There is no isolation at frequencies below the lowest resonance. Just above the highest resonant frequency, the isolation has a slope of -120 dB/decade characteristic of three resonant isolators in series. At higher frequencies the slope becomes shallower because of the finite Q of the resonances. In the band 1Hz<f<10Hz appear the peaks due to the three resonances, slightly shifted in frequency from their nominal values due to the coupling to the other resonances.

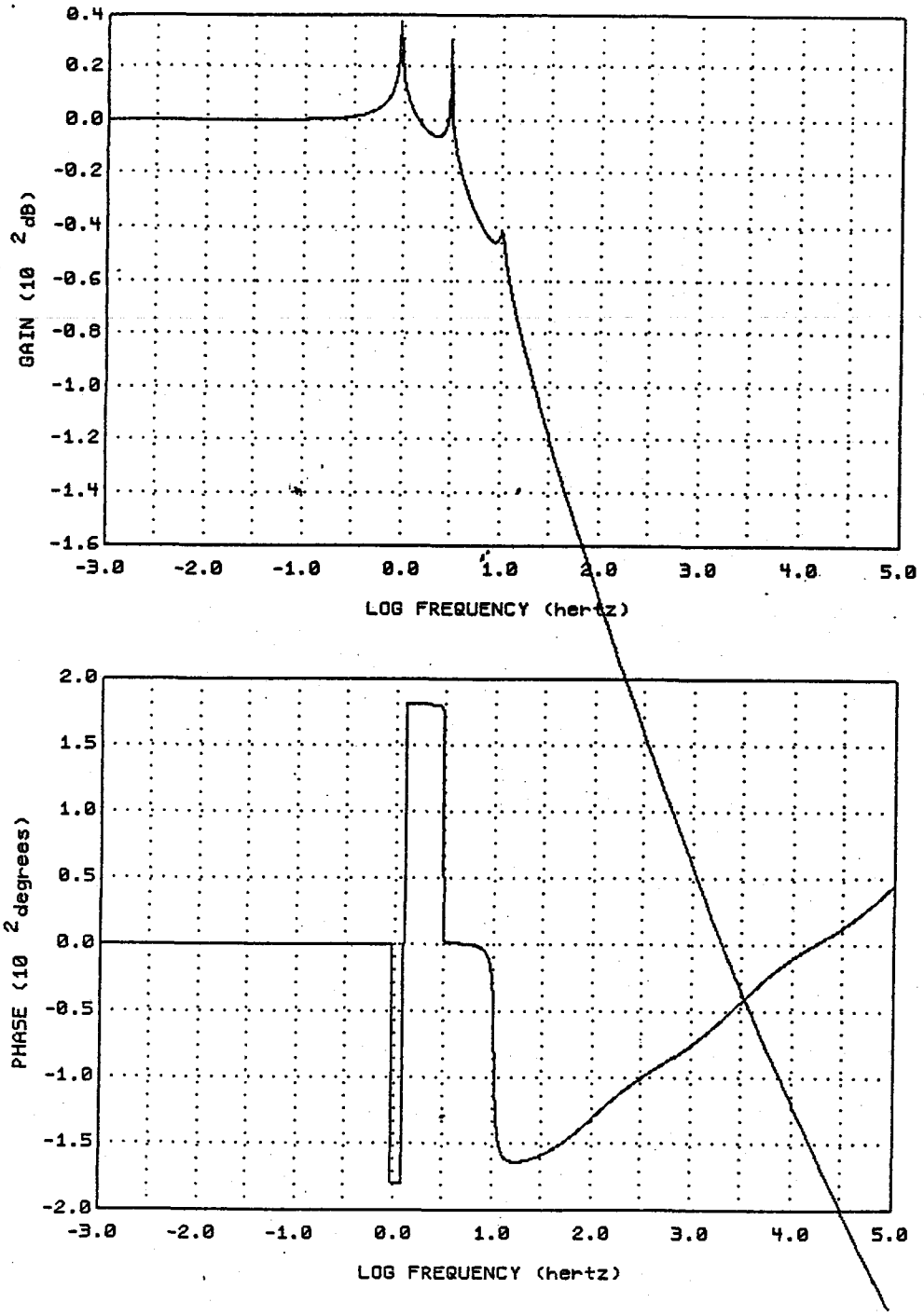

FIGURE 2: PASSIVE ISOLATION

2.2 Passive Isolation

The passive isolation of this system at 30 Hz is computed to be 120 dB, or 6 orders of magnitude in amplitude. At a quiet site, this would be nearly sufficient to make the seismic noise contribution smaller than 10^{-17} cm/ Hz at 30 Hz. So the simple design is fairly successful, if one is willing to tolerate a very steep increase in the seismic noise contribution as one goes lower in frequency. Furthermore, it would not be impractical to move all of the resonances down in frequency by a factor of 2 or 3, say, and thereby improve the isolation. Still, even more isolation would yield improved antenna performance in the band below the highest resonance, since the Brownian motion noise (which is the dominant noise below 30 Hz if $M_3Q_3=10^6$ tons) has a much shallower spectrum than the ground noise. In addition, the high Q low frequency resonance is certain to be troublesome without some active damping.

2.3 Active Isolation

The active vibration isolation scheme which we plan to incorporate uses the test mass M_3 as an inertial reference element, that is as a sort of hook to an inertial frame of reference. Measurement of the relative displacement x_3-x_2 gives an error signal which drives a linear actuator F_{c2} mounted between M_1 and M_2. A feedback force is applied in order to null x_3-x_2, thus tending to compensate for the other forces which are being applied to M_3. We have also included another actuator F_{c1}, to be driven by the error signal x_3-x_1. A working prototype of a (single loop) inertial stabilization system of

this sort is described by Saulson (1983b). A slightly different method of inertial stabilization is described by Robertson et al. (1982).

The performance of a feedback system is governed by its loop transfer function. Let the feedback force F_{c2} be given by

$$F_{c2} = \frac{F_2}{d_2} G_{c2}(f)(x_3-x_2) \tag{5}$$

where F_2/d_2 is an overall gain and $G_{c2}(f)$ is a compensation filter. From the solution of the equations of motion of the system (3), we find

$$\frac{(x_3-x_2)_{driven}}{F_{c2}} = \frac{1}{M_3} \frac{T_3(T_{11}+T_{21})}{T_{11}T_{22}-T_{12}T_{21}} \tag{6}$$

Thus the loop transfer function is

$$\frac{(x_3-x_2)_{driven}}{(x_3-x_2)} = \frac{F_2}{d_2 M_3} G_{c2}(f) \frac{T_3(T_{11}+T_{21})}{T_{11}T_{22}-T_{12}T_{21}} \tag{7}$$

A Bode plot of this function for $G_{c2}(f)$ = constant is given in Figure 3. The transfer function contains, in series, the resonances ω_{03} and ω_{02}. The resonance ω_{01} appears only in vestigial form--it does not cause any net phase shift. A feedback system with such a transfer function is absolutely stable for all values of the gain, although with vanishingly small phase margin. In a real system, the available gain will be limited by additional phase lags due to mechanical resonances in the structural members of the device. Nevertheless, it is possible to achieve high gain in the frequency band near 1Hz if the structural

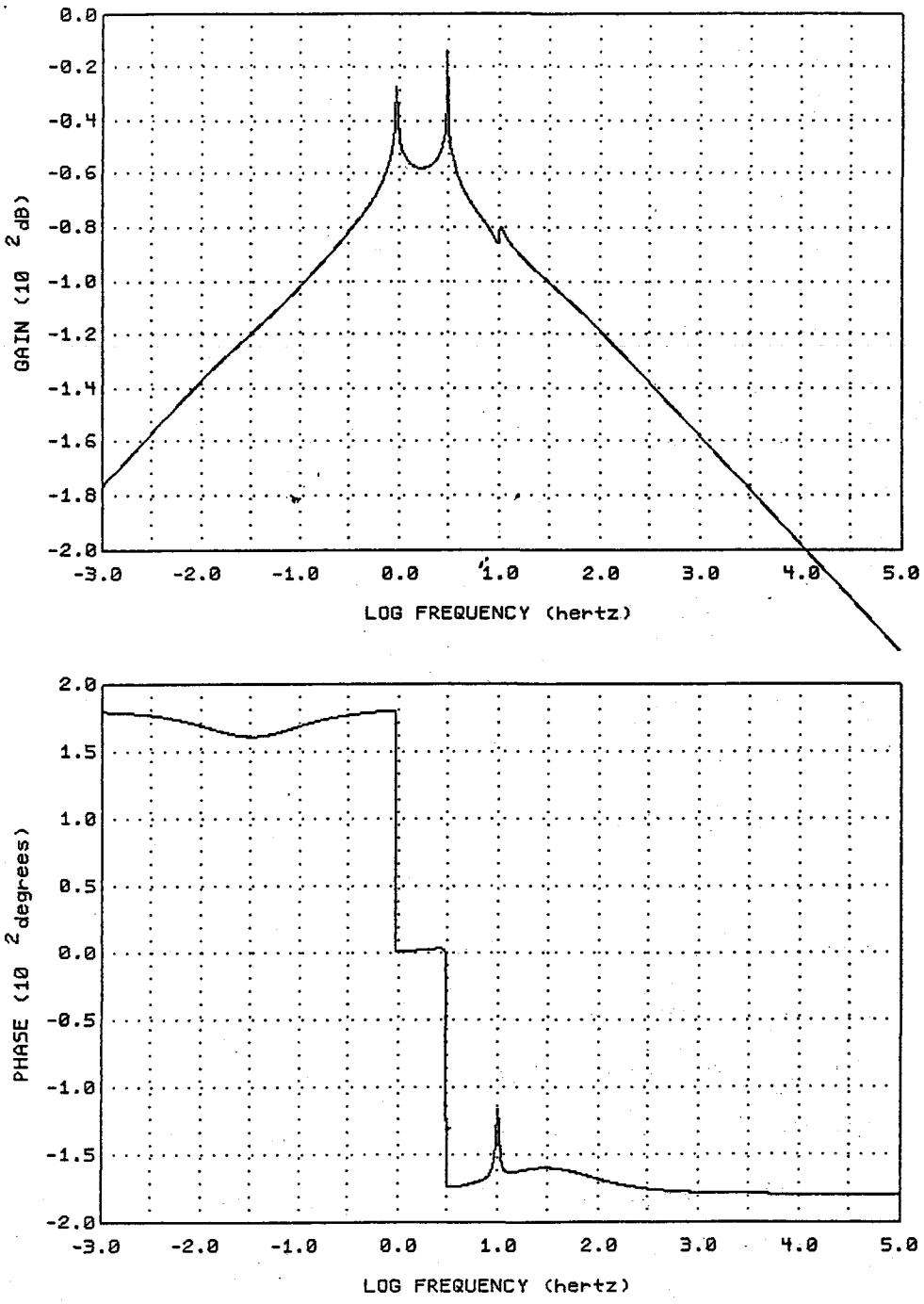

FIGURE 3: LOOP TRANSFER FUNCTION, INNER LOOP

resonances can be kept at relatively high frequencies, since the roll-off of gain is nearly f^{-2} when the phase is nearly -180 degrees. Judicious compensation can also improve the phase margin, making this a well-behaved servo. For more details, see the paper by Saulson (1983b). If we assume that the gain must be brought below 1 at frequencies above 100 Hz, then the additional seismic attenuation of the active isolation is that shown in Figure 4, and the net seismic transmission of the system is that shown in Figure 5.

To achieve even better low frequency isolation, we can use the outer feedback loop, where actuator F_{c1} is driven by x_3-x_1. The loop transfer function is found to be

$$\frac{(x_3-x_1)_{driven}}{(x_3-x_1)} = \frac{F_1}{d_1 M_3} G_{c1}(f) \frac{T_{21}(T_3+1)+T_{22}}{T_{11}T_{22}-T_{21}T_{12}}$$

where T_{12} and T_{22} contain feedback terms from actuator F_{c2}. That is to say that the functional form of the loop transfer function of the outer loop depends on the amount of gain in the inner feedback loop. This makes sense, since the operation of the inner loop does in fact alter the net transmission of force to M_3. A graph of the outer loop transfer function (with the value of inner loop gain used in Figures 4 and 5) is shown in Figure 6. It has a form similar to that of the inner loop transfer function, so the comments made above regarding stability and compensation apply here as well. A further comment is in

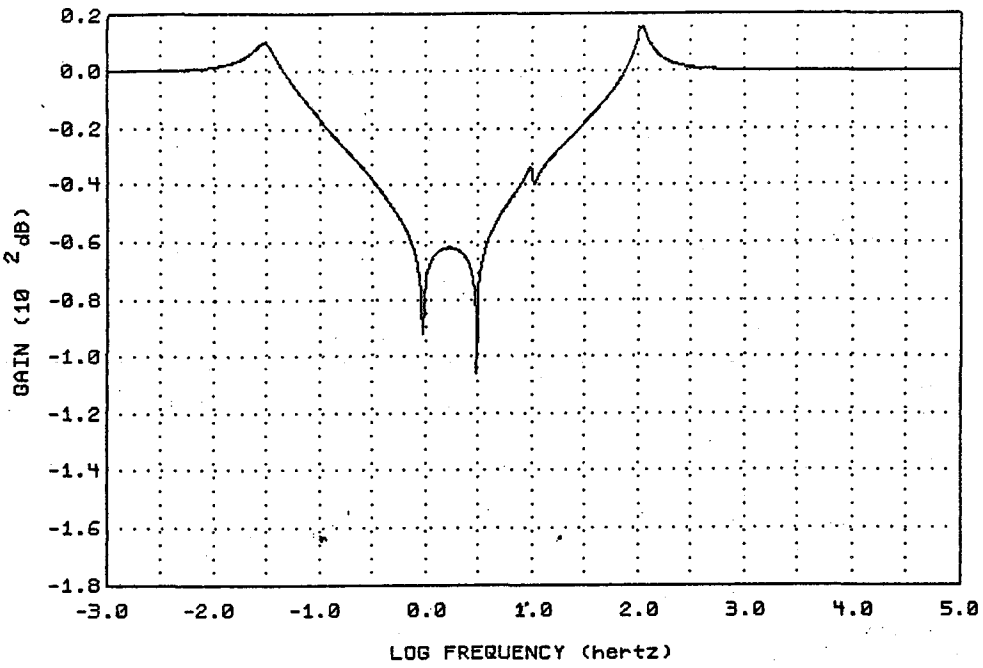

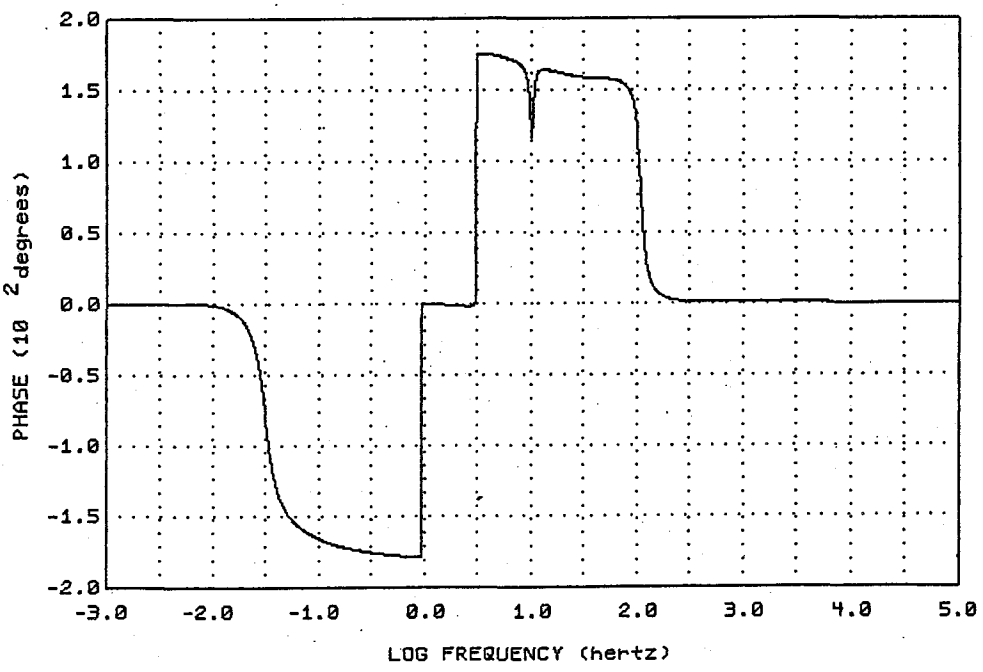

FIGURE 4: ADDITIONAL SEISMIC ATTENUATION FROM INNER LOOP

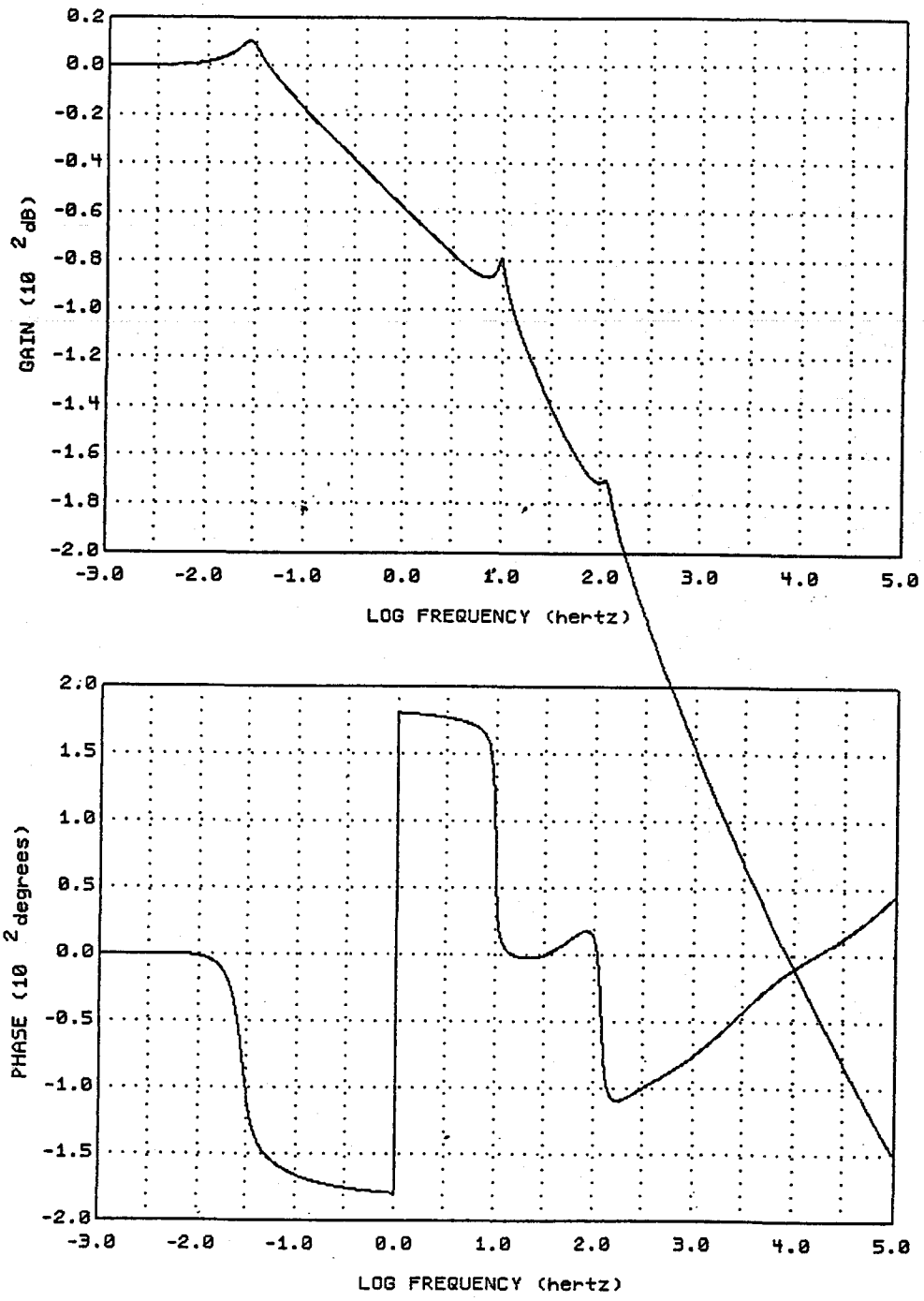

FIGURE 5: NET SEISMIC TRANSMISSION, INNER FEEDBACK LOOP ON

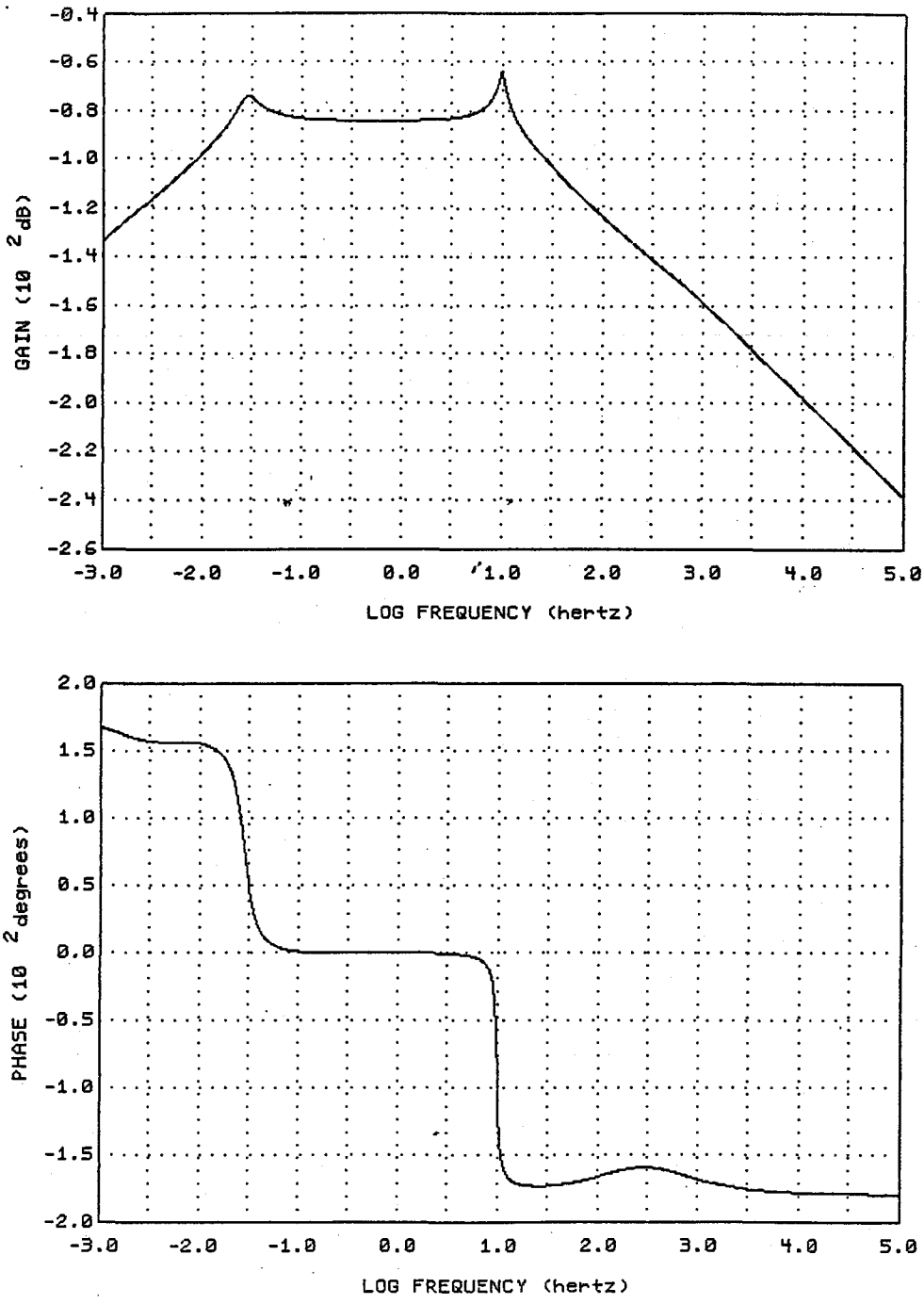

FIGURE 6: LOOP TRANSFER FUNCTION, OUTER LOOP

order, though. Higher gain can be achieved between the two resonances in this loop by using a compensation filter which adds enough phase lag in between them to bring the phase to nearly -180 degrees. Then the gain will fall nearly as steeply as f^{-2} over this range, giving higher gain at low frequencies for any given crossover frequency. Figure 7 shows the loop transfer function with one version of such a compensation filter. If we again assume that the crossover frequency equals 100 Hz, then the attenuation from this loop is that shown in Figure 8, and the total seismic transmission of the entire system, including the passive response and the effect of the inner loop, is shown in Figure 9. The net improvement of isolation due to the two active loops over the passive response alone is shown in Figure 10. There is no net improvement, obviously, at frequencies above the upper crossover frequency. Furthermore, because of the shape of the loop transfer function there is a lower crossover frequency below which there is no improvement either. Figure 11 shows the net motion of the test mass M_3 at a moderately quiet site, where the seismic spectrum is $x(f) = 10^{-7} \text{cm/Hz}^{\frac{1}{2}} \left(\frac{1\text{Hz}}{f}\right)^2$.

3.0 PRACTICAL CONSIDERATIONS

The foregoing discussion has shown that it is possible, in principle, to attain sufficient vibration isolation above 30 Hz, and substantial isolation to frequencies as low as 1 Hz, with a combined passive-active system. However, several important simplifications were made, the validity of which we will now discuss.

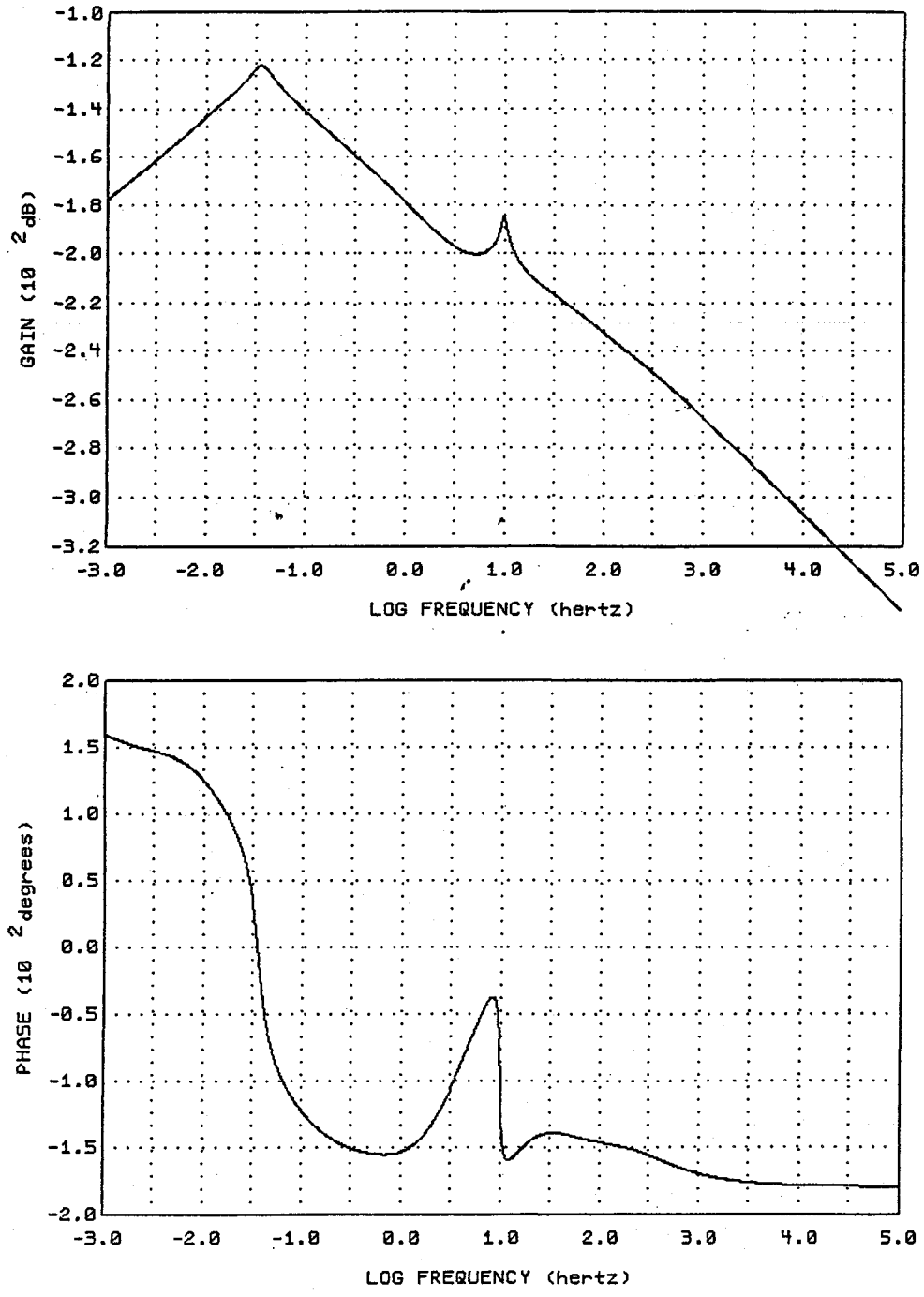

FIGURE 7: COMPENSATED LOOP TRANSFER FUNCTION, OUTER LOOP

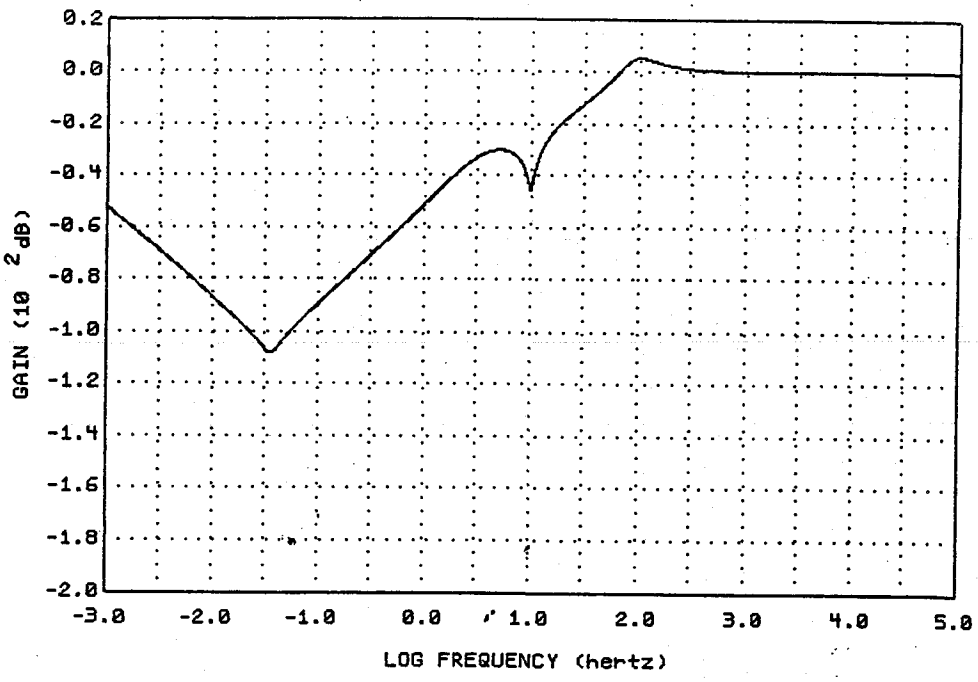

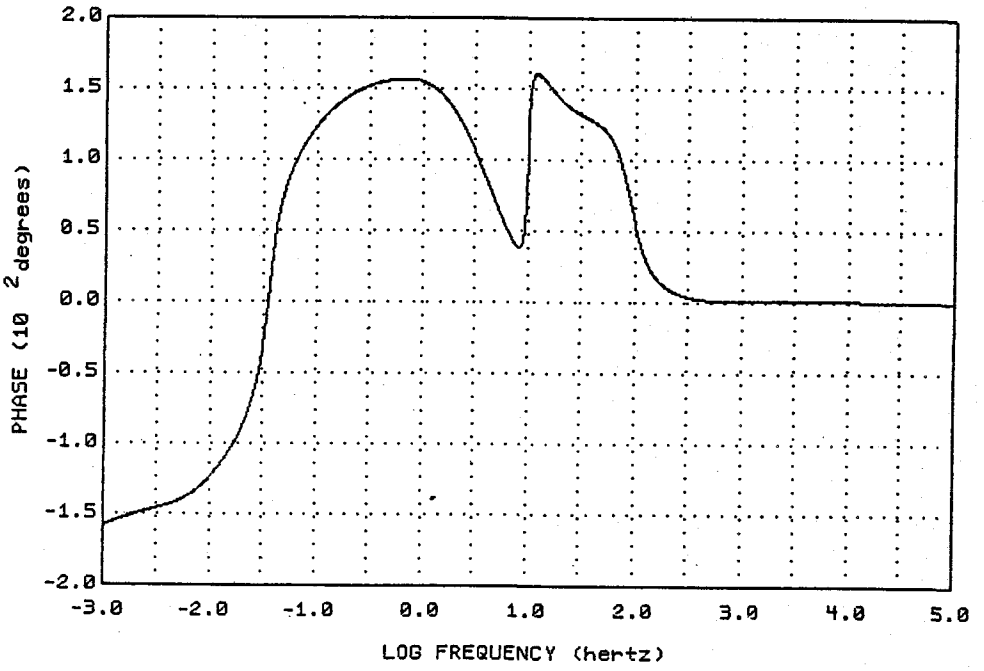

FIGURE 8: ADDITIONAL SEISMIC ATTENUATION FROM OUTER LOOP

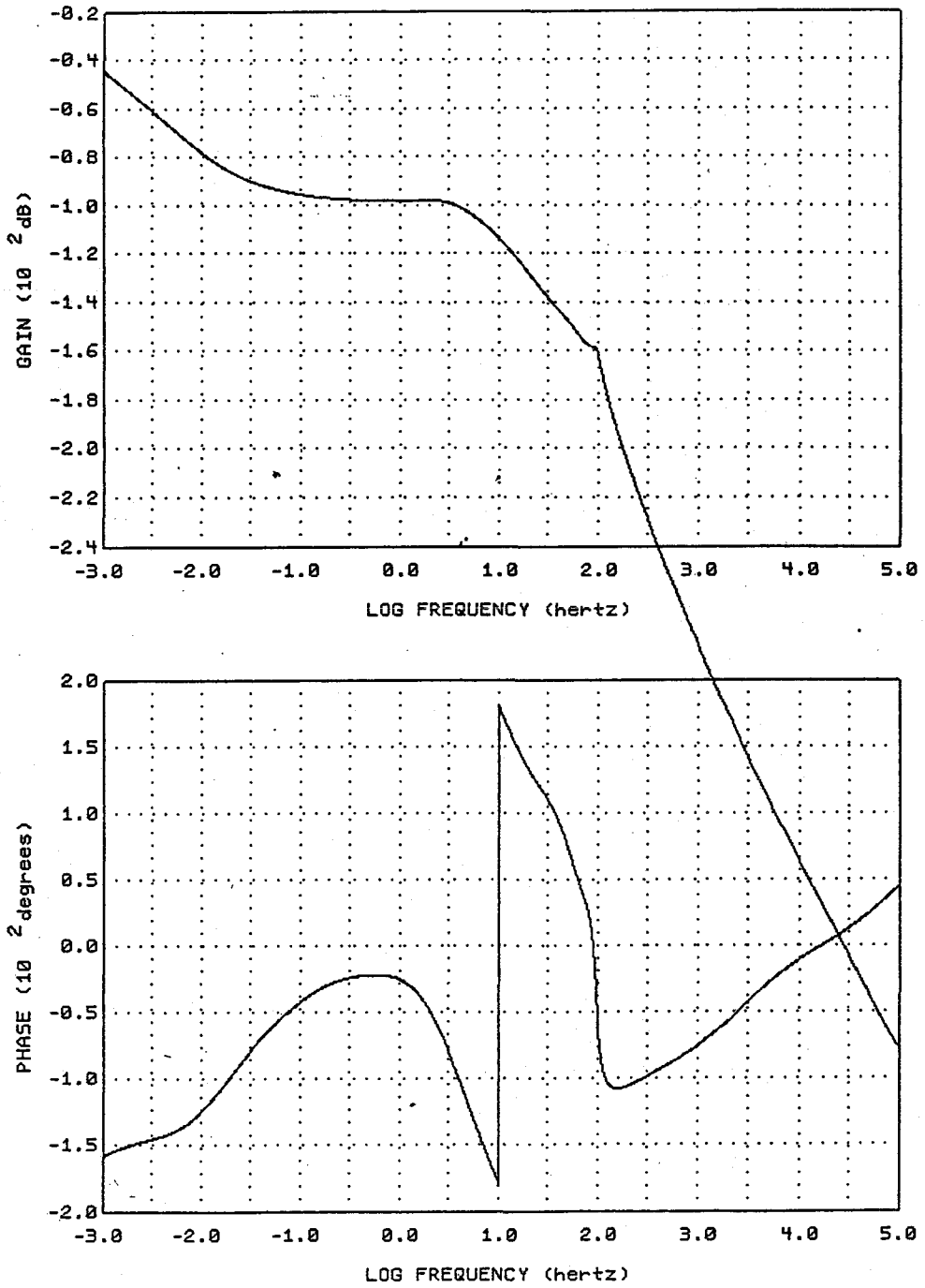

FIGURE 9: NET SEISMIC TRANSMISSION, BOTH FEEDBACK LOOPS ON

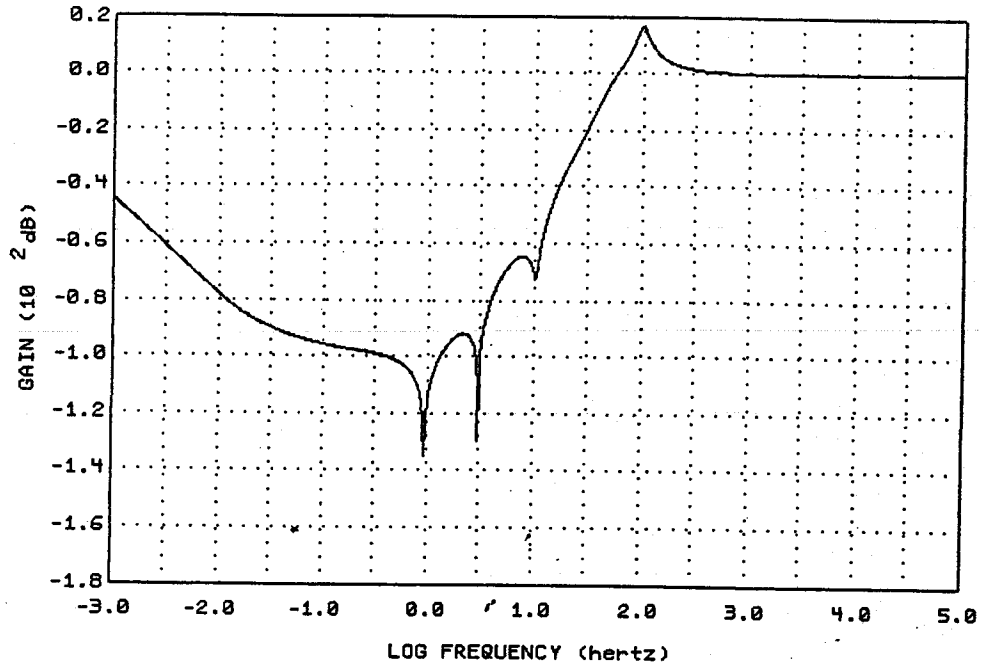

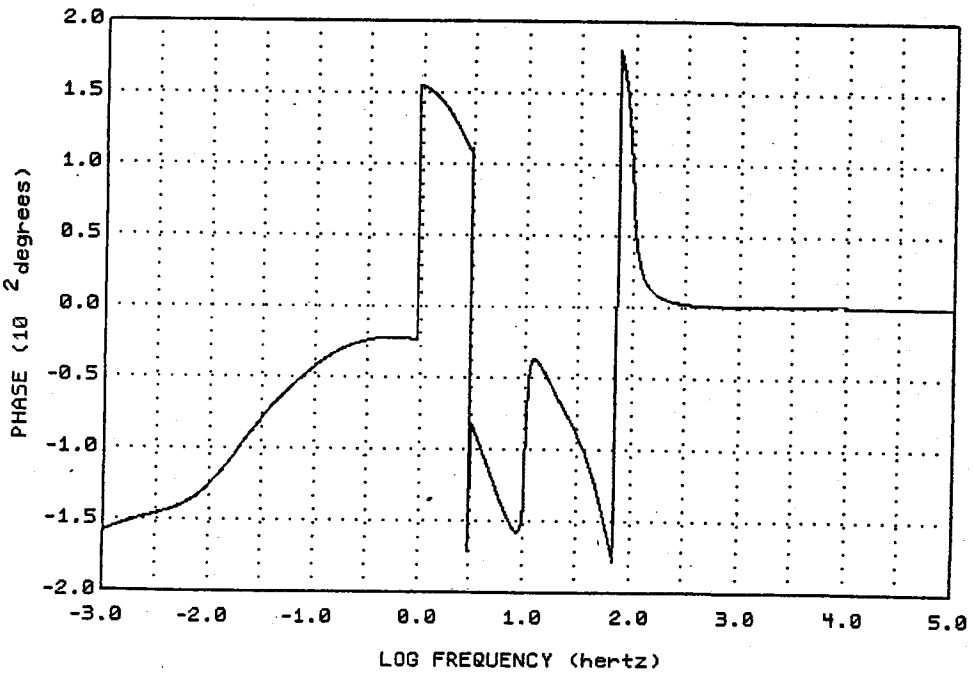

FIGURE 10: SEISMIC ATTENUATION DUE TO BOTH ACTIVE LOOPS

Figure 11: Seismically Induced Motion of Isolated Mass

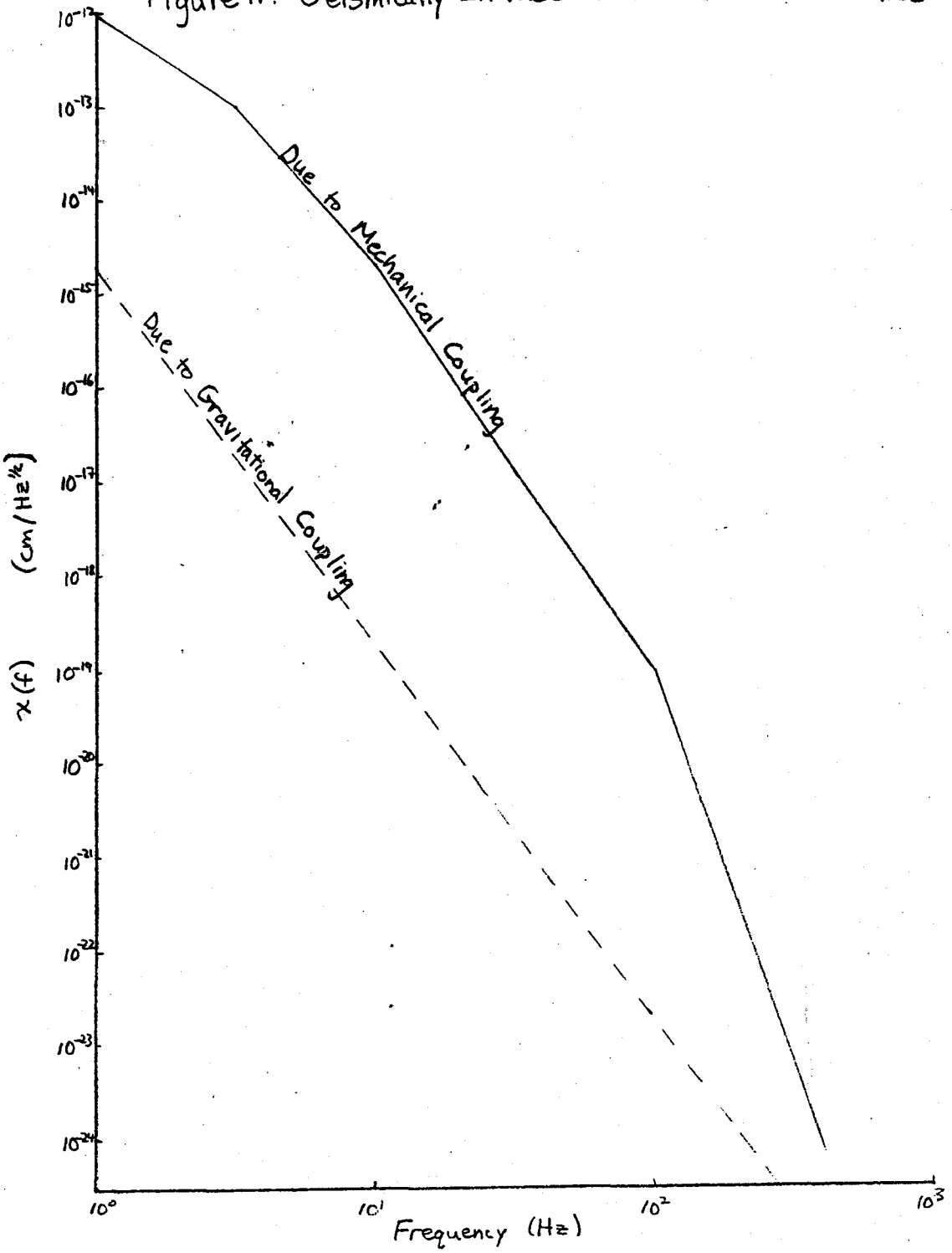

3.1 Cross-Coupling

The most important simplification made was the treatment of only one dimension of motion. A rigid body, such as the test mass M_3, has of course 3 dimensions of translational motion and 3 of rotation. It is necessary to design a system which can simultaneously meet the applicable vibration specifications in all relevant dimensions.

In principle, cross-coupling need not be a problem. It is easy to show that if a mass is suspended by a set of springs arranged with sufficient symmetry about its center of mass, then each of the six degrees of freedom is decoupled from the others and can be treated as a one-dimensional oscillator. The problem is somewhat more complicated with a pendulum suspension, which is probably required for M_3 because of the difficulty of achieving $Q = 10^6$ for a 1 ton mass with a room temperature spring suspension. A pendulum couples translation along a horizontal axis into a tilt of the mass about the orthogonal horizontal direction.

When feedback is considered, the cross-coupling is more serious. An active system of any sort of suspension which derives an error signal only from the displacement of a reference mass with respect to a frame can not distinguish whether it was a horizontal acceleration or a tilt of the frame which caused the displacement. In such a system, tilt excitation represents a noise source which feedback does not remove.

A simple model can be made of the shear wave component of seismic

noise to estimate the magnitude of the problem. The acceleration input term due to tilts is $g\sin\theta_e$, where g is the acceleration due to gravity, and θ_e is the tilt of the earth. If at a frequency ω the earth's amplitude of vertical motion if z_e, then it is easy to show that

$$\langle \sin\theta_e \rangle_{rms} = \frac{\omega}{2v_s} z_e \qquad (9)$$

This is to be compared to the translational acceleration input term $\omega^2 y_e$. Now it is known empirically that $y_e \simeq z_e$. Therefore, the ratio of acceleration due to tilt to acceleration due to translation is approximately

$$\frac{g\omega}{2v_s\omega_o^2} = 4\times10^{-4}\left(\frac{f}{1Hz}\right) \qquad (10)$$

if $\omega_o = 2\pi * 1$ Hz. Thus the gain at 3Hz, say, is limited to 1000 or less, which is rather restrictive in the presence of high Q resonances in the loop gain.

A more elaborate system can get around this limit. First, the test mass can be supported just above its center of mass, so that it has a low resonant frequency in the rocking mode. Then the orientation of the mass can be used as an angular reference (above the rocking frequency), in a similar fashion to the reference arm of Robertson et al. (1982). Specifically, in addition to the displacement of the center of mass of M_3 with respect to the frame (expressed as an angle θ_t),

one measures the angular orientation of the mass with respect to the frame, θ_r. Pure translation leaves $\theta_r = 0$, while pure rotation about the support point of the pendulum makes $\theta_t = \theta_r$. Therefore, the error signal for feedback force must be derived from $\theta_t - \theta_r$, while an error signal for feedback torque may be derived from θ_r. Thus, the feedback system requires two sets of differential sensors and two actuators to separately null translation and rotation.

The requirements for vibration isolation in the directions not parallel to the optic axis are less severe than for motion along the optic axis. Unfortunately the requirements are harder to specify since they depend in detail on the symmetries of the optical scheme and on the degree of DC misalignment. In principle, the interferometer can be made to be sensitive to transverse displacements (or rotations) of the end masses only in terms of second order in these small quantities. Without further study of the optics, it is difficult to say whether a particular design will suffice. One thing that is clear, though, is that the test mass at the vertex of the interferometer will have to meet the stringent specification along both horizontal directions, and so will require two orthogonal sets of sensors and actuators, along with a sufficiently symmetrical suspension. For the masses at the ends of the arms, this may not be required. The symmetry between axes does not extend to the vertical direction, in particular if we are required to use a pendulum suspension for the test masses. A pendulum is much

stiffer in the vertical direction than the horizontal, so the vertical direction has one fewer passive isolation stages than the horizontal directions. For the same reason, an inner active loop can not be made to work in the same way in the vertical as in the horizontal. This means that if the transverse isolation requirements are too severe, the vertical isolation will probably be where the problem is worst. It may be necessary to make a non-rigid connection between the pendulum and its support, although here a potentially serious cross-coupling problem may occur.

3.2 Internal Resonances

A second aspect of a real system that was not treated explicitly in the theoretical discussion above is the existence of internal mechanical resonances in the structural members. Yet, implicit in many of the design choices was the consideration that the total system performance be as insensitive as possible to the existence of such resonances. The system does not rely on extremely soft springs, or on an extremely long pendulum, either of which might have internal resonances of low frequency. There is only a ratio of less than two decades between the lowest resonant frequency and the frequency above which the system should be shot noise limited. Thus the design does not require transmission to fall like f^{-2} in any stage over a very large bandwidth. (In addition, this means that the outer stages can have rather low Q's without compromising the performance of the system, since there is no

need to restrict the f^{-1} asymptotic form of a finite Q resonance to a very high frequency. The Nyquist noise from the outer stages is substantially attenuated before it affects the test mass M_3.) Even though the seismic transmission may level off substantially above the frequency of the lowest structural resonance, the exciting spectrum is falling rather steeply, so it is unlikely that the high-frequency region will be contaminated by seismic noise.

The problem of the levelling off of the isolation due to internal resonances is more serious in the presence of anthropogenic sources of vibration, such as human speech or the sound of airplanes. In contrast to the steeply falling seismic spectrum, these latter sources often contain substantial power up to frequencies of 1 kHz or higher. Fortunately, highly refined techniques have been developed (by the gravitational wave bar detector groups, among others) for passive isolation at these higher frequencies. It will be important to employ low-pass acoustic filter stacks to attenuate high frequency noise.

The performance of the feedback loops does depend strongly on the frequency and Q of the lowest few structural resonances, since the loop gain must be below unity at all of the peaks in order to assure stability. It is only at frequencies below 30 Hz, however, that the performance of the whole system depends strongly on the gain in the active loops. The assumption of a crossover frequency at 100 Hz that was made in the discussion of theoretical system performance is not

overly ambitious, but even if it does not prove attainable the damping of the high Q pendulum resonance can still be accomplished. Over and above this goal, the more broad-band isolation at low frequencies that can be attained the better, down to the floor set by Nyquist noise and gravity gradient noise.

3.3 Construction

Nesting of the stages is a natural arrangement for several reasons. The outer stages, M_1 and M_2 , can probably be suspended by springs, so in a nested arrangement springs can be attached symmetrically about the masses to make the different directions of motion decoupled. Also, a nested system can be made quite compact, which has the advantages of high frequencies for structural resonances and also of economy in the construction of the vacuum housing which surrounds the system. A disadvantage may be awkwardness in initial construction and alignment, although remote adjustment of all critical spacings and angles will probably have to be provided in any case.

Building a system with the masses and resonant frequencies specified in the design presents no particular troubles. The $Q=10^6$ of M_3's suspension will probably require some care in the construction. The problem to be kept under control is flexure in the structure holding the pendulum, which could lead to too much internal damping in the materials. The Q's of the other stages can be quite low, of order 10 to 100, without impairing the isolation or adding significant Brownian motion noise to the test mass.

3.4 Sensors

In order for the feedback system to be successful, it is necessary that the displacement sensor not introduce a significant amount of noise. Amplifier noise in the sensor that drives the inner feedback loop (calibrated in terms of motion sensitivity) introduces mechanical noise of the same magnitude on M_2. Between M_2 and M_3 there is the attenuation of M_3's suspension, approximately equal to 1000 at 30 Hz. Thus if we want this noise to be insignificant, we need sensor noise to be less than $2*10^{-14}$ cm/Hz$^{1/2}$. Giffard (1980) designed a differential cavity resonator transducer which is a good prototype for the sensors for this system. The scheme is to construct two identical RF resonant cavities, arranged so that as the test mass moves one cavity is shortened while the other is lengthened. The cavities are driven by an oscillator which is tuned slightly off the resonant frequency of the cavities (in the balanced state). Motion of the mass is detected as a change in the relative reflection coefficients of the two cavities as one moves closer to resonance and the other moves further away. Giffard finds that the noise is given by

$$\frac{x_{rms}}{\text{Bandwidth}^{1/2}} = 10^{-15}\,\text{cm/Hz}^{1/2}\left(\frac{T_N}{100K}\right)^{1/2}\left(\frac{1W}{P}\right)^{1/2}\left(\frac{x_o}{1\,\text{cm}}\right)\left(\frac{10^5}{Q_u}\right)$$

where T_N is the amplifier noise temperature, P is the oscillator power, x_o is the effective cavity length, and Q_u is the unloaded quality factor of the resonant cavities. A reasonable design involves a carrier frequency of 10 GHz, and unrefrigerated GaAsFET amplifier

with a noise temperature of 100K, and cylindrical cavities 3cm long by 4cm in diameter driven in the TE_{011} mode. This mode is desirable because it is possible to attain values of $Q_u=2*10^4$, while allowing a small gap between the walls of the cavity and the moving end plate. With these design parameters we can attain the required displacement sensitivity if the oscillator power is around 300 mW. This seems quite feasible. (Giffard achieved a comparable sensitivity, although he used a different cavity design which involved a gap of only 10 microns between the two end faces of each cavity.)

REFERENCES

Fix, J.E., Bull. Seis. Soc. Am., 62, 1753, 1972

Giffard, R.P., unpublished research report, 1980

Robertson, N.A., Drever, R.W.P., Kerr, I., and Hough, J., J. Phys. E., 1101, 1982

Saulson, P.R. The Terrestrial Gravitational Noise on a Gravitational Wave Antenna, preprint, 1983a

Saulson, P.R., Active Vibration Isolation for Broad-Band Gravitational Wave Antennas, preprint, 1983b

Electromagnetic fields

Electric and magnetic fields cause noise principally by exerting force on the mirrors and the suspended end masses of the antenna. We plan to include electrostatic and magnetic shields to minimize the effect of stray fields, but the estimates in this section show that, even without this precaution, the noise introduced by electromagnetic fields is significantly less than the noise introduced by other noise sources in the system.

Electric fields

Electric fields in conducting vacuum chambers typically are $\sim 10^{-3}$ V/cm. These fields result from variations in the work function of surfaces and occur even when all surfaces in a system are constructed of the same material because the work function of one crystal face is different from that of another.

Temporal fluctuations in these fields are caused by impurity migrations and variations in adsorbed gas layers. There is little information in the literature about the correlation time of these fluctuations, except that at room temperature it seems to be longer than a few seconds and at cryogenic temperatures the fields may be constant to better than $\sim 10^{-12}$ V/cm for several hours.

The electric force F_e on a suspended mass with an exposed surface area A is given by

$$F_e = \frac{1}{4\pi} E^2 A \qquad (1)$$

where E is the fluctuating electric field at the surface.

Assuming that the power spectrum of the field fluctuations is similar to that of the flicker effect in vacuum tubes and the surface effects in semiconductors, both of which stem from slow large scale changes in the surface properties of materials, the electric force power spectrum may be modelled by

$$F^2(f) = \frac{2<F^2>\tau_o}{\pi(1+(\omega\tau_o)^2)} \qquad (2)$$

where $<F^2>$ is the average fluctuating force squared and τ_o is the correlation time of the fluctuations.

If the gravity wave frequency is much greater than $(1/\tau_o)$ and also is much greater than the resonant frequency of the suspension, the displacement power spectrum becomes

$$x^2(f) \sim \frac{F^2(f)}{m^2\omega^4} \sim \frac{<E^4>A^2}{512\pi^9 m^2 \tau_o f^6} \qquad (3)$$

Using the sample antenna parameters of $m \sim 10^6$ grams, $A \sim 8\times10^3 cm^2$, assuming a correlation time of $\tau_o \sim 1$ second and an electric field of $E \sim 10^{-3}$ V/cm = $(10^{-5}/3)$ statvolts/cm, the displacement power spectrum becomes

$$x^2(f) \sim \frac{5.0\ 10^{-34}}{f^6} \quad cm^2/Hz$$

For example then, an antenna with 5 km long interferometer arms would experience a strain amplitude noise of

$$h(f) \sim \frac{4.5 \quad 10^{-23}}{f^3} \text{ strain/Hz}^{\frac{1}{2}}$$

We note that even at 1 Hz this is three orders of magnitude smaller than the effect of thermal noise on the suspended mass.

Magnetic fields

Geomagnetic storms caused by ionospheric currents that are driven by the solar wind and cosmic rays create fluctuating magnetic fields at the surface of the Earth. The power spectrum of the magnetic field fluctuations in temperate regions at frequencies greater than about 10^{-3} Hz can be characterized crudely by a function similar to that used for the electric field fluctuations, Eq. 2, with a correlation time of the order of 1 minute and a field amplitude of approximately 10^{-5} gauss. Large pulses with amplitudes $\sim 5 \times 10^{-3}$ G are observed occasionally; the rise time of these larger pulses typically is a few minutes.

Fluctuating magnetic fields cause motions of the end masses on their suspensions as well as excitation of internal modes in the masses. The estimates made below are based on the approximation of no field penetration into the conductors or conducting coatings on dielectrics. In this limit the magnetic stresses (eddy current forces) are a maximum. We neglect the interaction of ferromagnetic impurities in the masses with the field fluctuations, this has been a problem in precision mechanical experiments but can be controlled by the proper choice of the mass material.

The compressional excitation of the mass due to magnetic stresses with frequency components below the lowest compressional resonance frequency of the mass is given by the displacement spectral density

$$x^2(f) = \frac{\langle B^2 \rangle^2 A^2}{32\pi^9 m^2 f_o^4 \tau_o f^2} \qquad (4)$$

where τ_o is the correlation time of the field fluctuations and f_o the resonance frequency of the lowest compressional mode.

For the sample parameters used previously and a lowest compressional mode frequency of 6KHz, the amplitude spectral density due the assumed magnetic field fluctuation spectrum becomes

$$x(f) \sim \frac{3\times10^{-24}}{f} \text{ cm/Hz}^{\frac{1}{2}} \quad f < f_o$$

A negligible effect.

Magnetically driven motions of the suspension require an estimate of the gradient of the magnetic pressures across the mass with frequency components higher than the suspension resonance frequency. The displacement spectral density for this case is given by

$$x^2(f) = \frac{\langle B^2 \rangle^2 A^2 t^2}{8\pi^7 m^2 c^2 \tau_o f^4}$$

t is the linear dimension of the mass along the optic axis. For the sample parameters

$$x(f) \sim \frac{3\times10^{-25}}{f^2} \text{ cm/Hz}^{\frac{1}{2}} \qquad f > f_{\text{suspension}}$$

which is again a negligible quantity.

Noise due to Cosmic Rays

The principal component of the high energy particle background at the surface of the Earth is muons with kinetic energies greater than 0.1 GeV. A muon that passes through or stops in one of the antenna masses imparts momentum, thereby causing a displacement of the mass.

The result of this section is that the muon noise is not a factor in determining the performance of a long baseline antenna.

At sea level the integral flux of muons incident on an antenna mass at a zenith angle θ is given approximately by

$$N_I(E,\theta) \sim \frac{3\times10^{-2}\cos^2\theta}{(E_o + (E-E_o)\cos\theta)^2} \quad \text{muons/cm}^2\text{sr sec} \qquad (1)$$

for energies larger than 0.1 Gev. Energies are expressed in Gev. E_o is the energy loss by muons in the zenith column of the atmosphere, approximately 3 Gev.

Muons lose energy in matter almost entirely through electromagnetic interactions so the energy loss per column density is only weakly dependent on energy for relativistic muons. For example, 1 GeV muons lose $\sim$5 MeV/gm/cm^2, while 10^4 GeV muons lose $\sim$30 MeV/gm/cm^2. In the following calculation we assume the energy loss is independent of the muon energy. For ease of estimation assume a spherical mass of diameter D. The average rate of x momentum imparted to the mass from one hemisphere is given by

$$\left\langle \frac{dP_x}{dt} \right\rangle = \frac{3\times10^{-3}}{4c} \left(\frac{\Delta E}{\sigma} \right) \pi D^3 \rho \int_{\theta=0}^{\pi/2} \int_{\phi=0}^{\pi} \sin\phi \sin^2\theta \cos^2\theta \, d\theta \, d\phi \qquad (2)$$

$\Delta E/\sigma$ is the energy loss per mass column density and ρ is the density

of the antenna mass.

The average rate of muon hits is then

$$\frac{dn}{dt} = \frac{3\times10^{-3}\pi^2 D^2}{4} \int_0^{\pi/2} \cos^2\theta \sin\phi \, d\phi \qquad (3)$$

The average x momentum per hit, Eq. 2/Eq. 3, is

$$P = \frac{\rho D}{4c} \left(\frac{\Delta E}{\sigma}\right) \qquad (4)$$

The average hit results in a displacement of the antenna mass mounted on the suspension of

$$\Delta x = \frac{1}{4} \frac{\rho D}{m\omega_o} \left(\frac{\Delta E}{\sigma}\right) \qquad (5)$$

Choosing the sample parameters D $\sim$50cm, a suspension period of 2 seconds, a mass of 10^6 gm with density ρ = 2.2 gm/cm^3 and an energy loss of the muons of 5 MeV/gram/cm^2, one arrives at a typical displacement $\Delta x \sim 1\times10^{-20}$cm. The average hit rate is 30 hits/sec. An event that could cause a displacement of 10^{-19} cm should occur about once a month. Neither of these displacements are of any consequence in a 5 km baseline antenna.

If the antenna output is measured over times that include many muon pulses, as it would be in a search for periodic sources or a stochastic background, the noise can be treated as a stationary distribution.

Under the assumptions that: the muon events are random, the frequency of hits is much greater than the resonant frequency of the suspension, and, for ease of calculation, that the magnitude of the momentum

impacts is the same for all muons, the spectral amplitude density of displacement of the antenna end masses is given by

$$x(f) = \frac{4\langle p\rangle \left\langle \frac{dn}{dt} \right\rangle^{\frac{1}{2}}}{m\omega^2} \quad \text{cm/Hz}^{\frac{1}{2}} \qquad (6)$$

$$= \frac{\left(\frac{\dot{\Delta E}}{\sigma}\right)\left(N_i(E)\right)^{\frac{1}{2}}}{\sqrt{32}\pi^2 c\ell f^2} \sim \frac{3\times 10^{-21}}{f^2}$$

Again, negligible in a 5 km baseline antenna.

Summary of Noise Sources

The following three figures show the total noise spectrum h(f), the sum of the spectra due to all of the noise sources discussed in the preceding section. Two of the figures display in detail the noise in an antenna of length 5 km. The third figure shows how the total noise spectrum depends on antenna length.

One should bear in mind that the sample parameters used in these graphs, derived from the prior calculations, have values we consider technically feasible in a first generation long baseline antenna system. In these projections of antenna performance none of the noise terms are set at limits which are fundamental in the sense that they cannot be reduced by improvements in the technology or by a new concept.

Figure 1 is a graph of the noise as a function of frequency in a 5 km antenna, under the assumption that the antenna is optimized at any given frequency by making the storage time $t_{stor}=1/f$. Thus, it shows the noise performance that can be achieved at each frequency with an antenna of the physical characteristics (length, end mass suspension, vacuum and laser power) specified on the graph. The uppermost curve, labelled "10", is the sum of the individual noise spectra labelled "1" through "9" which are identified in the key in the upper right hand corner of the figure.

Above f = 100 Hz, the dominant noise term is the Poisson noise

in the photodetection labelled "1". It is determined by the assumption of 100 watts of circulating optical power in the antenna. Between 20 Hz and 100 Hz, the strongest noise source is the Brownian motion of the end masses due to the finite Q of their suspensions (curve "4"). Near 100 Hz, the displacement of the mirrors due to the thermal excitation of the internal normal modes of the end masses ("5") is nearly as strong as these other two noise sources. Finally, below 20 Hz the noise is dominated by seismic noise which couples to the end masses through their suspensions (marked "7"). Noise terms which are negligible at all frequencies with the assumed parameters include index fluctuations in the residual gas in the vacuum system ("2" or "3"), forces due to varying electric fields in the end stations ("6"), the random gravitational force background ("8"), and the quantum mechanical measurement noise ("9").

Figure 2 is nearly the same as Figure 1, except that here it is assumed that the storage time is fixed at t_{stor} = 1 msec, independent of frequency. In other words, the graph shows the noise spectrum with a 5 km antenna with 60 bounces (30 spots on each mirror in a delay line or a Fabry-Perot finesse of 60) with the assumed parameters. The relative importance of the various noise sources is nearly the same as for the case represented in Figure 1. In this example the Poisson noise term dominates for all frequencies above 70 Hz. Also, in this case the internal thermal vibration noise of the end masses is never greater than one tenth as large as the dominant noise term at any frequency.

The total noise spectrum for antennas of four different lengths is shown in Figure 3. Here, as in Figure 1, we make the assumption that the antenna is optimized at any given frequency by setting $t_{stor} = 1/f$. On each curve is marked at several points the number of bounces (or finesse) required to satisfy this assumption.

At f = 3 kHz, all of the example antennas of 1/2 km or longer are limited by Poisson laser intensity noise. A 50 meter antenna has more noise because of the larger relative contribution of the white noise from internal vibrations of the end masses. At frequencies substantially below 100 Hz, all of the example antennas are dominated by stochastic forces, principally seismic noise. In this regime the sensitivity improves linearly with antenna length, and does not depend on the storage time. In the mid-frequency range of 100 Hz to 1 kHz, the length enters by determining the cross-over point between the stochastic force limit and the Poisson limit. Note that in order to achieve the limit shown on this graph in the mid-frequency band, a 5 km antenna would need to store the light for several hundred passes. As a general rule the optics becomes more complex and the quality demands on it more stringent as the number of bounces or the finesse increases. This fact must be weighed in comparing the performance in these examples.

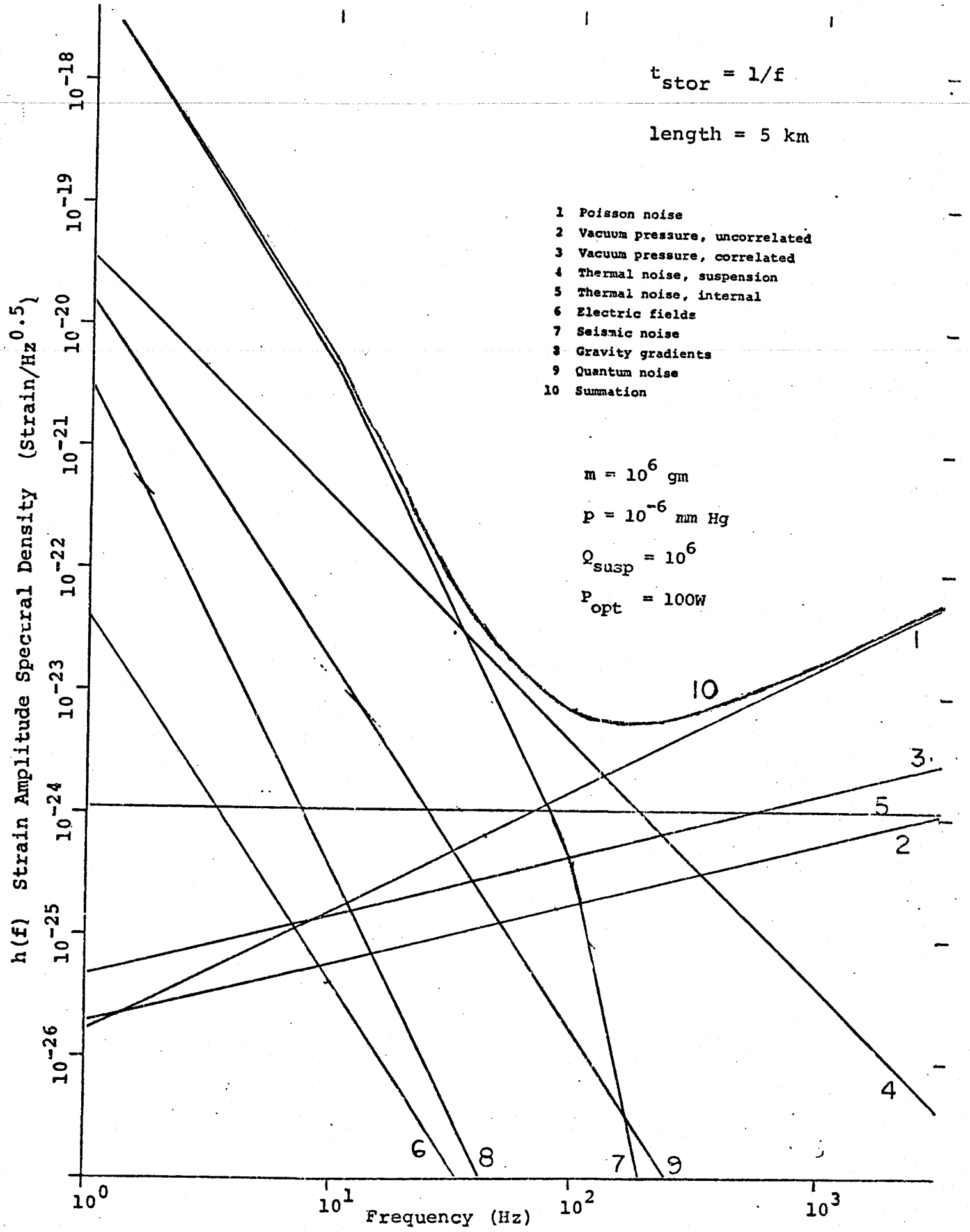
$t_{stor} = 1/f$
length = 5 km
1 Poisson noise
2 Vacuum pressure, uncorrelated
3 Vacuum pressure, correlated
4 Thermal noise, suspension
5 Thermal noise, internal
6 Electric fields
7 Seismic noise
8 Gravity gradients
9 Quantum noise
10 Summation
$m = 10^6$ gm
$p = 10^{-6}$ mm Hg
$Q_{susp} = 10^6$
$P_{opt} = 100W$
h(f) Strain Amplitude Spectral Density (Strain/Hz$^{0.5}$)
10^{-18}
10^{-19}
10^{-20}
10^{-21}
10^{-22}
10^{-23}
10^{-24}
10^{-25}
10^{-26}
10^0
10^1
10^2
10^3
Frequency (Hz)

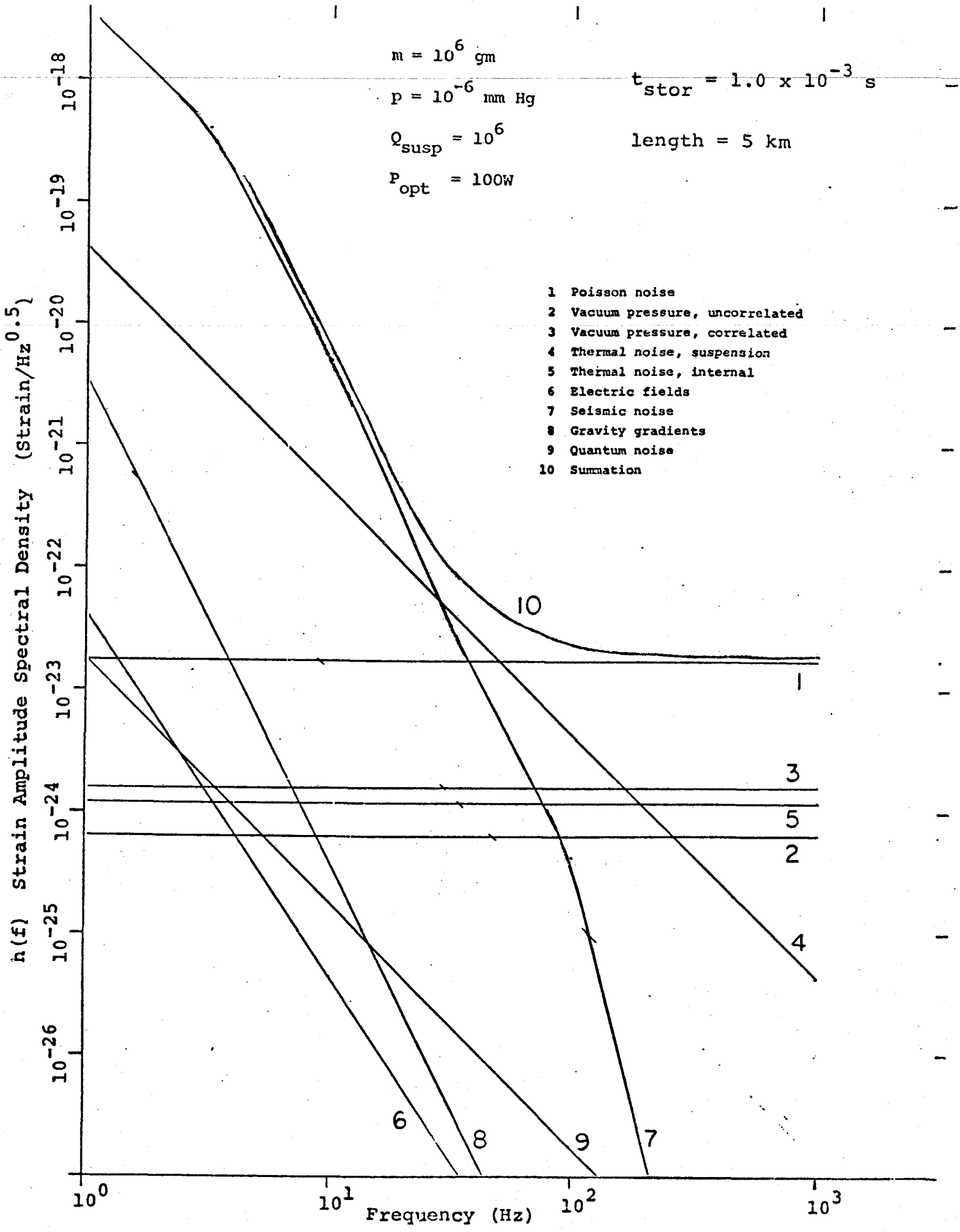
m = 10^6 gm
p = 10^-6 mm Hg
Q_susp = 10^6
P_opt = 100W
t_stor = 1.0 x 10^-3 s
length = 5 km
1 Poisson noise
2 Vacuum pressure, uncorrelated
3 Vacuum pressure, correlated
4 Thermal noise, suspension
5 Thermal noise, internal
6 Electric fields
7 Seismic noise
8 Gravity gradients
9 Quantum noise
10 Summation
h(f) Strain Amplitude Spectral Density (Strain/Hz^0.5)
Frequency (Hz)
10^-18
10^-19
10^-20
10^-21
10^-22
10^-23
10^-24
10^-25
10^-26
10^0
10^1
10^2
10^3

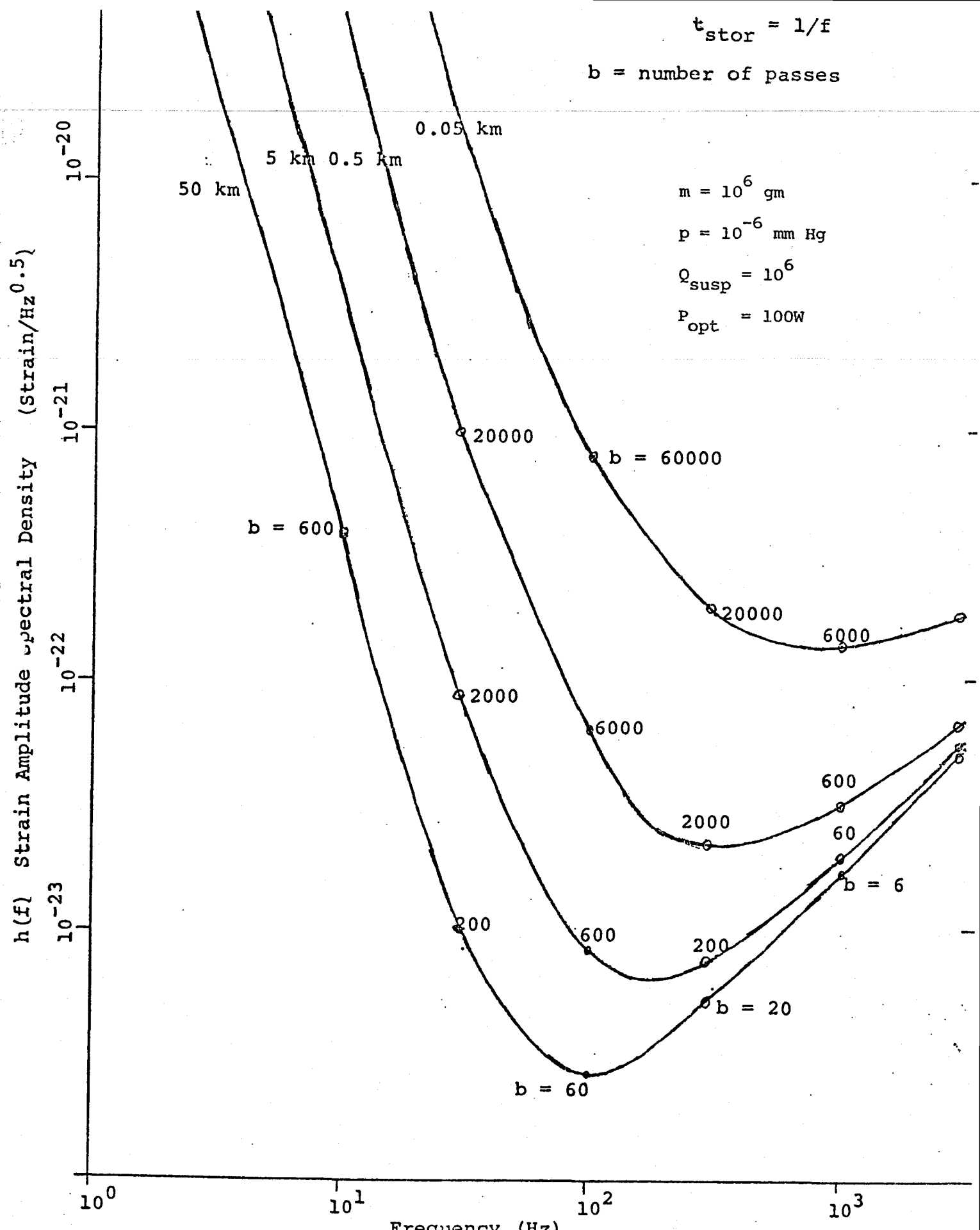
$t_{stor} = 1/f$
b = number of passes
0.05 km
0.5 km
5 km
50 km
$m = 10^6$ gm
$p = 10^{-6}$ mm Hg
$Q_{susp} = 10^6$
P_{opt} = 100W
b = 60000
20000
6000
2000
600
200
b = 60
b = 20
60
b = 6
10^{-20}
10^{-21}
10^{-22}
10^{-23}
h(f) Strain Amplitude Spectral Density (Strain/$Hz^{0.5}$)
10^0
10^1
10^2
10^3
Frequency (Hz)

TECHNICAL REPORT

VOLUME I

COST ESTIMATES FOR

A GRAVITY WAVE ANTENNA

C-87632

Prepared by

Arthur D. Little, Inc.
Acorn Park
Cambridge, Massachusetts

Prepared for

Prof. R. Weiss
Department of Physics
Massachusetts Institute of Technology
Cambridge, Massachusetts

September 1983

TABLE OF CONTENTS

Title	Page
ABSTRACT	1
1.0 INTRODUCTION	2
2.0 TECHNICAL BACKGROUND	5
3.0 PROJECT FORMULATION	6
4.0 EVACUATED ENCLOSURE	
4.1 TUBING SYSTEM	9
4.1.1 Structural Design	9
4.1.2 Initial Concept	12
4.1.3 Final Concept	15
4.2 VACUUM PUMPING SYSTEM	26
4.2.1 High Vacuum System	26
4.2.2 Rough Vacuum System	35
4.3 OTHER COMPONENTS	38
4.3.1 Expansion Tube Sections	40
4.3.2 Isolation Valves	42
4.3.3 Fine Alignment Provisions	46
4.4 COMPILATION OF EVACUATED ENCLOSURE COSTS	50
5.0 END STATIONS	55
5.1 DESIGN GUIDELINES	55
5.2 DESIGN CONCEPTS	57
5.2.1 Thermal Considerations	57
5.2.2 Alternative Concept	60

Title	Page
5.3 ENCLOSURE COSTS	60
5.4 VACUUM SYSTEM	63
5.4.1 Rough Pumping System Costs	64
5.4.2 High Vacuum Pumping System Costs	65
5.4.3 Summary of Vacuum Pump Costs	69
6.0 SUMMATION OF GWA COSTS	70

LIST OF FIGURES

		Page
Figure 1	Plans of Prototype GWA Arrays	3
Figure 2	Size and Weight of Vacuum Tube Enclosure	11
Figure 3	Initial Estimate of Cost of Fabricated Tube Sections of 40 Ft. Length Delivered at Site Ready for Installation	14
Figure 4	Procedure for Basis of Final Cost Estimates	18
Figure 5	Final Estimate of Cost to Fabricate Aluminum Tube	19
Figure 6	Final Estimated Costs to Fabricate Aluminum Tube	21
Figure 7A	Final Estimated Costs to Ship, Clean and Install Aluminum Tube for Minimum GWA	22
Figure 7B	Final Estimated Costs to Ship, Clean & Install Aluminum Tube for Upgraded GWA	23
Figure 7C	Final Estimated Costs to Ship, Clean and Install Aluminum Tube for Extended GWA	24
Figure 8	Comparative Estimated Total Cost for Fabricated, Cleaned and Installed Aluminum Tube	25
Figure 9	Number of High Vacuum Pumps Required Per Unit Length Vs. Pumping Speed	30
Figure 10	Installed Ion Pump Cost Vs. Ion Pump Speed	32
Figure 11	Total Estimated Cost of Installed Ion Pumping System Per Unit Length	33
Figure 12	Estimated Total Cost for Installed Minimum Cost Ion Pumping System Per Unit Length	34
Figure 13	Performance Requirements for Rough Vacuum Pumps	36
Figure 14	Installed Roughing Pump Cost Vs. Roughing Pump Speed	37
Figure 15	Estimated Cost of Installed Roughing Pump Vacuum System Per Unit Length	39
Figure 16	Estimated Costs of Bellows Expansion Sections	43
Figure 17	Estimated Costs of Isolation Valves	45

		Page
Figure 18A	Estimated Costs of System Elements for Minimum GWA	51
Figure 18B	Estimated Costs of System Elements for Upgraded GWA	52
Figure 18C	Estimated Costs of System Elements for Extended GWA	53
Figure 19	Total Estimated Cost of Fabricated and Installed Vacuum Enclosure System of Aluminum Tubing Including Vacuum Pumping Units, Gate Valves and Fine Alignment System	54
Figure 20	End Station Pressure Vessel Concept, Approach - 1	58
Figure 21	End Station Pressure Vessel Concept, Approach - 2	59
Figure 22	Estimated Costs to Fabricate, Ship, and Install End-Stations Enclosures	62
Figure 23A	Summary of Differential Costs for Vacion Pumps to Meet End-station Needs on Minimum GWA	67
Figure 23B	Summary of Differential Costs for Vacion Pumps to Meet End-station Needs on Upgraded and Extended GWA Options	68
Figure 24A	Total Estimated Cost of One Minimum GWA in Mid-1982 Dollars	71
Figure 24B	Total Estimated Cost of One Upgraded GWA in Mid-1982 Dollars	72
Figure 24C	Total Estimated Cost of One Extended GWA in Mid-1982 Dollars	73

LIST OF TABLES

		Page
Table 1	Tubing Requirements	10
Table 2	Recommended Procedure for Cleaning of Aluminum for Use in High Vacuum Systems	28
Table 3	Estimated Total Cost of Installed High Vacuum Pumping System	31
Table 4	Estimated Total Cost of Installed Rough Vacuum Pumping System	38
Table 5	Estimated Total Cost of Installed Bellows Expansion Sections	42
Table 6	Estimated Total Cost of Isolation Valves	46
Table 7	Estimated Total Cost for Installed Fine Alignment System	49
Table 8	Overall Design Guidelines for GWA End-stations	56
Table 9	Differential Vacion Pump Requirements for "Non-Optimum" and "Optimum" Location of Pumps	66

TECHNICAL REPORT

Volume I

September 1983

COST ESTIMATES FOR A GRAVITY WAVE ANTENNA

C-87632

ABSTRACT

Volume I presents cost estimates for the fabrication and installation of the evacuated enclosures that form the linear elements of typical gravity wave antennas, the end stations required for those antennas, and the vacuum pumping equipment required to achieve the specified level of vacuum within the enclosures and end stations. The cost estimates are for a single antenna and are presented graphically in parametric form. The single antenna is a component of a gravitational wave antenna system which, at a minimum, will consist of two antennas at continental separation. The cost savings resulting from common engineering and facilities have not been explicitly estimated. The primary parameter in these cost estimates is the diameter of the evacuated tubing which forms the evacuated enclosures. In addition, a breakdown of fixed costs (i.e., independent of length) and length-dependent costs are presented.

The cost estimating method is described. References, data and work sheets supporting the cost estimating process are incorporated as appendices in Volume II of this report.

1.0. INTRODUCTION

Prof. R. Weiss and his associates of the Massachusetts Institute of Technology (MIT) Dept. of Physics plan to design and construct a large gravity wave antenna (GWA) as one component of a large GWA system consisting, at a minimum, of two such antennas at continental separation. As envisioned, the GWA would consist of laser interferometers operating between masses suspended at the GWA corners and separated by baseline lengths on the order of 5 to 10 km. An initial concept consisted of a 10 km square GWA with all four sides and both diagonals active. This large GWA was subsequently judged to be too ambitious and abandoned in favor of the less extensive antennas shown in Figure 1. Figure 1 shows plan views of three GWA's: a Minimum GWA, an Upgraded GWA, and an Extended GWA.

The National Science Foundation (NSF) funded the initial phase of the proposed work -- to establish preliminary cost estimates for the construction of a GWA. To give credibility to the cost trade-offs and estimates that would be generated in this initial effort, Prof. Weiss solicited input from commercial organizations experienced in the several areas of technology that would be involved in the design and construction of the GWA. He selected Arthur D. Little, Inc. (ADL) to investigate three specific areas: 1) the evacuated enclosures that form the sides and diagonals of the GWA and which contain the interferometer optical beams, 2) the end stations which house the sensitive masses acting as terminals of the interferometer, and 3) several of the basic optical components required for the interferometers -- beam reflecting mirrors, high power lasers and electro-optic beam modulators.

In addition, he selected Stone and Webster Engineering Corp. (S&W), to support and augment the evacuated enclosure system design and cost estimation of ADL, particularly with respect to field construction considerations and costing, and to generate their own cost estimates for the associated structural support and environmental protection portions of the enclosure system and the end stations. They have also

PLANS OF GRAVITY WAVE ANTENNAS

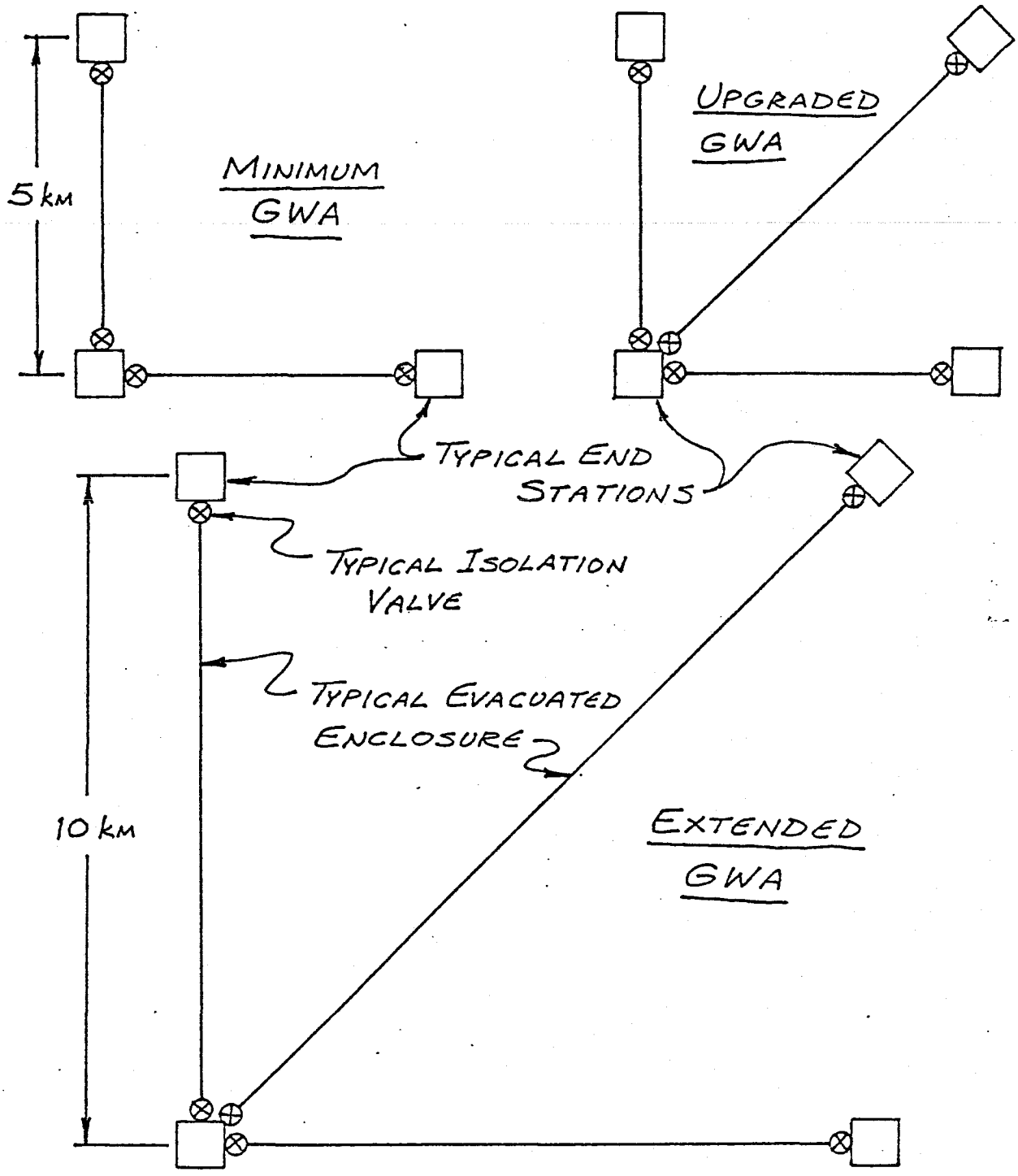

FIGURE 1

conducted a study to identify potential GWA sites. This approach was planned to produce realistic cost estimates, while freeing the MIT group to pursue the more critical scientific and technological concerns of the basic GWA concept.

This report presents the results of ADL's estimation of the cost of fabrication, installation and vacuum pumping equipment for the evacuated enclosures and the end stations of a single GWA. The cost savings resulting from common engineering and reuse of capital facilities for additional GWA's have not been explicitly estimated.

Section 4.0 of this report presents the cost estimates for the evacuated enclosures and their vacuum pumping equipment. Section 5.0 presents the same for the end stations. Section 6.0 combines the results of both for each of the GWA configurations considered. Our work on the basic optical components has been reported orally to Prof. Weiss et al. separately.

2.0. TECHNICAL BACKGROUND

To establish a suitable foundation for our cost estimates, we considered three configurations for the GWA based on the overall system requirements and expected performance. Prof. Weiss and his MIT GWA group established the probable layout of three progressive GWA's: the Minimum GWA, the Upgraded GWA and the Extended GWA. Each of these GWA's employ laser interferometers to dynamically measure the linear separation between suspended masses at each corner of the GWA. This scheme, measurement of the relative movement in the direction of each of the legs and also along a diagonal, will provide the appropriate information for successful operation of the GWA.

Because of scattering and "seeing" effects, the interferometers, and hence their beams, need to operate in a relatively high vacuum. Accordingly, evacuated end stations will have to be provided at each corner and evacuated enclosures along the sides and the diagonal of the GWA. Additionally, because line-of-sight is required in all directions between all corners, the entire GWA must lie within a single plane. In order to obtain the desired operational sensitivity, Prof. Weiss has predicated a GWA between 5 km and 10 km on a side. A GWA in this size range would require a substantial length of evacuated tubing to enclose the optical paths. Moreover, this tubing would require alignment, structural support and environmental protection over its entire length and would have to include appropriate vacuum pumping provisions.

The end stations necessary for any GWA of this general configuration would each require a large evacuated vessel with attendant structural support and vacuum pumping provisions.

3.0. PROJECT FORMULATION

Soon after starting work, ADL project personnel were briefed by the MIT GWA group on the overall concept of the proposed GWA. Subsequent discussions resulted in further definition of the system and assisted in the identification and clarification of system parameters to be used as guidelines in generating the output cost estimates. The guidelines established and mutually agreed to are as follows:

A. The diameter of the tubing forming the evacuated enclosure should remain unspecified between 12 and 48 inches until implications of the interferometer operation or some other factor determines the proper diameter.

B. The GWA's will be 5 km to 10 km on a side. At this size, fixed costs are to be examined to determine if they are small enough that the cost-per-unit-length can be used for interpolation within the size range in scaling costs to other sizes.

C. The maximum operational pressure within the evacuated enclosure system will be in the 10^{-6} to 10^{-7} Torr range, while the end stations may require a better vacuum; to as low as 10^{-8} Torr.

D. The detailed configuration, material used, method and location of fabrication and means of installation of the evacuated enclosure tubing and the end station vacuum vessels are unrestricted until clear-cut technical, fabrication or cost implications dictate otherwise.

E. The preferred means of pumping the high vacuum within the evacuated enclosure tubing system and the end stations is by ion-type pumps because they eliminate all sources of mechanical vibration, minimize operating and maintenance problems and

costs and readily provide remote sensing of vacuum system performance.

F. Cost estimates are to be generated separately for the evacuated enclosure tubing (including associated vacuum pumping equipment) forming the legs and diagonal of the GWA and for the end station vacuum enclosures (including their additional vacuum pumping equipment) required at the corners to house the suspended masses.

Using the above guidelines, we subdivided the ADL project into four individual tasks:

First: investigate the design, configuration, fabrication, installation and all other pertinent factors relative to and affecting the cost of the tubing for the evacuated enclosure system.

Second: investigate the vacuum requirements on the evacuated enclosure system and the pumping and associated equipment required to produce and maintain that vacuum level.

Third: consider the system operational requirements relative to the evacuated enclosure system and associated vacuum pumping equipment including structural support, environmental compatibility, initial and operational alignment, installation and maintenance access for the enclosure system, electrical power requirements, etc.

Fourth: investigate the design, configuration, fabrication, installation and all other pertinent factors relative to and affecting the cost of the evacuated end stations.

The first three tasks above are interdependent; the findings and considerations relative to one task area influence those of another.

Consequently, these three task efforts were performed in parallel. The fourth task was undertaken separately and at a later time than the first three. Each task was led by an individual project team member and close intertask communications were established and maintained. Each of the major task efforts is discussed in the following sections.

4.0. EVACUATED ENCLOSURE

4.1 TUBING SYSTEM

The evacuated enclosure forming the legs and diagonals of the GWA, like any vacuum enclosure, will be most economically constructed of round tubing or pipe because of the required internal vacuum. Because of the diameter (12 to 48 inches) and the extensive length of tubing required for the three GWA's shown in Figure 1, a massive amount of material will be required, even for a very thin tube wall, and the attendant material cost will be large. Consequently, the design of the evacuated enclosure tubing requires an optimization for minimum material usage.

4.1.1 Structural Design

The optimum material for the tubing was not readily apparent. However, practical considerations quickly reduced the material options to three: stainless steel, mild or ordinary carbon steel and aluminum. Stainless steel, although relative expensive, is strong, stiff and traditionally used in high vacuum systems because of its low outgassing (easily cleaned and good corrosion resistance) qualities and good weldability. Mild steel, although strong, stiff, weldable and relatively inexpensive, is seldom used in high vacuum systems because of its poor outgassing characteristics (susceptibility to corrosion and difficult cleaning). Aluminum, while not so strong or stiff, is light weight, has good weldability and corrosion resistance under controlled conditions, is moderately expensive on a per weight basis and is becoming more common in high vacuum systems as better cleaning techniques are developed.

Because of the different densities and structural properties of the three candidate materials, different optimization solutions for minimum material designs of the evacuated enclosure were anticipated. Conventional vacuum vessel design practice applies the requirements of

the ASME (American Society of Mechanical Engineers) Boiler and Pressure Vessel Code; Section VIII, Pressure Vessels; Division 1. The requirements of this code were employed in establishing suitable tubing designs. The basic design criterion is tube buckling under external pressure (internal vacuum) and a factor of safety of three was used. Under this criterion, stiffness, not strength, is the important material property and the option for increasing the equivalent wall stiffness of the tube by use of external stiffening rings was included. Required stiffening ring proportions were also defined using the ASME code. With this method, safe designs were derived for all three materials for straight tubing without stiffening rings and for tubing with stiffening rings at various spacings.

Subsequently, a number of design solutions were obtained that met the code stiffness requirements for the three materials (stainless steel and mild steel solutions were essentially identical) at four discrete diameters (12, 24, 36 and 48 inches). These solutions incorporated different spacing of stiffening rings. Each solution yielded a minimum wall thickness from which the volume and mass of required material were calculated per km length. When plotted (Figure 2), these data graphically display the relationships between the dependent variables (wall thickness, volume and mass of material per km) as functions of the independent parameters (type of material, tube diameter and spacing of stiffening rings). This plot is based on a 40-foot module, the longest tube section readily transportable by conventional over-the-highway trucks. The total number of 40-foot tube sections required for the three GWA's are tabulated below:

Table 1.
TUBING REQUIREMENTS

GWA Plan	Total Tube Length	Number of 40-ft. Sections
Minimum GWA	10.0 km/32,810 ft.	820
Upgraded GWA	17.07/56,007	1400
Extended GWA	34.14/112,013	2800

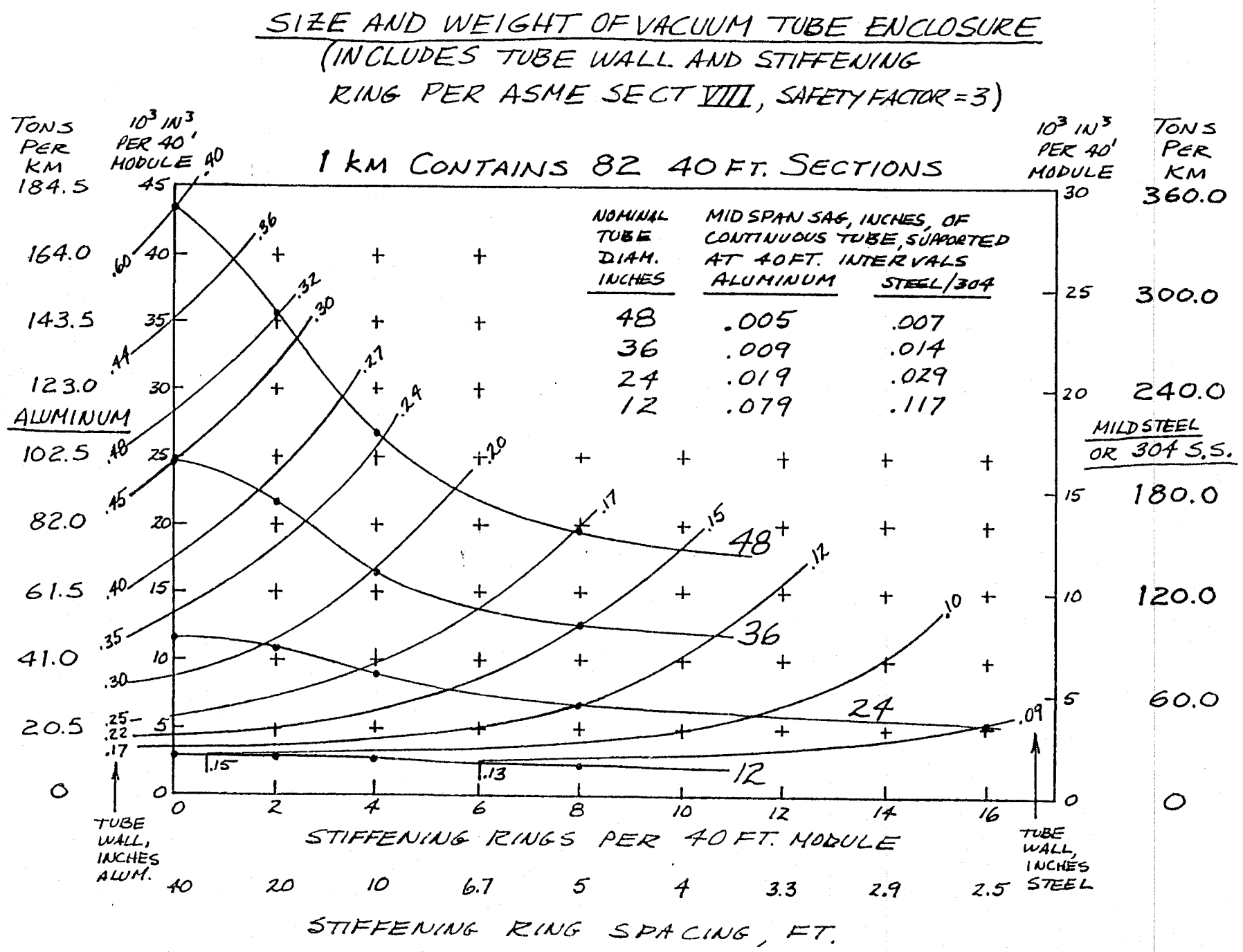
SIZE AND WEIGHT OF VACUUM TUBE ENCLOSURE
(INCLUDES TUBE WALL AND STIFFENING RING PER ASME SECT VIII, SAFETY FACTOR = 3)
1 KM CONTAINS 82 40 FT. SECTIONS
TONS PER KM
10³ IN³ PER 40' MODULE
ALUMINUM
MILD STEEL OR 304 S.S.
NOMINAL TUBE DIAM. INCHES
MID SPAN SAG, INCHES, OF CONTINUOUS TUBE, SUPPORTED AT 40 FT. INTERVALS
ALUMINUM
STEEL/304
48 .005 .007
36 .009 .014
24 .019 .029
12 .079 .117
184.5
164.0
143.5
123.0
102.5
82.0
61.5
41.0
20.5
0
360.0
300.0
240.0
180.0
120.0
60.0
0
45
40
35
30
25
20
15
10
5
0
STIFFENING RINGS PER 40 FT. MODULE
0 2 4 6 8 10 12 14 16
40 20 10 6.7 5 4 3.3 2.9 2.5
STIFFENING RING SPACING, FT.
TUBE WALL, INCHES ALUM.
TUBE WALL, INCHES STEEL
48
36
24
12

FIGURE 2

4.1.2 Initial Concept

An initial procedure for manufacture of this tubing was developed and used for the first cost estimates of the tubing of the evacuated enclosure system. The manufacturing sequence starts with procurement from the producer's rolling mill of sheet stock of the appropriate thickness and width in lengths of 40 feet. The sheet stock is next rolled to the appropriate diameter and the longitudinal joint automatically seam welded. For large diameter tubes where maximum rolled widths cannot accommodate the attendant circumference, tube sections are joined end-to-end by automatic seam welding to produce 40-foot lengths. Flanges are then rolled onto each end of the tube and the appropriate number and size of stiffening rings are welded on at appropriate spacing along the tube. At this point, the tube is leak checked, repaired if required, and the interior thoroughly cleaned to high vacuum quality. A seal cap is then placed on one end and the other end installed into a specially designed vacuum pumpout facility where it is evacuated while being baked out by externally applied heat. After satisfactory vacuum pressure level is achieved within the tube in the special pump-out facility, a seal cap is automatically applied to the open end and the tube is back filled to a slight overpressure with inert gas.

The on-site installation concept for this procedure was based on receiving the tube sections vacuum clean and sealed and then installing them clean with no further on-site cleaning.

Five separate categories of costs were identified and estimated:

1) tube raw material costs;

2) fixed and variable costs associated with tube fabrication;

3) fixed and variable costs for fabrication and attachment of stiffening rings;

4) miscellaneous costs for inspection, leak testing, cleaning, vacuum bake-out, sealing, etc; and

5) transportation to the site over a nominal 1500-mile distance via 40-foot over-the-highway tractor-trailer rigs.

The costs in these several categories were estimated by personnel experienced in appropriate fabrication techniques and operations involved and were spot checked against known values where possible. As an example, a study conducted by Dow Chemical Co. in 1977 (and updated in 1981) covering installed costs of small diameter corrosion-resistant piping systems contained several good check points for costs of carbon steel and stainless steel pipe. Likewise, the costs incurred at the Stanford Linear Accelerator Center (SLAC) in 1964 for a sizeable quantity of 24-inch-diameter aluminum tubing were found to agree with ADL generated costs when extrapolated to mid-1982 dollars by the appropriate inflation factor. Raw material costs were established, for 20-ton lots, to be $1.60 per pound for aluminum, $1.00 per pound for stainless steel and $0.25 per pound for mild steel in the mid-1982 time frame.

These initial cost estimates were based on the production of the 5600 sections that would have been needed for the initial full 10-km square GWA (since abandoned) and are judged to be accurate to within about ±30%. They are shown graphically in Figure 3. These plots show estimated costs per 40-foot section versus the number of stiffening rings in that 40 foot section for the three materials of interest and the four sizes in the 12- to 48-inch-diameter range.

These data reveal several interesting comparative relationships. In each size, the stainless steel tubing is substantially more costly than aluminum which in turn is more costly than mild steel. Also, there are significant cost savings in using a large number of stiffening rings, especially for the large-diameter tubing. These savings are less for the smaller tubes and slightly reversed for 12-inch-diameter tube. (This reversal effect may be lost in the inaccuracy of these estimates.) Based on the lengths required per Table 1 and these costs, the range of total cost of tubing for any of the GWA's shown in

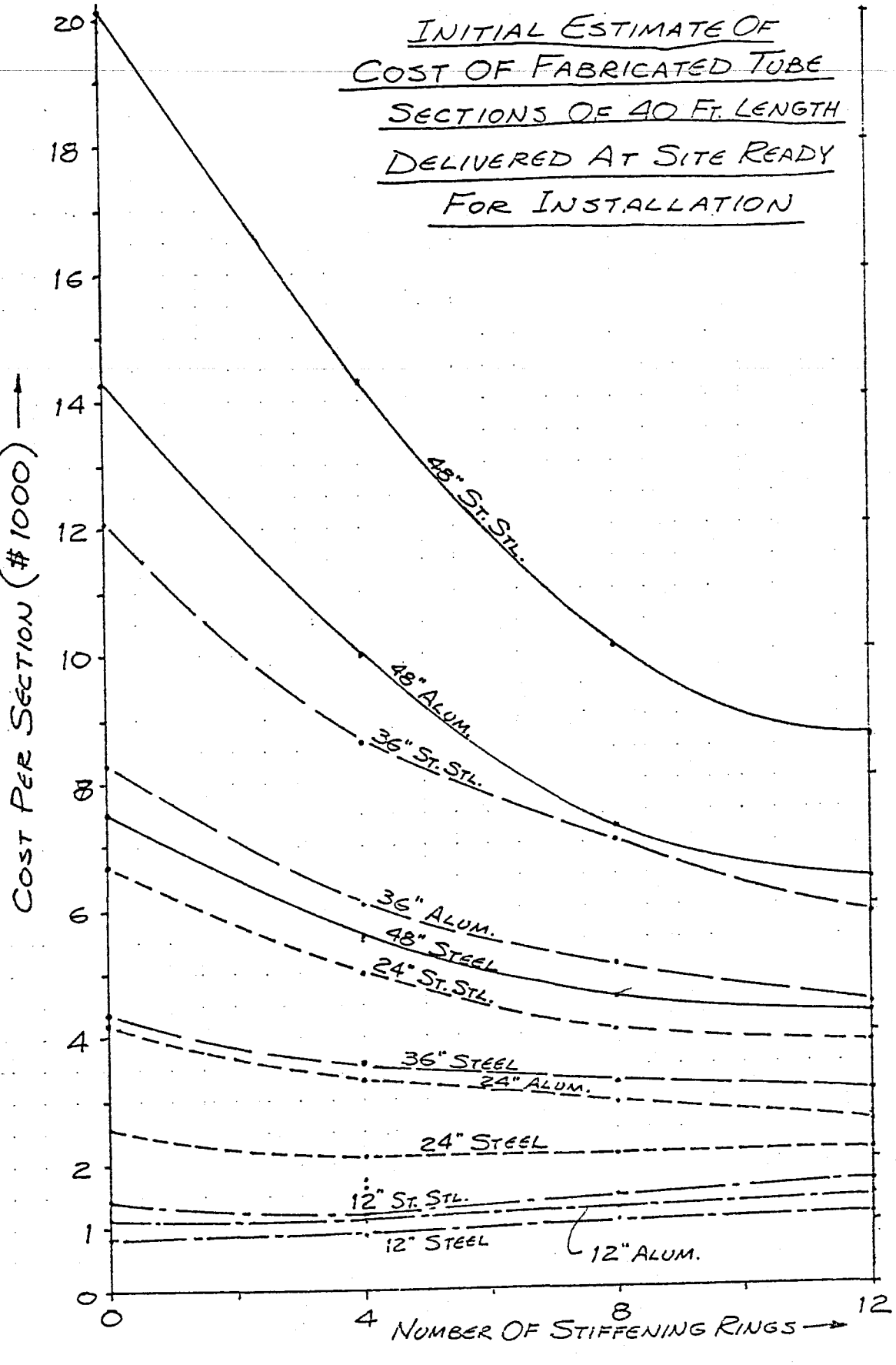
INITIAL ESTIMATE OF COST OF FABRICATED TUBE SECTIONS OF 40 FT. LENGTH DELIVERED AT SITE READY FOR INSTALLATION
COST PER SECTION (#1000)
NUMBER OF STIFFENING RINGS
0
1
2
4
6
8
10
12
14
16
18
20
0
4
8
12
48" ST. STL.
48" ALUM.
36" ST. STL.
36" ALUM.
48" STEEL
24" ST. STL.
36" STEEL
24" ALUM.
24" STEEL
12" ST. STL.
12" STEEL
12" ALUM.

FIGURE 3

Figure 1 substantiates the early concern that the vacuum enclosure costs would likely be a significant element in the total GWA facility cost, especially if the larger diameter tubing is necessary.

4.1.3 Final Concept

At this time in the project, work on the vacuum study task produced good evidence that outgassing problems would be substantial at the required vacuum level if mild steel tubing were to be used for the evacuated enclosure. Evaluating these potential problems against the estimated cost savings, as shown in Figure 3, the MIT GWA group, with concurrence by the ADL project team, decided to delete mild steel from further consideration.

The vacuum study effort also uncovered substantial evidence that aluminum was being used more frequently in high vacuum systems, especially for large systems where the cost savings of aluminum over stainless steel, as projected in Figure 3, would be substantial. This is made possible by the development of automatic welding techniques and equipment which routinely produce leak-tight welded joints and by the introduction of advanced surface-cleaning methods which reduce subsequent outgassing to acceptably low rates. Both factors are reported in recent high vacuum technology literature and were substantiated in fact during discussions with and a visit to the SLAC. Based on this evidence and encouraged by the projected cost savings over the use of stainless steel, the MIT GWA group, with concurrence by the ADL project team, selected aluminum as the material of choice for the GWA and, as such, the basis for subsequent cost estimates.

Reducing the material options to only one greatly facilitated the cost estimating effort and subsequent work was directed toward considerations pertinent to the fabrication of aluminum tubing only. The initial manufacturing procedure was rethought in terms of the newly defined cleaning procedures for aluminum for use in high vacuum systems, the use of automatic welding methods and the technical and

economic advantages of establishing facilities necessary to undertake selected operations at the GWA site. As a result, the initial manufacturing procedure was modified. This modified procedure was used as the basis for developing the final cost estimate for aluminum tubing.

The modified manufacturing procedure includes procurement of aluminum sheet of the appropriate thickness, width and length, rolling to a tube and automatic welding of the longitudinal and transverse seams as before. The appropriate stiffening rings are then welded onto the tube at the proper locations and the tube is inspected, leak-checked and repaired, if required. After the open ends are blocked and protected, the finished tubes are transported from the tube fabrication facility to the GWA site as before and stored at the site.

A cleaning facility would be constructed at the site and, just prior to movement near and placement in its final location, each tube would be thoroughly cleaned according to rigid procedural specifications and the open ends sealed with reusable seal caps. Each tube section would be then placed adjacent to the string of tubing already installed, attached to an automatic joint welding unit, aligned and the two ends to be joined stripped of their seal caps. The joint welding unit would have been programmed to automatically mill the two ends clean, square and to the proper profile, move the new tube into contact and proper alignment with the existing tube and perform a complete gas-backed full-penetration seam weld traverse around the joint. The automatic joint welding unit is a standard commercial product available from and developed by several organizations for joining of piping and tubing for field installation of large diameter, long, continuous piping systems. This new procedure changes the original cost structure by eliminating several steps done earlier at the tube fabrication facility and by modifying the site installation procedure significantly. Additionally, an opportunity was afforded to improve the accuracy of the costing process and to base the fixed cost apportionment on the more realistic lengths of tubing required for the three GWA plans per Table 1.

It should be noted that the cleaning facility, the automated welding machinery and the tube tooling, handling and transporting equipment required for the first GWA can be moved to and used at the sites of a second and succeeding GWA's. It is expected that moving and reestablishment cost will be low relative to the total value and that this will result in significant cost savings (i.e., the majority of the fixed costs) for any additional GWA beyond the initial GWA.

A recosting was performed for evacuated enclosures of aluminum tubing utilizing much of the original cost data and methods but employing a revised procedure for fabrication and installation as itemized in Figure 4. The results of the fabrication portion of this recosting are presented graphically in Figure 5. The format used is similar to that used in Figure 3 except that cost curves for the other materials have been deleted and curves for associated raw material costs have been included. We judge these cost estimates to be about ±20% accurate.

The fixed costs estimated for the special equipment, tooling, jigs, etc. required in the fabrication of the aluminum tube are relatively small. They range from $125,000 for 12-inch diameter tube to $275,000 for 48-inch diameter tube (see pages A-28 through A-31 in Appendix A). When apportioned over the reduced number of 40-foot sections required for the Minimum GWA, 820, the per section fixed costs vary from $152 for 12-inch diameter to $335 for 48-inch diameter. These per section costs are 16.2% and 5.4% of the minimum fabrication cost per section for the respective diameters. If apportioned over the 2800 sections needed for the extended GWA, the corresponding per section fixed costs are reduced to $45 and $98 which are 4.8% and 1.6% of the respective minimum fabrication costs. Based on the overall cost estimates having an accuracy of about ±20%, the variations of fixed cost percentages between 16.2% and 4.8%, and between 5.4% and 1.6% fall within this inaccuracy band. We judge that these fixed costs related to tube fabrication are thus small enough that they can be lumped together with the variable costs so that the resulting costs-per-unit-length are valid for any length of tubing required. Accordingly, for purposes

PROCEDURE FOR BASIS OF FINAL COST ESTIMATES

I - FABRICATION OF ALUMINUM TUBING:

1. Procure rolled plate of required thickness & size
2. Inspect for basic flaws; repair or reject
3. Form to tubing of required diameter & length
4. Weld seam(s)
5. Procure stiffening ring sections
6. Form stiffening rings
7. Install and weld stiffening rings onto tubes
8. Final inspect and leak check
9. Protect open ends for shipping & handling

II - INSTALLATION OF ALUMINUM TUBING:

1. Ship from fabrication facility to site
2. Offload and store at cleaning facility
3. Process through cleaning facility
4. Seal ends against contamination
5. Transport to general installation site
6. Offload and store at appropriate locations
7. Transport to specific installation point
8. Offload and place in position
9. Prepare ends in place with attachable mill
10. Move tube to final position & alignment
11. Weld to existing tube with attachable auto-welder
12. Inspect and leak check joint

FIGURE 4

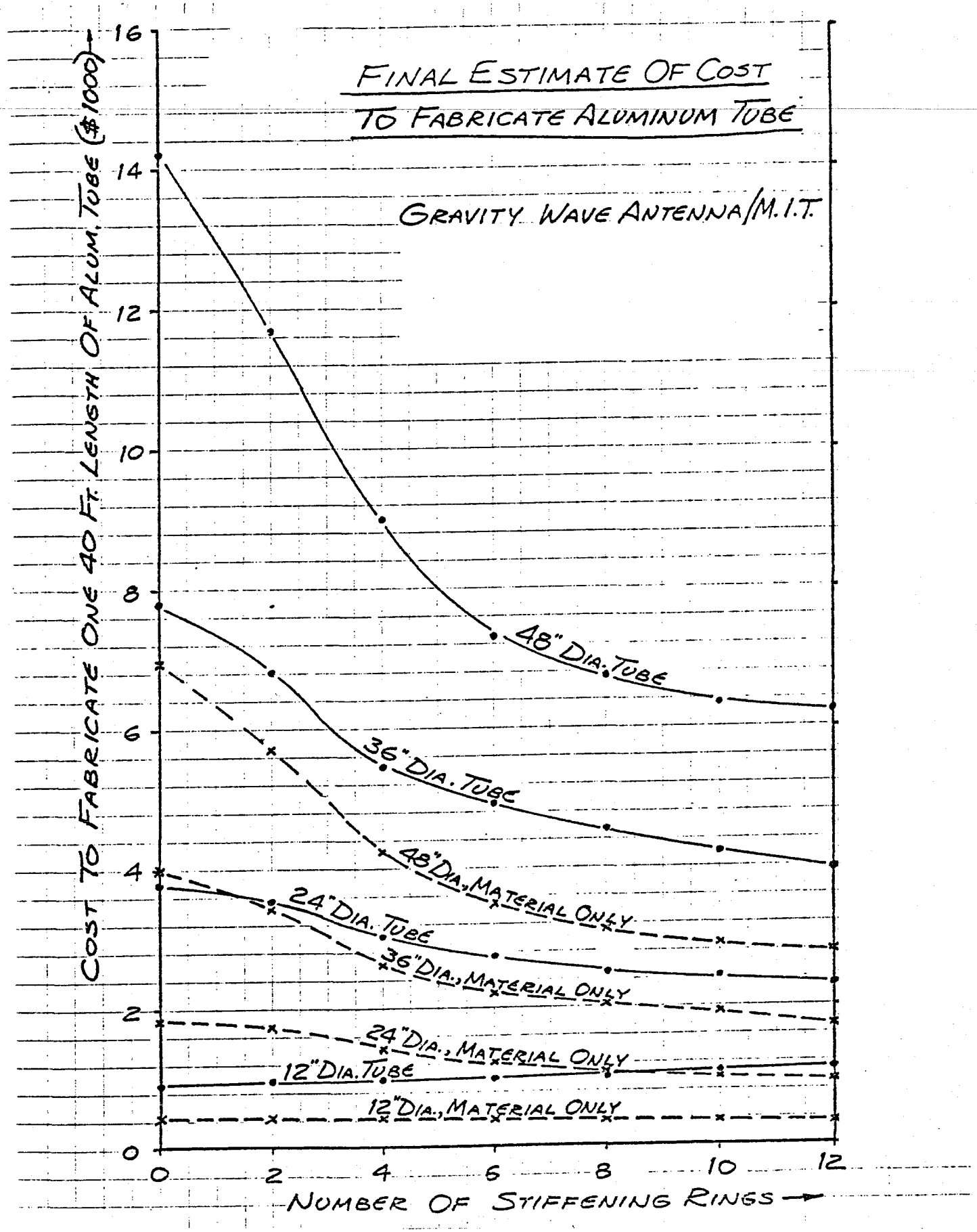
FINAL ESTIMATE OF COST
TO FABRICATE ALUMINUM TUBE
GRAVITY WAVE ANTENNA/M.I.T.
COST TO FABRICATE ONE 40 FT. LENGTH OF ALUM. TUBE ($1000)
NUMBER OF STIFFENING RINGS
48" DIA. TUBE
36" DIA. TUBE
48" DIA., MATERIAL ONLY
24" DIA. TUBE
36" DIA., MATERIAL ONLY
24" DIA., MATERIAL ONLY
12" DIA. TUBE
12" DIA., MATERIAL ONLY
0
2
4
6
8
10
12
14
16

FIGURE 5

of this preliminary cost estimate, we show only single values for fabrication cost per section of tubing, independent of which size GWA is under consideration.

By selecting the appropriate number of stiffening rings to minimize the fabrication cost for each tube diameter, the costs shown in Figure 5 are replotted in Figure 6 as minimum cost versus tube diameter. Figure 6 permits easy interpolation for any selected tube diameter within the guideline size range and clearly shows that the raw material costs constitute a significant fraction (approximately half) of the total fabrication costs.

The remainder of the total tubing cost, the shipping, cleaning and installation portion, is shown graphically in Figures 7A, 7B and 7C using the same format as in Figure 6. Three separate plots are used, one for each of the three GWA's shown in Figure 1. The fixed costs related to cleaning and installation are substantial and, when apportioned over the different vacuum enclosure lengths of the three GWA plans, affect the total cost per section. This applies only to the initial GWA, however, because a substantial portion of these fixed costs can be saved on subsequent GWA's as discussed earlier. Figures 7A, 7B and 7C display the several identifiable individual cost elements which make up the total installation cost as an aid to understanding the overall cost estimate. As can be seen, the fixed costs for on-site facilities and capital equipment -- mainly cleaning facilities, automatic welding equipment, leak detecting units, tube handling and maneuvering equipment, etc. -- although relatively small compared to the overall costs, are still large enough to influence the total installed costs beyond the inaccuracy band for the estimates.

The cost information contained in Figure 6 and in Figures 7A, 7B and 7C is combined in Figure 8 to show the comparative estimated total cost for the evacuated enclosures on a per unit length basis. These estimated total costs for the three GWA's include fabrication of the aluminum tube and its installation properly prepared and cleaned for

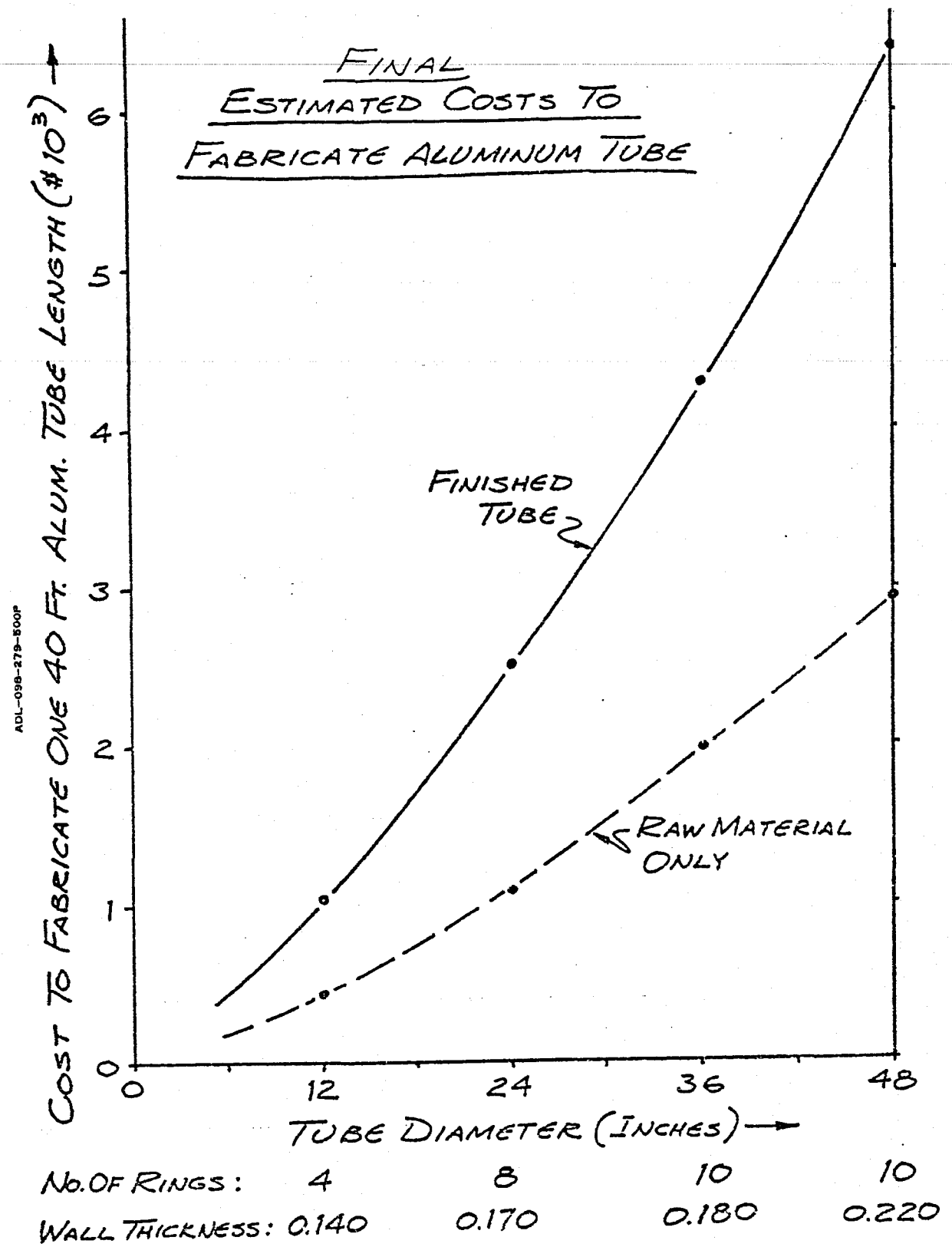
FINAL
ESTIMATED COSTS TO
FABRICATE ALUMINUM TUBE
COST TO FABRICATE ONE 40 FT. ALUM. TUBE LENGTH (10^3)
ADL-098-279-500P
0
1
2
3
4
5
6
FINISHED TUBE
RAW MATERIAL ONLY
0
12
24
36
48
TUBE DIAMETER (INCHES)
No. OF RINGS: 4 8 10 10
WALL THICKNESS: 0.140 0.170 0.180 0.220

FIGURE 6

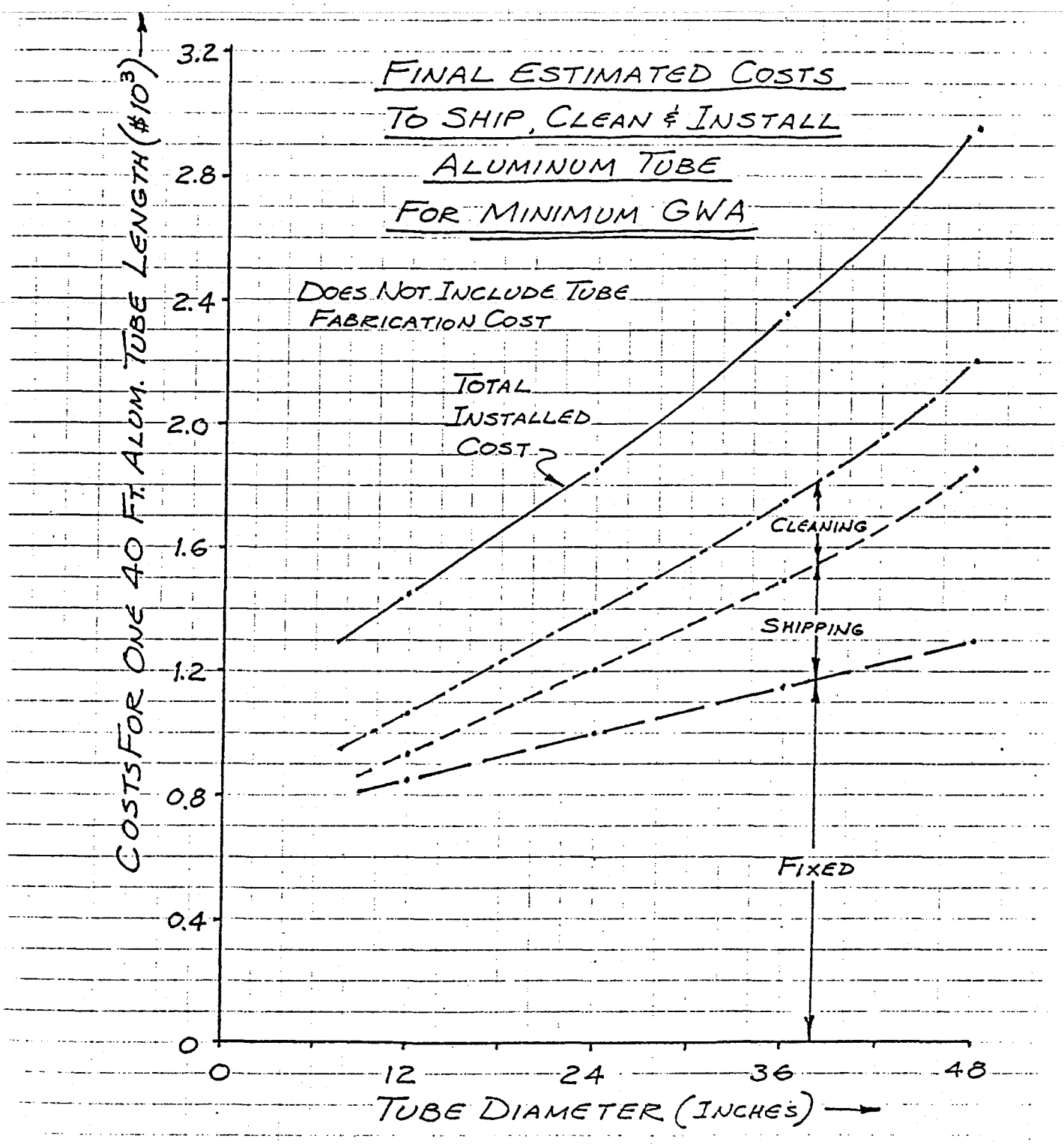
FINAL ESTIMATED COSTS
TO SHIP, CLEAN & INSTALL
ALUMINUM TUBE
FOR MINIMUM GWA
DOES NOT INCLUDE TUBE FABRICATION COST
TOTAL INSTALLED COST
CLEANING
SHIPPING
FIXED
COSTS FOR ONE 40 FT. ALUM. TUBE LENGTH (10^3)
3.2
2.8
2.4
2.0
1.6
1.2
0.8
0.4
0
0
12
24
36
48
TUBE DIAMETER (INCHES)

FIGURE 7A

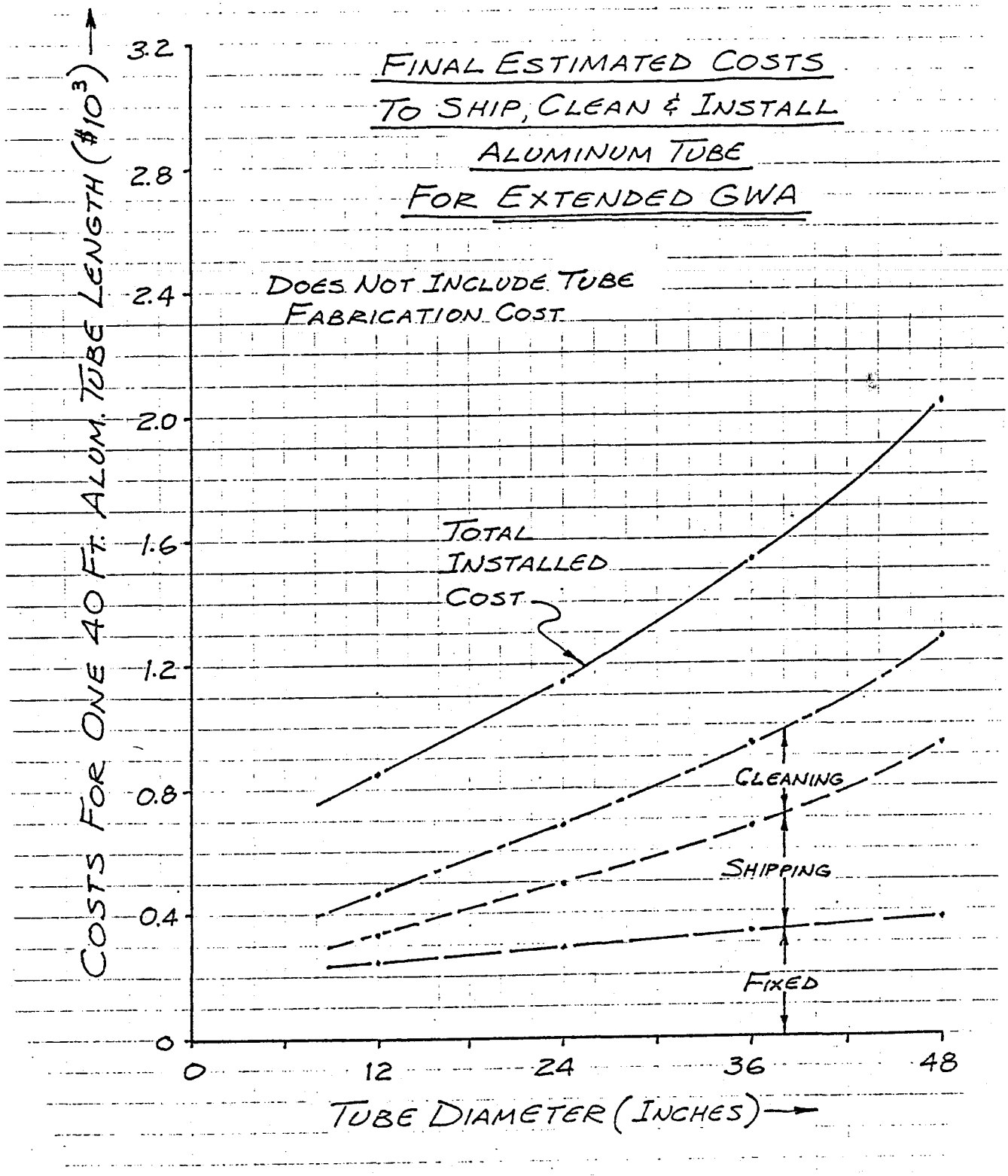
FINAL ESTIMATED COSTS
TO SHIP, CLEAN & INSTALL
ALUMINUM TUBE
FOR EXTENDED GWA
DOES NOT INCLUDE TUBE
FABRICATION COST
TOTAL
INSTALLED
COST
CLEANING
SHIPPING
FIXED
COSTS FOR ONE 40 FT. ALUM. TUBE LENGTH (10^3)
3.2
2.8
2.4
2.0
1.6
1.2
0.8
0.4
0
0
12
24
36
48
TUBE DIAMETER (INCHES)

FIGURE 7C

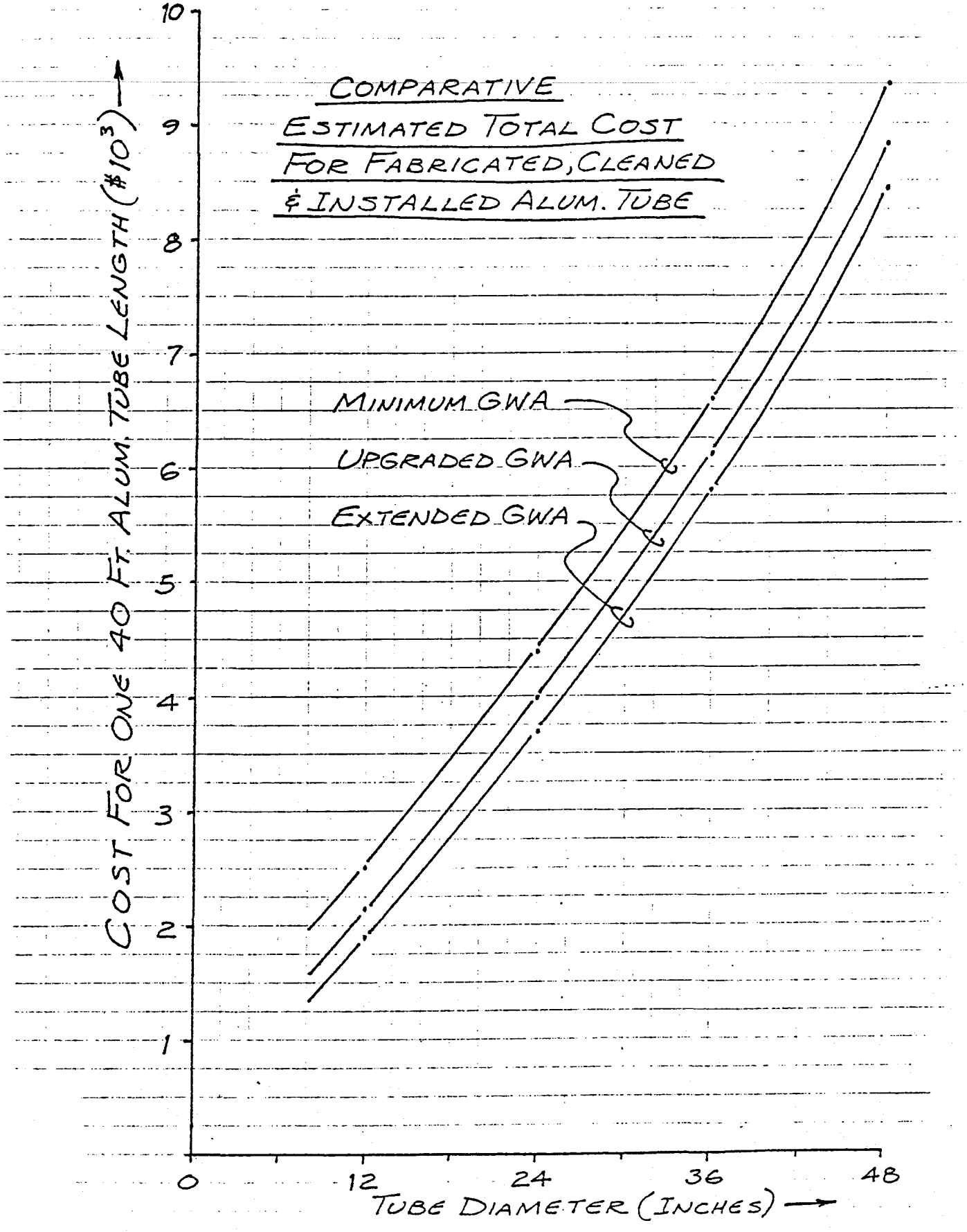
COMPARATIVE
ESTIMATED TOTAL COST
FOR FABRICATED, CLEANED
& INSTALLED ALUM. TUBE
MINIMUM GWA
UPGRADED GWA
EXTENDED GWA
COST FOR ONE 40 FT. ALUM. TUBE LENGTH (10^3)
10
9
8
7
6
5
4
3
2
1
0
12
24
36
48
TUBE DIAMETER (INCHES)

FIGURE 8

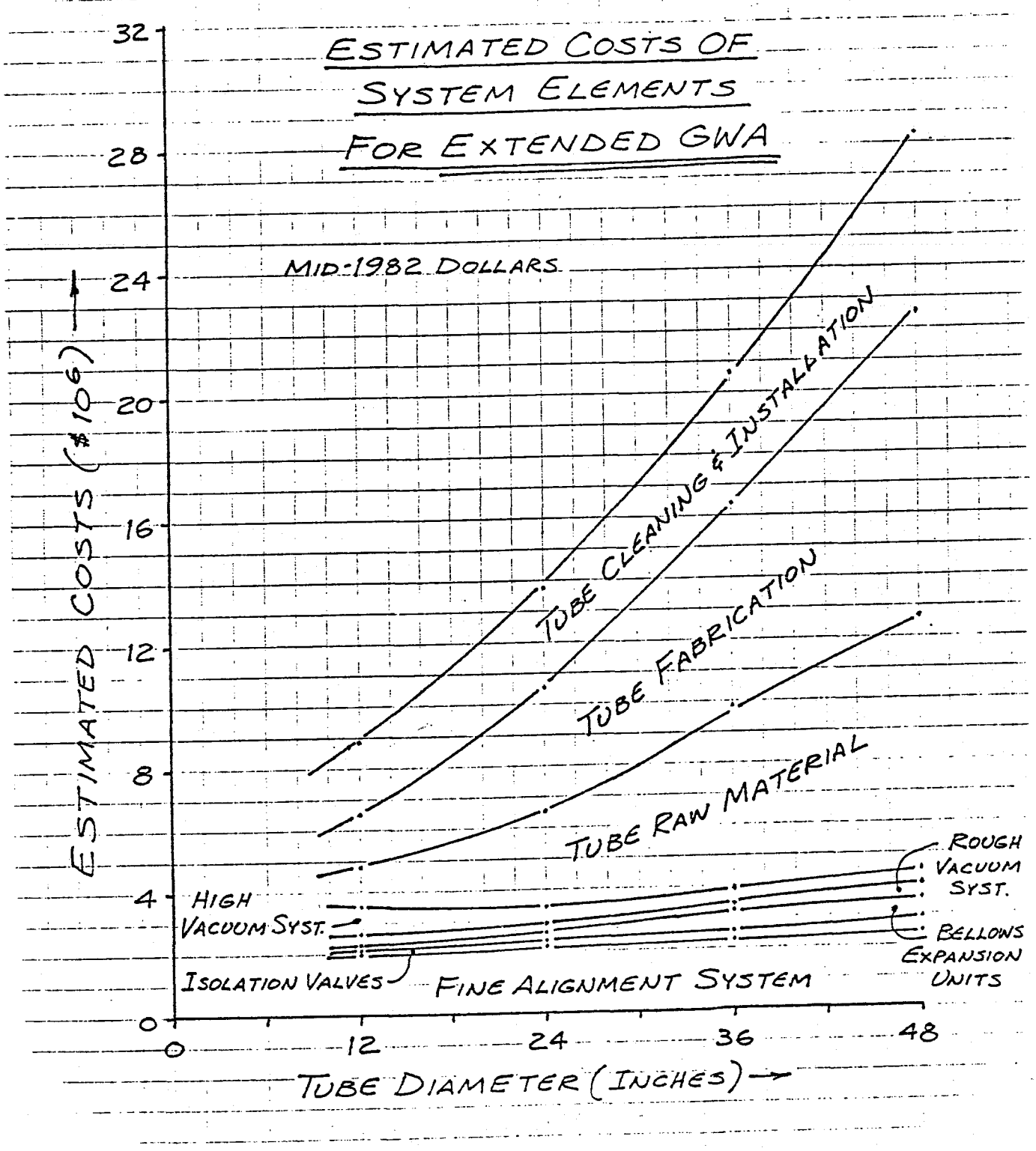
ESTIMATED COSTS OF SYSTEM ELEMENTS FOR EXTENDED GWA
MID-1982 DOLLARS
ESTIMATED COSTS ($10^6)
32
28
24
20
16
12
8
4
0
0
12
24
36
48
TUBE DIAMETER (INCHES)
TUBE CLEANING & INSTALLATION
TUBE FABRICATION
TUBE RAW MATERIAL
ROUGH VACUUM SYST.
HIGH VACUUM SYST.
BELLOWS EXPANSION UNITS
ISOLATION VALVES
FINE ALIGNMENT SYSTEM

FIGURE 18C

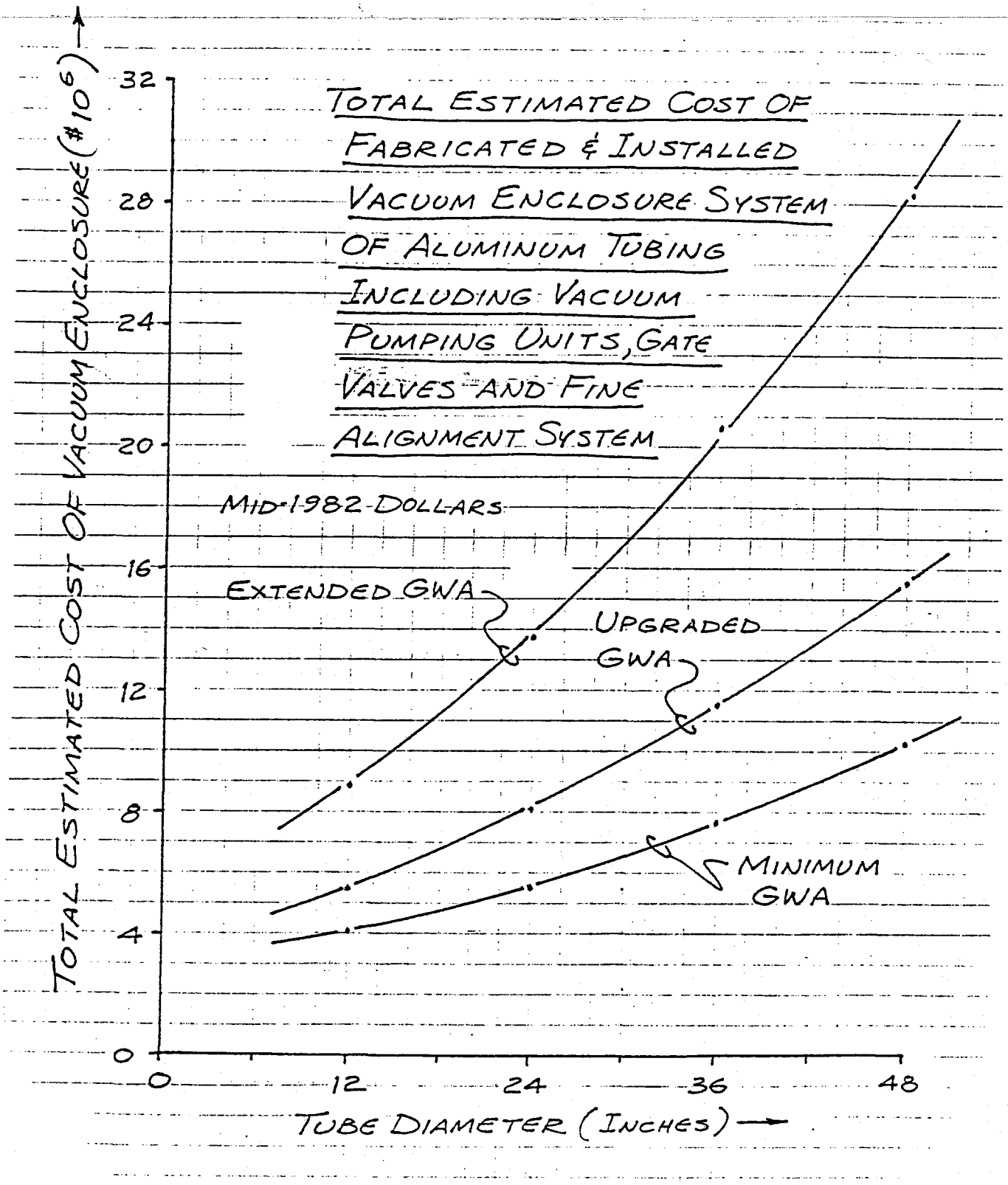
TOTAL ESTIMATED COST OF FABRICATED & INSTALLED VACUUM ENCLOSURE SYSTEM OF ALUMINUM TUBING INCLUDING VACUUM PUMPING UNITS, GATE VALVES AND FINE ALIGNMENT SYSTEM
MID-1982 DOLLARS
EXTENDED GWA
UPGRADED GWA
MINIMUM GWA
TOTAL ESTIMATED COST OF VACUUM ENCLOSURE (10^6)
TUBE DIAMETER (INCHES)
0
4
8
12
16
20
24
28
32
0
12
24
36
48

FIGURE 19

Table 8.

OVERALL DESIGN GUIDELINES FOR GWA END-STATIONS

- Number to be Built: 3 or 4
- Material: 304 Stainless Steel
- Ports:
  - 3 for Leg Enclosures (12 to 48-inch dia.)
  - 2 for Viewing (8-inch dia.)
  - 1 42-inch Access Door
  - ~12 Pumping Ports in Base Structure
- Design Considerations for Experiment Support
  - Maximum baseplate deflection due to vacuum: 0.4 inches
  - Maximum dynamic range of leveling servos: 0.4 inches
- Vacuum Level: 10^{-6} to 10^{-8} Torr
- Sealing Method: Metallic seals
- Maximum Pumping Time: 500 hours
- Vacuum Pumps:
  - Roughing Conventional*
  - High Vacuum Ion-type
- Bakeout Temperature: 392°F (200°C)
- Wires and Wire Penetrations:
  - 50 power leads
  - 25 shielded signal leads
  - 25 other non-shielded leads
  - Feedthroughs on bottom plate or dome.
- Inner Member Sizes (all cubic in shape):
  - Central Mass: 28-inch edge (outside surface only)
  - Frame 1: 52-inch edge (inner and outer surfaces)
  - Frame 2: 82-inch edge (inner and outer surfaces)
  - Frame 3: 102-inch edge (inner and outer surfaces)
- Other Enclosed Devices:
  - 3 Dielectric-coated Mirrors (~28-inch dia., max.)
  - Approximately 6 Servo-driven Motors and Capacitive Sensors for Alignment

of the limited number of end stations to be built (i.e., 3 or 4) and the possibility of a vacuum of 10^{-8} Torr, we decided that the units would be constructed of rolled and welded 304 stainless steel sheets for the side walls and a pressed or spun stainless steel torispherical head. We developed cost estimates for the bottom surface assuming that it could be either a flat plate (approach-1) or a torispherical dome (approach-2) similar to the head.

5.2 DESIGN CONCEPTS

Figures 20 and 21 are conceptual drawings of two approaches that we evaluated in developing cost estimates for the end stations. The concepts are labeled as "Approach-1" and "Approach-2," and are identical above the baseplate. Each approach assumes that the chambers are supported off of a concrete base structure. The baseplate for Approach-1 is a heavy, but simple, flat plate that was sized based on the maximum deflection criterion identified in Table 8. We expect that this approach would be the easiest to maintain in a clean condition appropriate to the end station vacuum requirements. Approach-2 includes a bottom flanged dome that is nominally the same as the head except that it also contains at least three internal support legs for the experiment, several external pads to support the enclosure base, approximately 12 10-inch pumping ports, and a flanged plate that will accommodate up to 100 wire feedthroughs.

5.2.1 Thermal Considerations

The 392°F (200°C) vacuum bakeout requirement will lead to considerable motion of the baseplate relative to its concrete support during the heating and cooling process. If the base is supported at a 6-foot radius, the tank radius will expand by approximately 0.33 inches during the heating process. Therefore, in each design approach, the base should be fixed at one point, and the remainder of the structure designed to allow radial motion due to thermal effects.

END STATION PRESSURE VESSEL CONCEPT, APPROACH-1

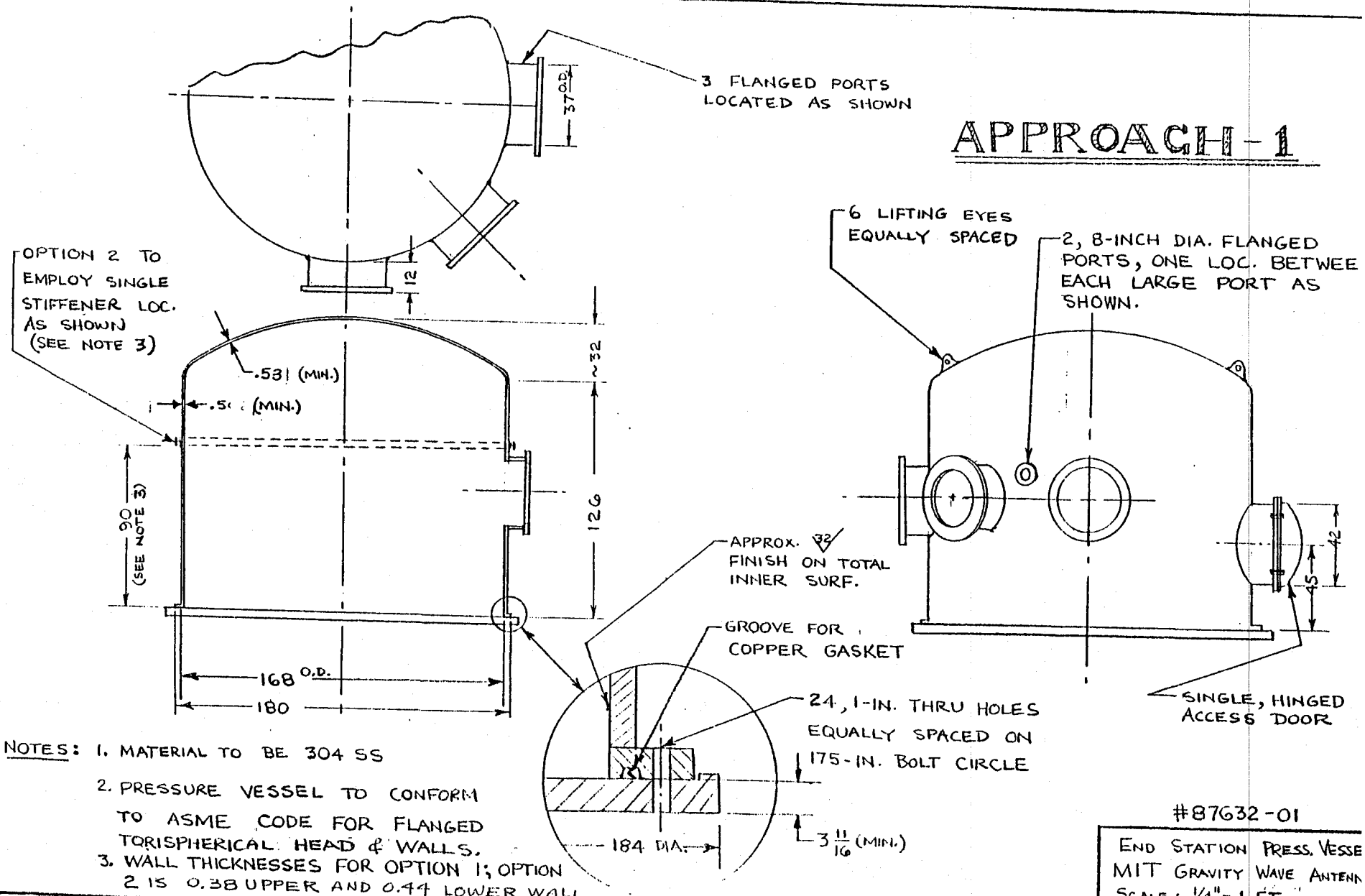

FIGURE 20

END-STATION PRESSURE VESSEL CONCEPT, APPROACH - 2

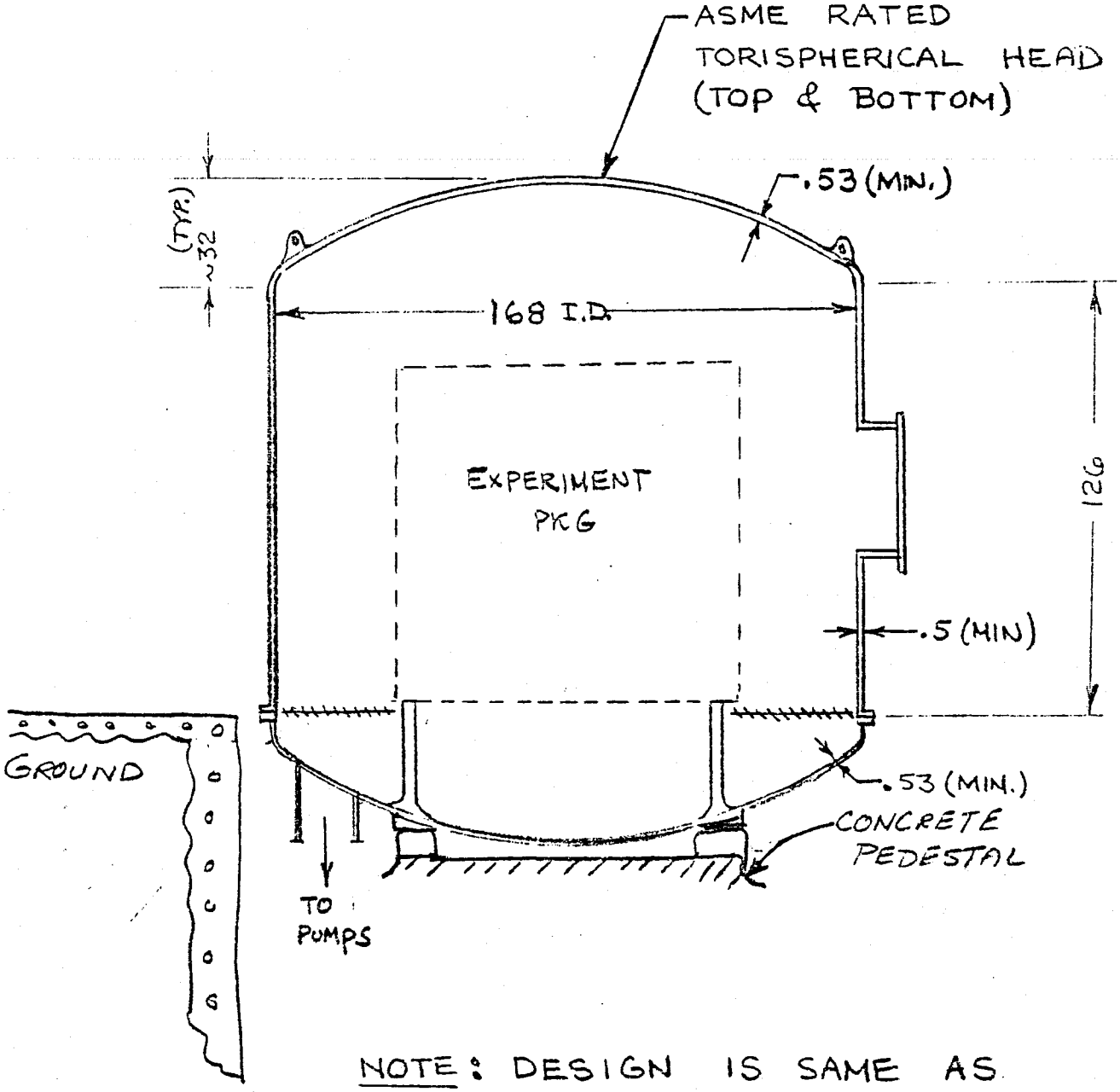

NOTE: DESIGN IS SAME AS APPROACH-1 EXCEPT FOR BOTTOM DOME.

FIGURE 21

In Approach-1, the end stations can be secured at the center and the baseplate allowed to slide radially on independent steel pads accurately imbedded in the concrete base. In approach-2, the enclosure base will be rigidly secured to one pad and the remainder of the pads allowed to slide relative to the fixed pad.

Variations in the alignment of the experiment package due to diurnal, seasonal, and shorter period vibrations in the earth will be accommodated by the leveling and alignment servos within the experiment housings.

5.2.2 Alternative Concept

A third, and potentially less expensive design approach was considered that consisted of a thin (~1-inch thick) base plate rigidly clamped throughout to a massive concrete base. With such an approach, the plate deflections arising from the vacuum-induced pressure differential would be restricted by the clamping scheme. The idea was discarded because strains associated with the bakeout temperatures would put severe stresses on the concrete pad. Concepts aimed at eliminating this concern soon made the whole approach cumbersome and more costly and complex than the approaches previously presented.

5.3 END-STATION ENCLOSURE COSTS

Two methods were employed in developing cost estimates for the vacuum enclosures shown in Figures 20 and 21. The first method was to employ Richardson's "Process Plant Construction Estimating Standards; Vol. 4, Process Equipment" to cost out each component required for the two approaches. Costs for handling and shipping were also included. Details are included in worksheets presented in Appendix H of Volume II.

The second approach was to submit the sketches shown in Figures 20 and 21 to a potential pressure vessel vendor to obtain a rough estimate

for fabricating each unit. The results obtained by each method were then compared and differences adjusted using engineering judgement.

Both costing methods led us to recommend that the approach shown in Figure 21 (i.e., Approach-2) be employed. We felt it to be approximately $40K less expensive than Approach 1 shown in Figure 20 for the fabrication of each end station. The difference results largely from the high weight and cost for the thick baseplate in Approach-1. We did not feel that the increased inner surface area in Approach-2 and increased difficulties in keeping the interior surfaces clean were major factors.

The cost for shipping the units was based on a 2000-mile trip using a calculation procedure recommend in Richardson's guide. The costs were then increased from those normally calculated based on weight alone, to account for the fact that the vacuum enclosures mounted on a flat-bed truck would constitute a "wide load" and exceed the height restriction of 13 feet 6 inches on most major highways. Therefore, based on discussions with movers, shippers, and fabricators, we felt a factor of two increase in shipping costs would be reasonable at this time.

The costs for installing and cleaning the units are very difficult to estimate unless a detailed man-loading study is conducted and costs for the specific labor categories, local wage structure (i.e., union or non-union), on-site engineering supervision and per diem costs are included. To gain insight on these potential costs, without doing the detailed work, we conducted discussions with vendors and arrived at a "best engineering estimate."

The results of this cost procedure are presented in Figure 22 for a single end station as a function of the port diameters which are consistent with the diameters considered for the enclosures discussed earlier. It should be noted in Figure 22 that the installation costs also include the costs for installing the 100 liter/sec end-station

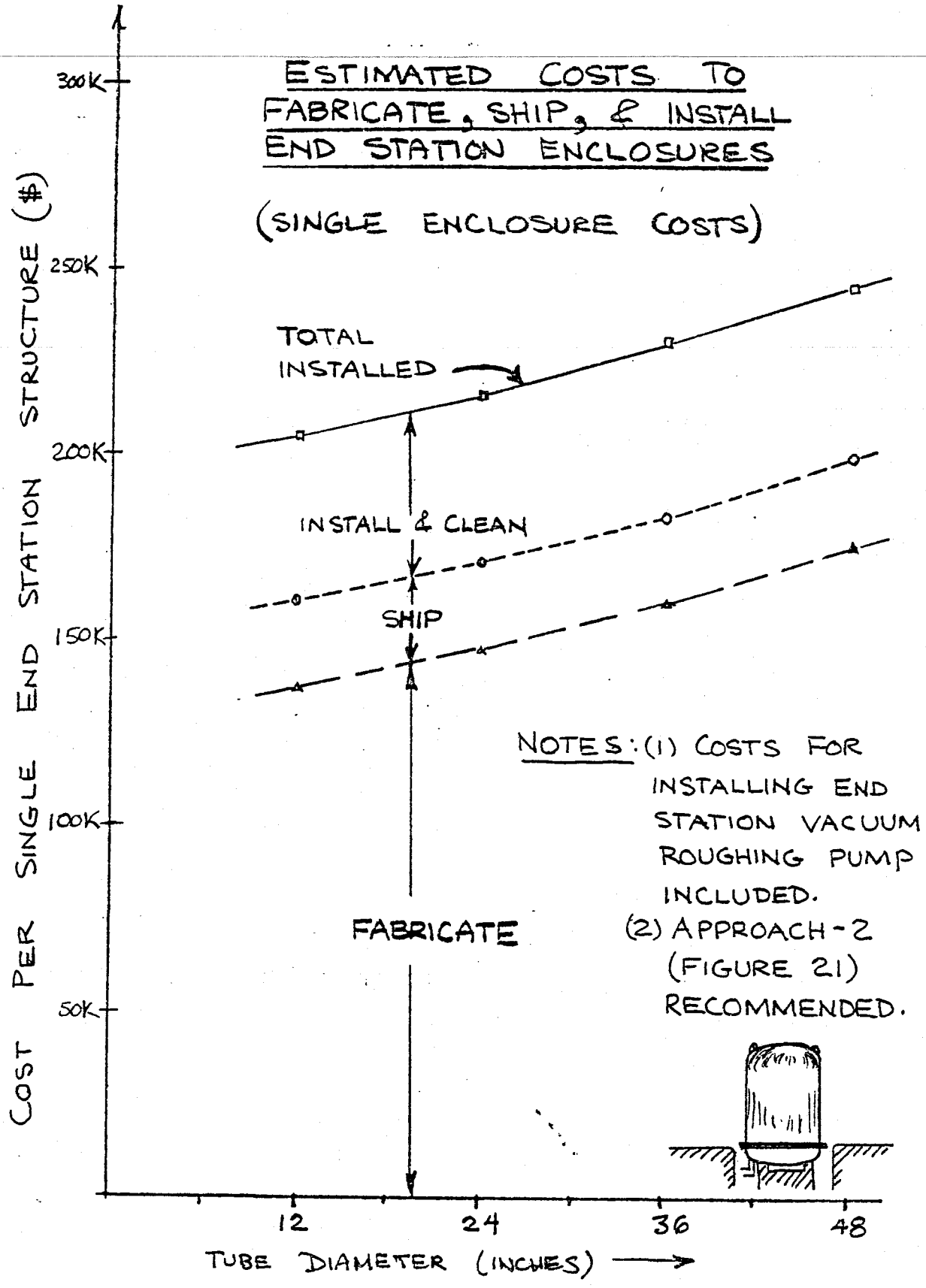
ESTIMATED COSTS TO FABRICATE, SHIP, & INSTALL END STATION ENCLOSURES
(SINGLE ENCLOSURE COSTS)
COST PER SINGLE END STATION STRUCTURE ($)
300K
250K
200K
150K
100K
50K
TOTAL INSTALLED
INSTALL & CLEAN
SHIP
FABRICATE
NOTES: (1) COSTS FOR INSTALLING END STATION VACUUM ROUGHING PUMP INCLUDED.
(2) APPROACH-2 (FIGURE 21) RECOMMENDED.
12
24
36
48
TUBE DIAMETER (INCHES)

FIGURE 22

roughing pump, but not the 12 high vacuum (i.e., ion-type) pumps. These costs are covered in section 5.4. In summary the enclosure costs are judged to be accurate to approximately ±$45,000.

5.4 VACUUM SYSTEM

A project goal is to achieve a vacuum level of as good as 10^{-8} Torr within the end stations of the GWA. As a result, a considerable amount of high vacuum pumping capacity (i.e., ion-type pumps) is required in the tube sections adjacent to the end stations to reduce the gas load on the end stations created by the tube enclosures. The number of ion pumps mounted in the line will vary with tube length, tube diameter, GWA plan and end station vacuum level. For completeness in this study, we derived a first order estimate of the differential costs for ion pumps as a function of these parameters.

As discussed in section 4.2, the average vacuum level in the various tube enclosures has been identified as 1.4×10^{-6} Torr. In the lowest cost enclosure design, discussed in that section, pumps would be installed at a spacing of approximately 1 km. At high vacuum levels, the end station pumping requirements will necessitate either of the following designs:

(1) The installation of several high vacuum pumps in the end stations themselves and several pumps in the enclosures immediately adjacent to the end stations ("non-optimum" design); or

(2) The installation of several pumps in the end stations and several pumps (fewer than in case (1)) in the enclosures spaced optimally to minimize the total number of pumps, while maintaining an average vacuum level of 1.4×10^{-6} Torr in the enclosure tubes (i.e., "optimum" design).

These options evolved because it is physically impossible to mount all pumps required to meet the total gas load on the end stations within the end stations themselves. For the major gas load on the end stations, when they are operating in the vacuum range of 10^{-7} to 10^{-8} Torr, is from the tubes themselves which are assumed to have an average vacuum of 1.4×10^{-6} Torr. Therefore, the second design approach would distribute pumping capacity along the line to allow each ion-type pump to function most effectively. For the purposes of this study, we have assumed that only 12 ion-type pumps can be installed in the base of the end stations and that the rest will be located on the tubing enclosures.

To facilitate the computation of overall GWA costs, the costs for vacuum pumping capacity required only for the addition of end stations will be presented. These costs are identified as differential costs over and above those discussed in section 4.2 for the tubing enclosures and consist of:

(1) end station costs (excluding foundation and external building structure),

(2) end-station roughing pump costs, and

(3) the ion-type pumps required in addition to those already recommended for the tubing enclosures.

Total vacuum pumping costs for the three GWA's previously defined are then determined by adding the costs identified in section 4.2 to the differential costs identified in this section.

5.4.1 Rough Pumping System Costs

The requirements for a roughing pump system to reduce the end-station pressure from atmospheric pressure (760 mm of Hg) to approximately 10^{-3} mm Hg (i.e., 10^{-3} Torr) are independent of the roughing pump calculations presented in section 4.2 for the tube enclosures as long as the time requirements are the same. For the case in which both the tubes and end stations must be pumped to 10^{-3} Torr in 50 hours, no

additional roughing pumps are required within the tubes in any GWA configuration due to the addition of the end stations.

Based on calculations provided in Appendix H of Volume II, the candidate end station design shown in Figure 21 contains an enclosed volume, V, of 2201 cubic feet (6.24×10^4 liters). A 50-hour pump-down transient from atmospheric pressure to 10^{-3} Torr, governed by the equation $\ln (P_f/p_i) = - q_p t/V$, leads to a rough pumping rate of $q_p = 47$ liters/sec. In this equation, p_f and p_i are the final and initial pressures respectively and t is time.

As a safety factor, this value will be assumed to be 100 liters/sec. and an installed cost of approximately $17,000 per end station for roughing pumps will be assumed based on Figure 14 in section 4.2. In reality, a pump of this size would reduce the end-station pressure to approximately 10^{-3} Torr in 24 hours.

5.4.2 High Vacuum Pumping System Costs

Preliminary analytical estimates indicate that many additional ion pumps are required if all the pumps are installed in or directly adjacent to the end station (design 1) as opposed to being distributed along the line in an optimum manner (design 2). The detailed calculations are contained in Appendix H. A comparison of the different number of pumps in each case is briefly summarized in Table 9 for the case of a vacuum of 10^{-8} Torr in the end stations and an average vacuum of 1.4×10^{-6} Torr in the tube enclosures for the Minimum GWA Array. Each pump is assumed to have a pumping capacity of 750 liters/sec, the largest size that is readily available. The ratios indicated in the last column of Table 9 are assumed to also hold to first order at vacuum levels of 10^{-7} and 10^{-6} Torr.

Table 9

DIFFERENTIAL* ION-TYPE PUMP REQUIREMENTS
FOR "NON-OPTIMUM" AND "OPTIMUM" LOCATION OF PUMPS

(End Station Vacuum = 10^{-8} Torr, Minimum GWA)

Pipe Diameter (Inches)	No. of Pumps at Non-Optimum Pump Spacing	No. Pumps at Optimum Pump Spacing	Ratio Non-Optimum / Optimum
12	64	33	1.94
24	110	44	2.50
36	176	57	3.09
48	232	66	3.52

*Differential requirements are additional pumps to meet only needs dictated by the addition of the end stations. All values for tubing enclosures (section 4.2) should be added to these values to obtain total numbers of ion pumps.

Ion pumps of the capacity studied cost approximately $18.4K each (installed). Therefore, the results of the analysis indicate that there is a great cost savings potential if the optimum spacing is employed. As a result, we addressed only the scheme that resulted in an optimized number of pumps in the costing effort presented below. It should be noted, too, that during a final design of the GWA, the pump capacity could be varied and pump numbers, sizes, and spacing further optimized on cost; while in this summary 750 liter/sec pumps were assumed in each case.

Figure 23A presents a summary of the analytical results for the Minimum GWA, and Figure 23B presents the same results for the Upgraded and Extended GWA's. Each figure indicates the differential numbers and costs for an "optimized" spacing of 750 liters/sec. pumps. The figures portray the results as a function of vacuum level, tube diameter, and type of GWA. It is important to note that the differential

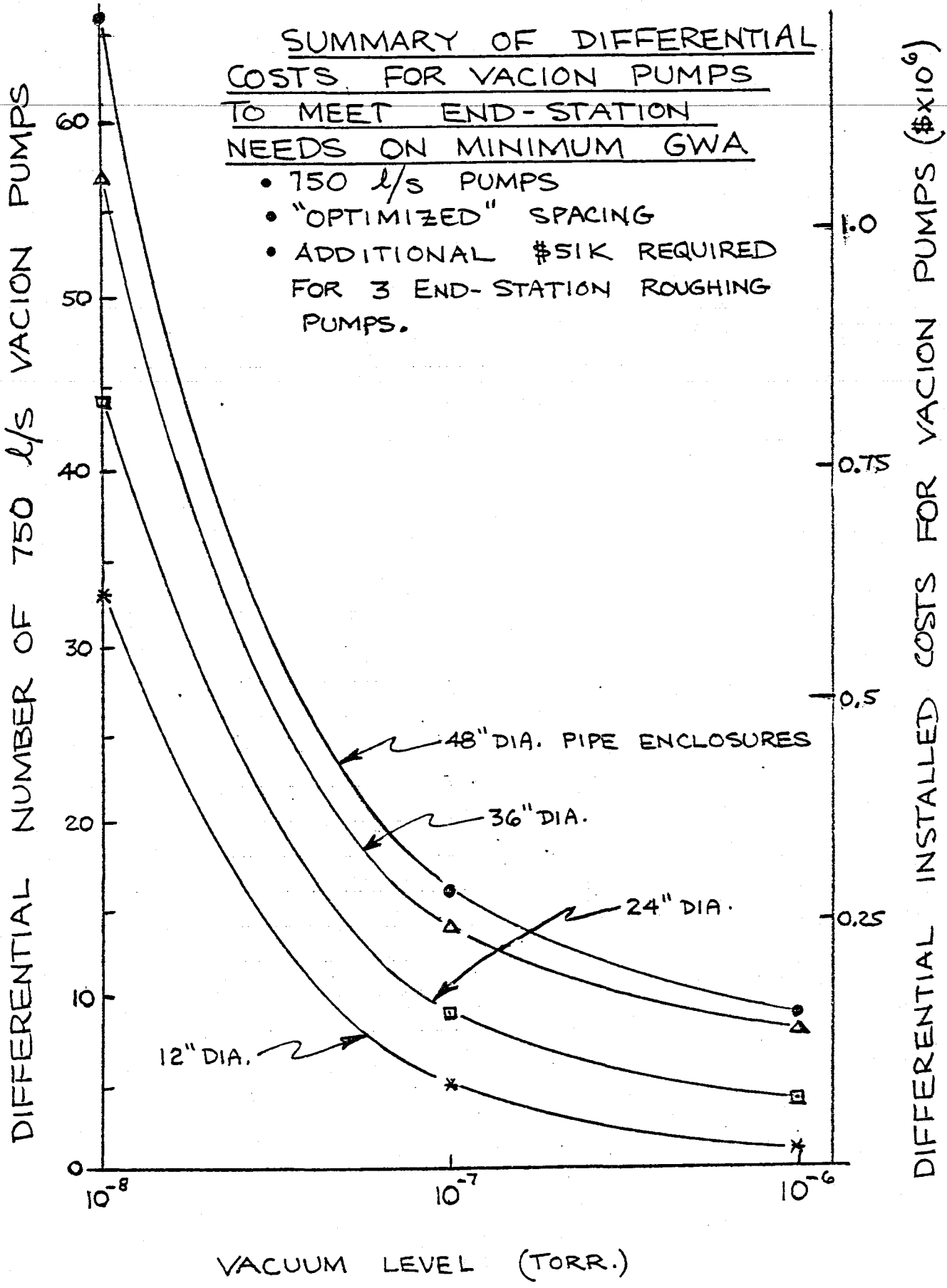
SUMMARY OF DIFFERENTIAL COSTS FOR VACION PUMPS TO MEET END-STATION NEEDS ON MINIMUM GWA
• 750 ℓ/s PUMPS
• "OPTIMIZED" SPACING
• ADDITIONAL $51K REQUIRED FOR 3 END-STATION ROUGHING PUMPS.
DIFFERENTIAL NUMBER OF 750 ℓ/s VACION PUMPS
DIFFERENTIAL INSTALLED COSTS FOR VACION PUMPS ($x10^6)
0
10
20
30
40
50
60
0.25
0.5
0.75
1.0
48" DIA. PIPE ENCLOSURES
36" DIA.
24" DIA.
12" DIA.
10^-8
10^-7
10^-6
VACUUM LEVEL (TORR.)

FIGURE 23A

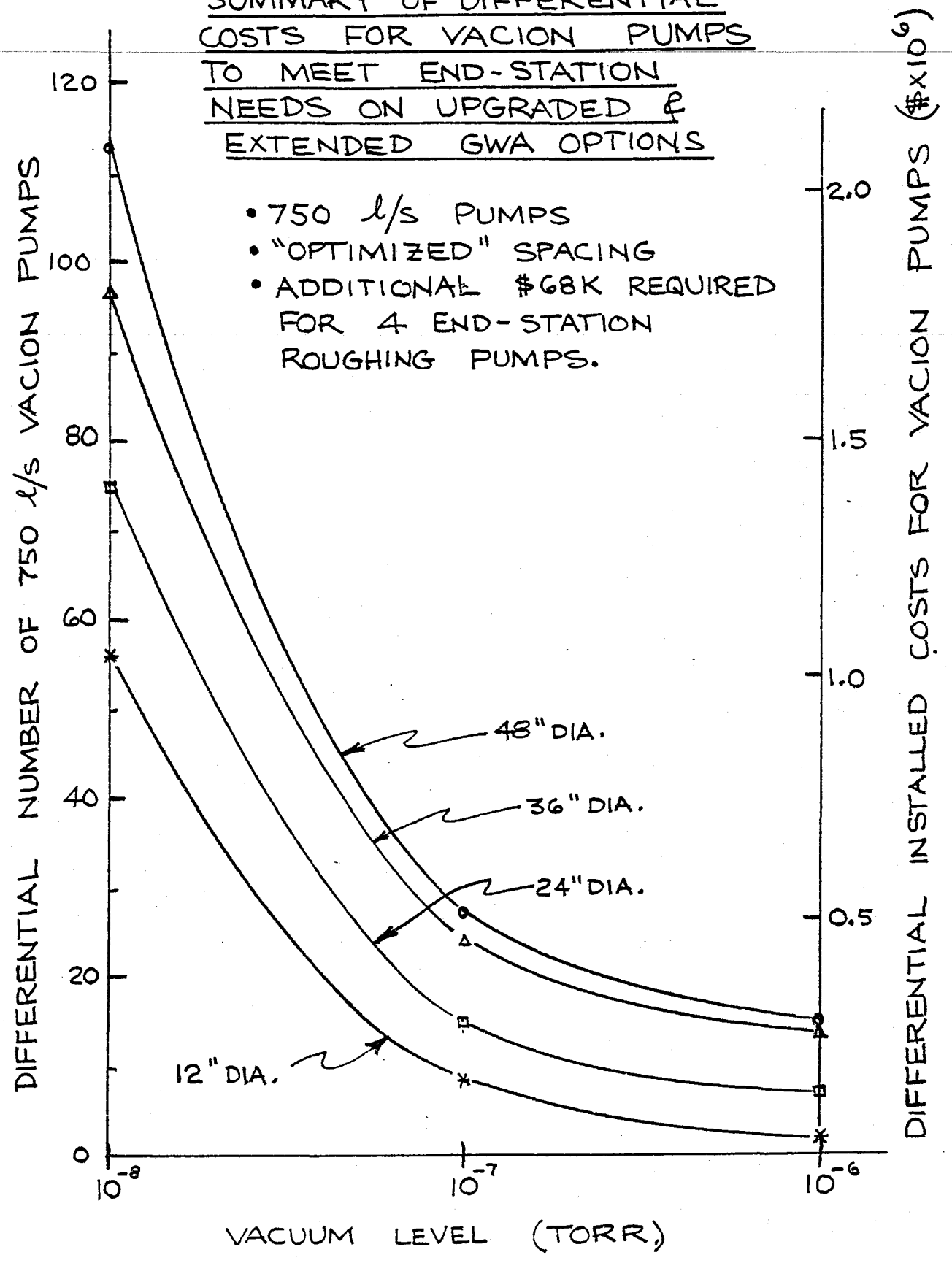
SUMMARY OF DIFFERENTIAL COSTS FOR VACION PUMPS TO MEET END-STATION NEEDS ON UPGRADED & EXTENDED GWA OPTIONS
• 750 ℓ/s PUMPS
• "OPTIMIZED" SPACING
• ADDITIONAL $68K REQUIRED FOR 4 END-STATION ROUGHING PUMPS.
DIFFERENTIAL NUMBER OF 750 ℓ/s VACION PUMPS
DIFFERENTIAL INSTALLED COSTS FOR VACION PUMPS ($x10^6)
VACUUM LEVEL (TORR)
48" DIA.
36" DIA.
24" DIA.
12" DIA.
0
20
40
60
80
100
120
0.5
1.0
1.5
2.0
10^{-8}
10^{-7}
10^{-6}

FIGURE 23B

6.0 SUMMATION OF GWA COSTS

The fabrication and installation costs for the evacuated enclosure and its vacuum pumping equipment have been generated in Section 4.0 and are presented in Figure 19 for the three GWA plans as a function of tube diameter. Additionally, in Section 5.0, the fabrication and installation costs for the individual end stations are displayed in Figure 22 and the incremental costs for their vacuum pumping equipment are shown in Figures 23A and 23B over a range of end station vacuum levels for the Minimum GWA and for the Upgraded or Extended GWA respectively. These separate costs have been summed appropriately to produce total estimated costs for each of the GWA plans. These are presented graphically as a function of tube diameter in Figures 24A, 24B and 24C for one Minimum GWA, one Upgraded GWA and one Extended GWA respectively. Each figure shows the estimated total cost for maintaining the end stations at either of two different vacuum levels; at 10^{-8} Torr or at 10^{-6} Torr (approximately the same vacuum level as within the majority of the evacuated enclosure). Also, each figure indicates the relative magnitude of the evacuated enclosure cost with respect to the total cost.

The costs shown in Figures 24A, 24B and 24C and in all preceding figures do not include the costs of structural support and protective housing for the end stations, evacuated enclosures and their vacuum pumping equipment. Additionally, costs for all other buildings, services and appurtenances of the GWA facility have not been addressed by ADL in this study and, hence, are not incorporated in this report. They will be included in the S&W report. Similarly, costs for the suspended masses, interferometer optics, instrumentation, etc. within the end stations have not been included in the ADL effort and are not contained in this report.

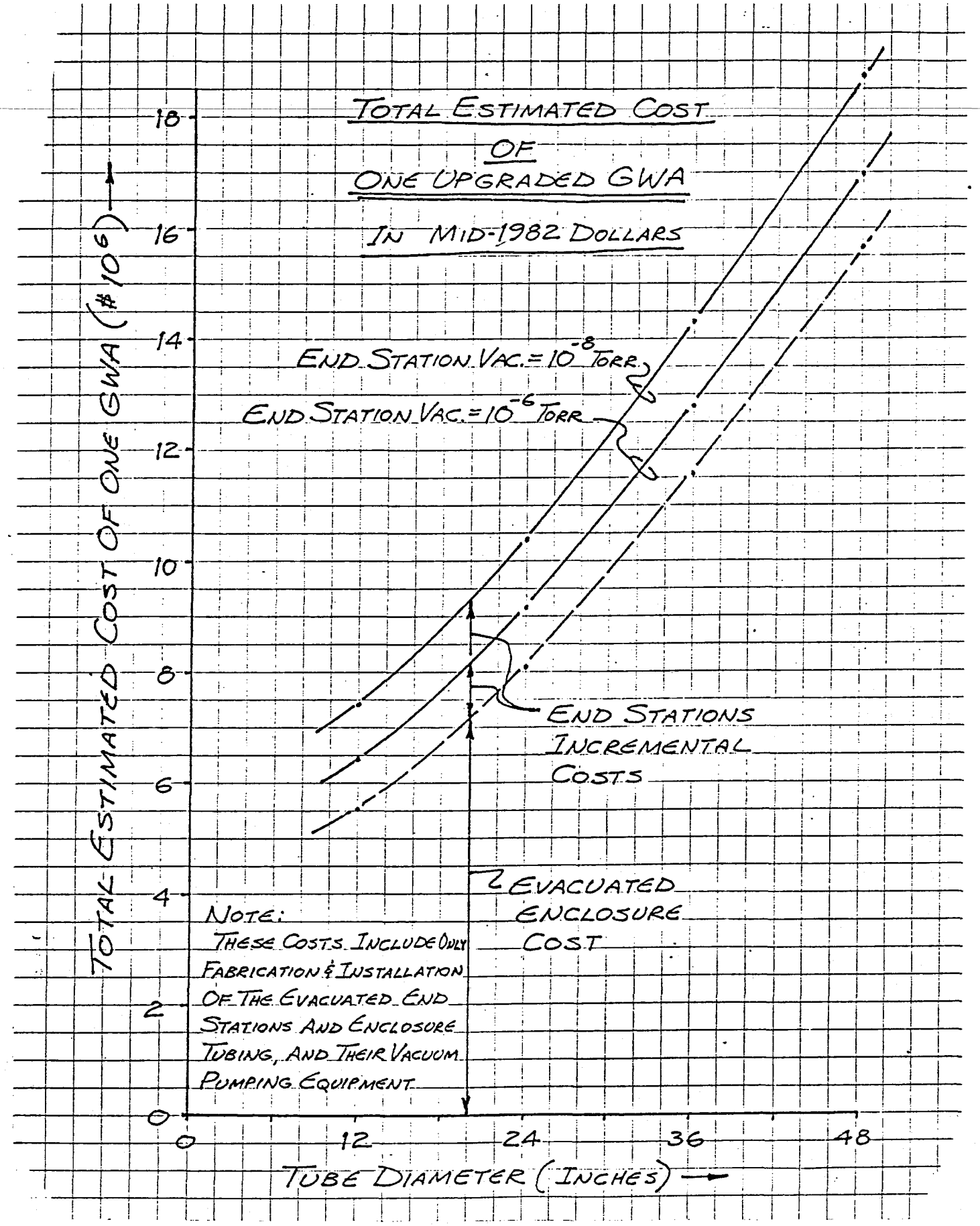
TOTAL ESTIMATED COST OF ONE UPGRADED GWA IN MID-1982 DOLLARS
END STATION VAC. = 10^{-8} TORR
END STATION VAC. = 10^{-6} TORR
END STATIONS INCREMENTAL COSTS
2 EVACUATED ENCLOSURE COST
NOTE: THESE COSTS INCLUDE ONLY FABRICATION & INSTALLATION OF THE EVACUATED END STATIONS AND ENCLOSURE TUBING, AND THEIR VACUUM PUMPING EQUIPMENT
TOTAL ESTIMATED COST OF ONE GWA (#10^6) →
0
2
4
6
8
10
12
14
16
18
0
12
24
36
48
TUBE DIAMETER (INCHES) →

FIGURE 24B

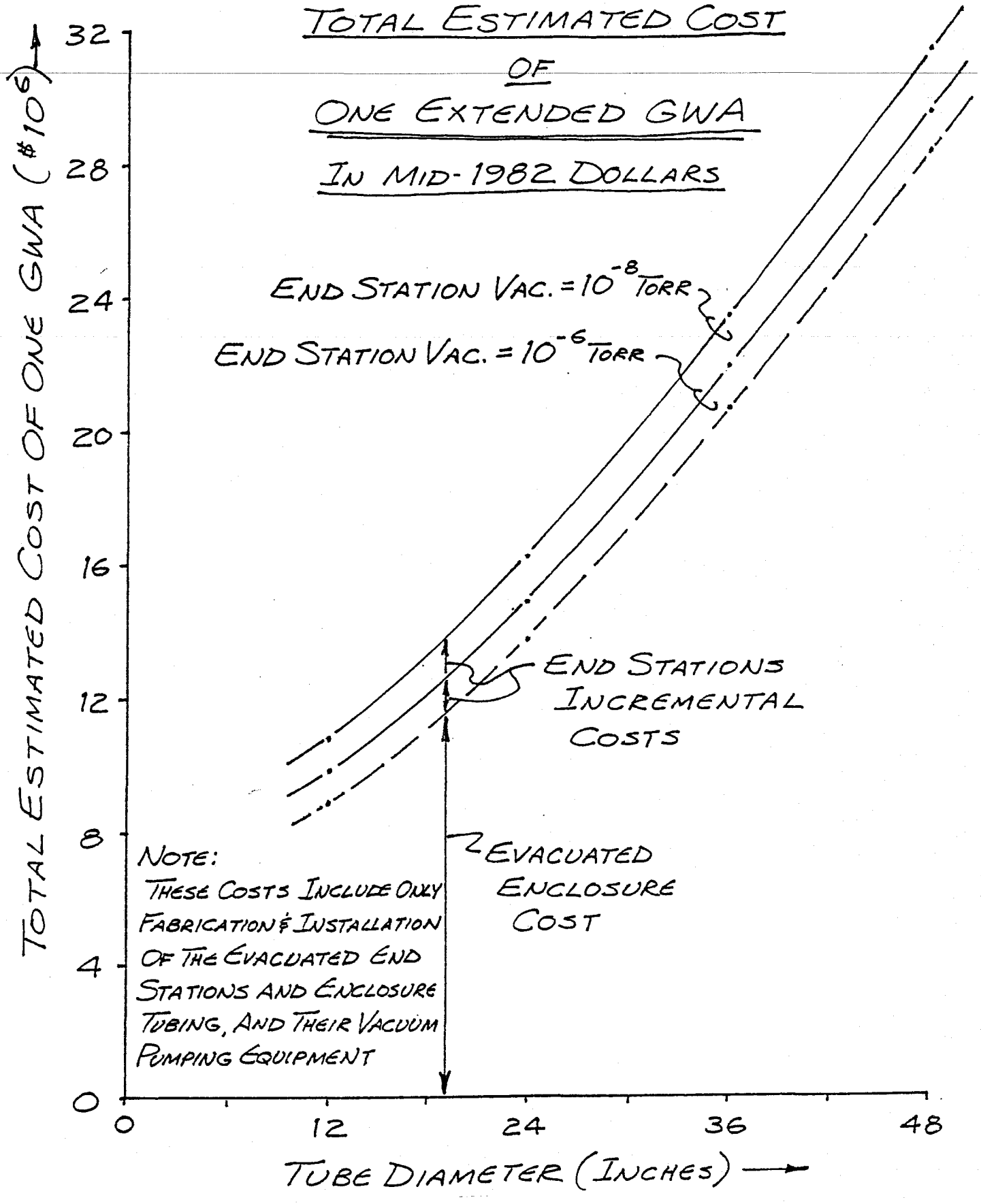
TOTAL ESTIMATED COST OF ONE EXTENDED GWA IN MID-1982 DOLLARS
TOTAL ESTIMATED COST OF ONE GWA ($10^6)
32
28
24
20
16
12
8
4
0
END STATION VAC. = 10^{-8} TORR
END STATION VAC. = 10^{-6} TORR
END STATIONS INCREMENTAL COSTS
EVACUATED ENCLOSURE COST
NOTE:
THESE COSTS INCLUDE ONLY FABRICATION & INSTALLATION OF THE EVACUATED END STATIONS AND ENCLOSURE TUBING, AND THEIR VACUUM PUMPING EQUIPMENT
0
12
24
36
48
TUBE DIAMETER (INCHES)

FIGURE 24C

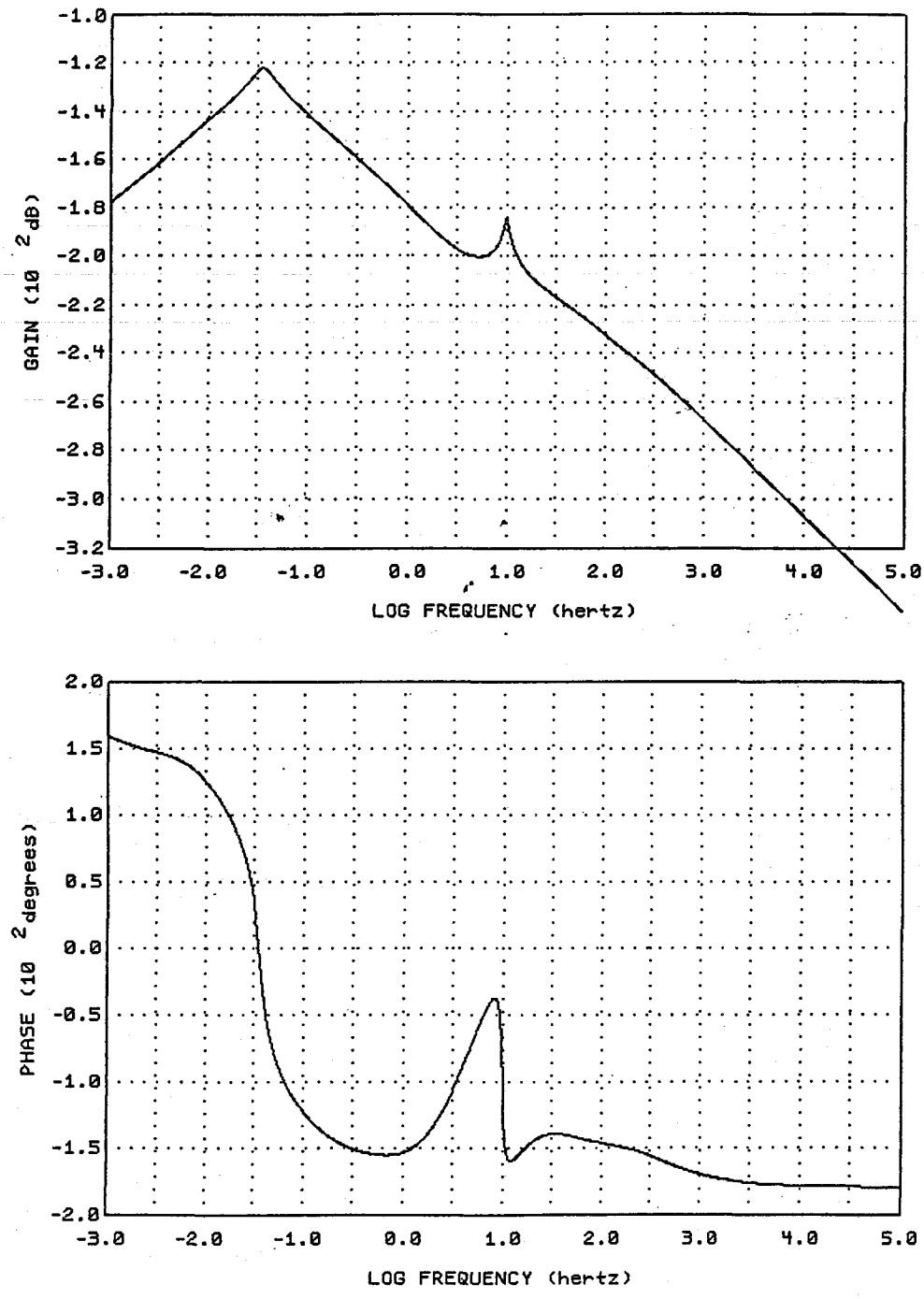

FIGURE 7: COMPENSATED LOOP TRANSFER FUNCTION, OUTER LOOP

order, though. Higher gain can be achieved between the two resonances in this loop by using a compensation filter which adds enough phase lag in between them to bring the phase to nearly -180 degrees. Then the gain will fall nearly as steeply as f^{-2} over this range, giving higher gain at low frequencies for any given crossover frequency. Figure 7 shows the loop transfer function with one version of such a compensation filter. If we again assume that the crossover frequency equals 100 Hz, then the attenuation from this loop is that shown in Figure 8, and the total seismic transmission of the entire system, including the passive response and the effect of the inner loop, is shown in Figure 9. The net improvement of isolation due to the two active loops over the passive response alone is shown in Figure 10. There is no net improvement, obviously, at frequencies above the upper crossover frequency. Furthermore, because of the shape of the loop transfer function there is a lower crossover frequency below which there is no improvement either. Figure 11 shows the net motion of the test mass M_3 at a moderately quiet site, where the seismic spectrum is $x(f) = 10^{-7} \text{cm/Hz}^{\frac{1}{2}} \left(\frac{1\text{Hz}}{f}\right)^2$.

3.0 PRACTICAL CONSIDERATIONS

The foregoing discussion has shown that it is possible, in principle, to attain sufficient vibration isolation above 30 Hz, and substantial isolation to frequencies as low as 1 Hz, with a combined passive-active system. However, several important simplifications were made, the validity of which we will now discuss.

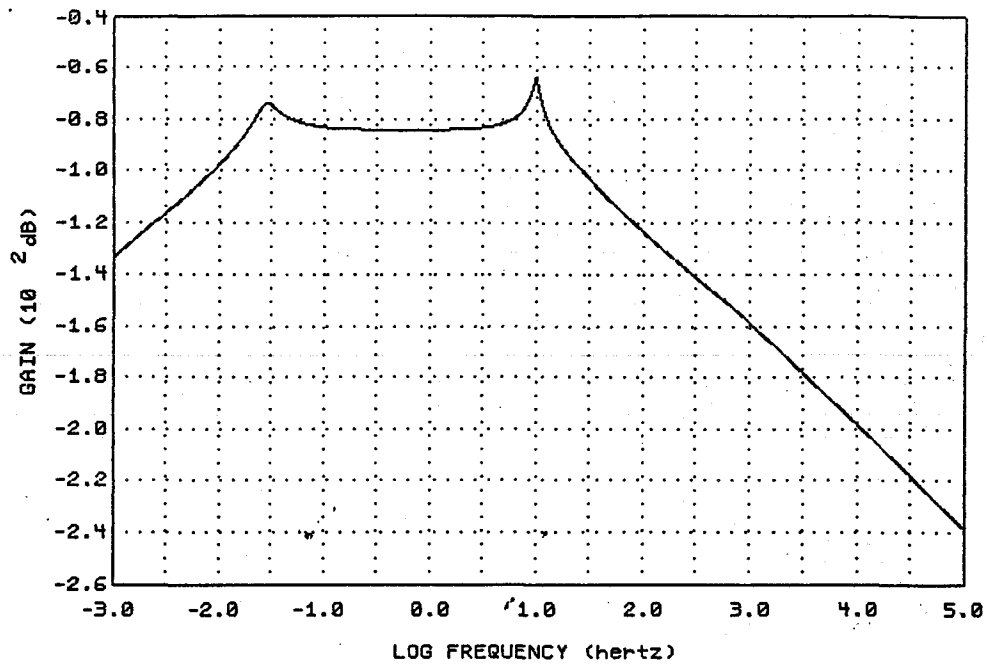

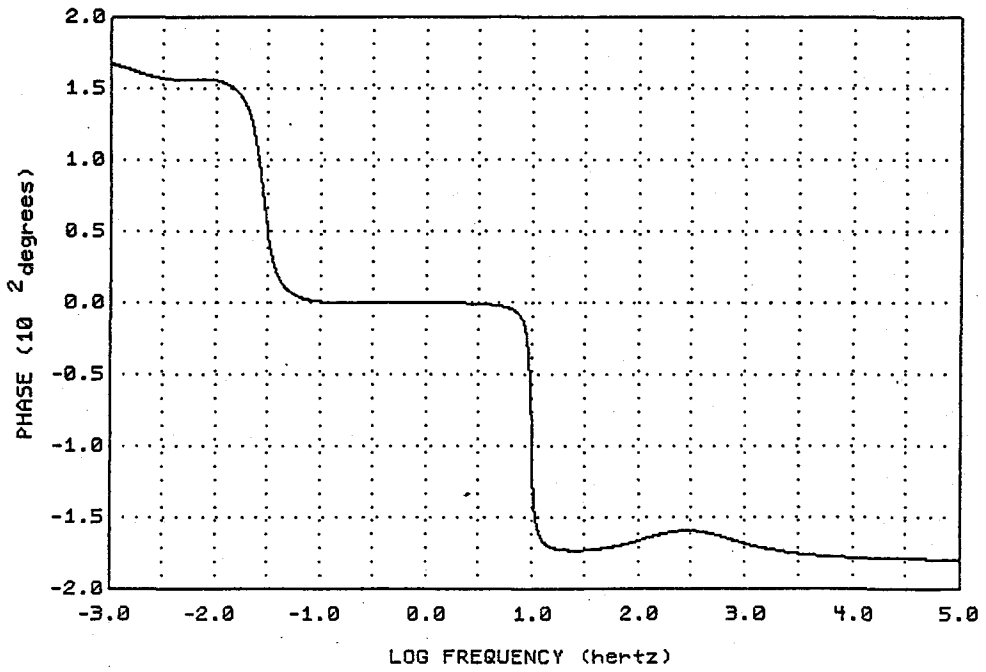

FIGURE 6: LOOP TRANSFER FUNCTION, OUTER LOOP

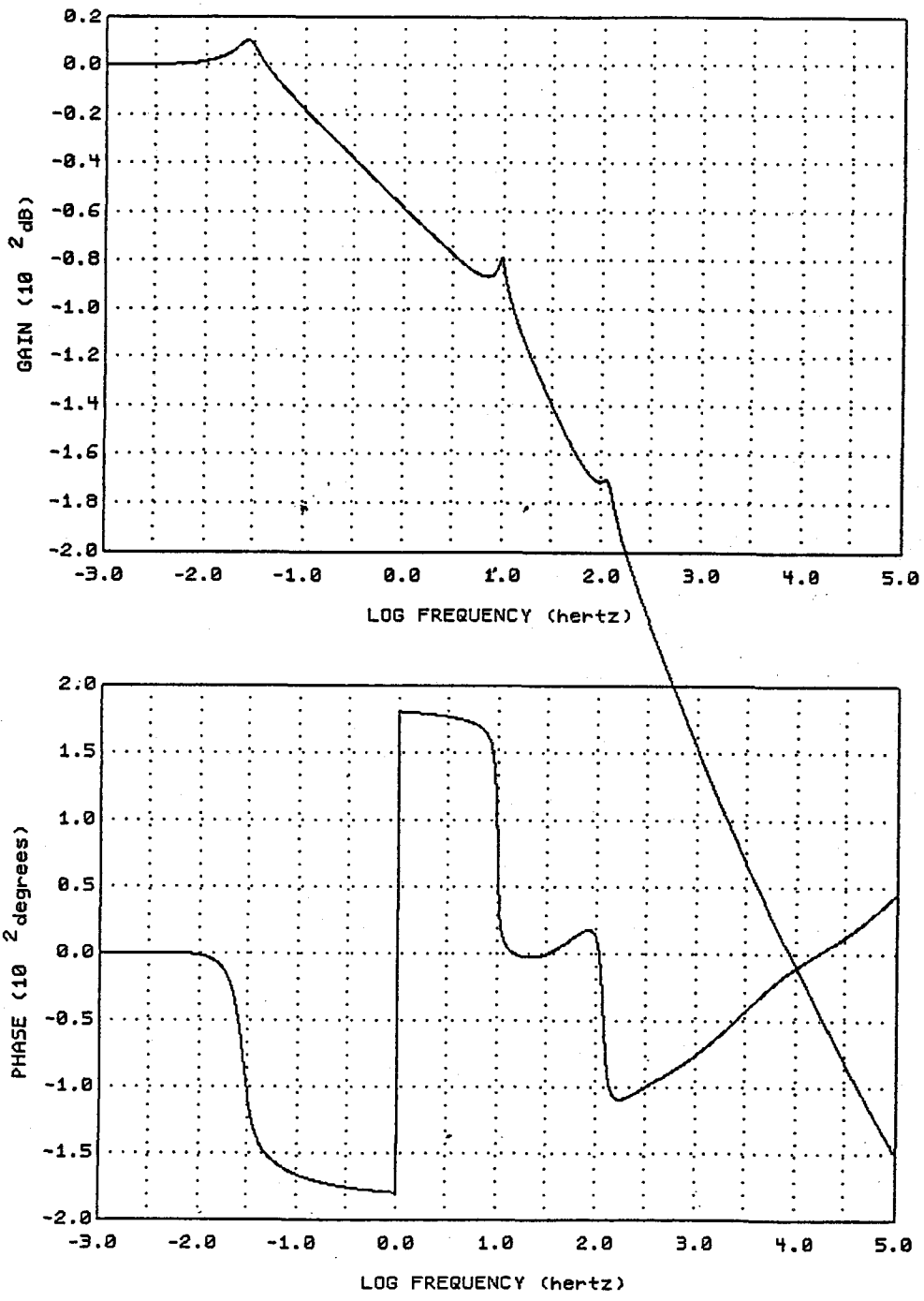

FIGURE 5: NET SEISMIC TRANSMISSION, INNER FEEDBACK LOOP ON

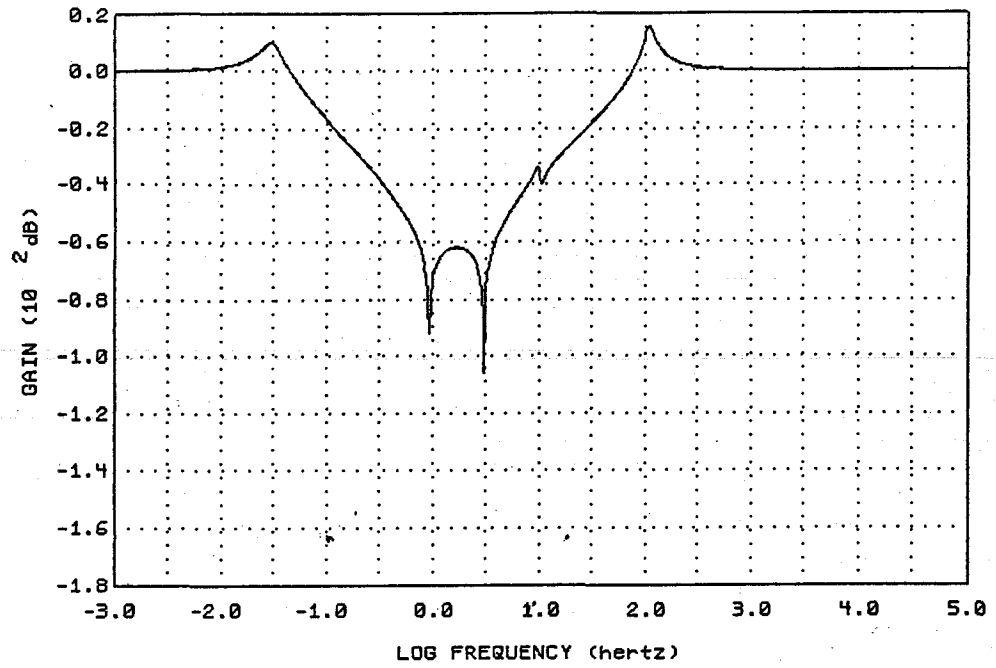

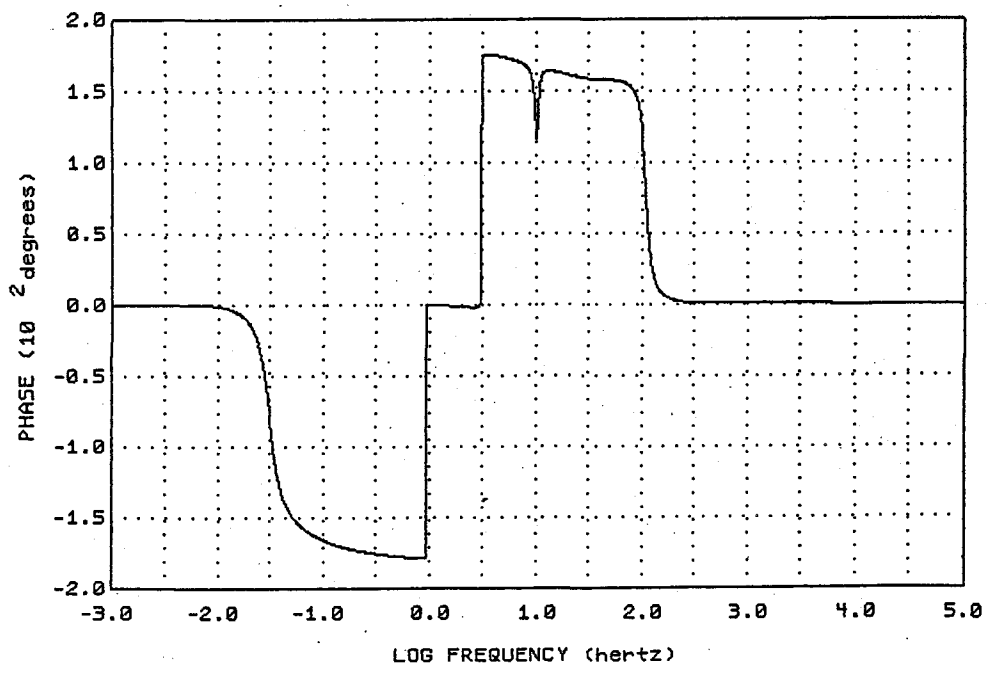

FIGURE 4: ADDITIONAL SEISMIC ATTENUATION FROM INNER LOOP

resonances can be kept at relatively high frequencies, since the roll-off of gain is nearly f^{-2} when the phase is nearly -180 degrees. Judicious compensation can also improve the phase margin, making this a well-behaved servo. For more details, see the paper by Saulson (1983b). If we assume that the gain must be brought below 1 at frequencies above 100 Hz, then the additional seismic attenuation of the active isolation is that shown in Figure 4, and the net seismic transmission of the system is that shown in Figure 5.

To achieve even better low frequency isolation, we can use the outer feedback loop, where actuator F_{c1} is driven by x_3-x_1. The loop transfer function is found to be

$$\frac{(x_3-x_1)_{driven}}{(x_3-x_1)} = \frac{F_1}{d_1 M_3} G_{c1}(f) \frac{T_{21}(T_3+1)+T_{22}}{T_{11}T_{22}-T_{21}T_{12}}$$

where T_{12} and T_{22} contain feedback terms from actuator F_{c2}. That is to say that the functional form of the loop transfer function of the outer loop depends on the amount of gain in the inner feedback loop. This makes sense, since the operation of the inner loop does in fact alter the net transmission of force to M_3. A graph of the outer loop transfer function (with the value of inner loop gain used in Figures 4 and 5) is shown in Figure 6. It has a form similar to that of the inner loop transfer function, so the comments made above regarding stability and compensation apply here as well. A further comment is in

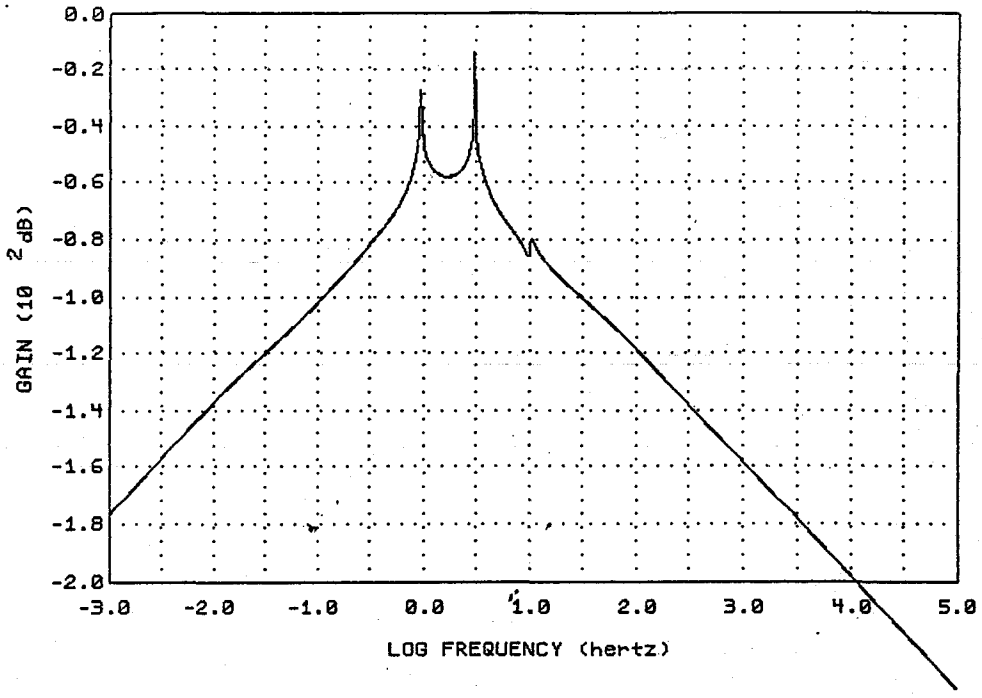

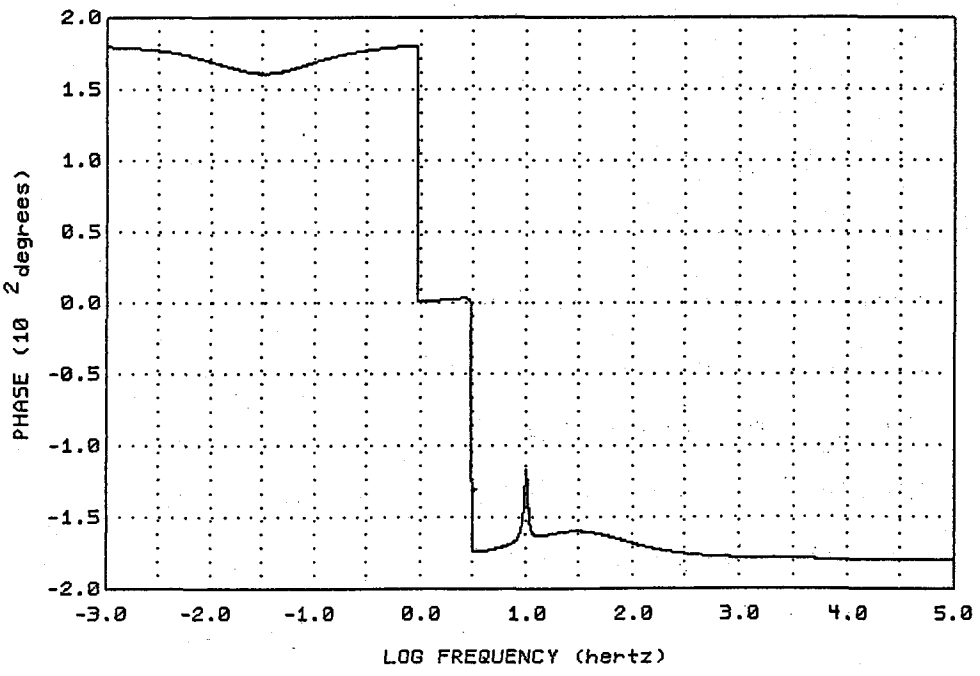

FIGURE 3: LOOP TRANSFER FUNCTION, INNER LOOP

this sort is described by Saulson (1983b). A slightly different method of inertial stabilization is described by Robertson et al. (1982).

The performance of a feedback system is governed by its loop transfer function. Let the feedback force F_{c2} be given by

$$F_{c2} = \frac{F_2}{d_2} G_{c2}(f)(x_3-x_2) \tag{5}$$

where F_2/d_2 is an overall gain and $G_{c2}(f)$ is a compensation filter. From the solution of the equations of motion of the system (3), we find

$$\frac{(x_3-x_2)_{driven}}{F_{c2}} = \frac{1}{M_3} \frac{T_3(T_{11}+T_{21})}{T_{11}T_{22}-T_{12}T_{21}} \tag{6}$$

Thus the loop transfer function is

$$\frac{(x_3-x_2)_{driven}}{(x_3-x_2)} = \frac{F_2}{d_2 M_3} G_{c2}(f) \frac{T_3(T_{11}+T_{21})}{T_{11}T_{22}-T_{12}T_{21}} \tag{7}$$

A Bode plot of this function for $G_{c2}(f)$ = constant is given in Figure 3. The transfer function contains, in series, the resonances ω_{03} and ω_{02}. The resonance ω_{01} appears only in vestigial form--it does not cause any net phase shift. A feedback system with such a transfer function is absolutely stable for all values of the gain, although with vanishingly small phase margin. In a real system, the available gain will be limited by additional phase lags due to mechanical resonances in the structural members of the device. Nevertheless, it is possible to achieve high gain in the frequency band near 1Hz if the structural

2.2 Passive Isolation

The passive isolation of this system at 30 Hz is computed to be 120 dB, or 6 orders of magnitude in amplitude. At a quiet site, this would be nearly sufficient to make the seismic noise contribution smaller than 10^{-17} cm/ Hz at 30 Hz. So the simple design is fairly successful, if one is willing to tolerate a very steep increase in the seismic noise contribution as one goes lower in frequency. Furthermore, it would not be impractical to move all of the resonances down in frequency by a factor of 2 or 3, say, and thereby improve the isolation. Still, even more isolation would yield improved antenna performance in the band below the highest resonance, since the Brownian motion noise (which is the dominant noise below 30 Hz if $M_3Q_3=10^6$ tons) has a much shallower spectrum than the ground noise. In addition, the high Q low frequency resonance is certain to be troublesome without some active damping.

2.3 Active Isolation

The active vibration isolation scheme which we plan to incorporate uses the test mass M_3 as an inertial reference element, that is as a sort of hook to an inertial frame of reference. Measurement of the relative displacement x_3-x_2 gives an error signal which drives a linear actuator F_{c2} mounted between M_1 and M_2. A feedback force is applied in order to null x_3-x_2, thus tending to compensate for the other forces which are being applied to M_3. We have also included another actuator F_{c1}, to be driven by the error signal x_3-x_1. A working prototype of a (single loop) inertial stabilization system of

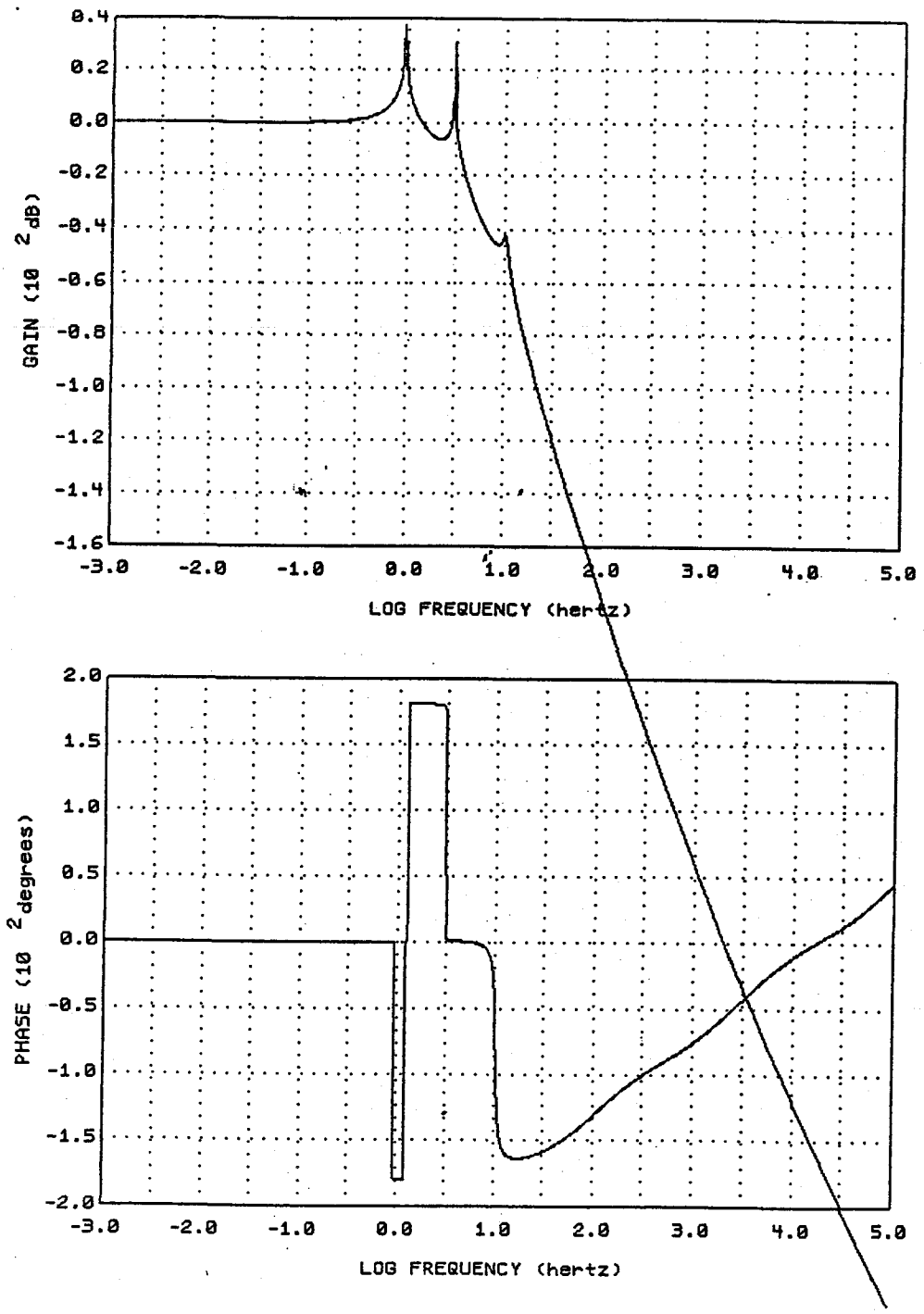

FIGURE 2: PASSIVE ISOLATION

To obtain concrete results we have to choose the values of 8 parameters: the three resonant frequencies, the 3 quality factors, and two mass ratios. (The overall mass scale does not affect the transfer functions.) We know that Q_3 must be around 10^6. Q_2 and Q_1 need not be as high, since there is isolation between them and M_3. We somewhat arbitrarily set $Q_2=10^3$ and $Q_1=10$. Inspection of elements T_{11} and T_{22} indicates that the cross-coupling terms have the form $\omega_{02}^2\mu_{21}$ (in T_{11}) and $\omega_{03}^2\mu_{32}$ (in T_{22}). If M_3 is as large as 1 ton, it would be a great advantage not to have to have $M_1>>M_2>>M_3$ to make the outer stages sufficiently stiff for proper operation of the servo loops. We obtained satisfactory results with $\mu_{21}=\mu_{32}=1$, but with progressively stiffer springs moving outward from M_3. We show the results for $\omega_{01}=2\pi*10$ Hz, $\omega_{02}=2\pi*3$ Hz, and $\omega_{03}=2\pi*1$ Hz.

Figure 2 shows the passive isolation of the system, obtained by solving for the transfer function x_3/x_g with the feedback terms T_{c1} and T_{c2} set equal to zero. This transfer function is given by equation (4), above. The form of the transfer function is easy to understand. There is no isolation at frequencies below the lowest resonance. Just above the highest resonant frequency, the isolation has a slope of -120 dB/decade characteristic of three resonant isolators in series. At higher frequencies the slope becomes shallower because of the finite Q of the resonances. In the band 1Hz<f<10Hz appear the peaks due to the three resonances, slightly shifted in frequency from their nominal values due to the coupling to the other resonances.

so that only the coordinates x_1 and x_2 remain. With these simplifications the equations (1) reduce to the 2 by 2 matrix equation

$$\begin{bmatrix} T_{11} & T_{12} \\ T_{21} & T_{22} \end{bmatrix} \begin{bmatrix} x_1 \\ x_2 \end{bmatrix} = \begin{bmatrix} T_g x_g \\ 0 \end{bmatrix} \tag{3}$$

where

$$T_{11} = \frac{1}{\mu_{21}\mu_{32}}\left(-\omega^2+\omega_{01}^2 + \frac{i\omega\omega_{01}}{Q_1} + \omega_{02}^2\mu_{21} + \frac{i\omega\omega_{02}}{Q_2} - \frac{T_{c1}}{M_1}\right),$$

$$T_{12} = \frac{1}{\mu_{32}}\left(-\omega_{02}^2 - \frac{i\omega\omega_{02}}{Q_2} + \frac{T_{c2}}{M_2}\right),$$

$$T_{21} = \frac{1}{\mu_{32}}\left(-\omega_{02}^2 - \frac{i\omega\omega_{02}}{Q_2}\right),$$

$$T_{22} = \frac{1}{\mu_{32}}\left(-\omega^2+\omega_{02}^2 + \frac{i\omega\omega_{02}}{Q_2} - \frac{T_{c2}}{M_2} - \omega_{03}^2\mu_{32}T_3 - \frac{i\omega\omega_{03}}{Q_3}\mu_{32}T_3\right)$$

$$T_g = \frac{1}{\mu_{21}\mu_{32}}\left(\omega_{01}^2 + \frac{i\omega\omega_{01}}{Q_1}\right).$$

In these equations T_{c1} represents the transfer function F_{c1}/x_1 and similarly $T_{c2} = F_{c2}/x_2$. Solving the system of equations gives the following transfer functions:

$$\frac{x_1}{x_g} = \frac{T_g T_{22}}{T_{11}T_{22}-T_{12}T_{21}}$$

$$\frac{x_2}{x_g} = \frac{-T_g T_{21}}{T_{11}T_{22}-T_{12}T_{21}} \tag{4}$$

$$\frac{x_3}{x_g} = \frac{-T_g T_{21}(T_3+1)}{T_{11}T_{22}-T_{12}T_{21}}.$$

coefficient of the suspension of the test mass, most likely a pendulum. M_3 is suspended from a second mass, M_2, which is in turn suspended from M_1. The whole system is, finally, suspended from a frame fixed to the ground. In addition, two linear actuators are installed, one between the ground and M_1, the second between M_1 and M_2.

The equations of motion for the system are:

$$M_1\ddot{x}_1 = -k_1(x_1-x_g) - f_1(\dot{x}_1-\dot{x}_g) - k_2(x_1-x_2) - f_2(\dot{x}_1-\dot{x}_2) + F_{c1} - F_{c2}$$

$$M_2\ddot{x}_2 = -k_2(x_2-x_1) - f_2(\dot{x}_2-\dot{x}_1) - k_3(x_2-x_3) - f_3(\dot{x}_2-\dot{x}_3) + F_{c2} \qquad (1)$$

$$M_3\ddot{x}_3 = -k_3(x_3-x_2) - f_3(\dot{x}_3-\dot{x}_2)$$

These equations are simplified as follows. First, for brevity of notation, define $\mu_{21} = M_2/M_1$ and $\mu_{32}=M_3/M_2$. Also, define $\omega_{01}^2=k_1/M_1$, $Q_1=M_1\omega_{01}/f_1$, and the analogous quantities for suspensions 2 and 3. We consider only the steady-state solutions, so we can make the ansatz $x = x(\omega)e^{i\omega t}$. Then $\dot{x} = i\omega x$, $\ddot{x} = -\omega^2 x$, and the system of equations becomes a set of simultaneous linear equations in the coordinates of the masses. Further, if we are only interested in the response of the system to forces from the motion of the ground (ignoring Nyquist force on M_3, for example), then we can express $x_3 - x_2$ as some transfer function times x_2:

$$x_3 - x_2 = \frac{\omega^2}{\omega_0^2-\omega^2+\frac{i\omega\omega_{03}}{Q_3}}\, x_2 \equiv T_3 x_2 \qquad (2)$$

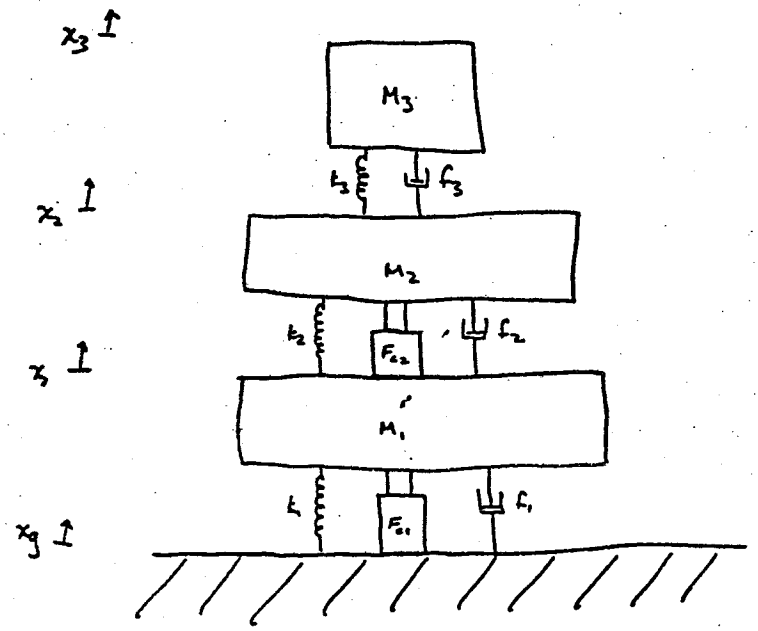

Figure 1: Schematic Diagram of Vibration Isolation System

In our proposed design, we have elected to avoid the headaches associated with cooling the test masses, but are left instead with the headache of large masses. A second important feature of this design is to make a cascade of several stages of isolation, rather than lowering the resonant frequency of a single stage. Even at the quietest site, an ideal suspension would have to have a period of 20 sec (for a pendulum, this would mean a length of 90 meters!) This simple calculation neglects internal resonances in the suspension's structural members, which make it difficult to achieve the theoretical isolation over more than two decades in frequency. A third aspect of the design is to make use of active vibration isolation in addition to passive isolation. This is especially valuable for frequencies near and below 30 Hz, less so above 30 Hz. Active isolation is included because a fairly elaborate servo control system will probably be required for DC alignment and low-noise damping of the high Q resonance, so using the sensors and actuators for broad band vibration reduction comes almost "for free."

2.0 THEORETICAL ANALYSIS

2.1 Equations of Motion

A schematic diagram of the sort of system we are considering is given in Figure 1. At this level of analysis we treat all the motions as one-dimensional, parallel to the x-axis. M_3 is the test mass itself, while k_3 and f_3 represent the spring constant and damping

the earth due to seismic motion has been evaluated by Saulson (1983a). The spectrum of test mass motion calculated there is $x = B*(1Hz/f)^4$, where B runs from 10^{-15} $cm/Hz^{1/2}$ at a quiet site to $3*10^{-13}$ $cm/Hz^{1/2}$ at a noisy site. Thus this noise term is larger than 10^{-17} $cm/Hz^{1/2}$ at frequencies below 3 to 13 Hz. The gravitational coupling of seismic noise to the test masses is, then, weaker than direct mechanical coupling. Yet, unlike mechanical coupling, the gravitational force can not be shielded, so this lacter term represents a true noise floor. (In principle, a regression scheme could remove some of this noise from the output of the antenna by recognizing the signature of a local tidal force on the antenna. However, the gravitational forces on the test masses are only strongly correlated at frequencies where the acoustic wavelength of the disturbance is large compared to the separation between the test masses. In the proposed system of 5 km baseline, this is only true at extremely low frequencies, especially if there is a non-negligible contribution due to atmospheric infrasound.)

This study has shown that the most serious mechanical noise source for the antenna is seismic vibration, followed in importance by Brownian motion of the test masses. In the rest of this section we will describe the conceptual design of a feasible test mass suspension which should reduce mechanical noise to below 10^{-17} $cm/Hz^{\frac{1}{2}}$ at all frequencies above 70 Hz, with appreciable reductions as well at lower frequencies. Few aspects of the design are dictated explicitly by the specifications, but we have tried to make reasonable choices.

1.0 Introduction

Two different mechanical noise sources will be considered here: seismic noise, and gravity gradient noise. By seismic noise is meant mechanical coupling of the test masses, through their supporting structures, to the low level vibration of the earth. Gravity gradient noise is motion due to the fluctuating gravitational forces on the test masses caused by acoustic density fluctuations in the material media (earth and atmosphere) surrounding the antenna, or due to the motion of massive bodies in the vicinity of the antenna.

A recent compilation of earth motion spectra is given by Fix (1972). Between 0.1 Hz and 10 Hz, the spectrum is approximately proportional to $(f/1\ \text{Hz})^{-2}$, where the constant of proportionality varies from 10^{-5} to $3*10^{-8}$ $\text{cm/Hz}^{\frac{1}{2}}$. If the spectra continued to fall with the same slope, even at the quietest places the earth motion exceeds the expected shot noise floor at all frequencies below 20 kHz. Thus the test masses must not have a rigid mechanical connection to the earth, but must instead be mechanically isolated. A simple form of isolation is a pendulum suspension of high Q, whose transmission is equal to $((f_0/f)^2$, where f_0 is the resonant frequency. A 1 Hz suspension would reduce the seismic noise to below 10^{-17} $\text{cm/Hz}^{\frac{1}{2}}$ above 250 Hz at the quietest locations, above 1 kHz at a noisy site.

The fluctuating gravitational force from density variations in

lowest frequency flexural mode for the sample dimensions given above is 22 KHz and therefore not important.

In summary, the most important thermal noise term that figures in the gravity antenna performance is the suspension noise at low frequencies and this is not a severe constraint in a first generation large baseline antenna of sufficient length. The improved performance in a second generation system may require modification in suspension and mass design.

t is the largest dimension, 2a in the above example, and c_{sh} is the transverse or shear sound velocity in the materials. σ is the Poisson ratio. The moving mass is the total mass. For sake of comparison using the same sample parameters as above; adding that the Poisson ratio for quartz, σ, is 0.17, one finds from Eq. 16, the lowest shear mode at 1.7KHz. Assuming a Q in shear of 10^4, the average amplitude density of thermal motions of the surface below 1.7 KHz, due to this mode alone is approximately, $x(f) = 1.8 \times 10^{-18} cm/Hz^{\frac{1}{2}}$. The strain limit imposed by this type of oscillation depends critically on the optical design, as already mentioned.

The final class of motions considered, flexural vibrations, involve both shear and compression. A good example of such a mode is the oscillation, perpendicular to the surface, of a thin mirror clamped at its edges. These are troublesome in current prototype interferometer designs, and their suppression indicates monolithic construction. The normal mode frequencies have been calculated in the theory of the oscillation of plates. For a circular plate with a clamped outer edge the normal mode frequencies are given by

$$f_{nm} = \frac{\pi t}{a^2} \left(\frac{Y}{3\rho(1-\sigma^2)}\right)^{\frac{1}{2}} \beta^2_{nm}$$

Here t is the plate thickness and a the radius. The indices n and m indicate the number of radial and azimuthal nodes of the oscillation. β is a constant dependent on the mode, for the lowest order mode having one radial node and no azimuthal dependence, $B_{10} = 1.015$. The next mode n = 1, m = 1, has a frequency 2.09 times higher. The

the material. The moving mass in these modes is 1/2m. The thermal noise displacement density is calculated by using Eq. 6. Summing over the modes gives

$$x^2(f) = \frac{8k\,Ta^2\rho^{\frac{1}{2}}}{\pi^3 Q A\, Y^{3/2}} \sum_{\substack{n=1 \\ \text{odd}}}^{\infty} \frac{1}{n^3} \qquad f < f_1 \qquad (15)$$

A is the cross section of the mass, Q is the value appropriate to the dissipation of the material in compression.

As an example consider a quartz (fused silica) mass of 10^6 grams having a cylindrical shape with length equal to the radius of 50cm. The Q for the compressional modes, if not compromised by the support, is 10^5 at room temperature. The lowest longitudinal mode frequency for this mass is 6KHz. The amplitude spectrum at frequencies less than 6KHz, given by Eq. 15, is $x(f) \sim 3\times10^{-19}$ cm/Hz$^{\frac{1}{2}}$. The limiting strain sensitivity in a 5km baseline from this noise source alone would be $h(f) \sim 6\times10^{-25}$ strain/Hz$^{\frac{1}{2}}$.

The modes involving pure shear (no internal volume changes) have both lower frequencies and lower Q. However in a symmetric and isotropic optical design, the fringe sensitivity to these modes can be reduced to second order in their amplitudes.

In the lowest frequency pure shear mode, the neutral plane of the oscillation bisects the largest dimension of the mass. The frequency of the mode is

$$f_{sh} = \frac{2}{\pi t}\, c_{sh} = \frac{\sqrt{2}}{\pi t} \left(\frac{Y}{2(1+\sigma)\,\rho}\right)^{\frac{1}{2}} \qquad (16)$$

of the others discussed so far.

b) Thermal noise at high frequencies.

The thermal excitation of the normal modes of the masses, mirrors, mirror mounts and optical components in the phase sensitive portions of the interferometer contribute high frequency noise. Thermal noise from this source is now being observed in all the prototype interferometric antennas and is not unexpected given their unoptimized mechanical designs.

The reduction of this high frequency thermal noise requires that the lowest oscillatory mode frequencies lie above the gravity wave frequency, that the modes have a high Q and that there be as few modes as possible. These requirements argue for simplicity of the design and monolithic construction of the masses and their associated optical components. The critical modes are those at the lowest frequency, as indicated by Eq. 6.

In a good design the low frequency longitudinal modes having components of motion along the optic axis, should dominate. Assuming that the mirrors are integral with the masses (monolithic construction), the low frequencies of the compressional modes are determined by the longitudinal sound speed and the linear dimension of the mass along the optic axis. The oscillation frequencies of these modes are given by

$$f_n = \frac{n}{2}\frac{c_L}{a} = \frac{m}{2a}\left(\frac{Y}{\rho}\right)^{\frac{1}{2}} \qquad (14)$$

n odd

where c_L is the longitudinal sound speed, a the thickness of the mass along the optic axis, Y the Young's modulus and ρ the density of

Here ρ_m is the density of the pendulum mass, a the length of a side of the mass if cubical, m_a the average mass of the residual gas atoms and n the number of atoms per cubic centimeter. ω_o is the pendulum resonance frequency. Eq. 11 applies in the limit where the mean free path of atoms in the residual gas is larger than a. Using the sample parameters T = 300°K, m = 10^6gm, a = 50 cm, τ_o = 2 sec pendulum period, a residual gas at 10^{-6} mm Hg composed primarily of N_2 yields a Q limited by gas damping of 5×10^9.

Eddy current damping in the unshielded earth's magnetic field can be a thermal noise source. At low frequencies where the skin depth is comparable and larger than the linear dimensions of the pendulum mass, the thermally driven electrical currents in a conducting mass produce fluctuating magnetic forces on the pendulum. This is another example of a "colored" Nyquist force. The Q due to this mechanism is independent of the volume and given by

$$Q_{eddy} = \frac{\rho a \omega_o c^2}{\sigma B^2} \qquad (13)$$

where B is the magnetic field at the mass, σ is the conductivity of the mass in cgs units and c the velocity of light. Using the same parameters as above, $\sigma \sim 5 \times 10^{17}$ sec^{-1}, typical of good conductors, and a field of 1/2 Gauss yields a $Q \sim 8 \times 10^4$. Modest magnetic shielding and/or the use of non-conducting masses, coated by a thin layer of conductor to avoid electric changing, reduces this damping mechanism, below the level

Q is 3×10^6. The diameter of each fiber is close to 2mm. Sapphire might be a better material but less is known about its internal losses in flexure.

The spectral density of thermal displacement noise at frequencies above the suspension resonance is given by Eq. 5. Using the above sample parameters it amounts to

$$x(f) \sim \frac{1 \times 10^{-14}}{f^2} \text{ cm/Hz}^{\frac{1}{2}}$$

at 300°K. The strain amplitude noise is

$$h(f) = \frac{2x(f)}{\ell} = \frac{2}{\sqrt{2}\pi^{3/2}} \left(\frac{kT}{mQ\tau_o}\right)^{\frac{1}{2}} \frac{1}{\ell f^2} \qquad (11)$$

where ℓ is the antenna baseline. The 2 comes from the fact that the thermal motions of all the antenna masses must be included. For a 5km long antenna, the low frequency thermal noise limit due to this cause varies as

$$h(f) = 4.2 \times 10^{-20}/f^2 \quad \text{strain/Hz}^{\frac{1}{2}} .$$

In second generation improvements on a large baseline gravitational antenna, electromagnetic field support suspensions or cryogenic operations could be contemplated to reduce this noise term but at present the added complexity is not warranted.

Damping due to Doppler friction by the residual gas is reduced by operating the pendulum in high vacuum. The Q due to gas damping is given by

$$Q_{gas} = \frac{\rho_m a w_o}{2\sqrt{3}(m_a kT)^{\frac{1}{2}} n} \qquad (12)$$

where Q_{mat} is the internal Q of the suspension material in flexure, generally 1/10 of the Q in pure compression, E_{grav} the energy stored as gravitational potential energy and $E_{elastic}$ the energy stored in flexure which is usually much smaller than E_{grav}.

Clearly to achieve a high Q one would like to make $E_{elastic}$ as small as possible which implies thin support members. However, the Q_{mat} is a strong inverse function of the internal stresses of the material beyond a critical stress, σ_{max}, so that an optimization must be performed. The magnitude of the suspended mass, an important parameter in the optimization, is however not only a function of this noise term and must be chosen by an overall minimization of the antenna noise budget.

If the mass is supported by a single cylindrical fiber, the overall pendulum Q is given by

$$Q = Q_{mat}\,(\sigma_{max})\,\frac{4\sqrt{\pi}L\sigma_{max}}{(Ymg)^{\frac{1}{2}}} = Q_{mat}(\sigma_{max})\,\frac{4L}{a^2\sqrt{\pi}}\,\left(\frac{mg}{Y}\right)^{\frac{1}{2}} \qquad (10)$$

where L is the length of the pendulum, m the supported mass, a the fiber radius and Y is Young's modulus for the material. If N fibers are used, each stressed to σ_{max}, the overall Q improves as $N^{\frac{1}{2}}$. For example, the ratio of the Q for a rectangular ribbon of thickness 2a and width w to that of a cylindrical fiber of radius a is $\left(\frac{3w}{8\pi a}\right)^{\frac{1}{2}}$.

Typical sample parameters for a 4 fiber quartz suspension at 300°K are $L = 10^2$ cm (2 second pendulum), $m = 10^6$ grams, $Y = 7\times10^{11}$ dynes/cm^2, $\sigma_{max} = 10^{-2}\,Y$ and $Q_{mat}(\sigma_{max}) = 10^4$ in flexure. The overall pendulum

where Q_{servo} is the actively damped Q. Typically, $Q_{servo}/Q_o \ll 1$ and one can loosely say the oscillator has been refrigerated to an effective temperature

$$T_{eff} = T \frac{Q_{servo}}{Q_o} \qquad (8)$$

which is true for the integral but unfortunately not in calculating the thermal noise at frequencies far from resonance.

With the above provisos in mind, we make an analysis of the magnitude of the thermal noise in the interferometric antenna.

a) Thermal noise at low frequencies.

The fundamental resonance frequency of the suspension is chosen to be smaller than the lowest gravitational wave frequency, so that limit of Equation 5 applies. Three sources of thermal noise important at low frequencies are considered: dissipation in the flexure of the pendulum support, residual gas damping and eddy current damping by unshielded magnetic fields.

In the presently conceived design, the thermal noise arising from the dissipation in the flexure of the pendulum suspension makes the largest contribution at low frequencies. Although the major part of the restoring force in a pendulum is gravitational and non-dissipative, a small portion is provided by the flexure of the suspension. Some of the elastic energy stored in the flexure is dissipated. The overall Q of the pendulum is given by

$$Q = Q_{mat} \left(\frac{E_{grav} + E_{elastic}}{E_{elastic}}\right) \sim Q_{mat} \frac{E_{grav}}{E_{elastic}} \qquad (9)$$

to compliant and lossier structures to achieve additional seismic isolation. Motions of the pendulum feed power to the support structure where it is dissipated. The Q of the pendulum is lowered by this, however the Nyquist force on the pendulum bob is not given by Eq. 2 but rather by Eq. 2 multiplied by the frequency dependent isolation transfer function of the pendulum. A proper calculation of the normal mode excitations of the coupled system with each normal mode driven by its own Nyquist force gives this result. The thermal motion of the pendulum is a superposition of the normal mode excitations.

Servo feedback damping is employed to reduce the rms amplitude and ringing time of the pendulum motion. In these schemes a signal proportional to the velocity of the pendulum is derived from a transducer (an interferometer, capacitance or inductance bridge). After filtering the signal is fed to a controller, which depending on the design exerts electrostatic or magnetic forces on the pendulum. Leaving aside for the moment, the additional noise that is generated by the transducer, which is small in practice but nevertheless imposes a fundamental limit in the technique, the damping of the pendulum has been altered without an increase in the Nyquist noise force. The power spectral density of the displacement noise is still given by equations 5 and 6 where the appropriate Q is the value with the servo system turned off. The rms displacement on the other hand is smaller and given by

$$x_{rms}^2 = \frac{2kT}{m\omega_o^2} \frac{Q_{servo}}{Q_o} \qquad (7)$$

$$x^2(f)_{\omega<<\omega_o} = \frac{4kT}{m\mathcal{Q}\omega_o^3} \qquad (6)$$

The net displacement spectral noise density is the incoherent sum of the contributions from all independent normal modes.

The thermal noise produced by gas damping (Doppler friction) is the classic example of a damping mechanism which is described by the model. The coherent part of the damping is due to the average momentum imparted to the gas while the noisy part comes from the fluctuations in the number of atoms hitting the oscillator. In this case the impulses of the atomic collisions imparted to the oscillator obey a Poisson distribution and therefore have a frequency independent power spectrum at frequencies lower than the average rate of atomic collisions with the oscillator. That other damping mechanisms, such as the various mechanisms of internal dissipation in solids, can really be modelled by a frequency independent stochastic force is at this time only a conjecture. The fact one is sure of is that the frequency integral of the stochastic force does give the equipartition value. The bar gravity antennas have demonstrated this beautifully.

There are situations where a blithe application of the model would give the wrong results. Two cases which occur in present interferometric antenna designs are good examples: the case of coupled oscillators and schemes employing active servo feedback damping. The vibration isolation systems at the end points of an interferometric gravity antenna are high Q pendulum suspensions which are attached

$h_{uncor}(f) = 6 \times 10^{-25}$ strain/$Hz^{\frac{1}{2}}$ $\quad$ $h_{cor}(f) = 1.6 \times 10^{-24}$ strain/$Hz^{\frac{1}{2}}$

Some of the other parameters interesting to note in this example are

$t_{transit} = 1.7 \times 10^{-5}$ sec

$t_{residence} \simeq 1 \times 10^{-4}$ sec

$\langle\phi\rangle = 1.1$ radians

$\langle\phi\rangle$ is the average phase shift of the light due to the gas in traversing an interferometer arm for t_{stor}.

Equations 13 and 15 are the results of this section. Instead of, as in other sections of this report, evaluating the requirements of the system to meet a specified h(f), it is more useful here to look at the break points in vacuum technology. Broadly speaking low vacuum technology using roughing pumps and elastometer seals allows system pressures of at best 10^{-3}mm Hg. This pressure is too high for antenna lengths considered economically feasible. The next level of vacuum technology employing additional pumps, diffusion, ion, or sorption pumps in addition to roughing pumps has a break at pressures of about 10^{-6} mm Hg. Vacuum system with pressures less than 10^{-6}mm Hg; the ultra high vacuum region, require further refinements such as metal to metal seals and the ability to be heated for outgassing while evacuated. As indicated in the Arthur D. Little study, we have chosen to price a vacuum system which is able to maintain 10^{-6}mm Hg in the light paths but which can be improved at some additional expense for operation at lower pressures if the need arises in a second generation development of the antenna system.

With a pressure of 10^{-6}mm Hg, consisting of N_2 at room temperature and a light wave length λ of 5145A°, the strain amplitude spectral noise due to vacuum fluctuations is given for the two cases as

$$h(f)_{uncor} = \frac{5.2\times10^{-25}}{t_s^{\frac{1}{2}}\,\ell^{\frac{1}{4}}} \qquad h(f)_{cor} = \frac{3.5\times10^{-23}}{t_s^{\frac{1}{2}}\,\ell^{\frac{1}{2}}}$$

in a 5km antenna with a 10^{-3} sec storage time the noises are

$$t_s = b\ell/c \qquad (12)$$

and the beam diameter of Equation 1. The equivalent strain spectral density is then

$$h^2_{uncor}(f) = \frac{2\alpha^2\rho}{t_s c v_t (\pi\lambda\ell)^{\frac{1}{2}}} \qquad f < 1/t_r \qquad (13)$$

The Spatially Correlated Case

We consider next an interferometer in which all the light is reflected back and forth through the same gas column. The light storage time t_s is greater than the residence time t_r of a thermally driven atom in the beam, and the residence time in turn is greater than the light transit time t_t (=ℓ/c) along the interferometer arm.

As before, the phase fluctuation introduced during one transit of the interferometer arm, $\Delta\phi_t$, is given by Equation 7. However, now, the phase fluctuations for a time equal to the atom residence time are correlated. The beam makes t_r/t_t transits through the same gas column fluctuation and on the average the beam samples t_s/t_r independent fluctuations in the arm during a storage time. The rms phase fluctuation becomes

$$\Delta\phi^2 = \left(\frac{t_r}{t_t}\right)^2 \Delta\phi_t^2 \quad \frac{t_s}{t_r} = \frac{t_r \; t_s}{t_t^2} \Delta\phi_t^2 \qquad (14)$$

Following the same steps as before the strain spectral density is given by

$$h^2_{cor}(f) = \frac{4\alpha^2\rho}{\pi V_t^2 \; t_s \ell} \qquad (15)$$

$$\Delta\phi^2 = \left[\frac{2\pi}{\lambda}\alpha\right]^2 \Delta\sigma^2 = \left[\frac{2\ \pi\ \alpha}{\lambda}\right]^2 \left[\frac{\rho\ \ell\ b}{\pi\ D^2/4}\right] \qquad (7)$$

A phase change causes an inferred change of the separation between the end masses according to

$$\Delta x = \left[\frac{\lambda}{2\pi b}\right] \Delta\phi \qquad (8)$$

so the fluctuation in the inferred length corresponding to the phase fluctuations, and hence to the column density fluctuations, is

$$\Delta x^2 = \left[\frac{\lambda}{2\pi b}\right]^2 \Delta\phi^2 = \frac{4\alpha^2\rho\ell}{b\pi D^2} \qquad (9)$$

To convert this to a power spectral density, we note that the relevant time scale of the fluctuations is the time that an atom resides in the light beam. This residence time t_r is approximately

$$t_r = \frac{D}{V_t} \qquad (10)$$

where V_t is the thermal velocity of the atom.

So, for frequencies less than $(1/t_r)$, the power spectral density of the inferred length fluctuations is

$$x^2(f) = t_r\ \Delta x^2 = \frac{4\alpha^2\rho\ell}{b\pi D V_t} \qquad (11)$$

A more useful formulation is to reexpress this noise in terms of the equivalent strain spectral density using the arm storage time, t_s, defined by

λ is the light wavelength. The beam diameter at the mirrors is $\sqrt{2}D$. For example, in a 5km arm antenna using 5145A laser light, the beam diameter at the mirrors is 5.7 cm.

Now, if the light beam is reflected to make b transits of the interferometer arm, the equilibrium value for the number of atoms<N> in the total gas column is

$$\langle N \rangle = \rho \, \ell \, b \quad (\pi D^2/4) \qquad (2)$$

where ρ is the average number of atoms per unit volume. The rms fluctuations about the equilibrium value, is

$$\Delta N^2 = \langle N \rangle \qquad (3)$$

The average column density of atoms is

$$\sigma = \frac{\langle N \rangle}{(\pi D^2/4)} \qquad (4)$$

While the fluctuation of column density is given by

$$\Delta\sigma^2 = \frac{\Delta N^2}{(\pi D^2/4)^2} = \frac{\rho \, \ell \, b}{(\pi D^2/4)} \qquad (5)$$

The index of refraction n of the gas column is

$$n = 1 + \alpha\rho \qquad (6)$$

where α is the effective molecular polarizability at λ . α for nitrogen $= 9.7 \times 10^{-24} \text{cm}^3/\text{atom}$. The rms phase fluctuation of the laser light that is caused by column density fluctuations is then given by

quirement is crucial because the minimization of the phase fluctuation noise is the prime justification for the vacuum system that is one of the most expensive components of the interferometric gravity wave antenna.

We have to consider two cases; interferometers where the multi-pass beams are spatially separated, as in the present versions of delay line systems, and those in which the beams coincide as in a Fabry Perot or delay line with spatially coincident but frequency tagged beams. The cases differ in the degree of correl ation of the phase noise due to column density fluctuations. As will be shown, the vacuum required by the two cases depends identically on several parameters but depends differently on the length of the interferometer arms.

The case of spatially separated beams.

We consider first a delay line interferometer in which the light beams that are reflected back and forth between the mirrors do not overlap anywhere.

To show that this idealization is physically realistic, we evaluate first the diameter of a light beam and the diameter of the spot size on the reflecting surfaces. Assume a symmetric cavity with spherical mirrors of radius of curvature, R, close to but not exactly equal to the interferometer arm length ℓ. The minimum beam diameter for a Gaussian beam, defined as 1/e intensity point, occurs at the cavity midpoint and is given by

$$D = \left(\frac{2\lambda\ell}{\pi}\right)^{\frac{1}{2}} \simeq 2\,\omega_0 \qquad (1)$$

Light propagation fluctuations due to pressure fluctuations

Residual gas molecules in the evacuated arms of the interferometer cause phase fluctuations of the laser light as it propagates back and forth between the mirrors. The magnitude of the resultant phase fluctuation noise is a function of the path length traversed by the light so this noise source is one of the few that tend to increase as the length of the interferometer arms is increased.

Although, in principle, there could be intermittent large fluctuations in gas density due to outgassing bursts, this does not appear to be an important problem in a clean vacuum system. Very little information on this subject is available in the literature. An experiment is now in progress to set a limit on this hypothetical phenomena. However, current informed opinion of those familiar with the large vacuum systems used in accelerator storage rings indicates that outgassing bursts, if they occur at all, certainly are extremely rare. (Ref: H.J. Halama, Brookhaven, private communication)

The phase fluctuations with which we are concerned are attributable to random fluctuations in the index of refraction of the propagating medium that arise because the number of molecules or atoms in a column of gas fluctuates randomly about some average or equilibrium value. This process is thermally driven and can be treated as having a stationary distribution.

The purpose of the calculations in this section, therefore, is to estimate the quality of the vacuum that is required to ensure that the magnitude of the noise which results from column density fluctuations is smaller than the magnitude of the other noises in the system. This re-

gives

$$h(f) \sim \frac{6 \times 10^{-19}}{f^{5/2}} \alpha \beta$$

at a pressure of 1×10^{-6} mm Hg.

The noise due to the pressure fluctuations of gas atoms interacting with surfaces at different but constant temperatures is handled in the same manner as the thermal noise discussed in a later section of this report. The thermal noise makes more stringent requirements on the quality of the vacuum than the radiometer effect.

The change in force on the surface due to a change in temperature is

$$\Delta F = \frac{n\, k_B\, \Delta T\, A}{4} \tag{21}$$

where n is the number density of gas atoms k_B, Boltzmann's constant, A, the surface area and ΔT the temperature change. Eq. 21 assumes complete accommodation of the emitted atoms to the surface temperature. Combining Eqs. 20 and 21 and reexpressing them in terms of spectral densities, yields a force amplitude density

$$F(f) = \frac{n\, k_B\, P\,(f)\, \beta}{4\, (\pi\, c\, k_t\, \rho)^{1/2}\, f^{1/2}} \tag{22}$$

where P (f) is the amplitude spectral density of the total power fluctuations and β is the fraction of the power absorbed by the surface. Using Eq. 15 as a model for the extrinsic power fluctuations and analyzing the motion of a free mass driven by the force density of Eq. 22 yields a strain spectral density of

$$h(f) \sim \frac{\alpha\, n\, \beta\, k_B\, P}{8\pi^2\, \ell\, m\, (\pi\, c\, k_t\, \rho)^{1/2}\, f^{5/2} \Delta f^{1/2}} \tag{23}$$

Here it is assumed that the pressure is most likely to be the unbalanced quantity. If the pressure is low enough this noise is of little consequence. Using the same sample parameters as above and in addition that $(\pi\, c\, k_t\, \rho)^{1/2} \sim 4 \times 10^6$ (cgs units) for fused quartz

Another noise source that is related to the light power is the so called radiometer effect because it is responsible for the rotation of the poorly evacuated radiometers seen in jeweler's windows. In a structure with temperature gradients, gas atoms that accommodate and then are reemitted by the hotter surfaces impart larger recoil momenta to the surface than those reemitted by colder parts. In an interferometric gravitational antenna the surfaces illuminated by the light will be hotter than the other parts and there will be net forces and torques on the masses due to the radiometer effect. The fluctuations in these forces can arise from laser power fluctuations coupled to a system unbalance or pressure fluctuations in the vicinity of the masses.

The fluctuations of the surface temperature of a mirror when illuminated by a light source with varying intensity is given by

$$T(f) = \frac{I_{abs}(f)}{(\pi\, c\, k_t\, \rho)^{1/2}\, f^{1/2}} \qquad (20)$$

ρ is the density of the material, k_t the thermal conductivity, c the specific heat and $I_{abs}(f)$ is the fluctuating intensity that is absorbed by the surface. Eq. 20 assumes that the temperature of the entire structure remains constant and that only the surface temperature fluctuates, and furthermore that radiative transport is less important than thermal diffusion.

In a 5 km antenna having $t_{st} = 1/f$, a mass 10^6 gm, $P_o = 100$ W, and $\Delta f = 1$ KHz

$$h(f) \sim \frac{10^{-11}\,\alpha\gamma}{f^3}$$

At best one might expect to balance the system to 1% so that it will become important, especially at low gravitational wave frequencies, to reduce α by actively controlling the light source amplitude fluctuations. This will not be a consideration in first generation antennas of sufficient length but cannot be neglected in future improvements.

There are also intrinsic and fundamental pressure fluctuations of the light pressure which are not correlated at the masses due to quantum fluctuations in the radiation field itself. These are discussed more extensively in Appendix A on the "naive" quantum limit of an antenna. Here for sake of completeness and comparison, we quote the strain limits imposed by them, which are

$$h(f) = \frac{\sqrt{8}\, t_{st}}{(2\pi)^2\, \ell^2\, m f^2} \left(\frac{h P_o c}{\lambda}\right)^{1/2} = \frac{\sqrt{8}}{(2\pi)^2\, \ell^2\, m f^3} \left(\frac{h P_o c}{\lambda}\right)^{1/2} \qquad (19)$$

$$t_{st} = \frac{1}{f}$$

Evaluating Eq. (19) for the same parameters as above

$$h(f) \sim \frac{1.8 \times 10^{-20}}{f^3}$$

To estimate the importance of this effect assume that the input power fluctuations are proportional to the power

$$\Delta P_{rms} = \alpha P . \tag{14}$$

and for ease of calculation that the power fluctuation spectrum is uniform over a band width Δf. The power spectral density of power fluctuations is

$$P^2(f) = \frac{\alpha^2 P_o^2}{\Delta f} \tag{15}$$

which by the radiation pressure produces a fluctuating force described by the force power spectral density

$$F^2(f) = \frac{4b^2 P^2(f)}{c^2} \tag{16}$$

The antenna masses respond as "free" above the suspension resonances. A single mass will therefore move with a displacement power spectral density of

$$x^2(f) = \frac{b^2 \alpha^2 P_o^2}{m^2 \omega^4 c^2 \Delta f} \tag{17}$$

where m is the mass and it is assumed that the input power has been split close to equally. Let there be a power or mass unbalance parameterized by γ which is zero if the system is balanced and one if totally unbalanced. The strain sensitivity of the system to this effect is given by

$$h(f) \sim \frac{\gamma \alpha t_{st} P_o}{2\pi^2 m f^2 \Delta f^{1/2} \ell^2} = \frac{\gamma \alpha P_o}{2\pi^2 m f^3 \Delta f^{1/2} \ell^2} \tag{18}$$

$$t_{st} = 1/f$$

where it is assumed that the gravitational wave is normally incident on the antenna in the most favorable polarization. Refer to the section on the antenna response function, for the more general case.

In an antenna illuminated by 100 watts and 1 msec storage time

$$h(f)_{gw} > \frac{1.7 \times 10^{-23}}{\text{sinc}\ (\omega\, t_{st/2})} \quad \text{strain/Hz}^{1/2} \qquad (13)$$

The effect of amplitude fluctuations of the light other than the intrinsic Poisson photodetection noise can be suppressed by proper design. The fringe interrogation schemes described in the section on the prototypes are specifically designed to put the fringe motion signal at a carrier frequency well above the frequencies where lasers have extrinsic amplitude noise. Furthermore, the null servo system designs which hold the fringe at a symmetry point, with sufficient loop gain will further suppress extrinsic amplitude noise. If need be the amplitude noise is also measurable directly in the fringe output independently of the fringe phase. In other words, there are many lines of defense and this noise source is not considered a problem.

Extrinsic amplitude noise of the light source with frequency components in the gravitational wave detection band must however be considered but in a different context. If there is an unbalance in the power circulating in the two interferometer arms or if the masses are not matched, the relative displacements of the arms will depend on the extrinsic amplitude fluctuations through radiation pressure fluctuations.

In a Fabry-Perot configuration as the multipass element in a Michelson interferometer, the output power fluctuations due to frequency instabilities are given by

$$P^2(f) = [P_o \left(\frac{\Delta F}{F} + \frac{\Delta \ell}{\ell}\right) 4\pi t_{st}]^2 \upsilon^2(f) \qquad (10)$$

ΔF and $\Delta \ell$ are the differences in finesse and length of the two cavities and $\upsilon^2(f)$ is the power spectral density of the light source frequency fluctuations in units of Hz^2/Hz. Equations 8 and 10 are only valid for the Fabry-Perot if $\delta t_{st} < 1$ which sets an independent condition on δ.

From equations 5, 6 and 10 the condition that Poisson noise dominates sets the following condition on the cavity matching and the power spectral density of the frequency fluctuations in a high contrast Fabry-Perot-Michelson system

$$\left(\frac{\Delta F}{F} + \frac{\Delta \ell}{\ell}\right) \upsilon(f) < \frac{1}{4\pi t_{st}} \left(\frac{hc}{2\eta\lambda P_o}\right)^{1/2} \qquad (11)$$

For an instrument with 95% contrast, $P_o = 100$ watts, $\eta = 1/2$, $t_{st} = 1$ msec, $\lambda = 5145\ A^o$. The product on the left hand side of Eq. 11 must be less than $5 \times 10^{-9}\ Hz/Hz^{1/2}$.

It is useful to reexpress the Poisson noise limit Eq. 8 in terms of the minimum detectable gravitational strain amplitude density, this is

$$h(f)_{gw} > \frac{1}{\sqrt{8\pi}\, t_{st} c} \left(\frac{hc\lambda}{\eta P_o}\right)^{1/2} \frac{1}{\text{sinc}\ (\omega t_{st/2})} \qquad (12)$$

Here B is the ratio of the unmodulated to the total incident power. The quantity in the square brackets determines the optimum phase modulation amplitude for a given value of B. For small values of B it is close to 1/2, at B = 0.1, an interferometer with 90% fringe contrast, it has grown to 1.0 and B = 0.2 it has become 1.6.

The Poisson limit for small values of B is

$$x^2(f) = \left(\frac{hc\lambda}{8\pi^2 b^2 \eta P_o}\right) \qquad cm^2/Hz \qquad (8)$$

for b = 60, η = 1/2, P_o = 100 watts, λ = 5145A°, $x(f) \sim 8.5 \times 10^{-18}$ $cm/Hz^{\frac{1}{2}}$. To apply equations 7 and 8 to the Fabry-Perot cavity replace b by F/π.

The fluctuating output power in the interferometer due to frequency instability has been analyzed by Armstrong (J. Opt. Soc. Am. 56, 1024, 1966) for a Michelson interferometer illuminated by light with Gaussian phase noise. The light source is characterized by a Lorentzian frequency width δ . In the limit where the frequency of the power fluctuations is less than δ and the difference in storage time in the two arms, τ, is such that $\delta\tau << 1$, the output power fluctuations are given by

$$P^2(f) = \frac{2}{3} P_o^2 \left(\frac{\delta\tau}{\delta}\right)^3 \qquad (9)$$

The condition that the Poisson noise dominates sets a limit on τ. δ is not a free parameter since the frequency width of the light source will be determined, in some of the interferometer designs, by requirements on the suppression of the noise from scattered light.

The transducer noise is analysed for both systems as the fluctuations in power incident on the photodetector. There are two main sources: the Poisson (shot) noise which can only be reduced by increasing the optical power circulating in the interferometer for a fixed quantum efficiency in the photodetector, and power fluctuations at the detector due to frequency or phase instabilities in the light source which can be reduced to small values by making the storage times in the two arms close to equal. The displacement noise spectral density is then related to the spectral density of the power fluctuations by

$$x^2(f) = P^2(f)/(\Delta P/\Delta x)^2 \qquad (4)$$

The Poisson noise is given by

$$P^2(f) = \frac{2hc}{\eta\lambda} \langle P_D \rangle \qquad \text{Watts}^2/\text{Hz} \qquad (5)$$

where η is the quantum efficiency of the photodetector and $\langle P_D \rangle$ is the average power incident on the photodetector. The average power from the antisymmetric port is

$$\langle P_D \rangle = \frac{(P_o - P_B)}{2}(1-\cos\Omega_o) + P_B \qquad (6)$$

In the best case the Poisson noise dominates and the displacement power spectral density becomes

$$x^2(f) = \left(\frac{hc\lambda}{4\pi^2 b^2 \eta P_o}\right)\left[\frac{(1-\cos\Omega_o) + 2B/(1-B)}{(1-B)\sin^2\Omega_o}\right] \qquad (7)$$

front distortion, $k = 2\pi/\lambda$. $\Omega(t)$ is the phase modulation signal assumed to be a square wave with amplitude Ω_o, and θ is either 0 if the beam emerges from the symmetric port or π if from the antisymmetric one. $x(t)$ is the differential motion of the mirrors that define the two arms.

The transducer gain is the change in output power with respect to change in the differential position taken at a symmetry point of the fringe, where $kb\ x(t)$ is close to zero. With the output observed at the antisymmetric port, the gain is given by

$$\frac{\Delta P}{\Delta x} = (P_o - P_B)\ \frac{2\pi b}{\lambda}\ \sin\Omega_o \qquad (2)$$

In a Michelson arrangement where the multipass cavities are Fabry-Perot cavities used in reflection, the transducer gain is

$$\frac{\Delta P}{\Delta x} = (P_o - P_B)\ \frac{2F}{\lambda}\ \sin\ \Omega_o \qquad (3)$$

where F is the finesse of the cavity given by

$$F = \pi/(1-R).$$

(1-R) is the transmission of the input mirror assuming that the reflectivity of the other mirror in the cavity is unity.

The light storage time in the delay line is $t_{st} = b\ell/c$ while in the Fabry-Perot it is $F\ell/\pi c$. ℓ is the separation of the mirrors

In this section in contrast with the section that developed the response of an electromagnetically coupled antenna to a gravitational wave, we adopt the viewpoint of the interferometer as a motion transducer. We first determine the gain of the motion transducer and then look at the noise terms that limit its performance. This more conventional approach applies both to interferometric systems that make phase comparisons at the end of a storage time like delay lines and those that gain phase sensitivity by multiple superposition of beams like the Fabry-Perot.

In the analysis we assume that the optical components are lossless except for scattering and wavefront distortion. In a small antenna this is a poor assumption, but in a first generation long baseline system it is applicable because of the smaller number of beam transits or finesse required to achieve optimal storage times and because of the advances being made in mirror reflectivities, which are approaching (1-R) of a few 10^{-4}.

The optical output power of a Michelson interferometer in which the optical phase is electrooptically modulated and in which the beam makes b transits in each arm is given by

$$P(t) = \left(\frac{P_o - P_B}{2}\right)(1 + \cos(kb\, x(t) - \theta + \Omega(t)) + P_B \qquad (1)$$

In this expression P_o is the input power, P_B is the unmodulated output power due to imperfections such as scattering and wave

NOISE SOURCES

In this section of the study we present an analysis of the various sources of noise that limit the strain sensitivity of a long baseline antenna. The order of the presentation is to begin with noise sources in the measurement of the time (phase) differences; the transducer noise and the noise incurred by the propagation of the light in an imperfect vacuum. The effect of stochastic forces on the masses follows. The section on vibration isolation includes the analysis of a scheme to reduce the effects of ground noise in a large baseline antenna.

The section ends with a graphical summary of all the noise sources that have been considered and displays the limiting antenna performance as a function of gravitational wave frequency for a range of antenna lengths.

The sample parameters used in the calculations and in the final graphs have values we consider technically feasible in a first generation long baseline antenna system. In these projections of antenna performance none of the noise terms are set at limits which are fundamental in the sense that they cannot be reduced by improvements in the technology or by a new concept.

Contract GC-A-290939
NSF Grant PHY-8109581

SWEC J.O. 14190.01

REPORT ON SITING STUDY
INTERFEROMETRIC BROAD BAND
GRAVITATIONAL ANTENNA

September, 1983

Stone & Webster Engineering Corporation
Boston, Massachusetts

TABLE OF CONTENTS

Section	Title	Page
1	INTRODUCTION	1-1
2	SURFACE SITES.	2-1
2.1	SITING CRITERIA.	2-1
2.2	PROCEDURE.	2-2
2.3	DESCRIPTION OF CANDIDATE SITES	2-4
2.4	REFERENCES FOR SURFACE SITES	2-17
3	MINE SITES	3-1
3.1	SITING CRITERIA.	3-1
3.2	PROCEDURE.	3-3
3.3	DESCRIPTION OF CANDIDATE SITES	3-4
3.4	REFERENCES FOR MINE SITES.	3-7
4	SUMMARY AND RECOMMENDATIONS FOR FURTHER STUDY. . .	4-1

LIST OF TABLES

Number	Title
2.2-1	Government Installations Considered
2.2-2	Candidate Areas for Surface Sites
3.2-1	Candidate Areas for Subsurface Sites
3.3-1	Decremental List of Subsurface Sites

LIST OF FIGURES

2.1-1	Locations of Seismic Zones
2.2-1	Government Installations Considered
2.2-2	Earthquake Epicenter Map of Western Arizona and Southern Portions of California, Nevada and Utah
2.3-1	Alamosa Area, Colorado
2.3-2	Bristol Lake, California
2.3-3	Edwards Air Force Base, California
2.3-4	Eglin Air Force Base, Florida
2.3-5	Fort Bliss, New Mexico
2.3-6	Fort Stewart, Georgia
2.3-7	Great Salt Lake Desert, Utah
2.3-8	Idaho National Engineering Laboratory, Idaho
2.3-9	Luke Air Force Range, Arizona
2.3-10	Lynndyl, Utah
2.3-11	Plains of San Augustin, New Mexico
2.3-12	San Cristobal Valley, Arizona
2.3-13	White Sands Missle Range, New Mexico
3.3-1	Cleveland Mine Map
3.3-2	Randolph Mine Map
3.3-3	Nash Draw Mine Map
4-1	Locations of Described Sites
4-2	Locations of Lands Managed by BLM

1. INTRODUCTION

This report presents the results of a study to identify potential sites for proposed interoferometric broad band gravitational antennas. The study was performed for the Massachusetts Institute of Technology (MIT) by Stone & Webster Engineering Corporation under Contract NO. GC-A-290939.

The objectives of the study were to verify that feasible antenna sites exist in the continental United States and to identify a realistic range of conditions at typical sites. These conditions would serve as input to preliminary estimates of site development costs for antenna installations. Identification of recommended antenna sites was not within the scope of this study.

The proposed antennas would have an L-shaped configuration in plan. The L is formed by two straight arms of highly evacuated pipe. MIT established that the study should consider sites at the ground surface and in subsurface mines. Both surface and mine sites should accommodate an antenna with arms at least 5 km (3.1 mi) long, but if mines of such extent do not exist, the longest potentially suitable mines should be identified. It would be preferable to identify an eastern site and a western site.

Results of the study of surface sites are presented in Section 2, and results of the study of mine sites are presented in Section 3. A summary and recommendations for additional study are presented in Section 4.

2.0 SURFACE SITES

2.1 CRITERIA FOR SELECTION OF CANDIDATE SURFACE SITES

Selection of candidate surface sites was based on the criteria given below.

2.1.1 Topography

Each arm of the antenna must provide a straight line of sight for the laser beam. Therefore, each arm must be flat or uniformly sloping along its 5 km length. This can be achieved most easily by building the antenna on relatively flat or uniformly sloping ground, where a minimum of site grading is required. Where this is not possible, high ground can be excavated and low ground can be filled, at added cost, to provide the appropriate vertical alignment of the antenna. However, to minimize the cost of construction, areas requiring cuts and fills of more than about 10 feet were avoided.

2.1.2 Land Use

Attempts were made to minimize interference with existing surface transportation networks. To qualify as a candidates site the proposed antenna must not interfere with traffic, because this could arouse local opposition to the construction of the antenna. Crossing of unpaved roads and of a few light duty paved roads was permitted. Crossing of oil and gas pipelines, railroads and canals was avoided. Areas which include state or national parks, wildlife refuges, Indian reservations, population centers, and mining or oil fields were excluded from consideration. Areas that are intensively farmed were also avoided.

Candidate sites should be located near a source of electric power, and should preferably be located near a source of cooling water for operating equipment. Developed sites with buildings that might be shared as a headquarters area for an antenna would also be preferable.

2.1.3 Seismicity and Vibrations

A strong earthquake might damage the vacuum pipe. Areas subject to strong ground shaking may also be subject to higher than average microseismic activity which might shake the mirrors and interfere with the performance of the antenna. The active seismic zones of the United States are shown in Figure 2.1-1 [1-4]. Sites within these zones were generally not considered in the siting study, unless they were near the edge of the zone.

Other potential sources of ground vibrations are railways, highways, airports, water waves, water falls, heavy

manufacturing, mining, and military operations such as bombing and artillery ranges. No actual ground vibration measurements were available or were made for this study. Sites were excluded from further consideration if they were within 1 mile of a primary highway or railway, or 3 miles from a commercial or major military airfield. Known bombing or artillery ranges were avoided, as were large water bodies and areas of heavy manufacturing and mining.

2.1.4 Floods and Drainage

Areas that appear to be subject to flooding were excluded from consideration because of potential damage to equipment and interruption of access. Also, areas where it would be difficult to construct the antenna across known drainage paths such as major creeks, rivers or washes were avoided. Large marshes and swamps were avoided because of difficult access and probable need for costly foundation improvement.

2.1.5 Accessibilty

If an area was found to contain multiple candidate sites, the more accessible sites were considered for further study. Areas that were more than 10 miles from the nearest paved road were excluded. Areas that were hundreds of miles from major population centers were also excluded, because they would be too far from the labor supply required for construction.

2.2 PROCEDURE

Consideration was first given to areas controlled by the federal government, which administers large tracts of land throughout the United States. Use of government land would eliminate the need to purchase an easement or right-of-way across private lands. It was also considered likely that many government installations would have electric power and potable water on site. Federal installations considered include military reservations, national engineering laboratories and agricultural experimental stations. Many of these installations would have the additional potential benefit of controlled access to the site. Locations of the installations were obtained from a current atlas of the United States.[5]

The government installations that were considered for siting a surface antenna are listed in Table 2.2-1, and their locations are shown in Figure 2.2-1. From this figure it is apparent that most of the larger installations lie in the western United States. There was some concern that potential sites in the east might be overlooked, and so all land in the following eastern states was considered: Maine, Vermont, New Hampshire,

Massachusetts, Rhode Island, Connecticut, New York, New Jersey, and North Carolina.

There was also some concern that many of the government administered areas in the west were military areas to which it might be impossible to obtain access. Therefore, private lands in Colorado and Nebraska were also considered as candidate areas.

Other specific areas for investigation were suggested by MIT. These included:

- Plains of San Augustin in New Mexico, the site of the Very Large Array of radio telescopes operated by the National Radio Astronomy Observatory (NRAO).

- Owens Valley in California, the site of a radio observatory operated by the California Institute of Technology.

- Clark Dry Lake in California, the site of a radio observatory operated by the University of Maryland.

There are a number of extensive playas or dry lake beds in Southern California, and a few of these were also selected for investigation.[5] These include Bristol Lake, Cadiz Lake, Coyote Lake, Danby Lake, Palen Dry Lake, Searles Lake, and Soda Lake. Rosamond and Rogers Lakes were also considered as part of the review of Edwards Air Force Base.

The candidate areas were checked to determine whether they were within or near the seismically active zones shown in Figure 2.1-1. Existing maps and reports showing the distribution of earthquakes were consulted to obtain more information concerning the seismicity of these areas [6-11]. Figure 2.2-2 is an example of such a map, with candidate sites superimposed.

Existing United States Geological Survey (USGS) topographic maps were examined to determine whether each candidate area contained one or more candidate sites with suitable topography and of sufficient size to accommodate a 5 km long L-shaped antenna. Most maps were available at a scale of 1:24,000 (1 in. equals 2,000 ft), but a few were only available at a scale of 1:62,500 (1 in. equals 5,208 ft). A template drawn to the appropriate scale was used in evaluating possible antenna orientations.

Results of this initial screening are summarized in Table 2.2-1, which indicates whether a site was found to be suitable or unsuitable. The primary reason for site unsuitablility is also given in the Table.

The candidate sites were identified by state, name of the USGS topographic map, and probable antenna orientation. For a number of sites, a profile was drawn of the existing ground surface along the more steeply sloping arm of the antenna, in order to estimate the heights of cut and fill required to produce a uniformly sloping grade for the antenna.

From the topographic maps, estimates were made of foundation material (soil or rock), availability of water and electric power, potential for flooding, and distance to the nearest highways, railroad and airports. Where electric power lines were not shown on the maps, electric utility companies were called and asked to identify power lines in the area. Distances to the nearest commercial air routes and military air operations areas were obtained from published airway maps covering U.S. air space below elevation 18,000 feet.[12]

The antenna alignment selected for discussion was drawn on a USGS topographic quadrangle (1:250,000 scale). Finally, the seismicity of the area within an approximately 40 mile square, centered on the alignment, was investigated using a computerized earthquake file prepared by the National Atmospheric and Oceanic Administration.[13] Events in this file took place within the period 1900-1979 and were reported by at least 5 monitoring stations. Output consists of date, time, latitude and longitude, and magnitude or Modified Mercalli epicentral intensity of the earthquake.

2.3 DESCRIPTION OF CANDIDATE SITES

Thirteen of the areas listed in Table 2.2-2 were considered sufficiently promising to warrant further investigation. These areas are:

- Alamosa Area, Colorado
- Bristol Lake, California
- Edwards Air Force Base, California
- Eglin Air Force Base, Florida
- Fort Bliss, New Mexico
- Fort Stewart, Georgia
- Great Salt Lake Desert, Utah
- Idaho National Engineering Laboratory, Utah
- Luke Air Force Range, Arizona

- Lynndyl, Utah
- Plains of San Augustin, New Mexico
- San Cristobal Valley, Arizona
- White Sands Missle Range, New Mexico

This section provides a brief description of the candidate surface sites, based upon the available literature.

2.3.1 Alamosa Area, Colorado

There are a number of areas in eastern Colorado that have moderately sloping terrain. However, the area with the flattest topography is the plains between the San Juan Mountains and the Sangre de Cristo Mountains in the southern part of the state. The area selected for investigation lies north of Alamosa, and south of Hooper. The lands in this area are privately owned and are used for farming. Representative USGS topographic quadrangles of the area are Harrance Lake, Hooper Southeast, Hooper East, Moffat North, Mount Pleasant School, and Shed's Camp (1:24,000 scale). The candidate site that was selected is located on the Hooper Southeast quadrangle.

The site is located approximately 7 miles north of Alamosa and approximately 100 miles southwest of Colorado Springs. Figure 2.3-1 shows the site location. The arms of the antenna would intersect at approximately latitude N. 37°35' and longitude W. 105°47'30". One arm of the antenna would bear N. 5° W. The ground surface along this arm ranges between approximately el 7530 and 7533 ft. The other arm of the antenna would bear approximately S. 85° W. The ground surface along this arm ranges between approximately el 7530 and 7543 ft. This alignment intersects unimproved roads at three locations, based upon the available topographic information.

Electric power is available from a Public Service of Colorado power line along State Route 17. The existence of canals and flowing wells indicates there should be an adequate source of water. There are no woods on site.

There are no recorded earthquake epicenters within 20 miles of the site. The nearest highway is State Route 17, and the nearest railroad is the Denver and Rio Grande Western. Both are located approximately 1 mile to the west. There are no sources of water-induced vibration in the area. The area appears to be under low level air route V484 from Alamosa to Gunnison, Colorado. This air route has a minimum enroute altitude of 14,600 ft. The

nearest airport is the Alamosa Municipal Airport, located approximately 11 miles to the south.

There does not appear to be any danger of flooding at this candidate site.

2.3.2 Bristol Lake, California

There are a number of extensive playas or dry lakes in Southern California. Among these are Bristol, Cadiz, Coyote, Danby, Owens, Palen, Rogers, Rosamond, Searles, and Soda Lakes. These playas are generally located between latitudes N. 33°30' and N. 36° and longitudes W. 115' and W. 118°30'. These playas might be considered attractive because of their flat topography. However, the playas are lower than the surrounding land. During rainy seasons, runoff from the surrounding mountains flows to the playas and forms temporary lakes. Although the extent and depth of these temporary lakes varies according to the rainfall, it is not uncommon in a wet year to have a temporary lake last for six to twelve weeks.

For this reason it would appear preferable to site the antenna on higher ground some distance from the playa. An example of such a site is one adjacent to Bristol Lake (see Figure 2.3-2).

The Bristol Lake site is located approximately 37 miles northeast of Twenty-Nine Palms, between the towns of Saltus and Cadiz. It is located on the east side of the lake at approximately latitude N. 34°30' and longitude W. 115°34'. One arm of the antenna would bear S. 24° E. between el 680 and 690 ft. The other arm would bear S. 66° W. between approximately el 625 and 680 ft. This places one end of the antenna approximately 1.9 miles south of the Atchison, Topeka, and Santa Fe Railroad. Access to the site is presently via a paved road from US 66 to Cadiz and then via an unimproved road. This alignment minimizes but does not eliminate interference with drainage toward the lake. The alignment crosses at least two washes or intermittent stream beds. Drainage structures would have to be provided to allow water to pass across the alignment.

Southern California Edison Co. provides electric power to the town of Cadiz, approximately 2 miles northeast of the site. There is no known source of fresh water at the site. A mineral recovery operation utilizing brine wells and evaporation ponds is located at the west side of Bristol Lake.

Commercial air route V538 passes over the south end of the antenna. The minimum enroute altitude along the route is 10,000 ft. Military training routes VR289 and IR 250 pass over the site, which is also immediately west of the Bristol Military

air operations area. The nearest airfield is 37 miles to the southwest, on Twenty-nine Palms Marine Corps. Base.

The site is in the southeast part of California, away from the highly seismic areas shown in Figure 2.2-2. There have been 5 earthquakes reported within 20 miles of the alignment. The closest earthquake occurred on May 20, 1932, and had a local magnitude of 3.5. The epicentral location is reported as N. 34.500° and W. 115.666°, approximately 4 miles west of the alignment. The largest reported earthquake within 20 miles of the alignment occurred on December 14, 1970, and had a local magnitude of 4.0. The epicenter is reported as N. 34.300° and W. 115.716°, approximately 18 miles southwest of the alignment.

2.3.3 Edwards Air Force Base, California

Edwards Air Force Base is located approximately 65 miles southwest of Bakersfield along Route 58. The area is generally flat with several playas (dry lakes) and little vegetation. Rogers and Rosamond playas on the Base are fully utilized as airfields and are not suitable sites for an antenna. A candidate site was selected between Buckhorn Lake and the southern boundary of the Base. The site location is shown in Figure 2.3-3.

The arms of the antenna would intersect at approximately latitude N. 34°47' and longitude W. 117°58'. One arm would bear N. 58° E. along ground ranging in elevation between 2315 and 2,325 ft. The other arm would bear N. 32° W. along ground ranging in elevation between el 2290 and 2325 ft. In this orientation, the antenna would cross one light duty road and two unimproved roads. A test track exists one-half mile north of the northeast arm. The intersection of the arms would be located approximately 0.25 miles northeast of a tracking station. Several dwellings are located one mile to the south, outside the Base.

There are many wells in the area. The site is located within a special use air space, and Edwards Air Force Auxiliary North Base is located approximately 6 miles to the northeast. Military training route VR 232 passes approximately 1 mile north of the site.

The greatest potential source of ground vibration at this site is seismicity. The site is located approximately 12 miles northeast of the San Andreas fault zone (see Figure 2.2-2). Approximately 120 earthquakes are listed as having occurred within 20 miles of the site. The largest event within a 20 mile radius was a local magnitude 5.0 event that occurred in 1952 at N. 34.516° and W. 118.183°. This epicenter is approximately 20 miles southwest of the site. The available data indicate that the area around Edwards Air Force Base is seismically active, and therefore is probably unsuitable for siting the antenna.

2.3.4 Eglin Air Force Base

Eglin Air Force Base is located east of Pensacola, Florida, and north of Fort Walton Beach. The base is near the Gulf of Mexico, but is separated from the Gulf by a barrier island and the Intracoastal Waterway. The Base extends approximately 55 miles in the east/west direction and approximately 17 miles in the north/south direction. A candidate site was selected for study near the west end of the Base, approximately 20 miles east of Pensacola and approximately one mile east of State Route 87. The site is approximately 5 miles north of the Gulf of Mexico, and is located on the USGS Ward Basin and Harold SE Quadrangles (1:24,000 scale). The site location is shown in Figure 2.3-4.

The site can accommodate an L-shaped antenna with arms 5 km long. The intersection of the arms would be located at approximately latitude N. 30°31' and longitude W. 86°53'. One arm would extend due north along ground ranging between elevations 105 and 140 ft. Cuts of 10 ft or less and fills of 15 ft or less would be required to provide a uniformly sloping ground surface along this arm. The other arm of the antenna would bear due east, along ground which varies in elevation between 110 and 120 ft. There is no potential for flooding at this site.

Auxiliary Air Field No. 7 is located approximately 2 miles northeast and Auxiliary Air Field No. 10 is located approximately 3 miles west of the antenna at its closest approach. Potential sources of vibration are military aircraft activity at the adjacent Auxiliary Air Fields, and activity at Eglin and Hurlbert Air Fields located 5-10 miles to the east. The entire base is located within air space designated as the Eglin Military Operations Area.

Potential sources of water induced vibrations are the Yellow River, located 2.5 miles to the north, East Bay located approximately 4.3 miles to the southwest and the Santa Rosa Sound located 7.3 miles to the south. No earthquakes have been recorded within 20 miles of the site.

The antenna would cross one light duty road, and 10 unimproved roads. An electrical power line is located along Route 87, approximately 1 mile west of the site. Water is probably available from wells that could be drilled in the area, but the quality of water is not known. The site is wooded and clearing would be required.

2.3.5 Fort Bliss Military Reservation, New Mexico

Fort Bliss Military Reservation is located approximately 17 miles south of Alamogordo, New Mexico and extends as far south as El Paso, Texas, a distance of approximately 65 miles. Most of the

Reservation is located in New Mexico. Fort Bliss contains extensive areas of low relief, and it may be possible to identify a number of potential sites having reasonable topography for a 5 km long L-shaped antenna. The main unknown is the extent of military activity at Fort Bliss. Much of the Reservation is an anti-aircraft range. To minimize potential vibration from military activity, a site should be located far from firing areas and bomb targets. A site was selected at the location shown in Figure 2.3-5. This location is reasonably close to a highway and railway, and thus may be far from firing areas. No bomb targets are shown on the topographic maps.

The candidate site is approximately 30 miles north of El Paso and approximately 4 miles west of US Route 54 and the adjacent Southern Pacific Railroad. Figure 2.3-5 shows the site location. There are lookout towers located approximately 2 miles southwest of the site. The road leading to the towers is used as a landing strip. Additional information would have to be obtained concerning the current and projected use of this area by the military.

The detailed topography of the site area is given on the USGS Newman Northeast quadrangle (1:24,000 scale). The intersection of the arms would be located at approximately latitude N. 32°10' and longitude W. 106°18'. One arm would have a bearing of approximately S. 1° W. The ground surface along this arm would range from approximately el 4,075 to 4,080 ft. The other arm would have a bearing of approximately S. 89° E. The ground surface along this arm would range from approximately el 4,080 to 4,093 ft. The antenna would cross two unimproved roads. Present access is by unimproved road directly from Route 54, or by light duty road from US Route 54 to the lookout towers, and then by unimproved road north to the antenna. There are no woods on site.

El Paso Electric Co. provides electricity along the road from State Route 54 to the observation towers 2 miles south of the site. A water main is also reported to exist along this road. There are also windmills and other sources of water in the area, as shown in Figure 2.3-5, and it should be possible to drill a well to obtain a water supply for construction and operation of the antenna. The quality of water obtained from the existing groundwater sources is not known.

The site is located in the Rio Grande Rift Zone. However, no earthquakes have been recorded within 20 miles of the site. As previously mentioned, the effects of military operations on ground vibrations at the site are unknown. There are no known sources of water induced vibration near the site. Traffic along US Route 54 and the Southern Pacific Railroad, some 1.8 miles to the east should not cause significant vibrations at the site.

According to published air maps, Condron Airfield is located approximately 8 miles northeast of the site. The nearest commercial air route is V19-94, approximately 3 miles to the south. This route has a minimum enroute altitude of 9,000 ft.

2.3.6 Fort Stewart Military Reservation, Georgia

Fort Stewart Military Reservation is located in the eastern portion of Georgia, immediately west of Savannah. It extends approximately 30 miles in the east-west direction and approximately 16 miles in the north-south direction. State Route 119 divides Fort Stewart into an eastern half and a western half. State Route 144 passes through the southern portion, roughly parallel to the southern boundary of the Reservation.

A candidate site was selected in the western half of Fort Stewart, between Route 144 and the southern boundary of the Reservation. This is approximately two miles west of the Fort Stewart headquarters area. The site location is shown in Figure 2.3-6. This site is located on the USGS Taylors Creek and Walthoursville quadrangles (1:24,000 scale). Taylors Creek flows east through this area, and a number of streams flow in a north-south direction to join the Creek. There are also a number of marshy areas on site. The entire area is wooded. Ground surface elevations in the area range from approximately el 50 ft along the eastern portion of Taylors Creek to approximately el 75 ft in the higher western areas.

The site can accommodate an L-shaped antenna with arms 5 km long. The alignment selected for study would have the intersection of the arms located approximately one mile south of Route 144 at latitude N. 31°54' and longitude W. 81°42'. One arm would bear approximately S. 20° E., crossing Taylors Creek and two of its tributaries. This arm would also cross two light duty roads and one unimproved road. The other arm would bear approximately S. 70° W. and would cross two tributaries of Taylors Creek and two unimproved roads. Electric power is probably available at the headquarters area two miles to the east. A well can be installed to obtain water at the site.

The site is located within the South Carolina-Georgia seismic zone. However, no earthquake epicenters have been reported within 20 miles of the site. The largest earthquake nearby was a Modified Mercalli VI event along the Savannah River approximately 35 miles to the northeast. The nearest airport is Wright Airfield located approximately five miles east of the site. This airfield has a runway length of 5,000 ft. Large areas of airspace on the west and south sides of Fort Stewart are reserved for military air operations, suggesting that there may be intensive aircraft activity in the site area. The nearest potential source of water-induced vibrations is Taylors Creek.

The nearest major population center is Savannah, located approximately 35 miles to the northeast.

If it can be demonstrated that the antenna can be located within about 0.3 miles of State Route 144 without experiencing excessive vibrations, then it may be possible to use an old railroad grade as the alignment for one arm of the antenna. The intersection of the arms would be located at approximately latitude N. 31°55' and longitude W. 81°41'. The arms would have bearings of S. 40° E. and S. 50° W. This orientation would cross Taylors Creek on the existing embankment, eliminating the need for a special crossing of the Creek.

2.3.7 Great Salt Lake Desert, Utah

The Great Salt Lake Desert is located in the northwest corner of Utah between longitude 113° W. and 114° W., and between latitudes 39°40' N. and 41°40' N. The entire area is part of the floor of ancient Lake Bonneville, and has very little relief. Highway access to the region is by Interstate I-80, which extends west from Salt Lake City to the Nevada border and passes through the middle of the Desert. Tracks of the Western Pacific Railroad parallel I-80 on the south side of the highway.

Although the Great Salt Lake Desert includes Hill Air Force Range, Wendover Air Force Range, Desert Test Center and Dugway Proving Grounds, all of which are U.S. military installations, consideration was instead given to non-military land along I-80 because it has equally suitable topography and because it is more accessible from the existing highway. The area along I-80 west of the Lake Side Mountains and east of the Bonneville Salt Flats was selected for study.

The land surface in the area of I-80 generally slopes downward to the north and west, reaching its lowest elevation locally at the Bonneville Salt Flats, which has an average elevation of 4,214 ft. Kaiser Aluminum and Chemical Corporation operates a mineral recovery operation on the Bonneville Salt Flats using brine wells and evaporation ponds. Ground slopes in the flatter areas in the area of I-80 are typically less than 1 foot per mile.

The ground surface on the Bonneville Salt Flats generally consists of carbonate muds that have either a soft puffy surface or a hard compact surface. In some places, the muds are overlain by gypsum sand dunes.[14] Runoff from the surrounding mountains flows onto the ancient lake bed and flows toward the Bonneville Salt Flats. Shallow ponds of water form in the lower areas during the winter, and the permanant ground water level in these areas is high.

Essentially the entire area west of Grayback Hills and east of the Bonneville Salt Flats contains potential sites for the antenna. It is recommended that the antenna be located on the east side of this area in order to minimize the possibility of flooding during winter, and to place the antenna closer to Salt Lake City area in order to reduce distance to construction work force, supply areas and transportation centers.

Two areas were selected for study as possible sites. These are the Aragonite NW quadrangle south of I-80 and the Knolls and Knolls 2 SE quadrangle north of I-80. The sites are approximately 30 miles east of the Bonneville Salt Flats, on lands administered by the U.S. Bureau of Land Management and the State of Utah.[15] The site location are shown in Figure 2.3-7. One area on the Aragonite NW quadrangle can accept a 5 km L-shaped configuration with the intersection of the arms at approximately latitude N. 40°39' and longitude W. 113°10'. One arm would bear N. 13° E. between el 4,257 and 4,260 ft. The other arm would bear N. 77° W. between el 4,254 and 4,260 ft. This area lies approximately 0.8 miles east of a mud flat having an average bottom elevation of approximately 4,242 ft. The mud flat is approximately 3.5 miles long by 2 miles wide and is probably a temporary lake during winter months.

The Knolls and Knolls 2 SE quadrangles can accommodate antenna arrangements larger than 5 km. A possible orientation would have the intersection of the arms at latitude N. 40°45' and longitude W. 113°22'. One arm would bear due north at approximately el 4,218 ft. The other arm would bear due east between el 4,218 and 4,220 ft. This area is denoted as a mud flat on the topographic maps and may be subject to shallow flooding during the winter months. It may be necessary to construct the antenna on a low embankment in this area. Although this area is low it is still higher than the level of the Great Salt Lake which, according to the topographic maps, stood at approximately el 4,195 ft in October 1969.

Access to the sites is by I-80 from Salt Lake City, located 75 to 85 miles to the east. Each of the sites requires construction of an access road from I-80. The site on Aragonite NW can only be reached by crossing the Western Pacific Railroad. The center point of the L would be located approximately 5 miles south of I-80. The center point of the other site would be located approximately 1 mile north of the highway.

Neither of the sites has a supply of fresh water available in the immediate vicinity. Reports on ground water quality beneath the Bonneville Salt Flats to the west indicates that the total dissolved solids content of the water ranges from approximately 70,000 to 330,000 ppm.[16] Therefore, it will probably be necessary to import water for construction, cooling and drinking

use, or to treat locally available water for those uses. A Utah Power & Light Co. electric power line extends along I 80 in the site area.

The sites are not located in an active seismic zone. Two earthquakes are listed as having occurred within 20 miles of the site in 1966, but no data are reported concerning their magnitude or epicentral intensity. Commercial air route V32-253 passes directly over the site north of I-80 and 3.4 miles north of the other site. Both sites are located approximately 10 miles from apparent bomb craters at the south end of Hill Air Force Range. The site south of I-80 may be influenced by waves in the temporary lake located approximately 0.8 miles away.

2.3.8 Idaho National Engineering Laboratory, Idaho

The Idaho National Engineering Laboratory is the site of the national nuclear reactor testing station, operated by the U.S. Department of Energy. The Laboratory is located 40 miles west of Idaho Falls along Route 20 on the Snake River Plain, a high plateau built up of basalt lava flows. The general location of this candidate site is shown in Figure 2.3-8.

The site is located on USGS Circular Butte quadrangle (1:24,000 scale). One possible orientation of the antenna would have the intersection of the arms at approximately N. 43°49' and W. 112°38'. One arm would bear due west at approximately el 4,790 ft. The other arm would bear due south between approximately el 4,787 and 4,790 ft.

Access to this area is by unimproved roads off Route 88 which runs along the west and north borders of the site. Dry channel Big Lost River runs on the opposite side of Route 88, and a canal crosses the south arm approximately 0.8 miles from the end. Power lines run throughout the site. The antenna alignment crosses four unimproved roads. Large buildings and railroad tracks are located approximately 2.5 miles north of the site.

The site is located in uncontrolled air space up to 14,500 ft elevation, and no commercial air routes cross the site. The Mud Lake-West Jefferson County Airport is located approximately 5 miles northeast and presents little problems from large aircraft because its longest runway is 3,330 ft.

The site is not located in an active seismic zone. No earthquake epicenters have been reported within 20 miles of the site.

2.3.9 Luke Air Force Range, Arizona

Luke Air Force Range extends from Yuma, Arizona, on the west to the Sand Tank Mountains on the east, a distance of approximately 135 miles. The most promising site on Luke Air Force Range lies on the north side of the Range between the towns of Stoval and Dateland. This site is approximately 65 miles east of Yuma. This candidate site is 5 miles south of interstate I-8 and the adjacent Southern Pacific Railroad. It is 3.5 miles southeast of the Stoval Airfield (see Figure 2.3.9). A road would have to be constructed from the site to I-8, possibly by way of the access road to the Stoval Airfield and Pimeria Well.

The candidate site is located on the northeast corner of the Mohawk Mountains NE quadrangle (1:24,000 scale). One possible alignment would have the intersection of the arms at approximately latitude N. 32°42' and longitude W. 113°34'. One arm of the antenna would bear approximately S. 21° E. along the el 400 ft contour, and the other would bear approximately N. 69° E. between el 400 and 447 ft. Estimated heights of cuts and fills along the antenna alignment are approximately 2 ft, based upon the existing contour information. An Arizona Power Co. electric line extends along Interstate 8 in the site area. Pimeria Well is located approximately 2.5 miles WNW of the intersection of the arms. It should be possible to drill a well at the site to obtain a water supply. The quality of water in the area would have to be investigated to determine whether treatment of the water is required. The area is not wooded.

There are no highways or railroads located within 5 miles of the site. Therefore, these are not potential vibration sources.

Two earthquakes have been reported in the Mohawk Mountains, approximately 11 miles south of the antenna alignment. One event occurred in 1958 and had a magnitude of 4.9. The other event occurred in 1942; no magnitude or epicentral intensity has been assigned to this event. No other earthquakes have been reported within 20 miles of the site.

Two other potential sources of vibrations are military aircraft operating over Luke Air Force Range, and activity at nearby airfields. The extent of military aircraft activity is unknown at this time. Activity at Stoval Airfield is probably limited to small aircraft, because the length of the largest runway is only 4000 ft. The Dateland Airfield, located 6 miles to the north, has a 6500 ft long runway which is oriented toward the site.

There does not appear to be any danger of flooding at this candidate site. The antenna would be located on high ground and would not intercept any major perennial or dry stream beds. San

Cristobal Wash is located approximately 0.4 miles from the end of the southeast arm of the antenna.

2.3.10 Lynndyl, Utah

The Lynndyl area is located in the Sevier Desert, approximately 95 miles southwest of Provo along US Route 6. The Sevier River flows southwest through the area, and an extensive irrigation network has been developed around the town of Delta, approximately 15 miles southwest of Lynndyl.

A candidate site for an antenna with arms 5 km long has been identified west of Lynndyl (see Figure 2.3-10). This area is shown on the USGS Lynndyl quandrangle (1:62,500 scale.) The arms of the antenna would intersect at approximately latitude N. 39°34' and longitude W. 112°27'. One arm would bear S. 35° E., parallel to an unimproved road leading from US Route 6. The existing ground surface elevation along this arm ranges between el 4,780 and el 4,790 ft. The other arm would bear S. 55° W. along ground which ranges in elevation from 4,760 ft to 4,790 ft. The antenna would be located approximately 1.8 miles northwest of US Route 6 and the adjacent Union Pacific Railroad. There are two railroad sidings at Lynndyl.

Access to the site is presently by unimproved road from US Route 6. Electric power is available approximately 0.2 miles from the east end of the antenna. Water wells are located 1 mile from the east end of the antenna, and windmills are located approximately 6 miles northwest of the intersection of the arms. This land is administered by the Bureau of Land Management and the State of Utah.[15]

The site is located approximately 10 miles west of the Intermountain Seismic Belt. Two earthquakes have been reported within 20 miles of the site. One had a body a magnitude of 3.4 and occurred in the East Tintic Mountains, approximately 19 miles NE of the site. The other had a body magnitude of 2.8 and occurred in the Canyon Mountains, approximately 17 miles SE of the site. An intensity VII earthquake occurred slightly more than 20 miles northeast of the site. This event occurred north of Jericho in 1900, and was the largest reported event in the area. The nearest source of water induced vibrations is the Sevier River, located approximately 3.2 miles to the southeast. The nearest airport is Delta Municipal Airport, located 3.5 miles to the south.

Commercial air route V21 crosses the antenna alignment. The minimum enroute altitude of this route is 10,300 ft. Commercial air route V257 crosses the southwest arm of the alignment; this route has a minimum altitude of 11,000 ft.

2.3.11 Plains of San Augustin, New Mexico

The Plains of San Augustin are located 60 miles west of Socorro along Route 60 between Datil and Magdalena. The candidate site is located on the following USGS topographic guadrangles: Augustin Well, Lion Mountain, Lion Mountain NW, and Arrowhead Well (1:24,000 scale). The site location is shown in Figure 2.3-11.

The Very Large Array (VLA), a radio telescope operated by the National Radio Astronomy Observatory, (NRAO), is located in this area. The telescope consists of a Y-shaped configuration of tracks with arms 13, 13, and 11.8 miles long. Varying arrangements of 28 mobile radio antennae are placed along this configuration. The NRAO has obtained a right-of-way for the VLA from public agencies and private land owners. The width of the right of way is typically 500 to 600 ft.[17]

A candidate site for the antenna is located 8 miles northwest from the vertex of the VLA. This location was selected for study because the antenna alignment does not cross light duty roads. The intersection of the arms would be located at latitude N. 34°12' and longitude W. 107°41'. The bearings of the arms would be N. 40° E. and S. 50° E. between el 7,000 and 7,030 ft. Route 60 is located 4.8 miles south at its closest approach to the alignment.

The alignment crosses 3 unimproved roads. There are several windmills and wells located in the area, so it should be possible to obtain water onsite by drilling a well. Electric power lines serve the VLA headquarter area approximately 8 miles away.[18] The area is located in an uncontrolled air space up to 14,500 ft mean sea level, with the closest airport being Socorro 60 miles to the east. The nearest commercial air route is V264, approximately 5 miles to the north. The minimum enroute altitude for this route is 12,000 ft. The site is not located in a seismic zone. No earthquakes have been reported within 20 miles of the site.

A land ownership map of the VLA site area[19] covers approximately two-thirds of the candidate site. The lands appear to be owned by the State of New Mexico and private landowners.

2.3.12 San Cristobal Valley, Arizona

This site was selected as a back-up to the site on Luke Air Force Range, in case access to the Range is prohibited. The site location is shown in Figure 2.3-12.

The site is located between the towns of Stoval and Dateland, Arizona, approximately 65 miles east of Yuma, Arizona. It is

north of Interstate 8 and south of the Gila River, on elevated land above the Gila River flood plain. Based on a summary map in the National Atlas of the USA,[20] it appears that the Bureau of Land Management administers scattered tracts (approximately 25-50 percent density) in this area.

The site is located on the USGS Texas Hill and Dateland Quadangles (1:24,000 scale). The intersection of the arms would be located approximately 3 miles west of Dateland, and approximately one mile north of Interstate 8, at latitude N. 32°47' and longitude W. 113°36'. The bearings of the antenna arms would be approximately N. 26° E. and N. 64° W. The NE arm would extend from approximate el of 410 to el 430 ft. The ground surface along the NW arm is at approximately el 410 ft. The antenna alignment crosses one unimproved road.

Access to this area is presently by unimproved road from Interstate 8. An Arizona Power Co. electric power line extends along Interstate 8 in the site area. The site is 1.2 miles south of the flood plain of the Gila River, and it should be possible to drill a well to obtain a supply of water at this location. The quality of groundwater in the area is unknown.

Two earthquakes have been reported in the Mohawk Mountains, approximately 20 miles south of the antenna alignment. One event occurred in 1958 and had a local magnitude of 4.9. The other event occurred in 1942; no magnitude or epicentral intensity has been assigned to this event.

Both Interstate 8 and the Southern Pacific Railroad are located approximately one mile south of the antenna alignment. The Dateland Airfield is located approximately 2.8 miles east of the site and Stoval Airfield is located approximately 3.5 miles to the southwest. Activity at these airports is probably restricted to small aircraft. The site lies below commercial air route V66, which has a minimum enroute altitude of 4,000 feet in the site area. Other aircraft activity in the site area would be that associated with the Luke Air Force Range located approximately two miles south of the proposed antenna location. The Gila River, and a drain located approximately 0.8 miles west of the site, are potential sources of water induced vibrations.

2.3.13 White Sands Missile Range, New Mexico

The White Sands Missile Range is located in southern New Mexico between Las Cruces and Soccoro. A possible site is located approximately 30 miles southwest of Alamogordo along U.S. Route 70. The site location is shown on Figure 2.3-13.

The site is located on USGS Lake Lucero SE and Lake Lucero SW quandrangles (1:24,000 scale). The intersection of the arms

would be at latitude N. 32°36' and longitude W. 106°23'. One arm would bear due east between el 3,935 and 3,975 ft. The other arm would bear due south between el 3,925 and to 3,935 ft. Route 70 is one mile east and a light duty road is located 0.2 miles west of this site. The antenna would cross one unimproved road.

Electric power and water appear to be accessible. At this site, power lines run along Route 70 and windmills are located throughout the area. Saunders Ranch is 1.6 miles southwest of the intersection of the arms, and the S. K. White Ranch is 1.25 miles west of the southern end.

Fort Bliss Anti-Aircraft Range is east of the site. A bomb target is located seven miles east and block house targets are located nine miles east-southeast of the east end of the antenna location. The site is located in uncontrolled air space, and there are no commercial air routes in the area. Alamogordo and Holloman airfields are 15 miles to the east. The site is in the Rio Grande Rift Zone. However, no earthquakes have been reported within 20 miles of the site.

2.4 REFERENCES FOR SURFACE SITES

2.4.1 Literature Cited

1. Bollinger, G.A. Seismicity of the Southeastern United States. Bulletin of the Seismological Society of America, Vol. 63, No. 5, October 1973.

2. Nuttli, O.W. The Seismicity of the Central United States. Geological Society of America. Reviews in Engineering Geology, Vol. 4, pp. 67-93, 1979.

3. Smith, R.B. and Sbar, M.L. Contemporary Tectonics and Seismicity of the Western United States with Emphasis on the Intermountain Seismic Belt. Geological Society of America Bulletin, Vol. 85, pp. 1205-1218, 1974

4. Sbar, M.L. and Sykes, L.R. Seismicity and Lithospheric Stress in New York and Adjacent Areas. Jour. Geophys. Res. V 82, pp. 5771-5786, 1977

5. Rand McNally Road Atlas of United States, Canada, and Mexico. Rand McNally & Company, 1983.

6. Barstow, N.L.; Brill, K.G., Jr.; Nuttli, O.W.; and Pomeroy, P.W. An Approach to Seismic Zonation for Siting Nuclear Electric Power Generating Facilities in the Eastern United States. NUREG/CR-1557. U. S. Nuclear Regulatory Commission, 1981.

7. Southern California Edison Company (SCE). San Onofre Nuclear Generating Station, Units 2 and 3. Preliminary Safety Report, Vol 3, App. 2C. SCE, 1970.

8. San Diego Gas & Electric Company (SDG&E). Sundesert Nuclear Plant Units 1 and 2, Preliminary Safety Analysis Report, App. A, Vol. 2. SDG&E, 1979.

9. Pacific Gas & Electric Company (PG&E). Diablo Canyon Preliminary Safety Analysis Report, Vol 3, App. C. PG&E, 1973.

10. Public Service Company of Colorado (PSC). Fort St. Vrain Final Safety Analysis Report, Vol 1. PSC, 1968.

11. Washington Public Power Supply System (WPPS). Nuclear Project No. 2. Final Safety Analysis Report, Vol 2 and 6. WPPS, 1977.

12. U. S. National Oceanic and Atmospheric Administration (NOAA). Enroute Low Attitude Flight Maps of United States. NOAA, 1983.

13. Abston, C. NOAA Earthquake Catalogue. U. S. National Oceanic and Atmospheric Administration, 1977.

14. Lines, G.C. Hydrology and Surface Morphology of the Bonneville Salt Flats and Pilot Valley Playa, Utah. U.S. Geological Survey Water Supply Paper No. 2057, 1979.

15. Areas of Responsibility and Land Status Map, State of Utah. U.S. Bureau of Land Management, 1977.

16. Lines, G.C. Selected Ground-Water Data, Bonneville Salt Flats and Pilot Valley, Western Utah. Utah Basic Data Release No. 30. U.S. Geological Survey, 1978.

17. Marymore, J. National Radio Astronomy Observatory. Personal Communication, 1983.

18. Sky and Telescope. The VLA Takes Shape. November, 1976.

19. Oster, L. National Science Foundation. Personal Communication, 1983.

20. The National Atlas of the United States of America, United States Geological Survey, pp. 272-273, 1970.

2.4.2 Organizations Contacted

Organization	Contact	Location and Telephone No.
Public Service Company of Colorado	Commercial Sales	Alamosa, CO (303) 882-3015
Southern California Edison Company	Commercial Sales	Twenty-Nine Palms, CA (714) 875-4290
Ft. Bliss Military Reservation	Physical Plant Engineer	Ft. Bliss, TX (915) 568-2121)
Utah Power & Light Company	Commercial Sales	Tooele, UT (801) 882-2238
Arizona Public Service Co.	Commercial Sales	Gila Bend, AZ (602) 683-2271
National Science Foundation	Dr. L. Oster, VLA Program Director	Washington, DC (202) 357-9857
National Radio Astronomy Observation	J. Marymore Legal Relations	Charlottesville, VA (804) 296-0211

TABLE 2.2-1

GOVERNMENT INSTALLATIONS CONSIDERED

1. Fort Lewis Military Reservation
2. Yakima Firing Range Military Reservation
3. Hanford Works (USDOE)
4. Beale A.F.B.
5. Fort Ord Military Reservation
6. Hunter Liggett Military Reservation
7. China Lake Naval Weapons Center
8. China Lake Naval Weapons Center
9. Fort Irwin Military Reservation
10. Edwards Air Force Base
11. Twentynine Palms Marine Corps Base
12. Camp Pendleton Marine Corps Base
13. Miramar Naval Air Station
14. National Parachute Test Range
15. Yuma Proving Ground
16. Luke Air Force Range
17. Nellis Bombing & Gunnery Range Complex
18. Dugway Proving Grounds
19. Desert Test Center
20. Wendover Range
21. Hill Air Force Range
22. Idaho National Engineering Laboratory
23. Rocky Mountain Arsenal
24. Fort Carson Military Reservation
25. Sandia Military Reservation
26. White Sands Missile Range
27. Fort Bliss Military Reservation
28. Lackland Air Force Base
29. Fort Hood Military Reservation
30. Fort Sill Military Reservation
31. Naval Ammunition Depot
32. Fort Riley Military Reservation
33. Camp Ripley Military Reservation
34. Fort Leonard Wood Military Reservation
35. Fort Chaffee Military Reservation
36. Fort Polk Military Reservation
37. Eglin Air Force Base
38. Fort Rucker Military Reservation
39. Fort Benning Military Reservation
40. Fort McClellan Military Reservation
41. Redstone Arsenal
42. Arnold Engineering Development Center
43. Oak Ridge National Laboratory
44. Fort Campbell Military Reservation
45. Blue Grass Army Depot
46. Fort Knox Military Reservation

TABLE 2.2-2 (Cont)

State	Installation or Area	Suitable (S) or Unsuitable (U)	Reason for Unsuitability
Indiana	Camp Atterbury	U	Topography, Land Use
Indiana	Crane Naval Weapons Support Center	U	Topography
Indiana	Jefferson Proving Ground	U	Topography
Kansas	Fort Riley Military Reservation	U	Topography, Land Use
Kentucky	Blue Grass Army Depot	U	Too developed
Kentucky	Fort Knox Military Reservation	U	Topography
Louisianna	Fort Polk Military Reservation	U	Topography
Maine	Entire State	U	Topography, Land Use
Maryland	Aberdeen Proving Ground	U	Insufficient Space
Maryland	National Agricultural Research Center	U	Insufficient Space
Massachusetts	Entire State	U	Topography, Land Use
Michigan	Camp Grayling Military Reservation	U	Topography
Minnesota	Camp Ripley Military Reservation	U	Topography, Drainage
Missouri	Fort Leonard Wood Military Reservation	U	Topography
Nebraska	Entire State	U	Topography, Land Use
Nevada	Nellis Bombing and Gunnery Range Complex	U	Topography, Drainage Land Use
New Hampshire	Entire State	U	Topography, Land Use
New Jersey	Entire State	U	Topography, Land Use
New Mexico	Fort Bliss Military Reservation	S	-
New Mexico	Sandia Military Reservation	U	Topography
New Mexico	Plains of San Augustin	S	-
New Mexico	White Sands Missle Range	S	-
New York	Entire State	U	Topography, Land Use
North Carolina	Entire State	U	Topography, Land Use, Drainage

TABLE 2.2-2 (Cont)

State	Installation or Area	Suitable (S) or Unsuitable (U)	Reason for Unsuitability
Oklahoma	Fort Sill Military Reservation	U	Topography
Oklahoma	Naval Ammunition Depot	U	Topography
Rhode Island	Entire State	U	Topography, Land Use
South Carolina	Fort Jackson Military Reservation	U	Topography
South Carolina	Savannah River Plant	U	Topography, Land Use
Tennessee	Arnold Engineering Development Center	U	Topography
Tennessee	Fort Campbell Military Reservation	U	Topography
Tennessee	Oak Ridge National Laboratory	U	Topography
Texas	Fort Hood Military Reservation	U	Topography
Texas	Lackland Air Force Base Training Annex	U	Insufficient Room
Utah	Desert Range Experimental Station	U	Topography
Utah	Great Salt Lake Desert	S	-
Utah	Lynndyl	S	-
Vermont	Entire State	U	Topography, Land Use
Virginia	Fort Eustis Military Reservation	U	Insufficient Space
Virginia	Fort A.P. Hill Military Reservation	U	Topography
Virginia	Fort Pickett Military Reservation	U	Topography
Virginia	Quantico Marine Corps Air Station	U	Topography
Washington	Fort Lewis	U	Seismicity
Washington	Hanford Reservation	U	Topography, Land Use
Washington	Yakima Firing Center	U	Bombing/Firing Range

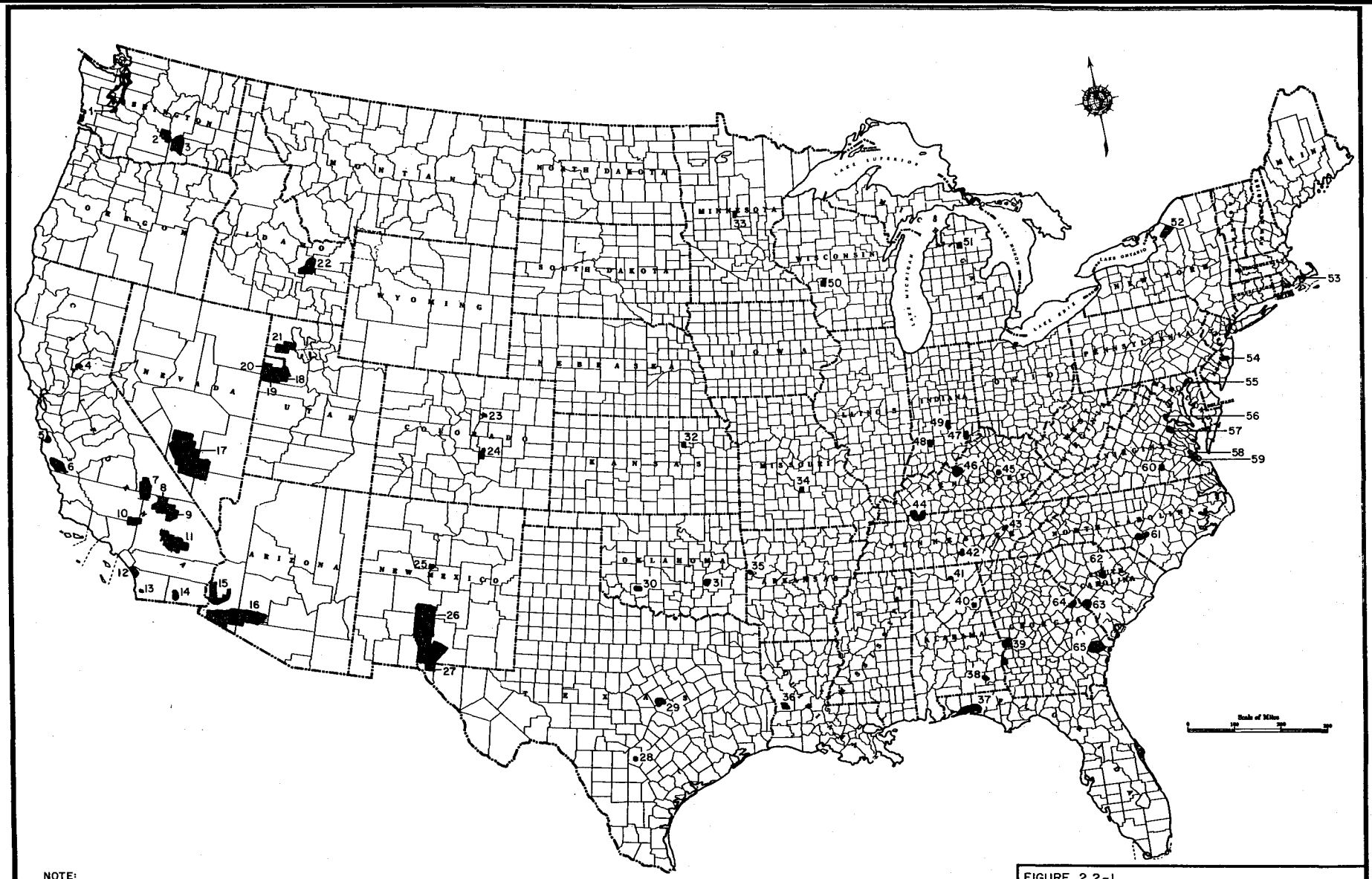

NOTE:
REFER TO TABLE 2.2-1 FOR
NAMES OF GOVERNMENT INSTALLATIONS
IDENTIFIED BY NUMBER IN THIS FIGURE.

FIGURE 2.2-1
LOCATIONS OF GOVERNMENT INSTALLATIONS
GWA SITING STUDY
STONE & WEBSTER ENGINEERING CORPORATION

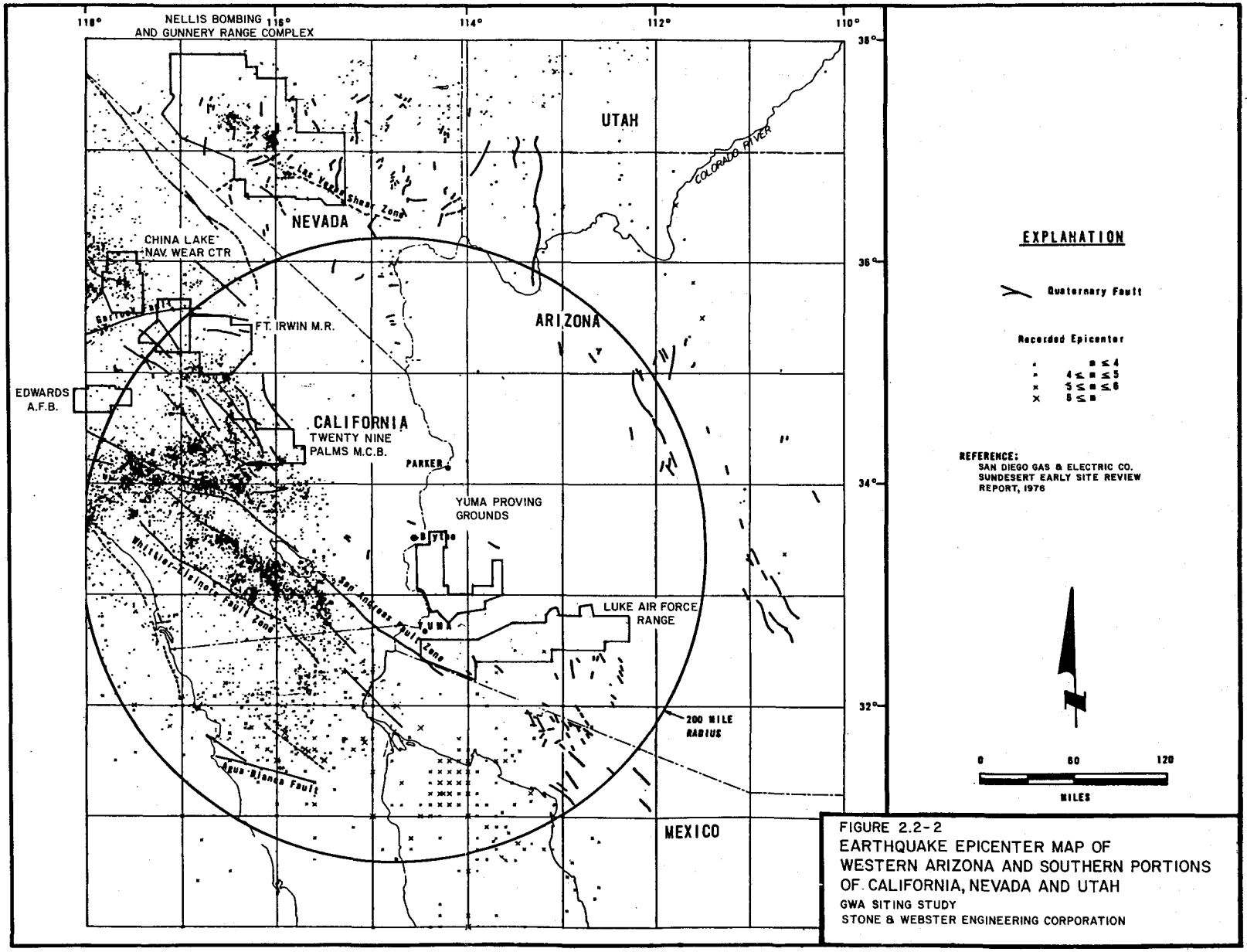

FIGURE 2.2-2
EARTHQUAKE EPICENTER MAP OF WESTERN ARIZONA AND SOUTHERN PORTIONS OF CALIFORNIA, NEVADA AND UTAH
GWA SITING STUDY
STONE & WEBSTER ENGINEERING CORPORATION

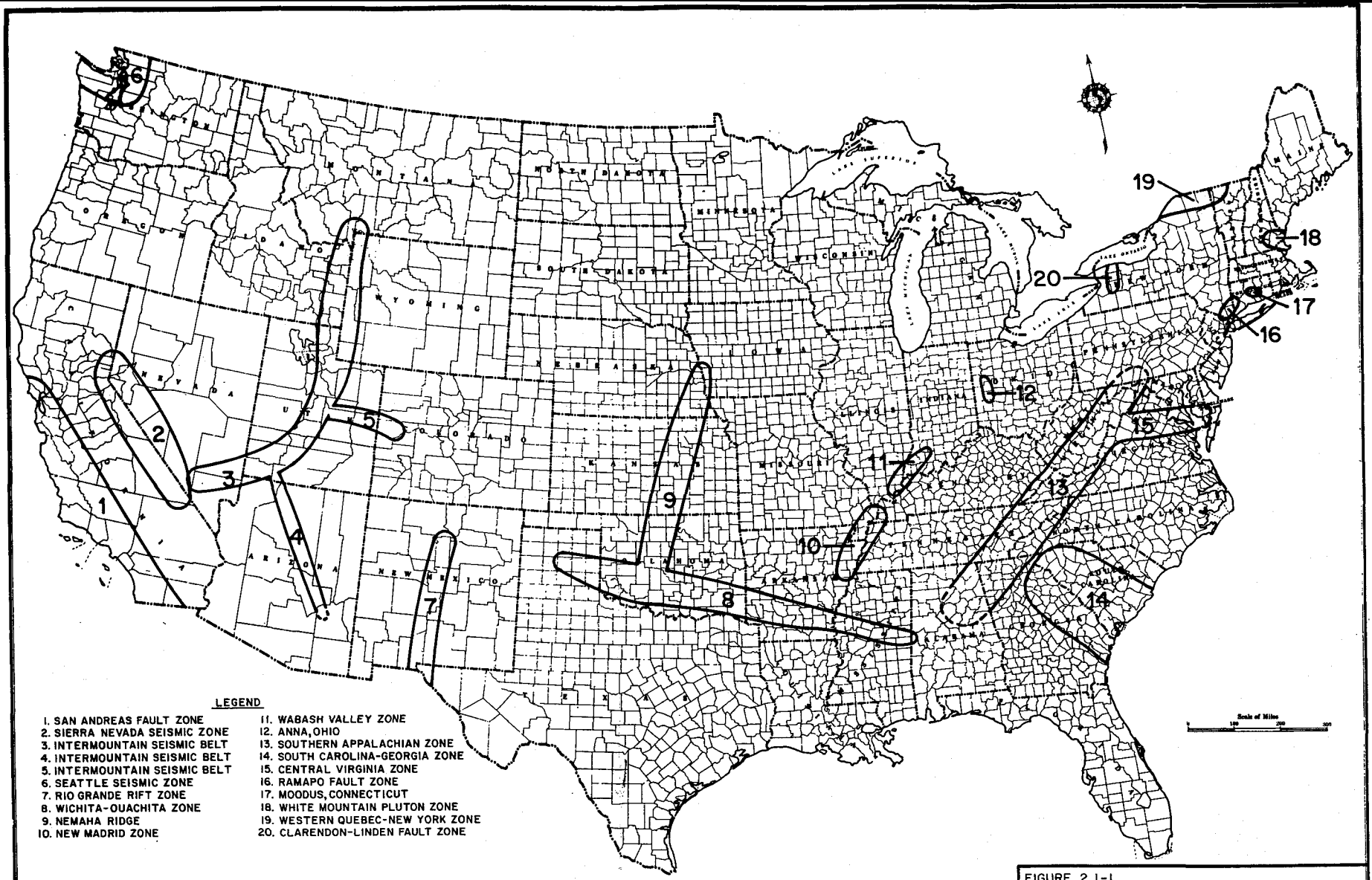

FIGURE 2.1-1
LOCATIONS OF SEISMIC ZONES
GWA SITING STUDY
STONE & WEBSTER ENGINEERING CORPORATION

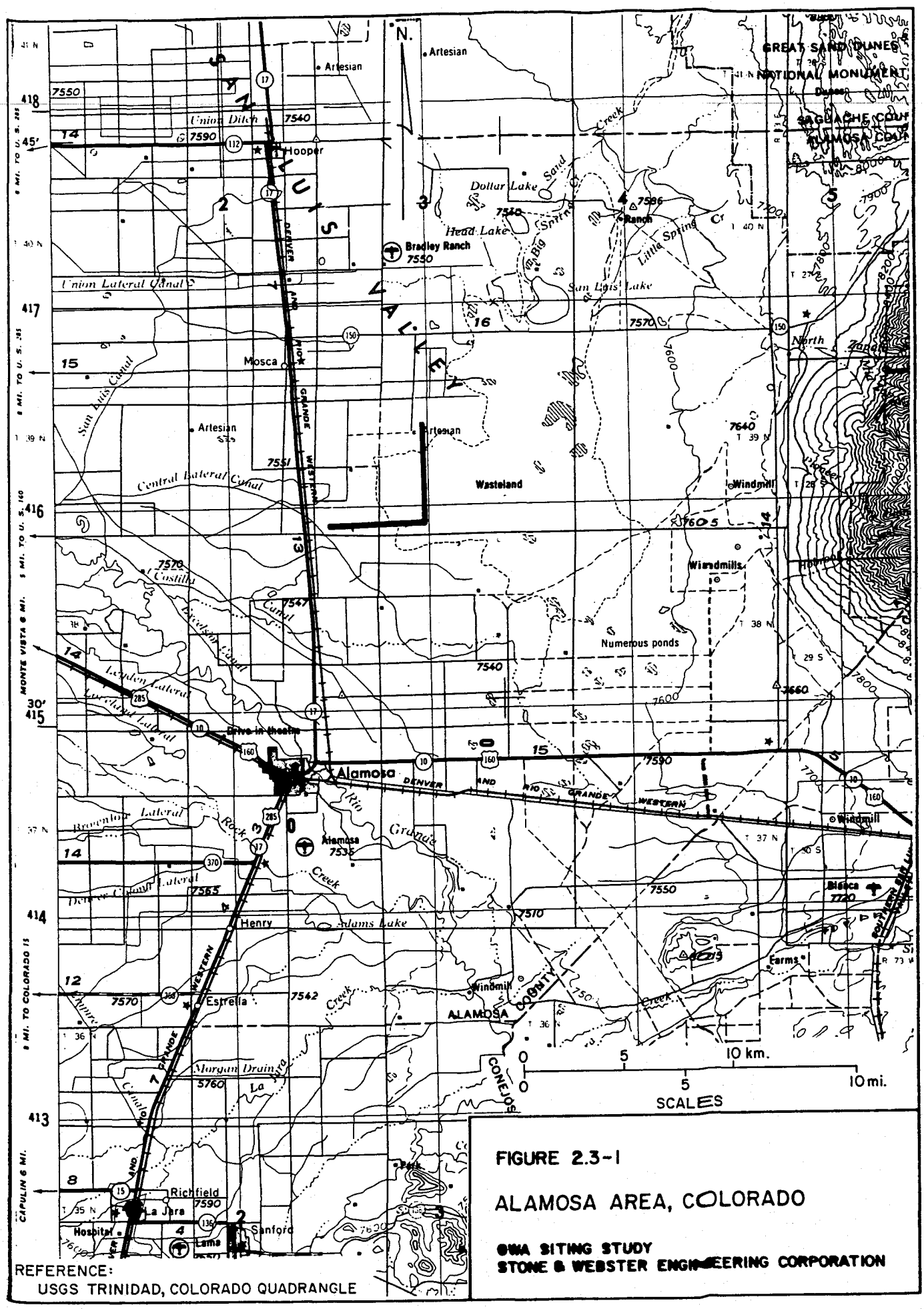

REFERENCE:
USGS TRINIDAD, COLORADO QUADRANGLE

FIGURE 2.3-1

ALAMOSA AREA, COLORADO

SWA SITING STUDY
STONE & WEBSTER ENGINEERING CORPORATION

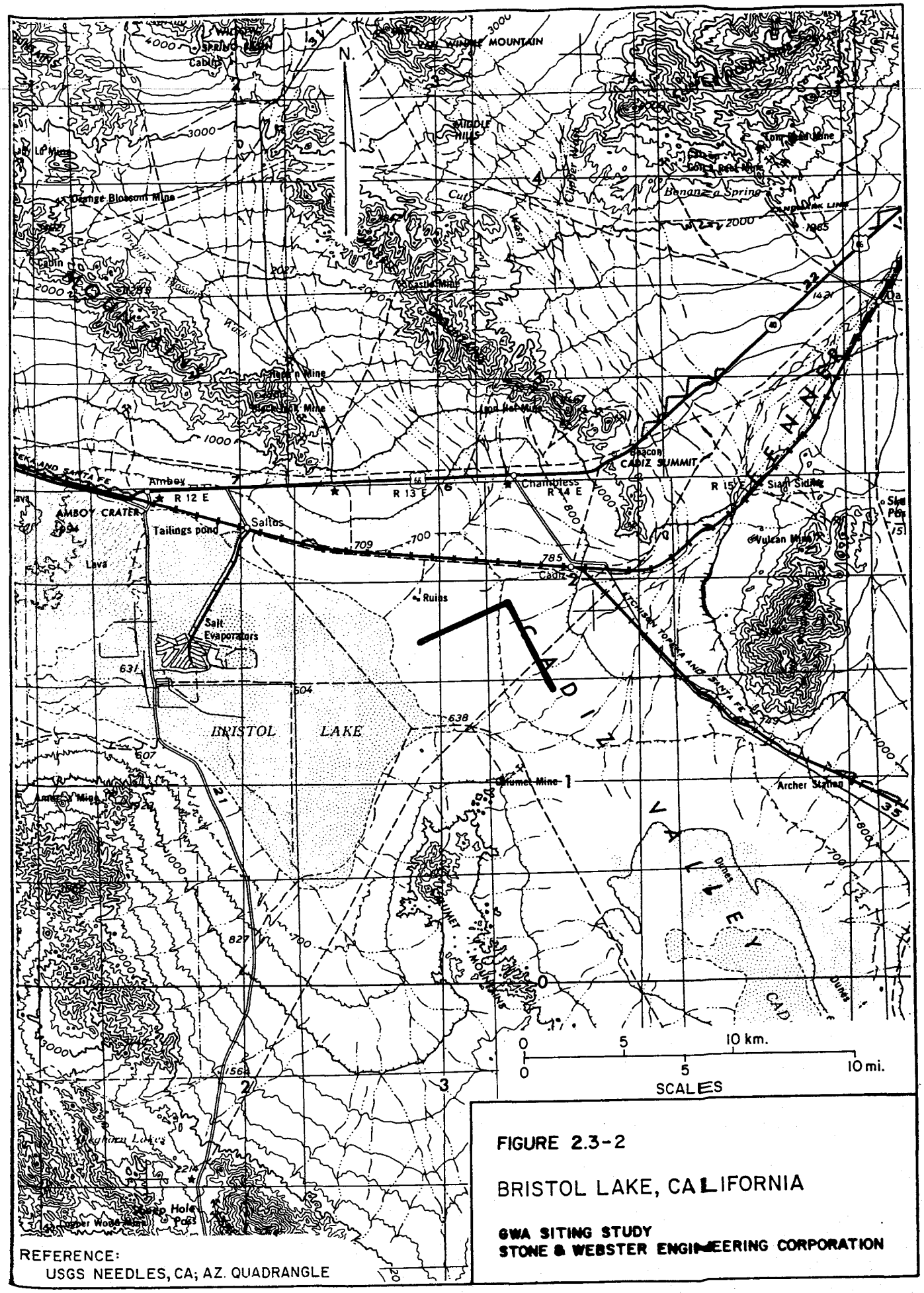

REFERENCE:
USGS NEEDLES, CA; AZ. QUADRANGLE

FIGURE 2.3-2

BRISTOL LAKE, CALIFORNIA

GWA SITING STUDY
STONE & WEBSTER ENGINEERING CORPORATION

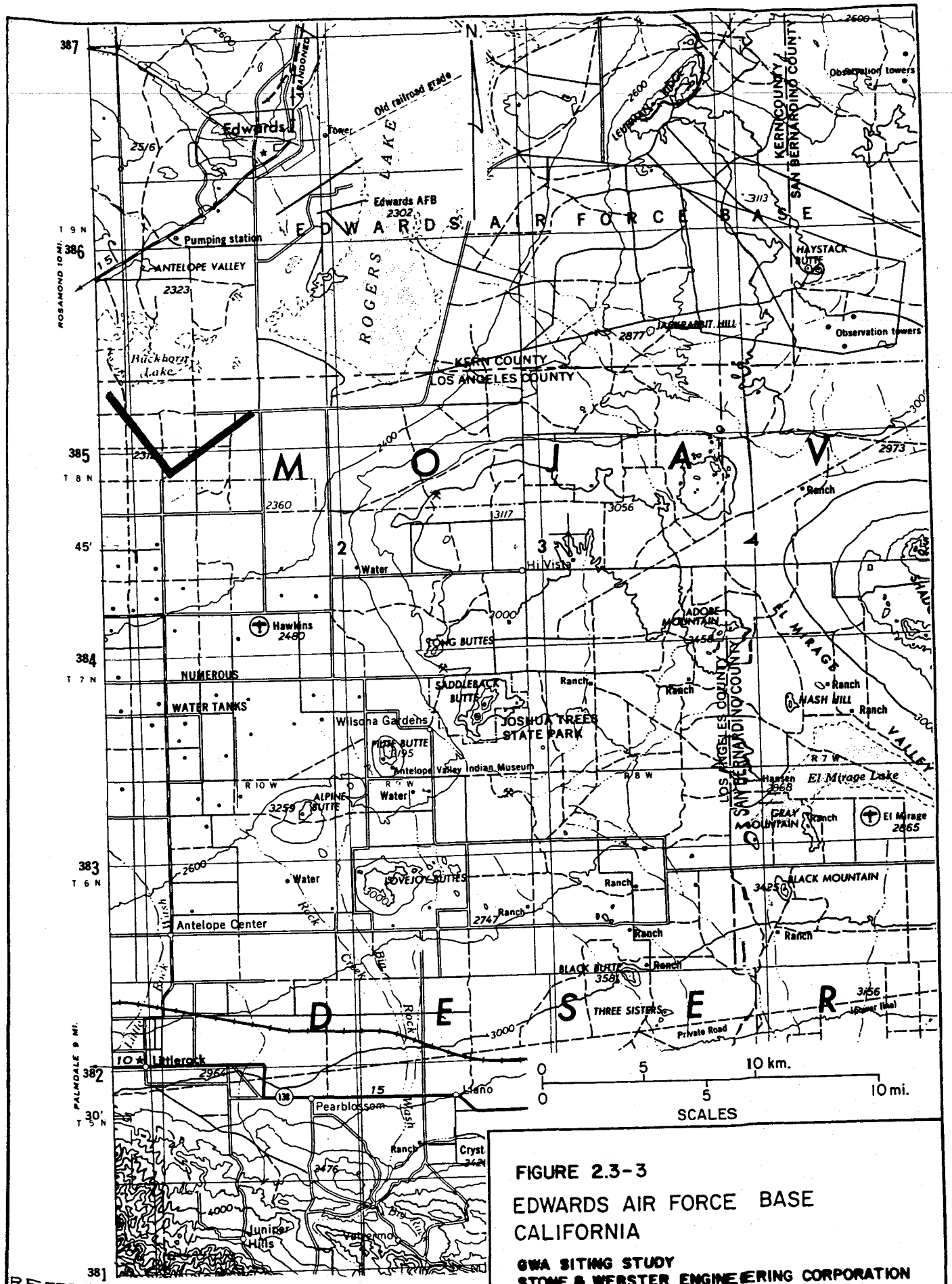

REFERENCE:
USGS SAN BERNARDINO, CALIFORNIA QUADRANGLE

FIGURE 2.3-3

EDWARDS AIR FORCE BASE
CALIFORNIA

GWA SITING STUDY
STONE & WEBSTER ENGINEERING CORPORATION

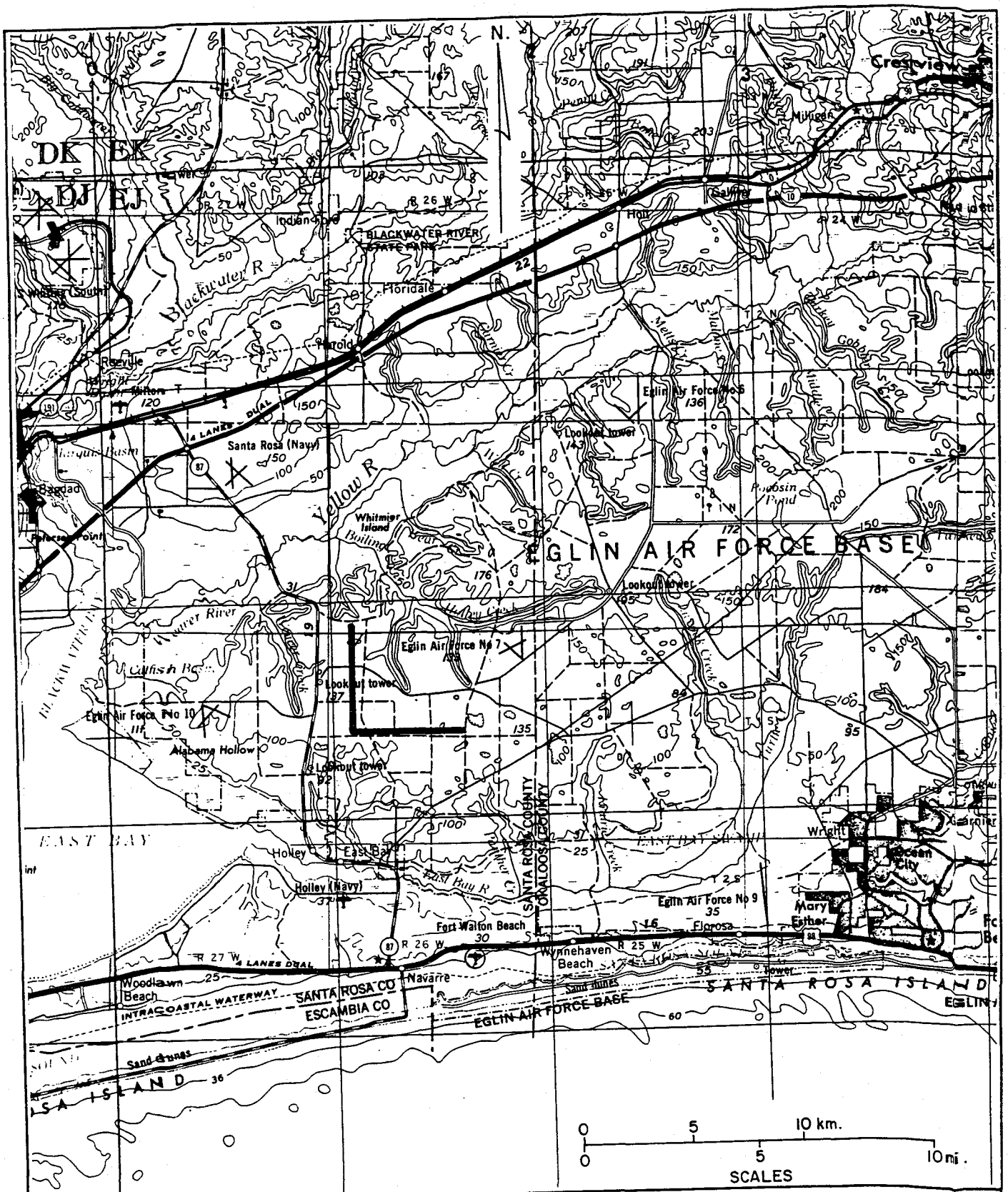

FIGURE 2.3-4

EGLIN AIR FORCE BASE, FLORIDA

GWA SITING STUDY
STONE & WEBSTER ENGINEERING CORPORATION

REFERENCE:
USGS PENSACOLA, FLORIDA QUADRANGLE

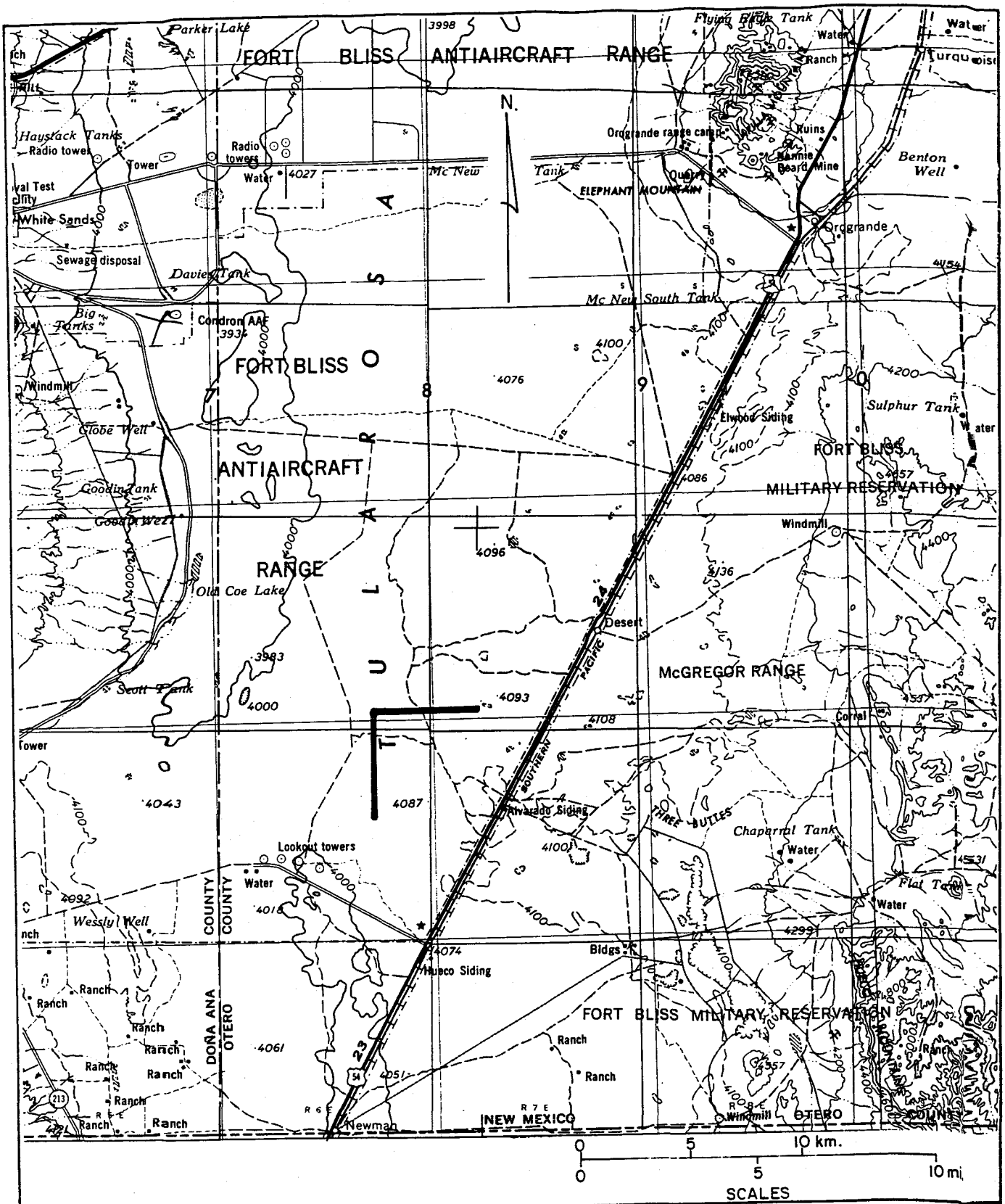

FIGURE 2.3-5

FORT BLISS, NEW MEXICO

GWA SITING STUDY
STONE & WEBSTER ENGINEERING CORPORATION

REFERENCE:
USGS LAS CRUCES, NEW MEXICO; TEXAS QUADRANGLE

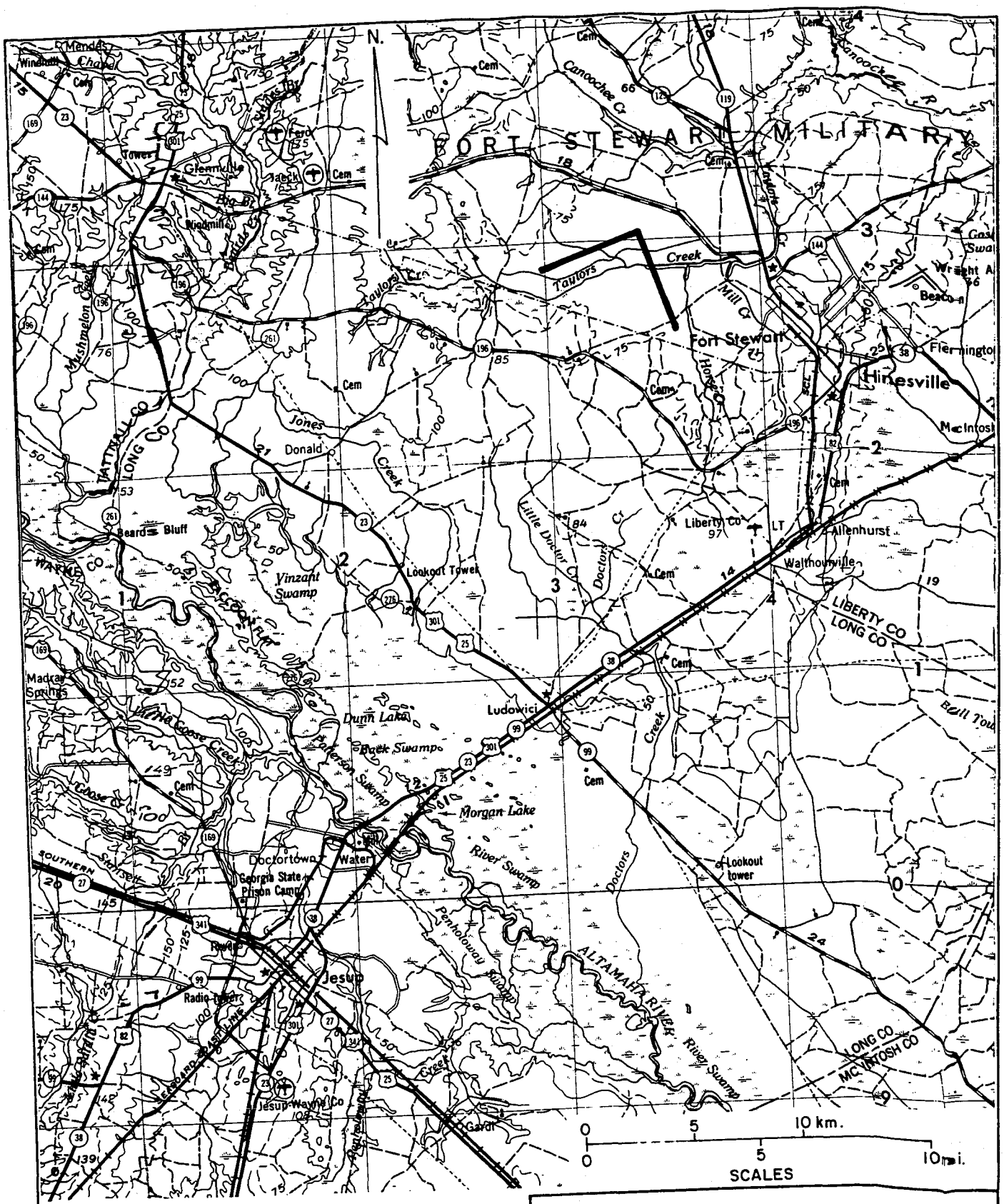

FIGURE 2.3-6

FORT STEWART, GEORGIA

GWA SITING STUDY
STONE & WEBSTER ENGINEERING CORPORATION

REFERENCE :
USGS BRUNSWICK, GEORGIA QUADRANGLE

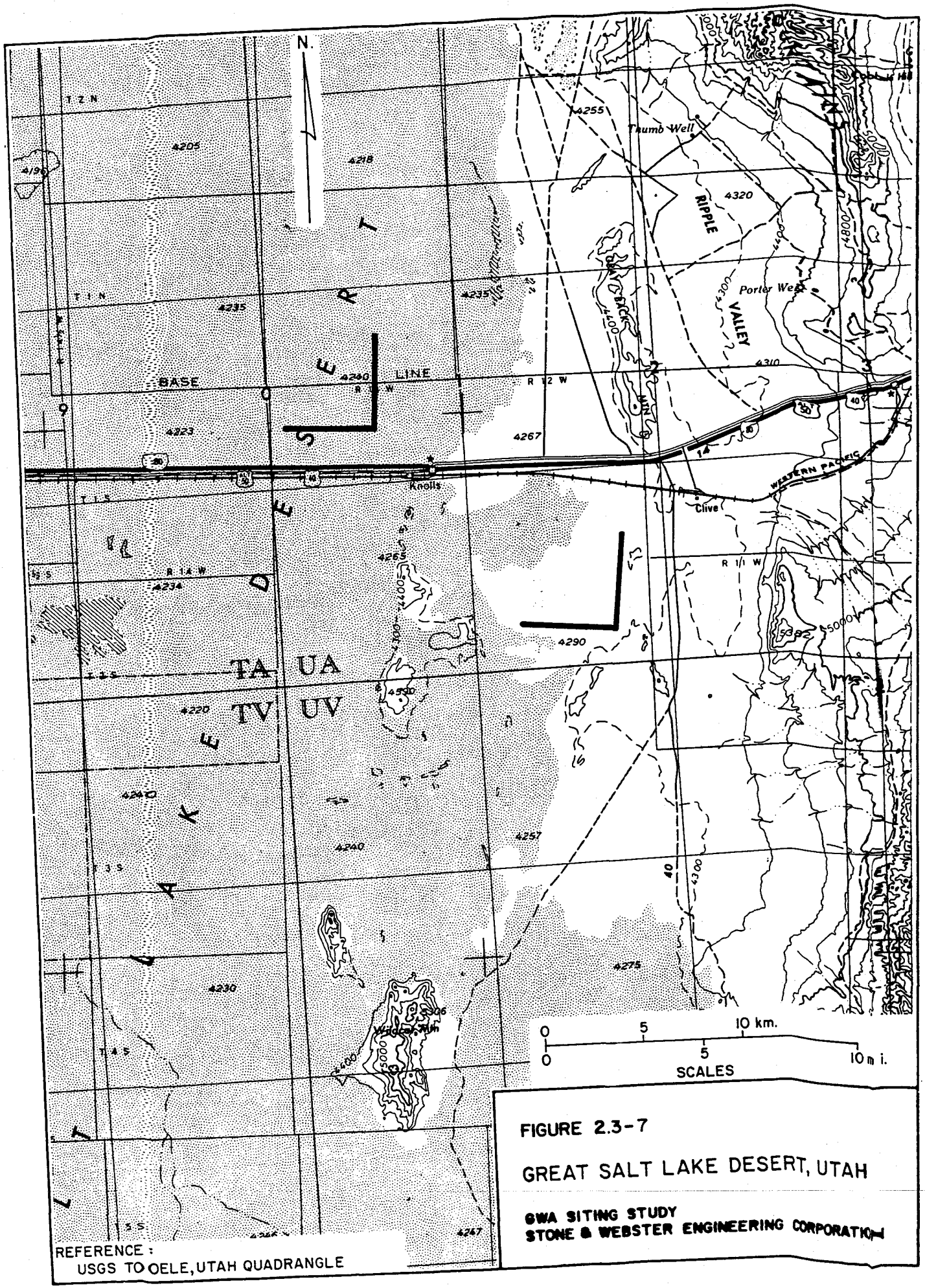

REFERENCE :
USGS TOOELE, UTAH QUADRANGLE

FIGURE 2.3-7

GREAT SALT LAKE DESERT, UTAH

GWA SITING STUDY
STONE & WEBSTER ENGINEERING CORPORATION

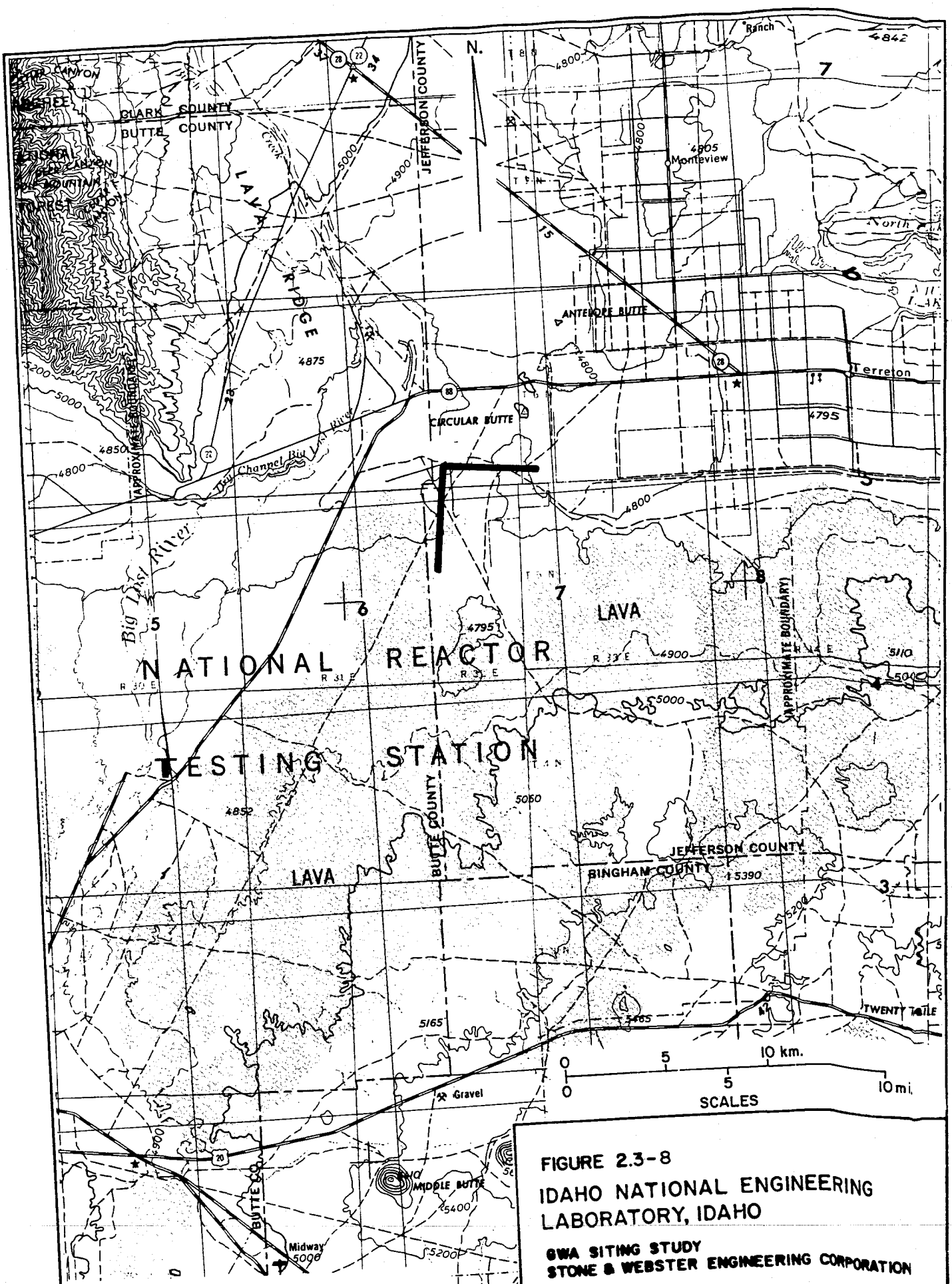

FIGURE 2.3-8

IDAHO NATIONAL ENGINEERING LABORATORY, IDAHO

GWA SITING STUDY
STONE & WEBSTER ENGINEERING CORPORATION

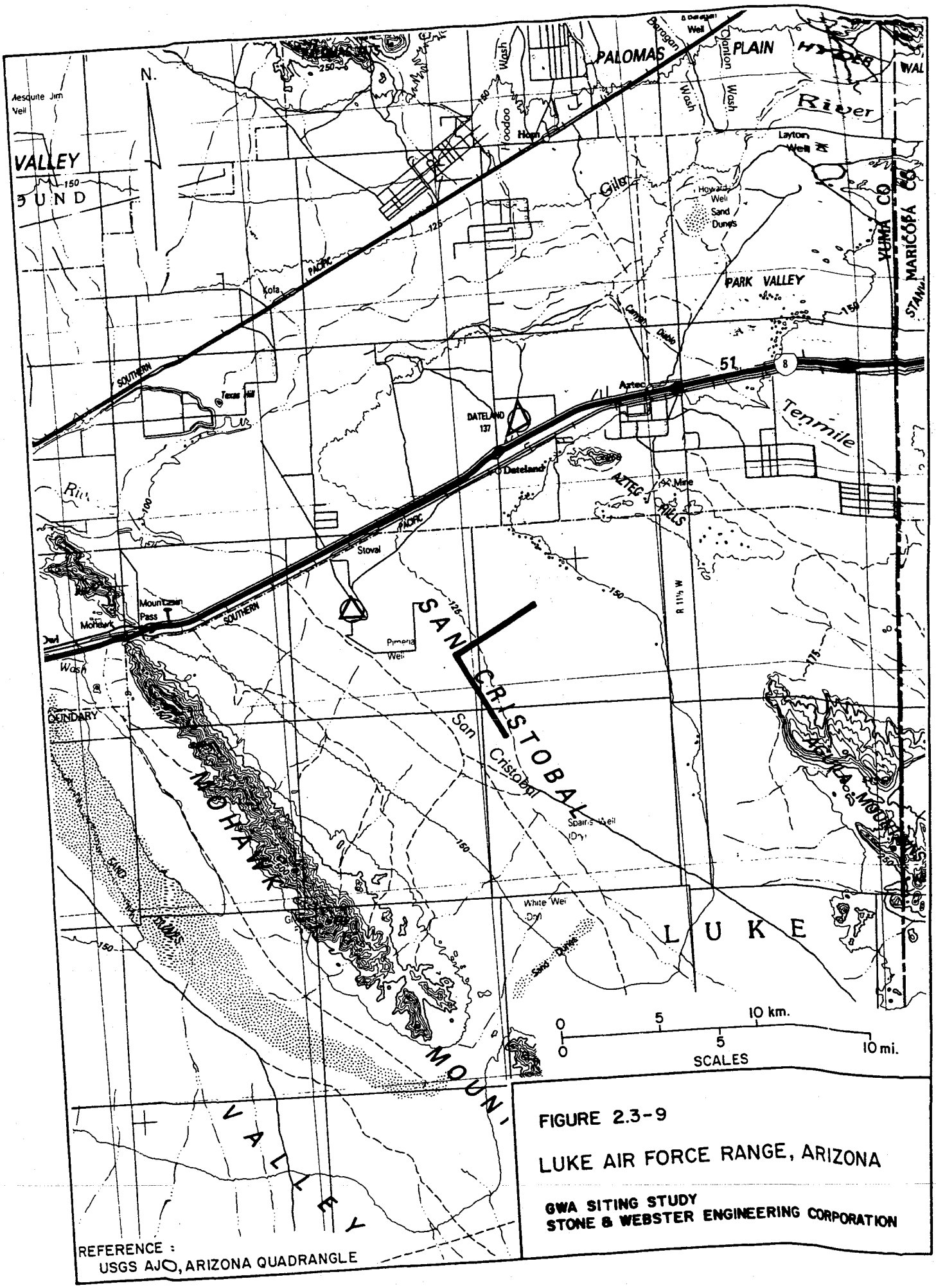

FIGURE 2.3-9

LUKE AIR FORCE RANGE, ARIZONA

GWA SITING STUDY
STONE & WEBSTER ENGINEERING CORPORATION

REFERENCE :
USGS AJO, ARIZONA QUADRANGLE

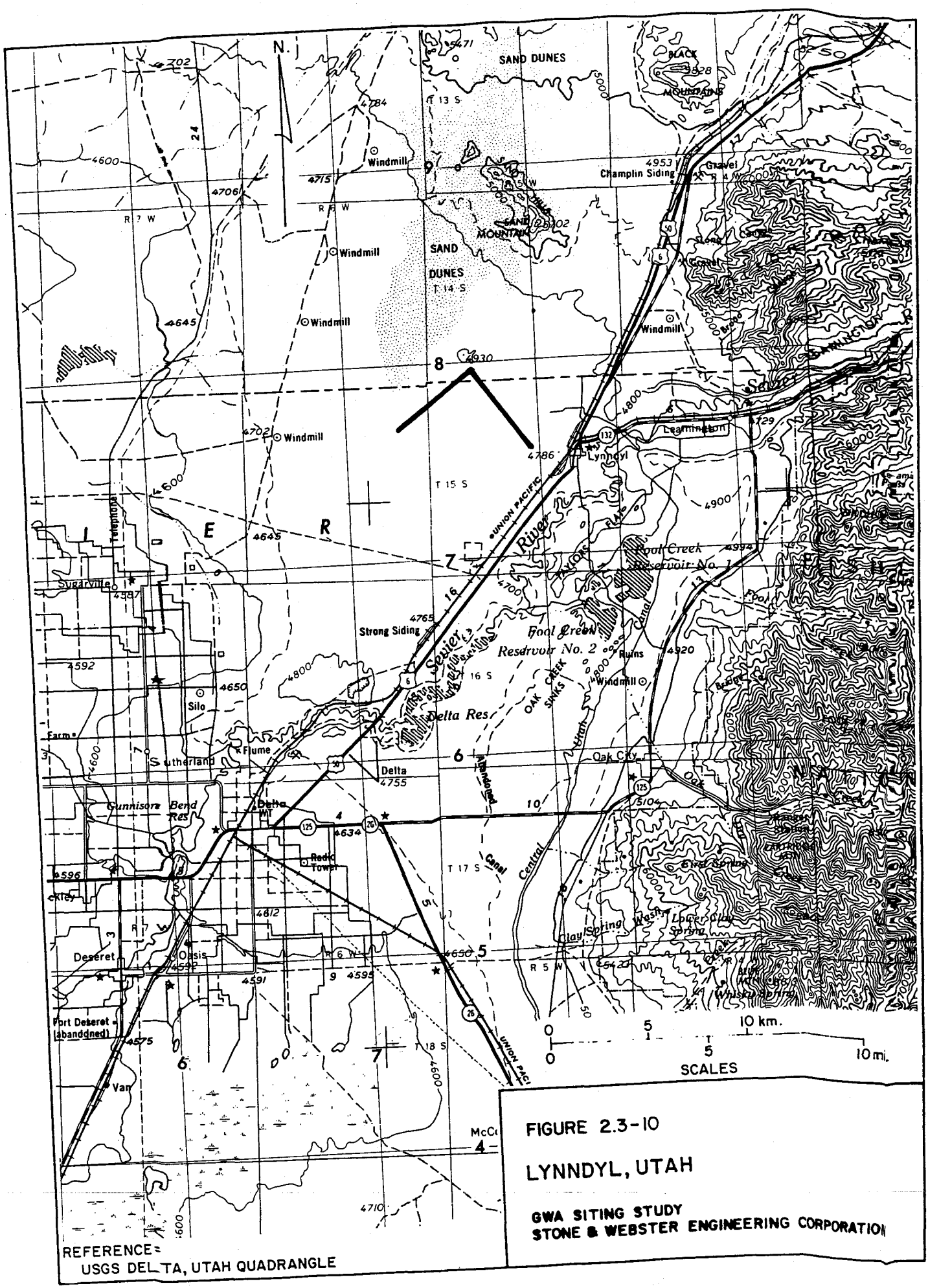

FIGURE 2.3-10

LYNNDYL, UTAH

GWA SITING STUDY
STONE & WEBSTER ENGINEERING CORPORATION

REFERENCE:
USGS DELTA, UTAH QUADRANGLE

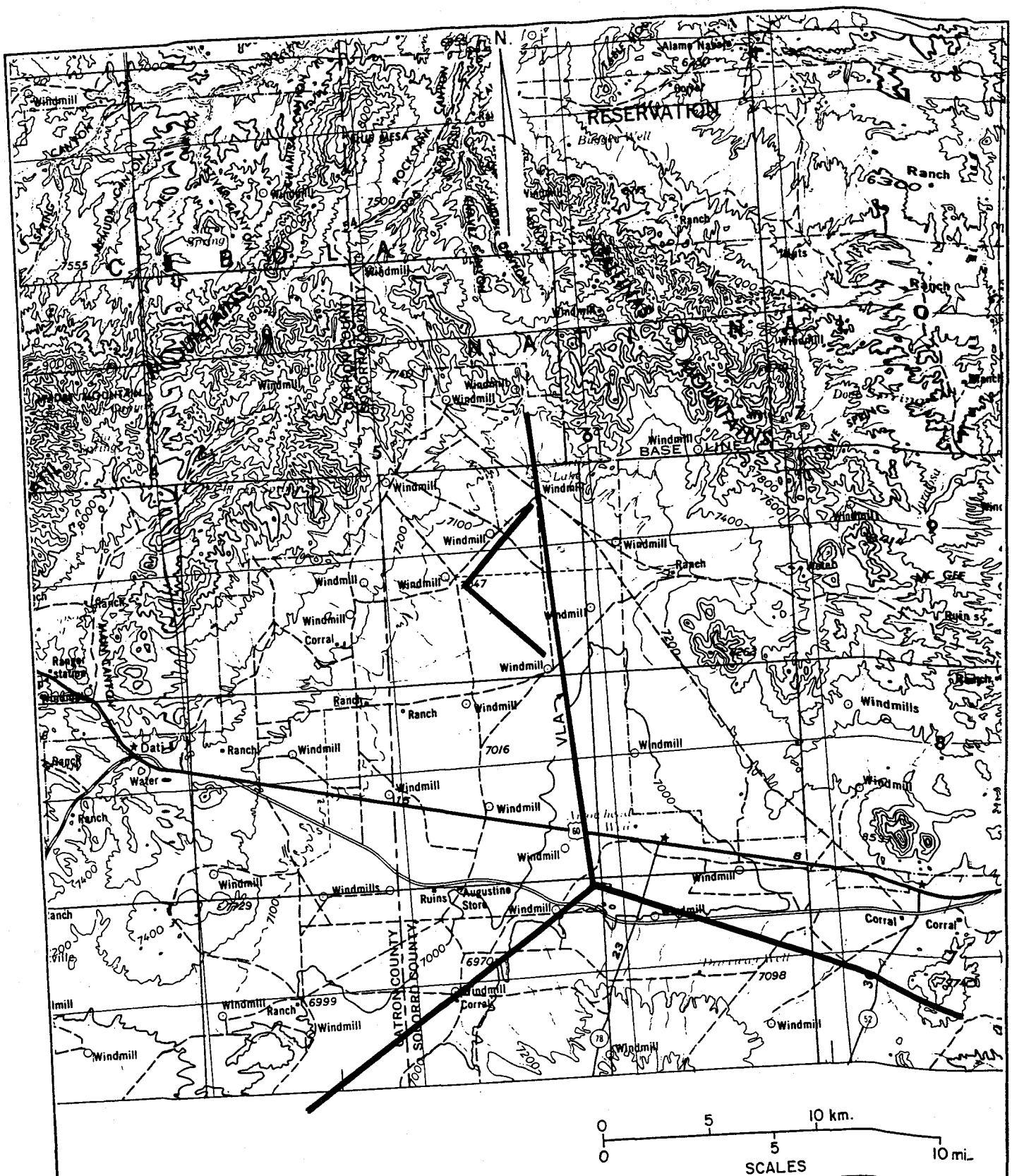

FIGURE 2.3-11

PLAINS OF SAN AUGUSTIN
NEW MEXICO

GWA SITING STUDY
STONE & WEBSTER ENGINEERING CORPORATION

REFERENCE :
USGS SOCORRO, NEW MEXICO QUADRANGLE

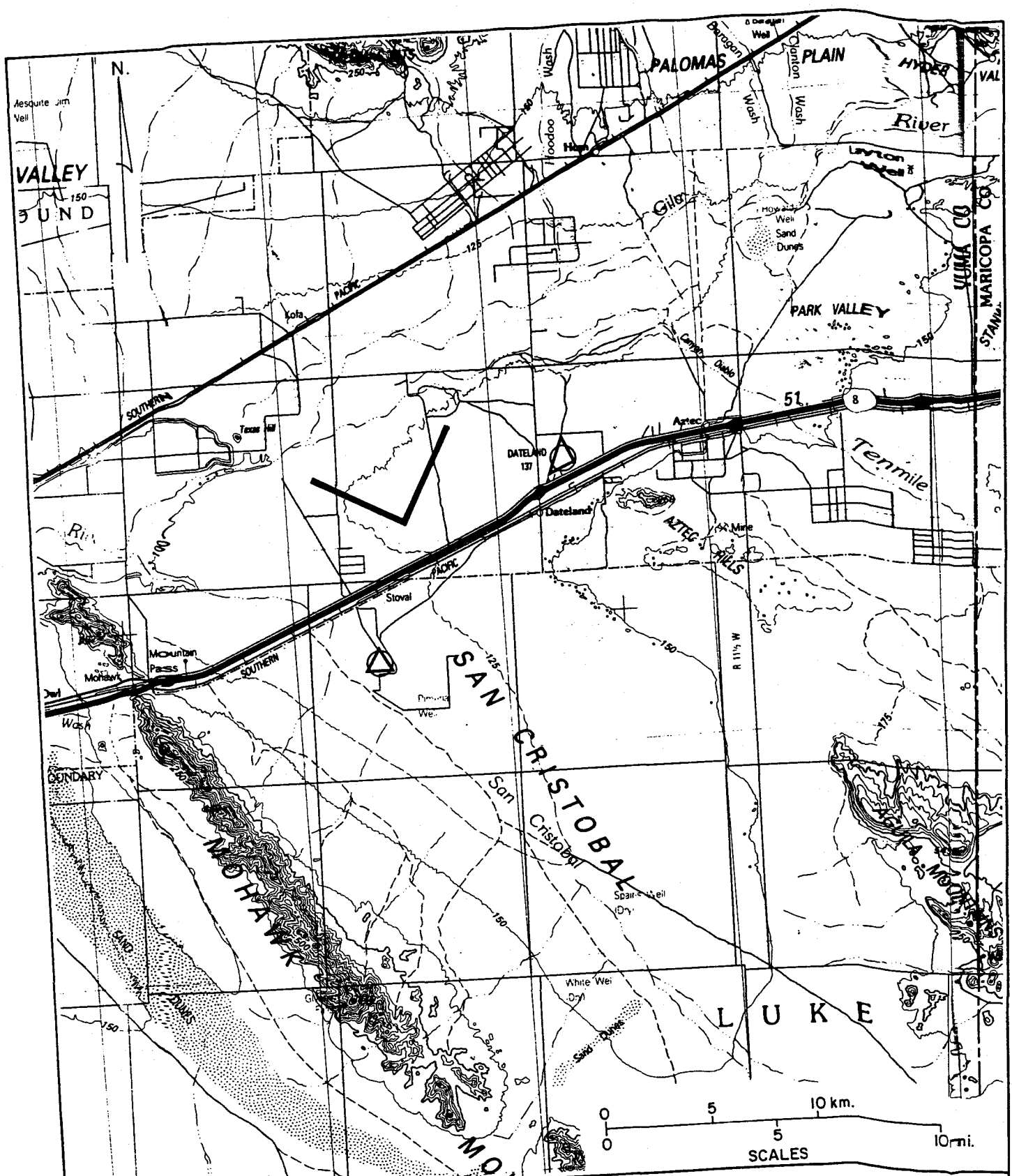

FIGURE 2.3-12

SAN CRISTOBAL VALLEY, ARIZONA

GWA SITING STUDY
STONE & WEBSTER ENGINEERING CORPORATION

REFERENCE:
USGS AJO, ARIZONA QUADRANGLE

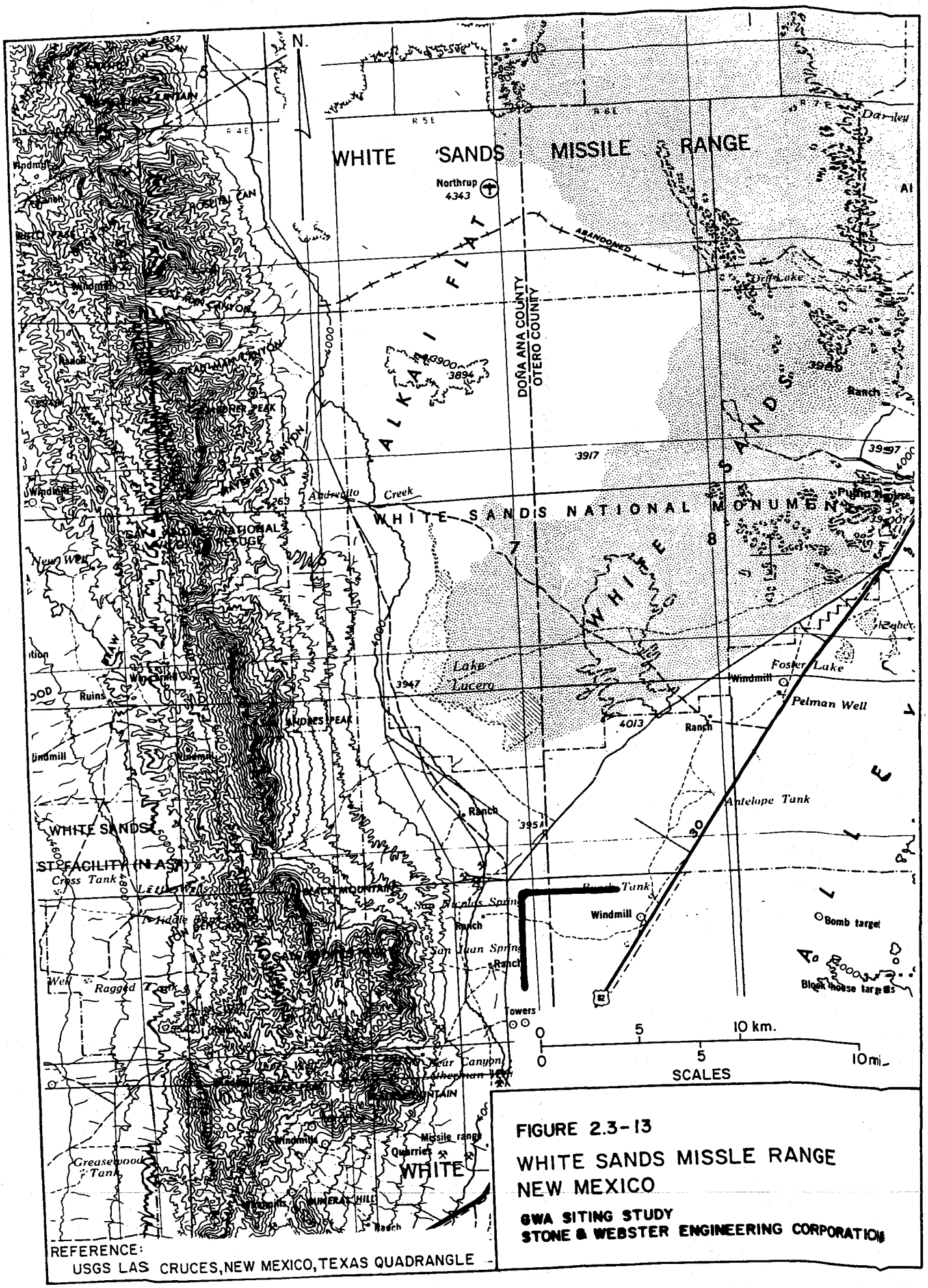

REFERENCE:
USGS LAS CRUCES, NEW MEXICO, TEXAS QUADRANGLE

FIGURE 2.3-13

WHITE SANDS MISSLE RANGE
NEW MEXICO

GWA SITING STUDY
STONE & WEBSTER ENGINEERING CORPORATION

3.0 SUBSURFACE SITES

There are a number of advantages in constructing an antenna of this type in a deep tunnel or mine. The antenna would be naturally isolated from many vibration sources, such as aircraft, railway and highway traffic. Temperatures at depth fluctuate much less than at the ground surface. The need to provide buildings to house support facilities might also be reduced.

For these reasons, a survey of existing mines and tunnels was performed to determine whether one or more of these facilities would be a suitable site for an L-shaped antenna with arms 5 km long. If no passages of this length exist, the study would identify the longest potentially suitable passages that might be available.

3.1 SITING CRITERIA FOR CANDIDATE SUBSURFACE SITES

The criteria for evaluating subsurface sites differs significantly from those for the surface sites. The major considerations for the subsurface sites are line-of-sight distances and configurations of passages. Additionally, other factors have been investigated.

Many mines are horizontally extensive, but few contain passages with substantial line-of-sight passages because this offers no inherent mining advantage. Most mineral deposits have irregular configurations, and the mines conform to those configurations. The mine site survey was directed toward those deposits which tend to form as planar ore bodies. Mineral occurrences that could be grouped in this category would include lead, zinc, copper, gypsum, salt, potash, limestone, trona (impure sodium carbonate), and coal. [1,2,3]

3.1.1 Passage Dimensions

Mine operators were asked for details concerning the existing underground passages. Additionally, operators were asked about the possibilities of modifying existing passages to give line-of-sight passages. The cross-sectional area of passages was also considered.

3.1.2 Passage Configuration

The right angle or near right angle configuration of the two passages was discussed. This configuration was not limited to the horizontal plane.

3.1.3 Type of Access

The type of access for transport tunnels, such as railroad, highway, and water is apparent. For mines, the type of access was discussed. Access to a mine can be by a horizontal passage (adit), inclined passage (decline or incline), or a vertical passage (shaft). Additionally, limitations were discussed that would have to be considered for movement of antenna equipment and material; for example, lengths of pipe to be used for the antenna.

3.1.4 Ground Stability and Groundwater Flow

Since mines are frequently located in areas of geological disturbances, such as mountainous regions, questions were asked concerning ground and rock stability. Groundwater flows and potential for water problems were also discussed.

3.1.5 Mining Activity

The projected levels of short-term and long-term mining activities were investigated. The possibility of utilizing disused mines to house the antenna was investigated.

The issue of projected mine activity is a complex one. Mine operators routinely make short-term projections about mining activities. Long-term projection are much more difficult to make since the operation of a mine is based upon the profitability of the operation. For many minerals a modest price change can cause the owner to change areas of mining activity or put the operation on standby status. A mine shutdown would not be as significant to a mine with a horizontal access passage as it would be to a mine with shaft access.

Also, projections of mining activity apply directly to the matter of mine maintenance. If a mine is situated in particulary stable rock, such as limestone, ground stability considerations are relatively unimportant. In mines with more complex geology and associated rock stability problems, mine maintenance is a major consideration and could represent a significant cost.

Maintenance costs of passages in an inactive mine would be higher than in an active mine due to the added costs of mobilization of equipment and personnel.

Depending upon the rock type and its acoustical characteristics, ambient vibration levels would probably be lower in a disused mine.

This question of projected mine activity and integrity of the passages has to be assessed carefully and on a mine by mine basis.

3.1.6 Depth Below Surface

Depths of passages below the surface were investigated.

3.1.7 Vibration and Seismicity

Depending upon the magnitude of the mining operation, techniques employed, proximity to potential host passages, rock type, and other variables, local mining activity may or may not produce significant vibration. The consideration of regional seismicity would be of the same importance as for surface sites. Zones of seismicity are shown in Figure 2.1-1. Most of the mines considered in this study are not found in these seismic zones.

3.1.8 Potential for Passage Modification

The possibility of passage modification including alteration of size or extension of length was discussed with the mine operators. The responses ranged from "not possible" due to rock stability or mineral claim boundaries to "possible" with the unit cost of excavation being the only real consideration.

3.1.9 Disposition Towards Participation

The willingness to provide a mine site for the antenna was discussed with those mine operations that met the majority of criteria already discussed. Of all of the criteria to be met in this study the length of time required to construct and operate the antenna was the most difficult consideration for the mine operators. Most operators were favorably disposed toward providing a site for a short time period. However, for the anticipated length of time for this experiment, only a few mines were interested. As it happens, these mines are among the most extensive of the underground facilities considered.

3.2 PROCEDURE

The mine site investigation began with telephone discussions with representatives of federal and state agencies and concluded with specific discussions with individual mine operators. Federal and state agencies contacted are listed below.

- The U.S. Bureau of Mines has responsibilities in mineral and mining statistics, mining technological research, minerals specialists, and other services related to the minerals industry.
- The U.S. Corps of Engineers has a direct involvement in major geotechnical projects concerning surface and subsurface facilities and was a source of subsurface information.
- The U.S. Bureau of Reclamation is involved in tunneling operations for major water supply projects, particularly in the western states.
- The U.S. Mine Safety and Health Administration (MSHA) is directly responsible for administering Federal mining regulations and inspecting all surface and subsurface mines.
- Contacts were made with various state mine inspectors. These inspectors have direct knowledge of all mining operations within their respective states.

Information provided by the federal and state agencies confirmed that mining operations were the only type of underground development that might offer the opportunity of locating a suitable long-term subsurface site for the antenna. Telephone calls were made to mining companies that might operate mines of any substantial extent. Information

pertaining to the criteria in Section 3.1 was obtained. Discussions with company personnel indicated quickly that only a limited number of underground operations could be considered for the antenna.

At this point in the subsurface survey, a list was assembled compiling the underground mines that might house the antenna. The mines and subsurface facilities are grouped by state (see Table 3.2-1).

3.3 DESCRIPTION OF CANDIDATE SITES

The candidate sites have been grouped into two categories: sites which meet many of the criteria and sites that can be considered for further investigation.

Mining operations can be found that have one passage with a length exceeding 5 km. However, as Table 3.3-1 indicates, there are no underground mines in the United States that have two orthogonal passages 5 km in length. This paucity of potential underground sites is a general reflection of attempts to minimize significant underground hauling distances. There is a point in mine development where it makes economic sense to sink a new shaft or drive a new opening from the surface in order to reach outlying portions of the mineral deposit.

Also, there are few developed mineral deposits that are so planar and undisturbed that significant line-of-sight distances can be excavated. There are a few mines that, due to specific mining considerations or surface ownership, have two passages 5 km in length, but these are not linear for a significant distance. Basically, underground mine passages are developed to best accommodate the local geological condition such as, local faulting and offset of the ore body, competency of the immediate rock, changing economics of mine development, and exploitation of portions of the ore body which might be mined at a profit.

Those mines that are listed in Table 3.3-1 have met the criteria of certain mine passage size, orthogonality or near orthogonality, ground stability, groundwater control, and general vibration levels. Portions of most of these mines are actively mined. For the purpose of this report, the mines are grouped by decrements of 1 km.

Only six of these mines appeared to warrant further investigation. The other mines were eliminated due to reasons such as limited life of the mine, serious long-term ground stability conditions, and major cost of maintaining those passages that would house the antenna. The locations of these six mines are shown in Figure 4-1. The mines and their current status are given below:

- Cleveland Mine, Ohio - active mining
- Randolph Mine, Missouri - active mining
- Nash Draw Mine, New Mexico - active mining
- Barberton Mine, Ohio - inactive

- Jonathan Mine, Ohio - inactive
- Mullins Mine, Kentucky - inactive

The following briefly describes the six mines that were considered:

3.3.1 Cleveland Mine

The Cleveland Mine is located in Cleveland, Ohio, at the mouth of the Cuyahoga River and extends under both the city and Lake Erie. This is a salt mine operated by the International Salt Company. With the present mine configuration, the operators could provide two orthogonal passages, each 1.7 km in length and apparently line-of-sight (see Figure 3.2-2). Access to the mine is by vertical shaft, with the mine about 1,765 ft below land surface. The salt is mined by the room and pillar method.

The salt is mined from passages 45 ft wide and 18 to 22 ft high. Pillars are 105 ft square, and are left to provide permanent support. The salt is blasted and mined by diesel-powered equipment and transported to underground hoisting facilities. The mine temperature is a constant 72°F.

Rock stability is not a major problem, although portions of the mine roof are supported with rock bolts. The mine is dry, so dewatering is not a consideration. The present mineral claim boundaries limited the possibilities of passage extension to about 0.2 km in one direction, and about 0.7 km in the other direction.

3.3.2 Randolph Mine

The mine is located near Kansas City, Missouri. This is a limestone mine operated by Midwest Mining Corporation. It would be possible to provide passage 1.6 km in length and another 1.4 km in length (see Figure 3.2-3). Portions of this mine have been developed as a subsurface industrial and business complex. Access is at street level, and the developed area has roads, utilities, and rail directly into the mine. There are a number of businesses located in the complex, including a post office, warehouses, and small manufacturing plants. The mine has been developed by quarrying horizontally into a limestone bluff. The mine is 140 ft below the surface. The passages are 65 ft wide and 12 to 16 ft high. The mine is supported by pillars which are 90 ft square. The temperature ranges from 58 to 62°F. The northern portion of the mine is actively being excavated by drilling and blasting methods.

Due to the proximity of the mine to the surface, groundwater does enter the mine. The small quantities of incoming water are removed via a drainage ditch and sump system. Since entrance to the mine is horizonital and the whole mine is at that elevation, the chances of flooding are nonexistent.

3.3.3 Nash Draw Mine

The Nash Draw Mine is located near Carlsbad, New Mexico. This mine was developed to extract potash, and is operated by the Duval Corporation. The longest orthogonal line-of-sight passages that are currently open are each 1.5 km in length (see Figure 3.2-4). The potash deposit is reached by vertical shafts extending approximately 1,100 ft below the surface. The potash is mined by the room and pillar method with passages 30 ft wide and 6 to 8 ft high. The pillars provide permanent support. The mine temperature is a constant 68°F. There is some possibility at this mine of extending the passages through mining and pillar alteration. The mine is dry with no groundwater problems. The location of mineral claim boundaries is such that passage lengths could be doubled without difficulty.

Duval Corporation indicated as this report was going to press that it wishes the Nash Draw Mine to be withdrawn from further consideration as an antenna site.

3.3.4 Barberton Mine

This inactive mine is owned by PPG Industries. The mine was deactivated in 1976 and all equipment, with the exception of the hoisting system, was removed. The mine produced limestone for glass production. The mine is near Akron, Ohio. Access to the mine, a room and pillar operation 2,600 ft below the surface, is by vertical shaft. Two orthogonal passages, one 0.6 km and the other 0.8 km, could be used. The passages are 32 ft wide and 17 ft high. The mine is completely dry with only minor water leakage at the shaft collars. The rock stability is very good with only some precautionary rock bolting at previous stationary equipment sites. The company has no plan to reopen the mine as the company ceased using limestone in their glass production in 1975. Mineral claim boundaries are sufficiently distant so that passage lengths could be doubled without difficulty.

3.3.5 Jonathan Mine

This inactive mine was previously operated and is still owned by the Columbia Cement Company. The mine, a limestone producer for cement production, is located near Zanesville, Ohio. The firm now mines limestone from a quarry in proximity to the underground mine. The mine has been developed by the room and pillar method. There are two orthogonal passages, each with a length of about 0.8 km, that might be suitable for the antenna. The mineral claim boundary distances are such that the passages could potentially be lengthened an additional 0.6 km in both directions.

Access to the mine is by horizontal adit entry. Thickness of the overlying rock is at least 150 ft. Rock stability is moderately good with the whole mine roof secured with rock bolts on 5 ft centers. The mine has no groundwater problems. The passages are 20 ft high and 30 ft wide with pillar dimensions ranging from 25 ft by 25 ft to 50 ft by 100 ft.

3.3.6 Mullins Mine

This inactive mine was previously operated and is currently controlled by Kentucky Stone Company. The mine is located near Mt. Vernon, Kentucky, and produced limestone during its 23 year lifetime before ceasing production 1979. It was mined by the room and pillar method. The present configuration would allow the placement of two 0.6 km orthogonal arms of the antenna. The passages could potentially be extended an additional 0.6 km before encountering mineral rights boundaries.

Access to the mine is by horizontal adit passages. The mine is situated in the side of a steep hill with a minimum thickness of overlying rock of at least 200 ft. The rock stability is very good with no need for rock bolts. There are no water problems; minor seepage is handled by ditch and sump. The passages are about 25 ft high and 50 ft wide with pillar dimensions of about 50 ft by 50 ft. Vibration monitoring has been done only in conjunction with blasting.

3.4 REFERENCES FOR MINE SITES

3.4.1 LITERATURE CITED

1. Engineering and Mining Journal, "International Directory of Mining and Mineral Processing Operations". New York, NY, 1982.

2. Coal Mining Directory, "Mining Informational Services", New York, NY, 1982.

3. Mineral Commodity Summaries, U.S. BUREAU OF MINES, WASHINGTON, DC, 1983.

3.4.2 Organizations Contacted

Agency, Company, or Mine	Contact	Location and Telephone No.
Allied Chemical Corp., Alchem Mine	C. MacLinden, Chief Mining Engineer	Green River, WY 307/875-3350
AMAX Chemical Corp., Eddy Mine	R. Kirby, General Manager	Carlsbad, NM 505/885-3157
AMAX Moly Corp. Henderson Mine and Tunnel	Chief Engineer	Golden, CO 303/234-9020
AMAX, Lead & Zinc Division	J. Peters, Chief Mining Engineer	Clayton, MO 314/626-4221
ASARCO, Inc.	Vice President, Mining	New York, NY 212/669-1000

Agency, Company, or Mine	Contact	Location and Telephone No.
Bethlehem Mining Co.	L. Shutty, Manager of Underground Mining	Ebbensburg, PA 814/472-8102
Black River Co., Inc., Black River Mine	R. Kuhneman, Mine Superintendent	Butler, KY 606/472-7721
Bunker Hill Co., Inc., Bunker Hill Mine	M. Swanson, Mine Manager	Kellogg, ID 208/784-1261
Coal Age Magazine	D. Brezovec, Mining Specialist	New York, NY 212/997-2196
Carbon County Coal Co.	D. Rauton, Mine Manager	Lander, WY 307/325-9471
Cargill Corp., Cayuga Mine	G. Peterson, Mine Manager	Lansing, NY 607/533-4221
Cominco American, Inc., Magmont Mine	P. Sweeney, Chief Geologist	Bixby, MO 314/626-4231
CONOCO, Coal Division	D. Petrie, Director of Coal Mining	Morgantown, WV 304/983-2251
Consolidated Coal Co.	W. Furtall, Asst. Mine Manager	Acton, PA 412/746-3400
Consultant	Robert Thoms	Baton Rouge, LA 504/769-5277
FMC, Westvaco Mine	M. Fenton, Mine Superintendent	Green River, WY 307/875-2580
IMC, Ltd., Esterhazy Mine	E. Sidler, Chief Engineer	Esterhazy, Saskatchewan 306/745-3931
International Minerals & Chemicals Corp., IMC Mine	R. Hougland, General Manager	Carlsbad, NM 505/887-2871
Mississippi Chemical Co., Mississippi Mine	J. Walls, Manager	Carlsbad, NM 505/887-5591
Mississippi Lime Co., St. Genevieve Mine	L. Fieg, Mine Manager	St. Genevieve, MO 314/883-5731
Mississippi Limestone Producers Association	N. McDonald, President	St. Louis, MO 314/635-0208

Agency, Company, or Mine	Contact	Location and Telephone No.
Morton Salt Co., Chicago Mine	J. Head, Chief Mining Engineer	Chicago, IL 312/621-5884
Morton Salt Co.	F. Elder, Senior Mining Engineer	Paynesville, OH 216/354-9901
National Crushed Stone Association	E. Renninger, President	Washington, DC 202/342-1100
PCA, Inc., PCA Mine	T. Donaldson, Mine Manager	Carlsbad, NM 505/887-2844
Peabody Coal Co.	S. Sorrell, Director of Mining Engineering	Pittsburgh, PA 618/398-7950
Jack Parker Consultants	Jack Parker, President	White Pine, MI 906/885-5445
PCA, Ltd., Rokainville Mine	M. Wooley, Chief Engineer	Rokainville, Saskatchewan 306/645-2870
St. Joe Minerals Co., Inc.	P. Meyers, Chief Geologist	Bonne Terre, MO 314/244-5261
Society of Mining Engineers	T. O'Niel, Editor	Boulder, CO 303/973-9550
State Mine Inspectors	A. Hanson Mine Inspector	Knoxville, TN 615/673-4581
	L. Kimmel, Director	Pittsburgh, PA 412/439-7460
	R. Gatti Mine Inspector	Columbus, OH 614/466-4248
	D. Hanna Mine Inspector	Rock Springs, WY 307/362-5222
Tennessee Chemical Co., Gordonsville Mine	Chief Mining Engineer	Gordonsville, TN 615/496-3331
Union Carbide Corp., Bishop Mine	M. Sherman, Mine Superintendent	Bishop, CA 619/387-2501
U.S. Gypsum Co.	Mining Engineering Division	Chicago, IL 312/321-4000

Agency, Company, or Mine	Contact	Location and Telephone No.
U.S. Steel Corp.	F. Neely, Chief Mining Engineer	Uniontown, PA 412/430-2249
U.S. Committee of Tunneling Technology	J. Wagner, Chairman	Washington, DC 202/334-3136
U.S. Bureau of Mines	J. Presseu, Gypsum Specialist	Washington, DC 202/634-1206
	W. Miller, Mining Research	Washington, DC 202/634-1233
	J. Burlison, Mining Management Services	Carlsbad, NM 505/885-8881
	D. Kostick, Salt Specialist	Washington, DC 202/634-1177
	M. Jolley, Copper Specialist	Washington, DC 202/634-1071
	R. Schmidt, Div. of Research	Minneapolis, MN 612/725-3455
	D. Bolstad, Div. of Research	Spokane, WA 509/404-1610
	J. Paron, Limestone Specialist	Washington, DC 202/634-1185
	J. Paone, Experimental Studies	Brucetor, PA 202/634-4740
	J. Searls, Potash Specialist	Washington, DC 202/634-1190
	D. Barna, Div. of Mining Technology	Washington, DC 202/634-1233
	S. Guys, Engineering Research	Washington, DC 202/343-4054
	C. Wang, Mining Research	Washington, DC 202/634-1268
U.S. Bureau of Reclamation	K. Schulman, Water Conveyance Branch	Denver, CO 303/234-4379
U.S. Corp of Engineers	Planning Division of Civil Works	Washington, DC 202/272-0115

Agency, Company, or Mine	Contact	Location and Telephone No.
U.S. Mine Safety & Health Administration	J. Coldwell, Regional Office	Topeka, KS 913/205-2636
	C. Ellis, Central Office	Washington, DC 202/235-2146
	North Central Office	Vincennes, IN 812/882-0696
Vulcan Materials Co., Inc., Frederick Mine	Mine Superintendent	Frederick, KY 606/266-1176
White Pine Copper Co., Inc., White Pine Mine	Mining Engineering Dept.	White Pine, MI 906/885-5111

TABLE 3.2-1

CANDIDATE AREAS FOR SUBSURFACE SITES

State	Mine or Facility	Comments (1,2,3)
Arizona	Lakeshore Mine	0.2 km x 0.2 km
	Superior Mine	0.1 km x 0.3 km
California	Bishop Mine	0.6 km x 1.0 km - the long passage is a haulage tunnel
Colorado	Henderson Mine	0.2 km x 0.3 km
	Henderson East Tunnel	16.3 km - Curvature of earth haulage tunnel with no significant Orthogonal passage
Idaho	Bunker Hill Mine	0.8 km x 0.9 km - one passage is a haulage tunnel
	Lucky Friday Mine	0.4 km x 0.8 km
Illinois	U.S. Gypsum Co.	maximum of 0.6 km x 0.6 km in the largest of their six mines
	Mississippi Lime Mine	0.7 km x 0.7 km
	Chicago Mine	1.6 km x 1.6 km - to be abandoned; significant rock stability problems, very extensive maintenance
	Prairie du Rocher Mine	0.3 km x 0.4 km
	Vulcan Mine	0.4 km x 0.4 km
Indiana	Shoals Mine	0.4 km x 0.4 km
	Chicago Metro Sewer Comm.	0.8 km x 1.4 km - lack of availability (sewer system)
	Coal Mines - general	0.2 km x 0.2 km
Iowa	Sperry Mine	0.3 km x 0.3 km
Kentucky	Dravo Mine	0.3 km x 0.3 km
	Black River Mine	0.4 km x 0.5 km
	Princeton Mine	0.6 km x 0.6 km
	Mullins Mine	0.5 km x 0.5 km - disused mine
	Frederick Mine	1.0 km x 1.1 km
Louisiana	Jefferson Island	
	Avery Island	
Michigan	White Pine Mine	0.3 km x 0.9 km - the long passage is a haulage tunnel
	Detroit Mine (International Salt)	1.0 km x 1.0 km

(1) Unless otherwise noted, the distances indicated are line-of-sight.
(2) Unless otherwise noted, the mines and passages are actively used.
(3) States not listed do not contain any mines or subsurface passages that could be considered for the antenna.

TABLE 3.2-1

CANDIDATE AREAS FOR SUBSURFACE SITES (Cont)

State	Mine or Facility	Comments (1,2,3)
Missouri	Randolph Mine (Great Midwest Mining)	1.4 km x 1.6 km
	Buick Mine	0.3 km x 4.0 km - the long passage is a haulage tunnel
	St. Genevieve Mine	0.6 km x 0.6 km
	Magmont Mine	0.3 km x 2.0 km - one passage is a haulage tunnel
	Viburnum Mine	0.3 km x 1.5 km - the long passage is a haulage tunnel
	Fletcher Mine	0.6 km x 2.0 km - haulage passages
	Brock Mine	0.4 km x 0.7 km
	Heath Mine	0.3 km x 3.0 km - the long passage is a haulage tunnel
New Jersey	Sterling Hill Mine	0.1 km x 0.1 km
New Mexico	Eddy Mine	0.7 km x 0.8 km - mine on standby status, to be reactivated with improved market
	Nash Draw Mine (Duval Corp.)	1.5 km x 1.5 km
	Mississippi Chem. Mine	0.4 km x 0.4 km - abandoned, hoisting equipment removed
	IMC Mine	0.2 km x 0.2 km - no interest by management
	PCA Mine	0.2 km x 0.3 km - no interest by management
New York	Retsof Mine (International Salt)	1.0 km x 1.0 km
	Cayuga Mine(Lansing)	0.9 km x 1.0 km
	Seneca Mine	0.6 km x 0.7 km
Ohio	Cleveland Mine (International Salt)	1.7 km X 1.7 km
	U.S. Corp. of Engineers	Underground shelter study
	Jonathan Mine	0.8 km X 0.9 km
	Fairport Mine	0.6 km x 0.9 km - disused mine
	Barberton Mine	0.6 km X 0.8 km - disused mine
	Zanesville Mine	0.7 km X 1.1 km
	Paynesville Mine	0.6 km X 0.9 km
Pennsylvania	Bethlehem Corp.	0.5 km x 0.5 km - the most extensive configuration in their mines
	Peabody Coal Co.	0.2 km x 0.3 km - the most extensive configuration in their mines
	CONOCO	0.7 km X 0.5 km - the most extensive configuration in their mines
	Consolidated Coal Co.	0.4 km X 4.2 km - the long passage is a haulage tunnel
	U.S. Steel Co.	0.3 km X 0.3 km - the most extensive configuration in their mines
	U.S. Corp. of Engineers	Underground shelter study
South Dakota	Homestake Mine	0.3 km x 0.4 km - haulage passages

(1) Unless otherwise noted, the distances indicated are line-of-sight.
(2) Unless otherwise noted, the mines and passages are actively used.
(3) States not listed do not contain any mines or subsurface passages that could be considered for the antenna.

TABLE 3.2-1

CANDIDATE AREAS FOR SUBSURFACE SITES (Cont)

State	Mine or Facility	Comments (1,2,3)
Tennessee	Mascot Mine	0.4 km X 0.4 km
	New Market Mine	0.2 km x 0.3 km
	Gleason Mine	0.3 km x 0.3 km
	Gordonsville Mine	0.3 km x 0.3 km
Utah	Park City Mine	0.3 km x 0.3 km
	Bat Tunnel (Bur. of Reclam.)	12.8 km - one passage only (water tunnel)
	Hades Tunnel (Bur. of Reclam.)	7.2 km - one passage only (water tunnel)
Virginia	Kimballton Mine	0.2 km x 0.3 km
Washington	Pend Orielle Mine	0.1 km x 0.2 km
West Virginia	Consolidated Coal	0.2 km x 0.2 km - the most extensive configuration in their mines
Wyoming	Westvaco Mine	0.2 km x 0.3 km
	Alchem Mine	0.2 km x 0.4 km - no interest by management
	Carbon County Coal Co.	0.6 km x 0.8 km - mining technique employed not suitable for passage excavation

(1) Unless otherwise noted, the distances indicated are line-of-sight.
(2) Unless otherwise noted, the mines and passages are actively used.
(3) States not listed do not contain any mines or subsurface passages that could be considered for the antenna.

TABLE NO. 3.3-1

DECREMENTAL LIST OF SUBSURFACE SITES

Length	Sites
5.0 km or longer	None
4.0 km to 5.0 km	None
3.0 km to 4.0 km	None
2.0 km to 3.0 km	None
1.0 km to 2.0 km	Cleveland mine, 1.7 km x 1.7 km, Cleveland, Ohio, International Salt Co.
	Nash Draw mine, 1.5 km x 1.5 km, Carlsbad, NM, Duval Corp.
	Randolph mine, 1.4 km x 1.6 km, Kansas City, MO, Great Midwest Mining Corp.
0.5 km to 1.0 km	Jonathan mine, 0.8 km x 0.8 km, near Zanesville, OH, Columbia Cement Co.
	Barberton mine, 0.6 km x 0.6 km, near Akron, OH, PPG Industries, Inc.
	Mullins mine, 0.6 km x 0.6 km, Mt. Vernon, KY, the Kentucky Stone Co.

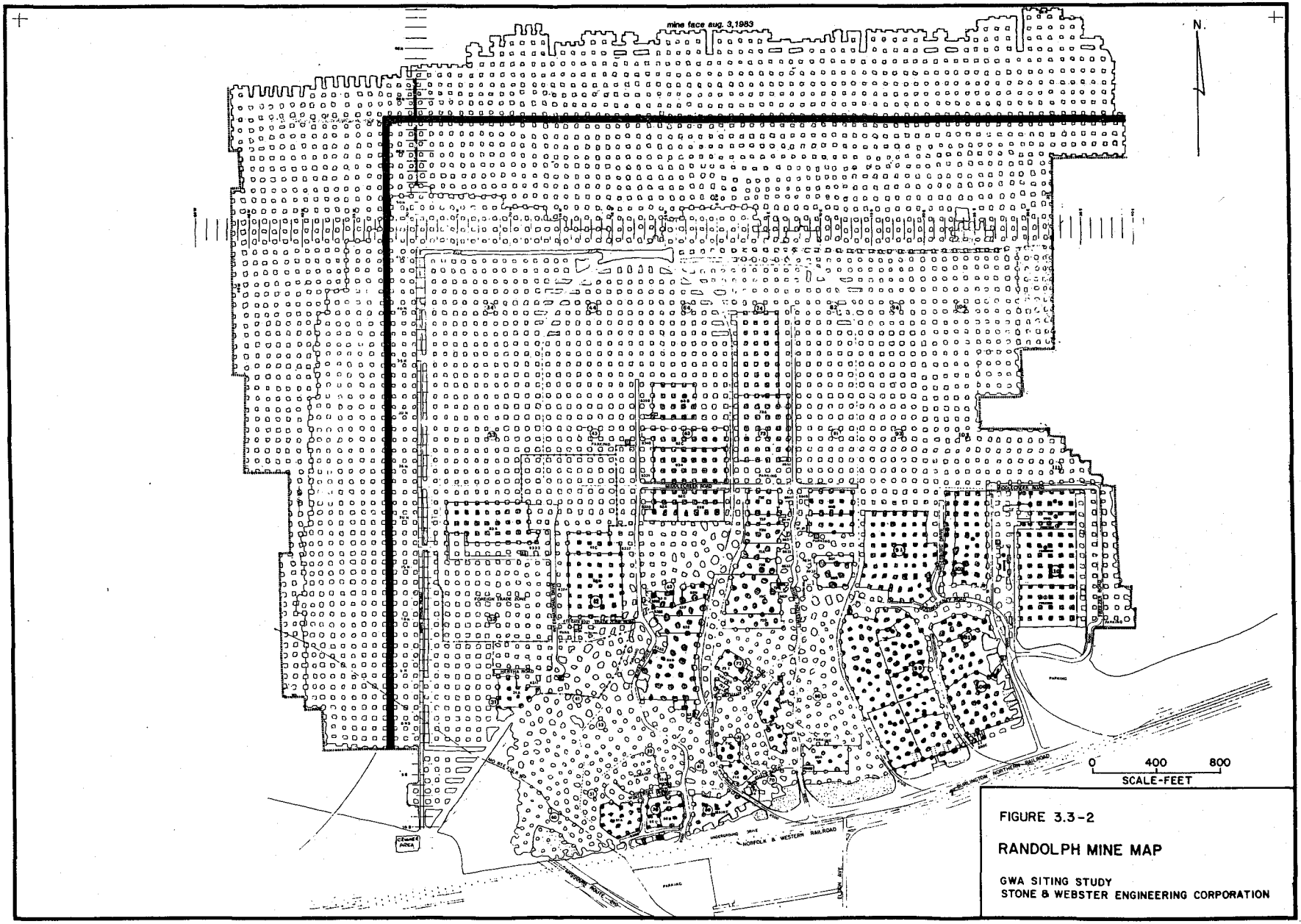

FIGURE 3.3-2

RANDOLPH MINE MAP

GWA SITING STUDY
STONE & WEBSTER ENGINEERING CORPORATION

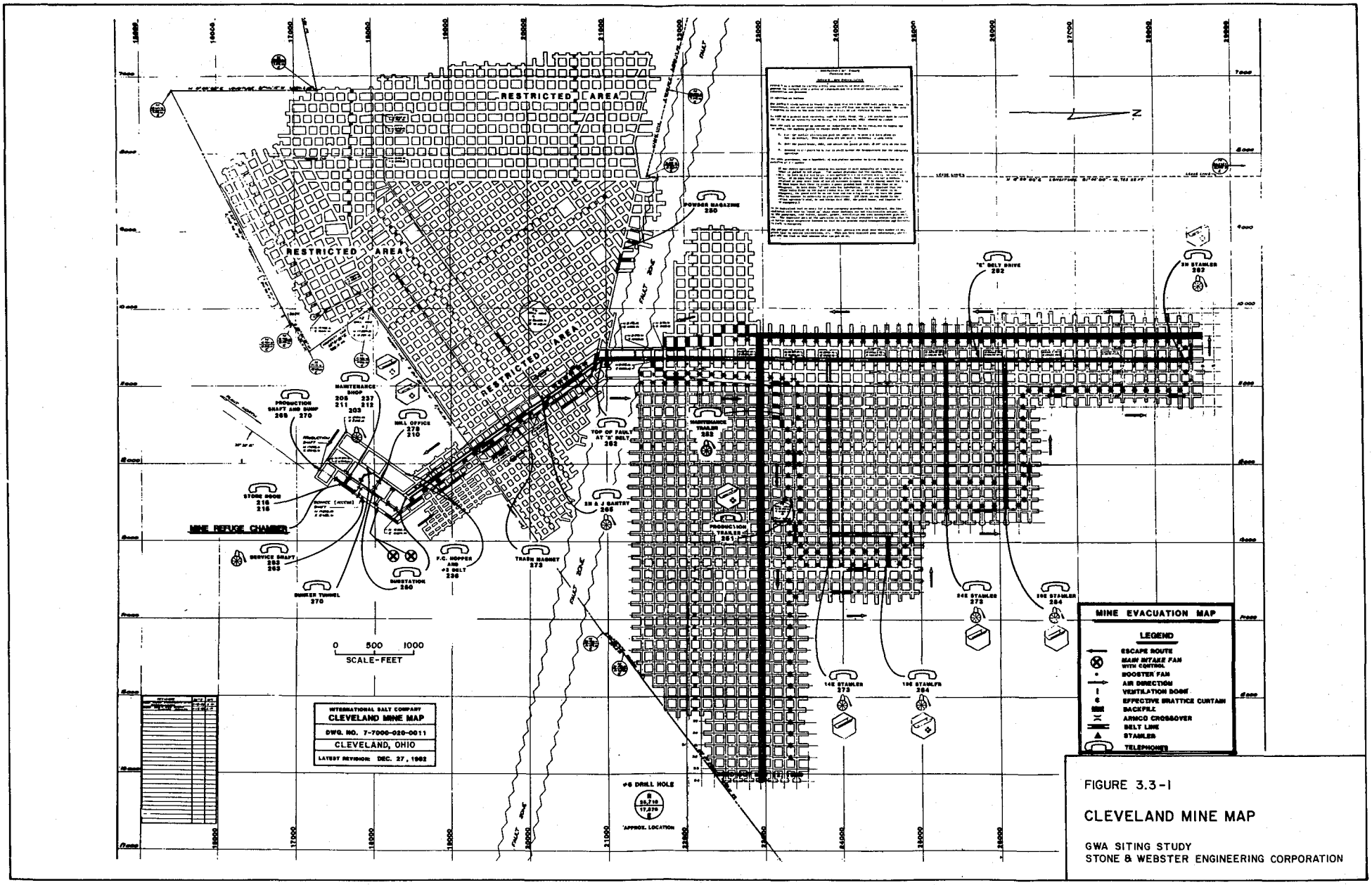

FIGURE 3.3-1

CLEVELAND MINE MAP

GWA SITING STUDY
STONE & WEBSTER ENGINEERING CORPORATION

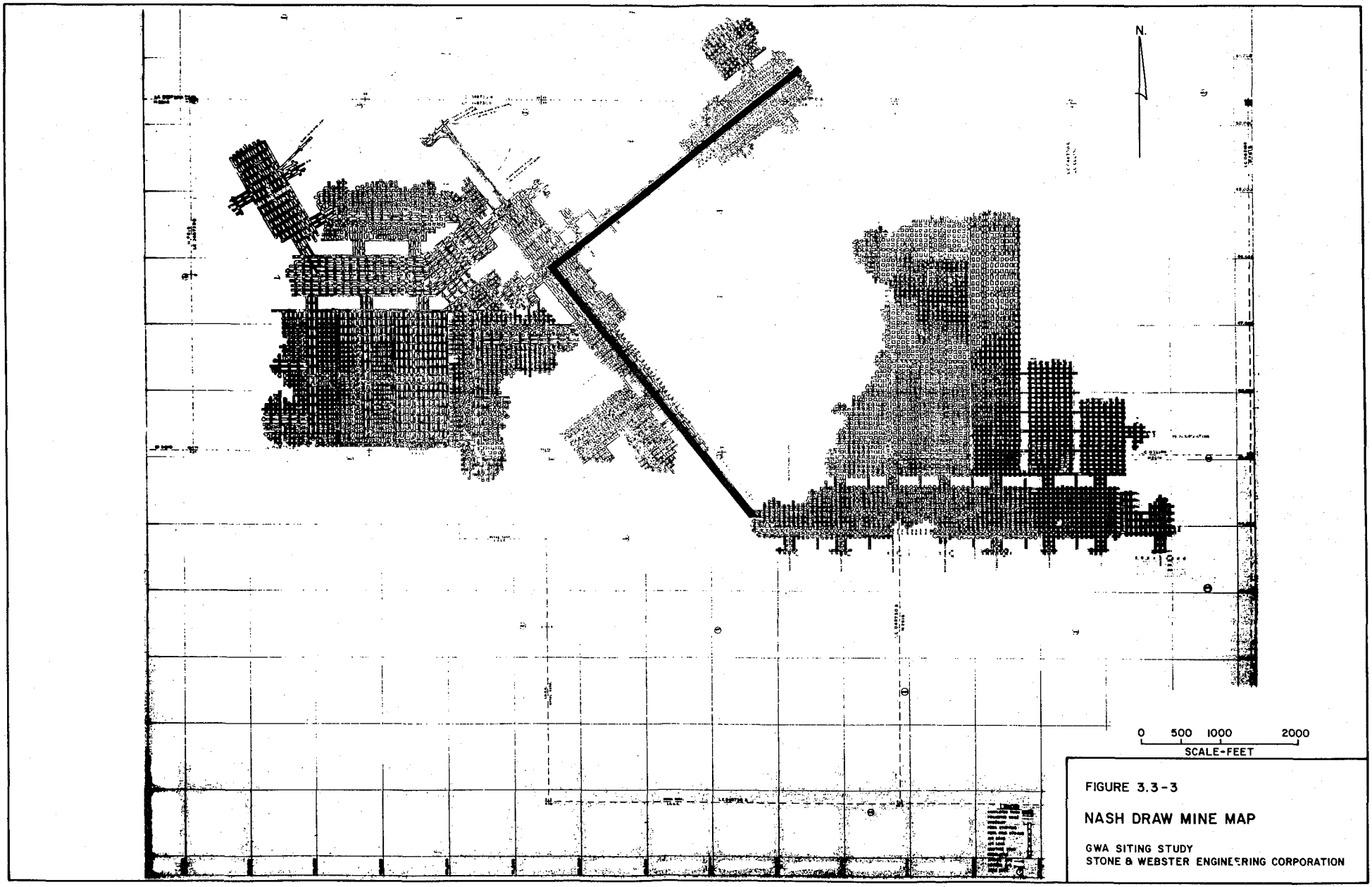

FIGURE 3.3-3

NASH DRAW MINE MAP

GWA SITING STUDY
STONE & WEBSTER ENGINEERING CORPORATION

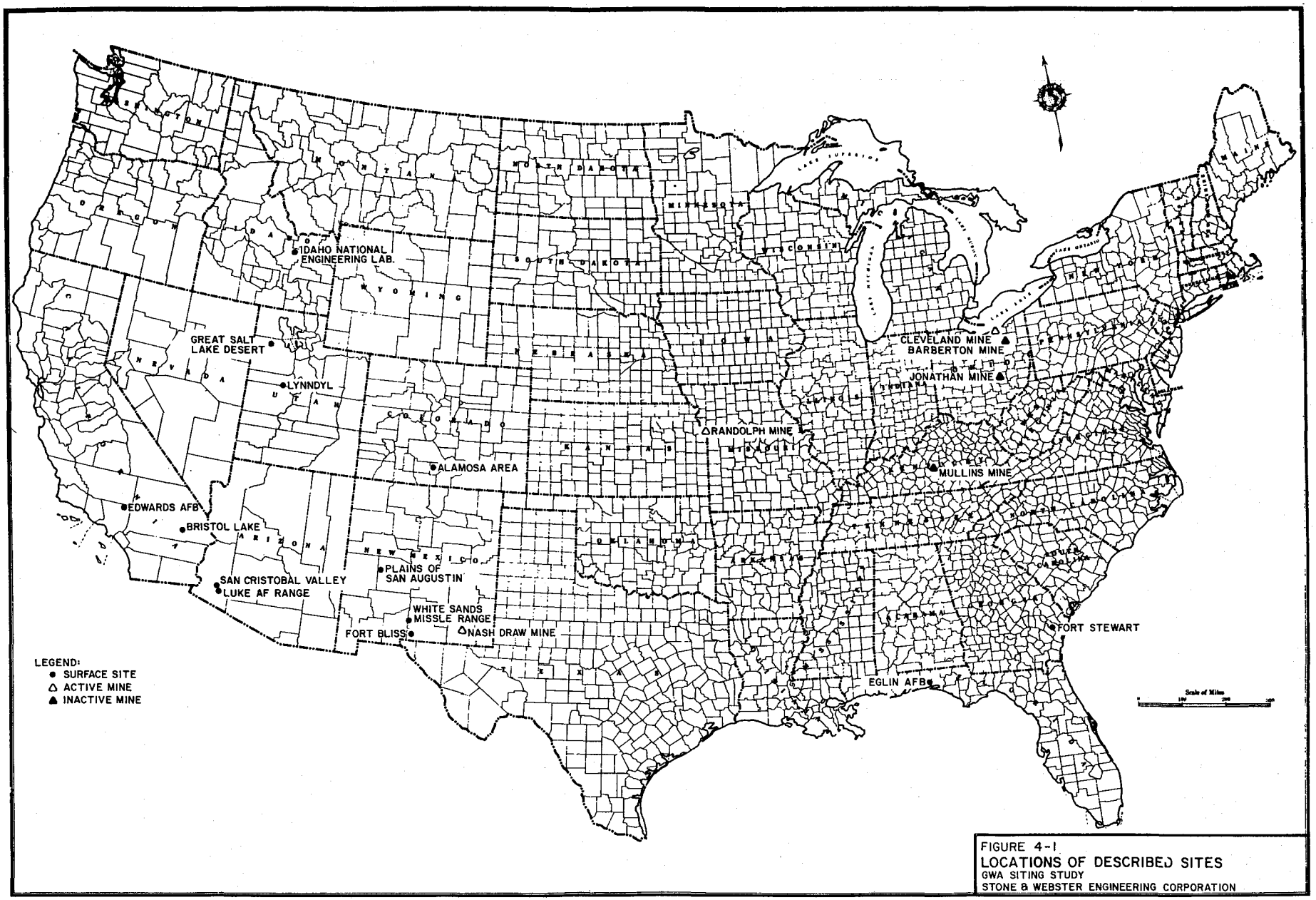

FIGURE 4-1
LOCATIONS OF DESCRIBED SITES
GWA SITING STUDY
STONE & WEBSTER ENGINEERING CORPORATION

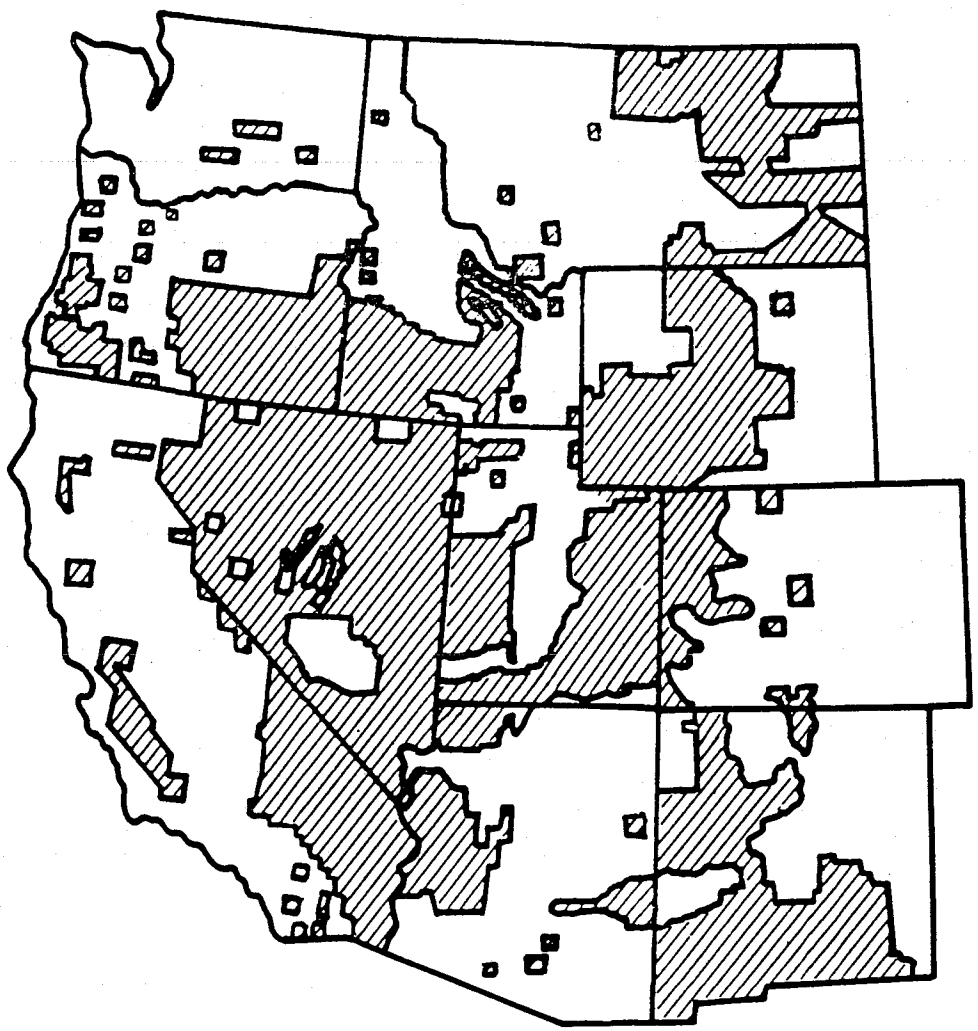

Legend

LANDS MANAGED BY BLM

FIGURE 4-2

PUBLIC LANDS IN THE
WESTERN UNITED STATES

GWA SITING STUDY
STONE & WEBSTER ENGINEERING CORPORATION

SWEC J.O. 14190.02

CONCEPTUAL STUDIES AND COST ESTIMATES FOR SURFACE AND SUBSURFACE INSTALLATION OF AN INTERFEROMETRIC GRAVITATIONAL WAVE ANTENNA

September 1983

Stone & Webster Engineering Corp.
Boston, MA

TABLE OF CONTENTS

SECTION	TITLE	PAGE
5	Introduction.....	1
6	Surface Installation.....	2
6.1	Common Factors In All Surface Installations.....	2
6.2	Scheme 1.....	7
6.2.1	Estimated Costs of Scheme 1.....	8
6.3	Scheme 2.....	10
6.3.1	Estimated Costs of Scheme 2.....	11
6.4	Scheme 3.....	11
6.4.1	Estimated Costs of Scheme 3.....	11
7	Mine Installation.....	12
7.1	Passage Dimensions.....	12
7.2	Installation Description.....	12
7.2.1	Estimated Costs of the Mine Installation.....	14
8	Summary.....	15
9	Cost Estimation Details.....	21

List of Tables

Number	Title	Page
6.20	Summer and Winter Daily Temperature Variation in Vacuum Tube Metal	7
6.21	Influence on Vacuum Tube Support Spacing by Tube Diameter, Insulation Thickness and Wind	8
6.22	Cost Summary of Scheme 1	9
6.30	Cost Summary of Scheme 2	11
6.40	Cost Summary of Scheme 3	11
7.20	Cost Summary of Mine Installation	14
8.10-8.12	Summary Tables	18-20

List of Figures

5.100	Support for Scheme 1	3
5.101	Support and Vacuum Tube Protection for Scheme 2	3
5.102	Support and Vacuum Protection for Scheme 3	4
6.200	Layout of Surface Installation	5
6.201	End Station Building for Schemes 1 and 2	65
6.203	Typical Reinforced Concrete Pile and Cap for Fixed and Sliding Support	66
6.204	Support Spacing for Surface Installation of Vacuum Tube	67
6.401	End Station Building for Scheme 3	68
7.100	Layout of Mine Installation	69
7.101	Support Spacing for Mine Installation of Vacuum Tube	70
7.102	Typical Reinforced Concrete Fixed and Sliding Support	71
7.103	End Station Vault for Mine Installation	72

5 Introduction

This report presents the results of conceptual studies of both a mine installation and a surface installation of an Interferometric Broad Band Gravitational Wave Antenna.

The studies were performed for the Massachusetts Institute of Technology (MIT) by Stone & Webster Engineering Corporation (SWEC) under Contract No. GC-A-290939.

The objective of the studies was to develop several approaches for ground-level installation of an antenna, as well as to understand how such an antenna might be installed in a mine. In evaluating the various construction schemes, the costs of the various alternatives represent one of the most important ways of discriminating among them. The other consideration is the degree to which the antenna structure is protected against environmental perturbations which might degrade the performance of the antenna. Such perturbations include temperature fluctuations (both on a daily and a yearly scale), and wind loading or other mechanical forces on the vacuum tubes.

The work concentrated on three specific schemes for ground-level installation. A minimum cost option, with insulated vacuum tubes mounted in the open air, is labelled Scheme 1. (A possible upgrade to Scheme 1 is the addition of a pair of walls on either side of the tube to reduce the fluctuating forces due to the wind). Good protection against the elements would be provided if, instead, the vacuum tubes were buried under a substantial layer of earth. In order to provide access to the tubes for maintenance, the tube should be placed in some sort of watertight culvert large enough for a person to walk in. This idea is labelled Scheme 3. An intermediate option, Scheme 2, is to place the tubes inside the culvert at ground level, with an earth berm placed over the culvert. This provides nearly as much protection for the apparatus, perhaps with some cost saving. Figures 5.100, 5.101 and 5.102 present sketches of these three installation schemes.

A mine, as long as it is selected for proper rock competency and freedom from ground water problems, provides an environment for the antenna at least as good as Scheme 3. In addition, a location far beneath the surface places the apparatus at some distance from the acoustic and gravitational disturbances caused by human, animal and meteorological activity. Unfortunately, our survey of mines (discussed elsewhere in the report) failed to uncover any mines with orthogonal passages of sufficient extent to house the antenna. Therefore, the first task of the study of mine installation was to ascertain the cost of extending an existing mine to the proper dimensions. The rest of this phase of the study consisted of assessing the additional costs of installing the antenna in the enlarged mine.

We discuss the various ground-level schemes in section 6 and the mine installation in section 7. The estimated cost of the antenna installation is given in a summary table for each scheme, which lists the costs for each of the major parts of the task. These costs are grouped in two categories: those costs which do not depend on the length of the interferometer arms (fixed costs) and those costs which are proportional to the length of the arms (variable costs). To a good approximation, the cost of an antenna installation of any length between 1 and 10 kilometer arm length can be obtained by scaling the variable costs by the arm length and adding the fixed costs. For definiteness, total costs are given for an antenna configuration with two arms each 5 kilometers in length (called the "minimum configuration" in the section of the report concerning the vacuum tubes). For each scheme, the costs are presented for four different vacuum tube diameters: 12", 24", 36" and 48".

It is important to note which costs are not included in the discussion of this section. All of the costs of the vacuum itself (the vacuum tube, pumps, end station vacuum vessels and the cleaning and assembly of all of the above) are treated separately in the section written by Arthur D. Little, Inc. The costs of the interferometer optics, including lasers and all other instrumentation costs, are also treated elswehere. The costs which are studied in this section are those which involve installing the vacuum system, suitably protected, at the antenna site, as well as all other costs having to do with providing the buildings and services (power, water and working space) necessary for the experiment.

A summary is presented in section 8 and details of the cost estimates are presented (in worksheet form) in section 9.

6 Surface Installation

6.1 Common Factors In All Surface Installations

Each end station is housed in a pre-engineered building 40'-0" wide x 62'-0" long x 34'-0" high. The building is furnished with insulated siding, lighting and power, forced ventilation, electric heating and a 12 ton capacity pendant operated bridge crane. A movable partition is also provided to separate the end station area from the machine shop area. The end station area is 40'-0" x 44'-0). This provides ample floor space for lay-down of the removable portion of the end station vacuum vessel and the end station internals. The machine shop area is 40'-0" x 18'-0". The machine shop will contain machine tools and welding equipment necessary for the maintenance, repair or modification of the end station internals. Drinking water and chemical sanitation facilities are also provided. The support structure for the end station and the high vacuum pump room are located beneath the building. A 20'-0" wide x 20'-0" high rolling door is provided at the machine shop end of the building for delivery or removal of all of the contained equipment.

SCHEME 1

TUBE SIZE

12"
24"
36"
48"

INSULATION

6", 9", 12"

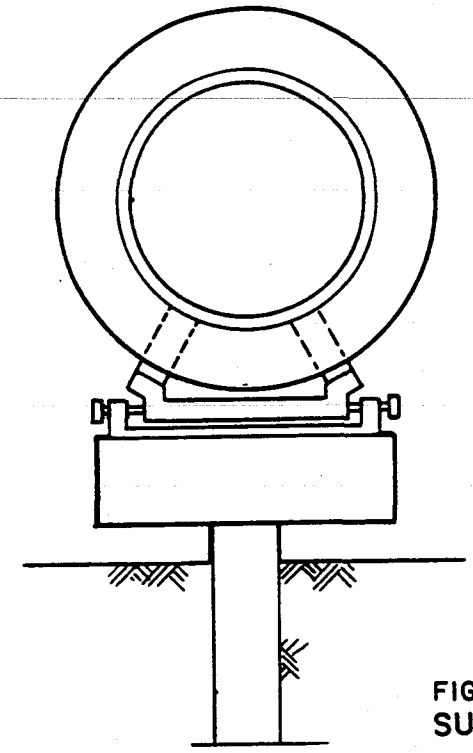

FIGURE 5.100
SUPPORT FOR SCHEME 1

SCHEME 2

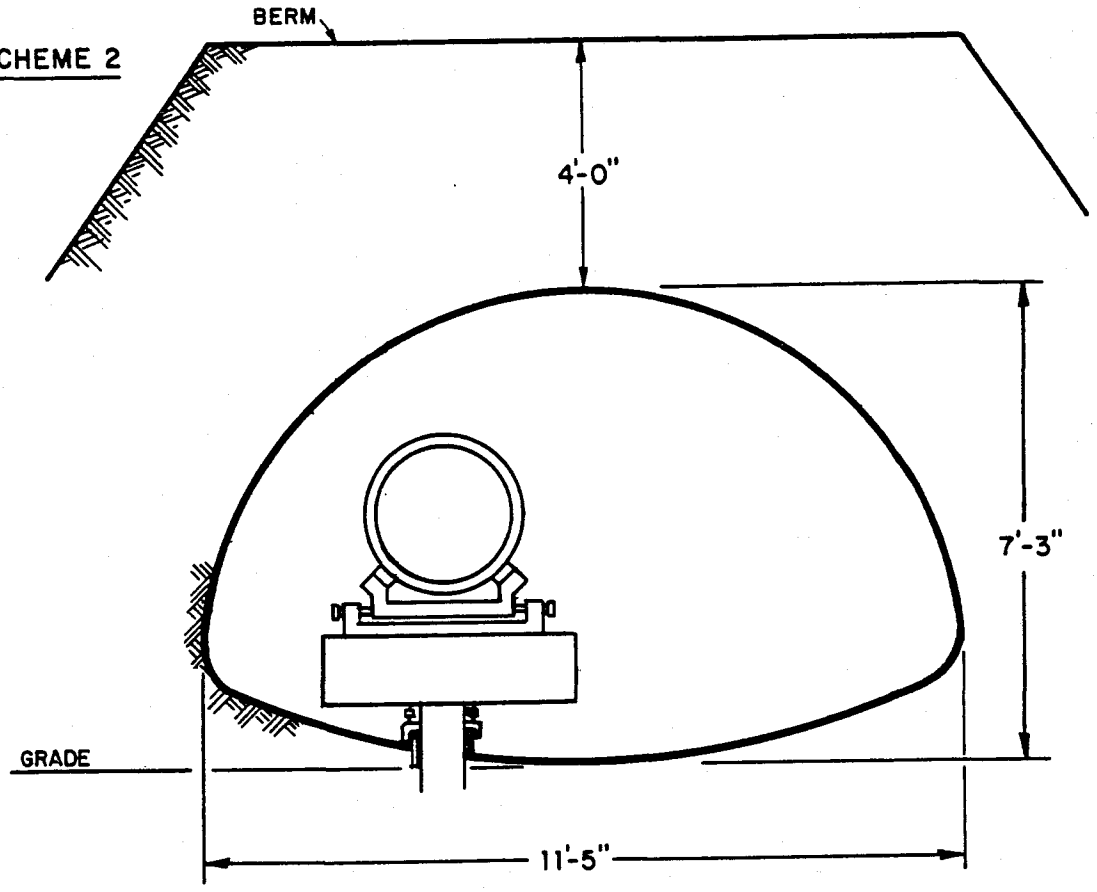

FIGURE 5.101
SUPPORT AND VACUUM TUBE PROTECTION FOR SCHEME 2

SCHEME 3

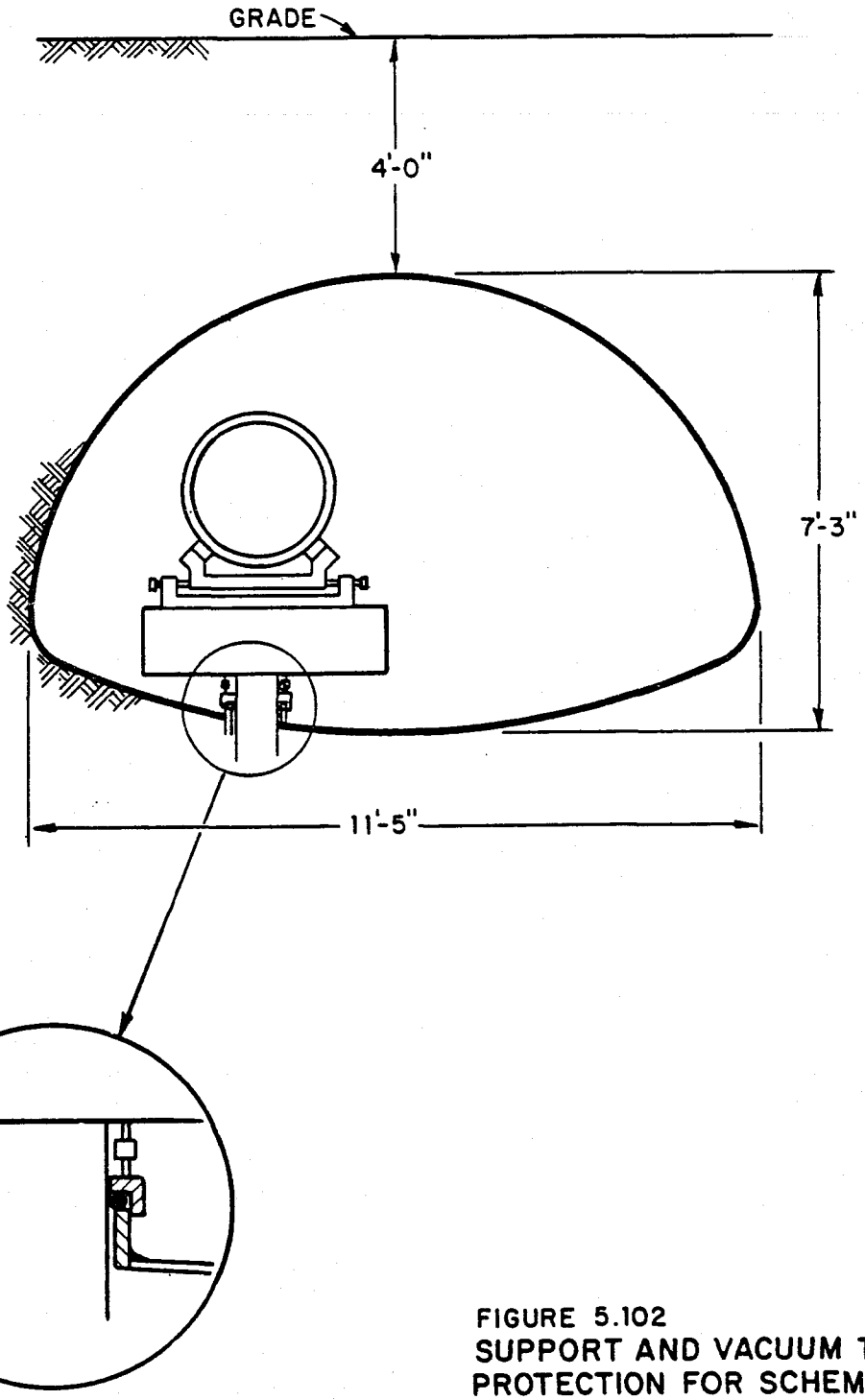

FIGURE 5.102
SUPPORT AND VACUUM TUBE
PROTECTION FOR SCHEME 3

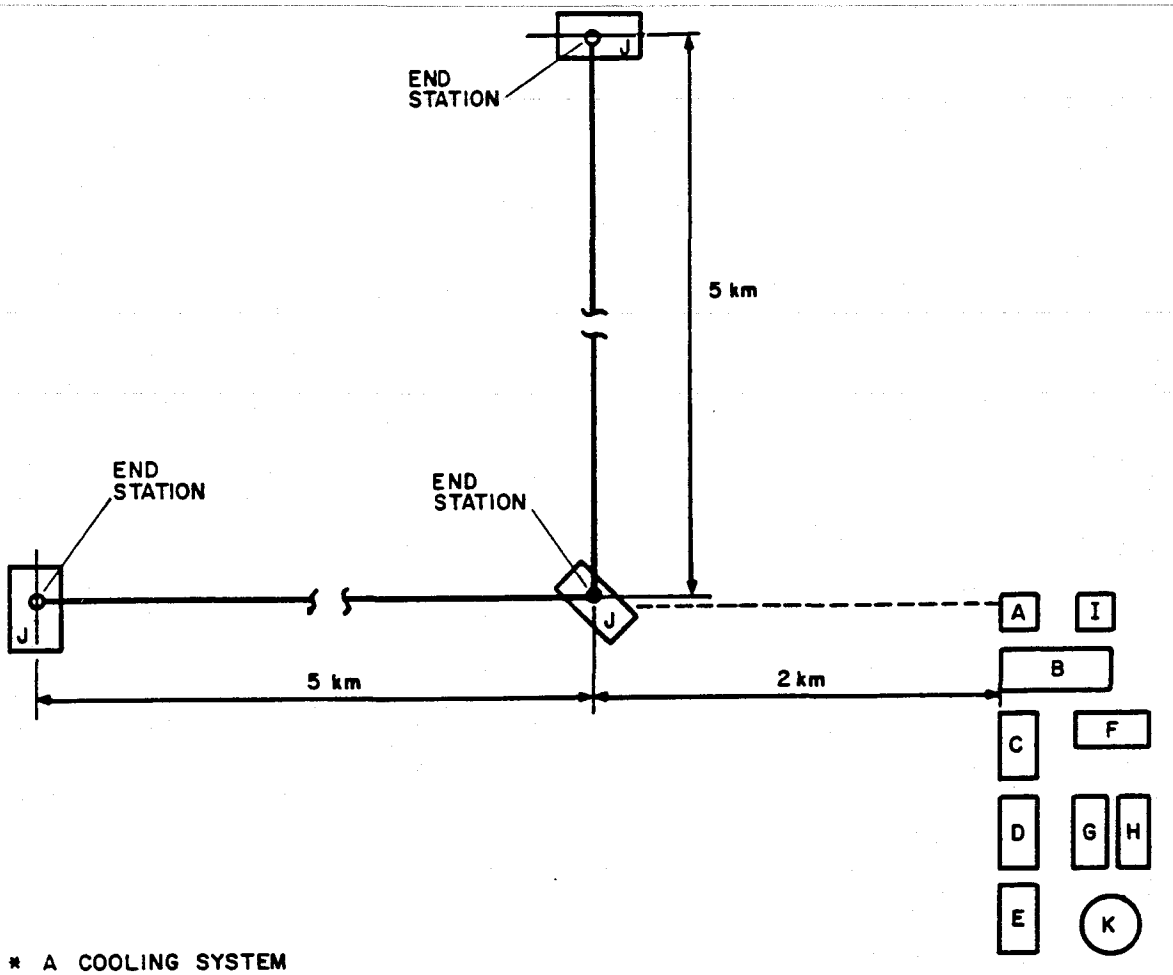

* A COOLING SYSTEM
B CENTRAL MAINTENANCE FACILITY BLDG. (40x60x20)
C COMPUTER & CONTROL TRAILER
D OFFICE TRAILER
E OFFICE TRAILER
F RECREATION & CAFETERIA TRAILER
G LIVING QUARTERS TRAILER
H LIVING QUARTERS TRAILER
I POWER TRANSFORMERS & SWITCHES
J END STATION BLDG.
K POTABLE WATER STORAGE TANK (3000 Gal. CAP.) (FILL TWICE/MONTH)

* COOLING SYSTEM CONSISTS OF:
30 TON CAPACITY CHILLER
15 hp CIRC. PUMP @ 100 GPM
3" IPS BURIED FEED AND RETURN PIPES W/1½" INSUL.
50/50 GLYCOL/WATER MIXTURE

FIGURE 6.200
LAYOUT OF SURFACE INSTALLATION

The cooling system for the lasers consists of a 30 ton chiller with an air cooled condenser and a 15 horse power 100 gallon per minute pump circulating 50% glycol-water coolant mixture to the equipment being cooled. The feed and return pipes are insulated and buried for protection.

A compound consisting of the cooling system, a central maintenance facility buildings, a computer and control trailer, two office trailers, two living quarters trailers, a recreation and cafeteria trailer, power transformers and switches and potable water storage tank is located two kilometers from the end station at the interferometer vertex.

The central maintenance facility building is a pre-engineered building 40'-0" wide x 60'-0" large x 20'-0" high complete with insulated siding, lighting and power, forced ventilation and electric heating.

The computer and control trailer is 20'-0" long x 8'-0" wide and is furnished with air conditioning, lighting and outlets, and a chemical toilet.

The office trailers are each 32'-0" long x 8'-0" wide and are furnished with air conditioning, lighting and outlets, desks, chairs, a reference table, filing cabinets and a chemical toilet.

The living quarters trailers are each 20'-0" long x 10'-0" wide and are furnished with an air conditioner, four single beds, four metal lockers, four folding steel chairs, a chemical toilet and a shower stall.

The recreation and cafeteria trailer is 36'-0" long x 10'-0" wide and is furnished with a six burner electric range with oven, a range hood, an 18 C.F. refrigerator/freezer, a 30 gallon cap. electric hot water heater, a stainless steel sink, serving cabinets, chairs, sofa and dining tables.

All trailers are electrically heated.

The potable water storage tank is a 3,000 gallon capacity skid mounted tank complete with piping, fittings and valves to tie-in to the trailers.

The potable water will be delivered by tank truck on a twice per month basis. The tank will be insulated and furnished with an anti-freezing electric heater.

All sink and shower drains are collected in a holding tank and removed by tank truck twice per month.

The site substation consists of one 3750 kVA transformer for the antenna, one 750 kVA transformer for station service and six 13.8 kVA switch gear with breakers. In these studies, for each case, it was assumed that a power transmission line run of eight miles would be required.

Figure 6.200 illustrates the layout of the Scheme 1 Surface Installation.

Figure 6.201 illustrates the layout of an End Station Building.

Figure 5.100 illustrates a typical support for a Scheme 1 above ground insulated tube.

Figure 6.203 illustrates a typical reinforced concrete pile and cap that is used for both the fixed and the sliding vacuum tube supports.

Figure 6.204 illustrates the support spacing for the 12", 24", 36" and 48" vacuum tube for 0", 6", 9" and 12" of insulation for Schemes 1, 2 and 3.

6.2 Scheme 1

Scheme 1 is based on an outdoor installation with the vacuum tube exposed to the elements. The study has been made for a 12 inch, 24 inch, 36 inch and a 48 inch diameter tube, for an uninsulated case and for a case where each is insulated with 6 inch, 9 inch and 12 inch of 4.5 pcf density fiberglass with aluminum lagging. Each size of tube was studied for metal temperature variation over a 72 hour period for a typical mid-summer day in the hottest of the sites evaluated and for a typical mid-winter day in the coldest of the sites evaluated. The mid-summer site selected was near Yuma, Arizona, where the mid-July daily ambient temperature varies from a low of 81°F to a mid-day high of 117°F with daily insolation equal to 84 BTU/Ft^2. The mid-winter site selected was near Alamosa, Colorado, where the daily ambient temperature varies from a low of -10°F to a mid-day high of 35°F.

A finite difference computer program was used to evaluate the hourly change in the metal temperature of each size of tube for each of the three thicknesses of insulation. The resultant daily extremes are given in Table 6.20.

TUBE DIAMETER	INSULATION THICKNESS	SUMMER DAILY TEMP. VARIATION		WINTER DAILY TEMP. VARIATION	
		LOW	HIGH	LOW	HIGH
12"	0"	81 F	150 F	-10 F	35 F
	6"	96 F	102 F	8 F	14 F
	9"	96 F	102 F	8 F	14 F
	12"	95 F	100 F	7.5 F	13 F
24"	0"	81 F	153 F	-10 F	36 F
	6"	96 F	102 F	8 F	14 F
	9"	95 F	100 F	6.5 F	13 F
	12"	94 F	98 F	5.5 F	10.5 F
36"	0"	81 F	155 F	-10 F	38 F
	6"	96 F	102 F	8 F	14 F
	9"	95 F	100 F	7.5 F	13 F
	12"	94 F	98 F	7 F	11 F
48"	0"	81 F	160 F	-10 F	39 F
	6"	95 F	101 F	7.5 F	13.5 F
	9"	93 F	97 F	6 F	10 F
	12"	92 F	96 F	5 F	8.5 F

TABLE 6.20
Summer and Winter Daily Temperature Variation in Vacuum Tube Metal

The spacing between supports was evaluated for each size of tube for each of the three thicknesses of insulation when exposed to 70 mph winds and when protected from the effects of the wind by completely effective shield walls, one on either side of the tube. The maximum tube deflection allowed under all combinations of loadings was 1 cm.

The results of the evaluation are given in Table 6.21.

TUBE DIAMETER	INSULATION THICKNESS	SUPPORT SPACING	
		With Wind Shield	Without Wind Shield
12"	0"	49'-4"	41'-6"
	6"	35'-2 1/2"	30'-9 3/4"
	9"	35'-2 1/2"	30'-9 3/4"
	12"	30'-9 3/4"	27'-4 5/8"
24"	0"	61'-7"	49'-4"
	6"	49'-4"	49'-4"
	9"	49'-4"	41'-1"
	12"	49'-0"	41'-1"
36"	0"	82'-2"	61'-7"
	6"	61'-7 1/2"	61'-7"
	9"	61'-7 1/2"	49'-4"
	12"	61'-7 1/2"	49'-4"
48"	0"	82'-2"	61'-7"
	6"	82'-2"	61'-7"
	9"	61'-7 1/2"	61'-7"
	12"	61'-7 1/2"	61'-7"

TABLE 6.21

Influence on Vacuum Tube Support Spacing by Tube Diameter, Insulation Thickness and Wind

6.2.1 Estimated Costs of Scheme 1

The estimated costs of the variations studied for Scheme 1 are presented in detail in section 9, pages 21 to 30 and 53 to 61. Table 6.22 summarizes these costs.

Fixed Costs Independent of Length	Tube Size	Insulation Thickness	Insulation Cost Per KM	Clearing and Grading Cost Per KM	Electrical Cost for Antenna Arms Per KM	Support Cost Without Windwalls Per KM	Support Costs with Windwalls Per KM	Cost of Windwalls Per KM	Total Cost Per KM	Total Cost For Two 5KM Arms + Fixed Costs
$4,880,600	12"	6	$110,830	$9,800	$99,880	$122,364			$342,874	$ 8,309,340
		9	173,460	9,800	99,880	138,072			421,212	9,092,720
		12	244,940	9,800	99,880	170,742			525,362	10,134,220
		6	110,830	9,800	99,880		$109,690	$236,221	566,421	10,544,810
		9	173,460	9,800	99,880		123,772	236,221	643,133	11,311,922
		12	244,940	9,800	99,880		154,650	236,221	745,491	12,335,502
$4880,600	24"	6	$197,720	$9,800	$99,880	$104,214			$411,614	$ 8,996,740
		9	298,390	9,800	99,880	157,674			565,744	10,538,040
		12	409,880	9,800	99,880	171,402			690,962	11,790,220
		6	197,720	9,800	99,880		$104,214	$236,221	647,835	11,358,945
		9	298,390	9,800	99,880		133,360	236,221	777,651	12,657,103
		12	409,880	9,800	99,880		150,177	236,221	905,958	13,940,175
$4,880,600	36"	6	$334,460	$9,800	$99,880	$155,694			$599,834	$10,878,940
		9	502,670	9,800	99,880	206,514			818,864	13,069,240
		12	683,670	9,800	99,880	255,156			1,048,506	15,365,660
		6	334,460	9,800	99,880		$155,694	$236,221	836,055	13,241,145
		9	502,670	9,800	99,880		166,862	236,221	1,015,433	15,034,928
		12	683,670	9,800	99,880		208,636	236,221	1,238,207	17,262,663
$4,880,600	48"	6	$484,960	$9,800	$99,880	$258,951			$835,591	$13,416,510
		9	738,430	9,800	99,880	276,771			1,124,881	16,129,410
		12	991,570	9,800	99,880	293,403			1,394,653	18,827,130
		6	484,960	9,800	99,880		$237,080	$236,221	1,067,941	15,560,006
		9	738,430	9,800	99,880		276,771	236,221	1,361,102	18,491,615
		12	991,570	9,800	99,880		293,403	236,221	1,630,874	21,189,335

TABLE 6.22
Cost Summary of Scheme 1

From Table 6.20, it is evident that there is an insignificant gain in thermal stability of the vacuum tube when using more than 6 inches of insulation.

From Table 6.22 it is clear that the use of windwalls increases the total cost of the installation for any size vacuum tube being considered.

6.3 Scheme 2

Scheme 2 is based on protecting the vacuum tube from the elements by locating it within a multi-plate pipe-arch layed on compacted soil on ground level and thermally stabilizing the atmosphere within the pipe arch by berming over it with earth to a minimum thickness of 4'-0". With this thickness of earth cover, the atmosphere within the pipe arch will vary from a winter low of 35F, based on a prolonged daily temperature variation from -10F to 35F to a summer high of 70F based on a prolonged daily temperature variation from 81F to 117F. The berm material is stabilized against erosion by planting native foliage on its surface.

The multi-plate pipe-arch is 11'-5" wide x 7'-3" high. It is fabricated of corrugated galvanized steel curved panels which are bolted together at the site, forming a water-tight tube.

At construction, the lower segment of the pipe-arch is layed on a bed of compacted soil. A hole for each vacuum tube support pile is cut in the lower segment and the piles are driven. The reinforced concrete pile caps are then poured with all of the pile cap bearing plates level and plane throughout the entire length of the vacuum tube within 2 mm. Before installing the vacuum tube, each pile penetration through the lower segment of the pipe arch is mechanically sealed with an elastomer "0" ring to maintain water-tightness. The "0" ring consists of a solid cylindrical length of low durometer elastomeric material that is wraped around the pile and then cemented to form a ring. A two section cap is placed over the "0" ring and bolted together to form an essentially solid gland ring. The "0" ring is compressed by four jacking screws, sealing off the pile penetration to the passage of ground water.

After the vacuum tube installation has been completed, the upper segment of the pipe-arch is bolted in place and is bermed over with earth. Figure 6.300 illustrates Scheme 2.

Three foot diameter access hatches with bolted water-tight covers are located approximately 800 meters apart along the run of the pipe-arch for access to the high vacuum pumping systems operating on the vacuum tube.

Bermed over 11'-5" wide x 7'-3" high multi-plate pipe-arch sections are tee'd to the main pipe-arch along its run as required, to house the vacuum roughing pumps.

Figure 6.203 illustrates a typical reinforced concrete pile and cap that is used for both fixed and sliding vacuum tube supports and Figure 6.104 illustrates the support spacing for the 12", 24", 36" and 48" vacuum tube for Scheme 2. The support spacing is based on an allowable maximum tube deflection of 1 cm.

The end station buildings, the laser cooling system, the central maintenance facility building, the computer and control trailer, the office trailers, living quarters trailers, recreation and cafeteria trailer, switch yard and potable water tank are all as described in Scheme 1.

Estimated Costs of Scheme 2

The estimated costs of the variations studied for Scheme 2 are presented in detail in Section 9, pages 31 to 34 and 53 to 61. Table 6.30 summarizes these costs.

FIXED COSTS INDEPENDENT OF LENGTH	TUBE SIZE	COST OF MULTI-PLATE PIPE-ARCH PER KM	COST OF CLEARING & GRADING PER KM	COST OF BERM PER KM	COST OF SUPPORTS PER KM	ELECTRICAL COSTS FOR ANTENNA RUN PER KM	TOTAL COST PER KM	TOTAL COST FOR TWO 5KM ARMS + FIXED COSTS
$4,880,600	12"	$688,590	$13,770	$150,840	$76,504	$99,880	$1,029,584	$15,176,440
	24"	688,590	13,770	150,840	77,968	99,880	1,031,048	15,191,080
	36"	688,590	13,770	150,840	55,748	99,880	1,008,828	14,968,880
	48"	688,590	13,770	150,840	65,744	99,880	1,018,824	15,068,840

TABLE 6.30
Cost Summary of Scheme 2

6.4 Scheme 3

Scheme 3, as illustrated in Figures 5.102 and 6.401, is identical to Scheme 2 with the exception that the multi-plate pipe-arch is layed on a gravel bed and buried below grade with 4'-0" of earth cover. The cover is stabilized against erosion by planting native foliage on its surface.

6.4.1 Estimated Costs of Scheme 3

The estimated Costs of the variations studied for Scheme 3 are presented in detail in Section 9, pages 31 to 34 and 53 to 61. Table 6.40 summarizes these costs.

FIXED COSTS INDEPENDENT OF LENGTH	TUBE SIZE	COST OF MULTI-PLATE PIPE-ARCH PER KM	COST OF CLEARING PER KM	TRENCHING BEDDING & BACK FILLING PER KM	COST OF SUPPORTS PER KM	ELECTRICAL COSTS FOR ANTENNA RUN PER KM	TOTAL COST PER KM	TOTAL COST FOR TWO 5KM ARMS + FIXED COSTS
$4,880,600	12"	$688,590	$27,870	$249,200	$76,504	$99,880	$1,142,044	$16,301,04C
	24"	688,590	27,870	249,200	77,968	99,880	1,143,508	16,315,6
	36"	688,590	27,870	249,200	55,748	99,880	1,121,288	16,093,4
	48"	688,590	27,870	249,200	65,744	99,880	1,131,284	16,193,44C

TABLE 6.40
Cost Summary of Scheme 3

7 Mine Installation

7.1 Passage Dimensions

A review of Table 3.2-1 of Section 3.0 "Subsurface Sites" reveals that few of the candidate mines have passage lengths exceeding 1 km in length. In this study, therefore, substantial tunneling was assumed, so that the vacuum tube would be comparable in length and diameter variations with that used for the above ground installation study.

7.2 Installations Description

Figure 7.100 illustrates the layout of mine installation.

Two sets of assumptions are made about the extent of pre-existing passages. As a best case, an available line-of-sight passage length of 1 km was assumed for each leg of the vacuum tube, requiring 4 km of tunneling at each leg. As a worst case, it was assumed that a full 10 km of tunneling is required. The cost of tunneling is minimized when typical mining cross sections are used, and therefore a 10'-0" high x 12'-0" wide tunnel was selected for the study. Each end station is housed in an excavated vault 40'-0" wide x 62'-0" long x 34'-0" high. The vault is furnished with lighting and power and a 12 ton capacity pendant operated bridge crane. Drinking water is supplied from a storage tank and chemical sanitation facilities are also provided. A movable partition is also provided to separate the end station area from the machine shop area. The end station area is 40'-0" x 44'-0". This provides ample floor space for lay-down of the removable portion of the end station vacuum vessel and the end station internals. The machine shop area is 40'-0" x 18'-0". The machine shop contains machine tools and welding equipment necessary for the maintenance, repair or modification of the end station internals. The support structure for the end station of the high vacuum pump room, the end station floor, the machine shop floor and the bridge crane column bases are constructed of reinforced concrete.

The study revealed that, for all of the mines investigated, access by either horizontal passage or vertical passage will limit the largest piece of equipment to be taken into the mine to 6'-0" x 6'-0" x 40'-0" long x 8 tons maximum weight.

Because of this limitation, three one and one half cubic yard portable concrete mixers and a two yard loading hopper and conveyor will be brought into the mine for mixing the concrete. The sand cement and aggregate will be dry mixed on the surface and brought into the mine in tilt-body mine wagons. After the concreting within the vault has been completed, a portable derrick will be installed for use in erecting the 12 ton crane. The portable derrick is a standard item of construction equipment, capable of being assembled and disassembled without recourse to lifting equipment for use in restricted areas.

The following elements have increased the Fixed Costs for the Mine Scheme as compared to Schemes 1, 2 and 3:

1. Surface cooling system lines to lasers in mine
2. Vault excavation for end stations and difficulty of working in vault
3. Electrical and I&C ties to antenna array in mine
4. Ventilation to end stations

The end station vacuum vessel will be fabricated in place. Portable rotating rolls, welding equipment, a drilling machine and a portable milling machine will be installed for this purpose. The portable milling machine is available from several sources and is necessary for machining the body and head, flanges of the vacuum vessel after all welding has been completed.

Forced ventilation fans and duct-work are installed as an adjunct to the existing mine ventilation equipment for ventilating the end station vaults and vacuum tube tunnels.

Lighting and power are provided along the run of each tunnel for use in operating and maintaining the roughing pumps and the high vacuum pumps.

The laser cooling system, the central maintenance facility building, the computer and control tractor, the office trailers, living quarters trailers, recreation and cafeteria trailer, switch yard and potable water tank are all as described in Scheme 1 and are located on the surface above the mine.

Figure 7.103 illustrates an end station vault. Figure 7.101 illustrates the support spacing for the 12", 24", 36" and 48" vacuum tube within the mine tunnels. The support spacing is based on an allowable maximum tube deflection of 1 cm.

Figure 7.102 illustrates a typical reinforced concrete support that is used for both fixed and sliding vacuum tube supports.

7.2.1 Estimated Costs of the Mine Installation

The estimated costs of mine installation for the variations of vacuum tube sizes studies, are presented in Section 9, pages 35 to 52 and 53 to 61.

Table 7.20 summarizes these costs.
NOTE: **

FIXED COSTS INDEPENDENT OF LENGTH	TUBE SIZE	COST OF TUNNELING PER KM	COST OF TUNNEL VENTILATION PER KM	ELECTRICAL COSTS FOR ANTENNA RUN PER KM	COST OF SUPPORTS PER KM	TOTAL COST PER KM	TOTAL COST TWO 5KM ARM + FIXED COST
$6,610,000	12"	$656,000	$46,000	$88,000	$73,970	$ (863,970)	$15,249,700
		902,000	46,000	88,000	73,970	(1,109,970)	17,709,700
	24"	656,000	46,000	88,000	83,590	(873,590)	15,345,900
		902,000	46,000	88,000	83,590	(1,119,590)	17,805,900
	36"	656,000	46,000	88,000	63,340	(853,340)	15,143,400
		902,000	46,000	88,000	63,340	(1,099,340)	17,603,400
	48"	656,000	46,000	88,000	77,620	(867,620)	15,286,200
		902,000	46,000	88,000	77,620	(1,113,620)	17,746,200
$6,610,000	12"	$656,000	$46,000	$88,000	$73,970	$ (836,970)	$13,521,760
		902,000	46,000	88,000	73,970	(1,109,970)	15,489,760
	24"	656,000	46,000	88,000	83,590	(873,590)	13,598,720
		902,000	46,000	88,000	83,590	(1,119,590)	15,566,720
	36"	656,000	46,000	88,000	63,340	(853,340)	13,436,720
		902,000	46,000	88,000	63,340	(1,099,340)	15,404,720
	48"	656,000	46,000	88,000	77,620	(867,620)	13,550,960
		902,000	46,000	88,000	77,620	(1,113,620)	15,518,960

TABLE 7.20
Cost Summary of Mine Installation

Table 7.20
Cost Summary of Mine Installation

( ) = Range Low / High

Low Range = $200* per Linear Foot
High Range = $275* per Linear Foot

* See Section 9, page 42

** In the case where portions of the tunnel are already excavated, the total cost is less than the sum of the fixed cost and the product of the cost/unit length times 10 km.

8 Summary

In order to compare the various installation schemes, we present a summary of the costs in Tables 8.10, 8.11 and 8.12.

8.1 Fixed Costs

The fixed costs, shown in Table 9.10, are very similar for all schemes. These costs are dominated by the cost of providing electric power to the antenna site. The largest demand for power is the approximately 100 kilowatts required to achieve 100 watts of optical power in an Argon laser. About 20% of the electrical cost is due to an assumed 8 mile long connection between an existing high voltage transmission line and the site. (This cost may be larger or smaller, depending on the length of the line required at the actual site). An additional cost is added in the mine case for bringing the power from the surface level to the instrument.

The next largest fixed cost is in the end station buildings. This cost is slightly larger for Scheme 3 because of the required excavation below grade. It is substantailly larger in a mine, in part because the entire volume of the end station must be excavated from the rock, and in part because a pre-engineered building can not be used.

The other fixed costs are for the cooling system for the laser, and for the buildings in the control compound. The costs of the latter are identical in the four schemes, while the cooling cost is larger for the mine because of the extra run from laser to heat exchanger. The one additional cost which is specific to the mine is the cost of a ventilation system.

These fixed costs, which would have to be borne no matter how short the antenna arms were made, are not inconsequential. For the three ground-level schemes, the total of fixed costs is approximately $4.6 million. For the mine installation, the total is nearly $6.5 million.

8.2 Variable Costs

There is more distinction between the different construction schemes in the variable costs, since it is in the protection of the interferometer arms that the schemes vary. These costs are summarized in Table 9.11.

Scheme 1 is the only one in which the tubes are insulated. In addition, a larger number of tube supports are used to keep tube deflection below 1 cm even in a strong wind (70 mph). In the variant which uses a wind wall, the extra cost in supports is not needed, but is replaced by an even larger cost for the walls themselves. Still, the total variable cost is only of order one half of the totals for the other schemes.

Schemes 2 and 3 have variable costs which are quite similar. This is because these costs are dominated by the cost of the galvanized steel culvert which encloses the vacuum tube in both schemes. The total variable cost for Scheme 2 is about 10% less than for Scheme 3 because forming the berm involves less extensive earth-moving than does trenching.

Perhaps the most remarkable outcome of the cost study is the rather close agreement between the variable costs for the mine installation and for Schemes 2 and 3. In the mine, the culvert would serve no purpose. The large cost is instead extending the mine itself to the proper dimensions. The mining cost varies greatly from mine to mine, so the chart lists a range of costs believed to span the conditions one is likely to encounter in suitable mines. At the high end of the range, the total variable cost closely matches that of Scheme 3. At the low end, the cost is below that of Scheme 2.

8.3 Total Costs and General Remarks

The sum of the fixed and variable costs is listed in Table 9.12. As expected, Scheme 1 (without wind walls) is the least expensive, with the total varying from $9.0 million for an antenna with 24" tubes to $10.9 million for 36" tubing. Scheme 2 is next at roughly $15.0 million, with Scheme 3 only slightly high than $16 million. Because of uncertainty in mining cost and the size of the pre-existing mine which would be used, it seems fairest to quote the total cost for construction in a mine in a range from $13.5 million to $17.9 million.

On the basis of cost alone, Scheme 1 is clearly to be preferred. But the sacrifice which is asked in terms of a less benign thermal and mechanical environment is so great that one should hesitate to choose this as the method of installation. No one would think of building a particle accelerator out of doors. This is not a particle accelerator, yet it is a large, painstakingly aligned high vacuum system. The risk of additional noise in the instrument is high, as is the risk that the vacuum system itself will suffer additional maintenance problems. Adding the wind walls reduces some, but not all of these concerns, and adds over $1 million to the cost.

In terms of providing a benign environment, the mine installation is probably the best choice. Compared to Schemes 2 and 3, there does not even appear to be much, if any, additional cost. Yet there is one fact not emphasized so far which may show up as an additional cost. The techniques used in mining allow an advance of the mine face of only about 10 feet per working shift (independent of face cross-section). Thus it would take at least 1.5 to 2 years to excavate a tunnel of the required size, even with a three shift operation. Such an intensive effort would of course raise labor costs, while the delay is costly in itself, if not in an easily quantifiable way.

The costing exercise summarized here has been made in terms of installing one antenna, but the gravitational wave detection project will require (at least) two antennas. It is interesting to consider whether there can be cost savings from spreading some costs over the larger system. In the construction it does not appear that these can amount to more than a few percent, mainly from the sharing of engineering costs, which will probably be assessed as a fixed percentage increment on the project budget. The construction materials incorporated are for the most part standard items, and the economies of scale have already been attained in projecting the costs for a single antenna.

Scheme No.	Support Buildings	End Stations	Cooling System	Ventilation	Transmission Line - 8 Miles & Line To Tunnel	Power Distrib.	Line Tie-In	Wiring To Vaults	Total Fixed Cost
1.	112	807	250	---	680	1,831	950	250	4,880
2.	112	807	250	---	680	1,831	950	250	4,880
3.	112	864	250	---	680	1,831	950	250	4,937
								Use	4,940
4.	112	1,560	350	260	1,330	1,831	950	220	6,613
								Use	6,610

TABLE 8.10 - FIXED COST INDEPENDENT OF LENGTH (10^3 $)

Scheme No. & Tube Size	Clearing & Grading	Trenching, Bedding & Backfill	Tunneling 10'x12'	Ventil. Tunnel	Supports	Insulation (Based on 6")	Tube Housing	Berm	Electrical	Total Per Km
1										
12"	10	---	---	--	122	111	---	---	100 =	343
24"	10	---	---	--	104	198	---	---	100 =	412
36"	10	---	---	--	156	334	---	---	100 =	600
48"	10	---	---	--	259	485	---	---	100 =	854
2										
12"	14	---	---	--	76	---	689	151	100 =	1,030
24"	14	---	---	--	78	---	689	151	100 =	1,032
36"	14	---	---	--	56	---	689	151	100 =	1,010
48"	14	---	---	--	66	---	689	151	100 =	1,020
3										
12"	28	249	---	--	76	---	689	---	100 =	1,142
24"	28	249	---	--	78	---	689	---	100 =	1,144
36"	28	249	---	--	56	---	689	---	100 =	1,122
48"	28	249	---	--	66	---	689	---	100 =	1,132
4(Mine)										
12"	--	---	656	46	74	---	---	---	88 =	864
24"	--	---	656	46	84	---	---	---	88 =	874
36"	--	---	656	46	63	---	---	---	88 =	853
48"	--	---	656	46	78	---	---	---	88 =	868
12"	--	---	902	46	74	---	---	---	88 =	1,110
24"	--	---	902	46	84	---	---	---	88 =	1,120
36"	--	---	902	46	63	---	---	---	88 =	1,099
48"	--	---	902	46	78	---	---	---	88 =	1,114

TABLE 8.11 - COSTS DEPENDENT ON LENGTH (10^3 $/Km)

Scheme No.		Tube Size		Fixed $	Total Variable Costs K$	Total M$
1		12"		$4,880	$3,430	8.3
		24"		4,880	4,120	9.0
		36"		4,880	6,000	10.9
		48"		4,880	8,540	13.4
2		12"		4,880	10,300	15.2
		24"		4,880	10,320	15.2
		36"		4,880	10,100	15.0
		48"		4,880	10,200	15.1
3		12"		4,940	11,420	16.4
		24"		4,940	11,440	16.4
		36"		4,940	11,220	16.2
		48"		4,940	11,320	16.3
4	(Mine)	12"	8 KM of Tunneling	6,610	(6,912) (8,880)	(13.5) (15.5)
		24"		6,610	(6,992) (8,960)	(13.6) (15.6)
		36"		6,610	(6,824) (8,792)	(13.4) (15.4)
		48"		6,610	(6,944) (8,912)	(13.6) (15.5)
		12"	10 KM of Tunneling	6,610	(8,640) (11,100)	(15.2) (17.7)
		24"		6,610	(8,740) (11,200)	(15.3) (17.8)
		36"		6,610	(8,530) (10,990)	(15.1) (17.6)
		48"		6,610	(8,680) (11,140)	(15.3) (17.7)

TABLE 8.12 - TOTAL COSTS - ARM LENGTH - 5km

( ) = Range $\begin{matrix}\text{Low}\\ \text{High}\end{matrix}$

Low Range = $200* per Linear Foot
High Range = $275* per Linear Foot

* See Section 9, Page 42.

▲ 5010.10

STONE & WEBSTER ENGINEERING CORPORATION

CALCULATION SHEET — Preliminary — NOTED SEP 27 1983 A.D. Eurla

Page No. 5.1.1

Client MIT — Location — Est. No. — J.O. No. 14190.02

Subject Interferometric Broad Band Gravitational Antenna — Date — Checked — By — By A.T. Fujita

SUMMARY - SCHEME NO. 1 (W & W/O Windwall)

Tube Size	Insulation Thickness	Insulation Cost	Clearing & Grading	Support Cost w/ Windwall	Support Cost w/o Windwall	Cost of Windwall	Electrical for Antenna Run	Total Cost-Variable	Cost/Km	Total Cost	Based on
		* $	$	$	$	$	$	$	$	$	
12"Ø	6"	1,108,300	98,000		1,223,640		998,800	= 3,428,740	342,874	8,309,340	0
	9"	1,734,600			1,380,720			= 4,212,120	421,212	9,092,720	0
	12"	2,449,400			1,707,420			= 5,253,620	525,362	10,134,220	0
	6	1,108,300		1,096,905		2,362,205		= 5,664,210	566,421	10,544,810	0
	9	1,734,600		1,237,717		↓		= 6,431,320	643,132	11,311,920	2
	12	2,449,400		1,546,497				= 7,454,900	745,490	12,335,550	2
24"Ø	6	1,977,200			1,042,140			= 4,116,140	411,614	8,996,740	
	9	2,983,900			1,576,740			= 5,657,440	565,744	10,538,040	0
	12	4,098,800			1,714,020			= 6,909,620	690,962	11,790,220	0
	6	1,977,200		1,042,140		2,362,205		= 6,478,345	647,835	11,358,945	5
	9	2,983,900		1,333,598		↓		= 7,776,503	777,650	12,657,103	5
	12	4,098,800		1,501,770				= 9,059,575	905,958	13,940,175	5
36"Ø	6	3,344,600			1,556,940			= 5,998,340	599,834	10,878,940	0
	9	5,026,700			2,065,140			= 8,188,640	818,864	13,069,240	0
	12	6,836,700			2,551,560			= 10,485,060	1,048,506	15,365,660	0
	6	3,344,600		1,556,940		2,362,205		= 8,360,540	836,054	13,241,145	5
	9	5,026,700		1,668,623		↓		= 10,154,330	1,015,433	15,034,928	8
	12	6,836,700		2,086,358				= 12,382,063	1,238,206	17,262,663	3
48"Ø	6	4,849,600			2,589,510			= 8,535,910	853,591	13,416,510	0
	9	7,384,300			2,767,710			= 11,248,810	1,124,881	16,129,410	0
	12	9,915,700			2,934,030			= 13,946,530	1,394,653	18,827,130	0
	6	4,849,600		2,370,801		2,362,205		= 10,679,406	1,067,941	15,560,006	
	9	7,384,300		2,767,710		↓		= 13,611,015	1,361,102	18,491,615	5
	12	9,915,700		2,934,030				= 16,308,735	1,630,874	21,189,335	5
	↑	↑	↓	↓	↓	↓	↓				
	* 4,880,600										

* Fixed Costs Independent of Length

RECAP - SCHEME NO. 1 - SUPPORTS
(Above Ground - No Wind Barrier)

12" Tube

Insulation Thickness	FRANKI Piles #	Caps #	Steel Plate #	Subtotal #		No. of Supports	Total #	Pipe Assemblies Total # Fixed	Sliding	Total Supports #
6 "	300	400	150 =	850	×	1,122 =	953,700	5,940	264,000 =	1,223,640
9 "	300	500	190 =	990	×	1,122 =	1,110,780	5,940	264,000 =	1,380,720
12 "	300	600	220 =	1,120	×	1,254 =	1,404,480	5,940	297,000 =	1,707,420

24" Tube

6 "	380	600	220 =	1,200	×	726 =	871,200	5,940	165,000 =	1,042,140
9 "	380	960	260 =	1,600	×	858 =	1,372,800	5,940	198,000 =	1,576,740
12 "	380	1,080	300 =	1,760	×	858 =	1,510,080	5,940	198,000 =	1,714,020

36" Tube

6 "	640	1,420	300 =	2,360	×	594 =	1,401,840	7,260	147,840 =	1,556,940
9 "	640	1,600	340 =	2,580	×	726 =	1,873,080	7,260	184,800 =	2,065,140
12 "	880	2,000	370 =	3,250	×	726 =	2,359,500	7,260	184,800 =	2,551,560

48" Tube

6 "	1,200	2,500	370 =	4,070	×	594 =	2,417,580	8,250	163,680 =	2,589,510
9 "	1,200	2,760	410 =	4,370	×	594 =	2,595,780	8,250	163,680 =	2,767,710
12 "	1,200	3,000	450 =	4,650	×	594 =	2,762,100	8,250	163,680 =	2,934,030

▲ 5010.1D STONE & WEBSTER ENGINEERING CORPORATION Preliminary

CALCULATION SHEET NOTED SEP 27 1983 A.D.Furia

Client MIT Location Est. No. J.O. No. 4190.02

Subject Interferometric Broad Band Gravitational Antenna Date By A.D. FURIA

Checked By

Based on Revised By

Cast-in-Place Concrete Piles
(FRANKI - Pressure Injected Footings)

Incl. Mobilization & Demobilization, Concrete & Reinforcing (1% Vertical & 2% Spiral)

8" ø × 35'-0" (Av. Lgth.)	=	$ 8.52/VLF	= $300
10" ø × 35'-0" (" ")	=	$ 10.72/VLF	= 380
12" ø × 35'-0" (" ")	=	$ 18.31/VLF	= 640
14" ø × 35'-0" (" ")	=	$ 25.13/VLF	= 880
16" ø × 35'-0" (" ")	=	$ 34.31/VLF	= 1,200

Caps (Incl. Forms, Reinf)

L	W	H	Caps $	** 1/8" Insulating Board, Pile Cut-Off & Leveling, 3/8"ø Studs × 4"L $		* Steel Plate - 2½" Th. 8"W - 68#/LF $
24"	12"	12"	50	350	= 400	136 LBS × $1.10 = 150
30"	12"	12"	65	435	= 500	170 " × " = 190
36"	12"	12"	70	530	= 600	204 " × " = 220
42"	12"	12"	85	615	= 700	238 " × " = 260
42"	14"	14"	115	845	= 960	238 " × " = 260
48"	12"	12"	95	705	= 800	272 " × " = 300
48"	14"	14"	130	950	= 1,080	272 " × " = 300
48"	16"	16"	170	1,250	= 1,420	272 " × " = 300
54"	12"	12"	110	790	= 900	306 " × " = 340
54"	16"	16"	190	1,410	= 1,600	306 " × " = 340
60"	12"	12"	120	880	= 1,000	340 " × " = 370
60"	18"	16"	240	1,760	= 2,000	340 " × " = 370
60"	20"	18"	300	2,200	= 2,500	340 " × " = 370
66"	12"	12"	145	955	= 1,100	374 " × " = 410
66"	20"	18"	330	2,430	= 2,760	374 " × " = 410
72"	12"	12"	145	1,055	= 1,200	408 " × " = 450
72"	20"	18"	360	2,640	= 3,000	408 " × " = 450

* Set & Bolt To Cap

** Includes checking level of each pile with transit and cutting if required, purchase and set studs for steel plate in cap, checking level of caps and grinding to final tolerances and purchasing & setting insulating board between steel plate and Aluminum.

▲ 5010.1D

STONE & WEBSTER ENGINEERING CORPORATION

CALCULATION SHEET

Page No. 24.

Preliminary

Item

Client MIT Location Est. No. NOTED OCT 3 1983 A.D. Furia J.O. No. 14190.02

Subject Interferometric Broad Band Gravitational Antenna Date By A.V. Furia

Based on Pipe Assemblies - Fixed & Sliding Revised By Checked By

PIPE ASSEMBLIES

Scheme No.	Tube Size	Insulation Thickness	FIXED No. of Supports	FIXED Unit Cost EA	FIXED Total $	SLIDING No. of Supports	SLIDING Unit Cost	SLIDING Total $	Total $
1	12"Ø	6"	66	$ 90.	= 5,940	1056	$ 250.	= 264,000	269,940
		9"	66	90.	= 5,940	1056	250.	= 264,000	269,940
		12"	66	90.	= 5,940	1188	250.	= 297,000	302,940
	24"Ø	6"	66	90.	= 5,940	660	250.	= 165,000	170,940
		9"	66	90.	= 5,940	792	250.	= 198,000	203,940
		12"	66	90.	= 5,940	792	250.	= 198,000	203,940
	36"Ø	6"	66	110.	= 7,260	528	280.	= 147,840	155,100
		9"	66	110.	= 7,260	660	280.	= 184,800	192,060
		12"	66	110.	= 7,260	660	280.	= 184,800	192,060
	48"Ø	6"	66	125.	= 8,250	528	310.	= 163,680	171,930
		9"	66	125.	= 8,250	528	310.	= 163,680	171,930
		12"	66	125.	= 8,250	528	310.	= 163,680	171,930
2	12"Ø	0"	196	90.	= 17,640	528	250.	= 132,000	149,640
	24"Ø	0"	196	90.	= 17,640	396	250.	= 99,000	116,640
	36"Ø	0"	196	110.	= 21,560	264	280.	= 73,920	95,480
	48"Ø	0"	196	125.	= 24,500	264	310.	= 81,840	106,340
3 & 4	12"Ø	0"	196	90.	= 17,640	528	250.	= 132,000	149,640
	24"Ø	0"	196	90.	= 17,640	396	250.	= 99,000	116,640
	36"Ø	0"	196	110.	= 21,560	264	280.	= 73,920	95,480
	48"Ø	0"	196	125.	= 24,500	264	310.	= 81,840	106,340

MIT
Interferometric Broad Band
Gravitational Antenna
J.O.14190.02

NOTED SEP 27 1983 A.D.Furia

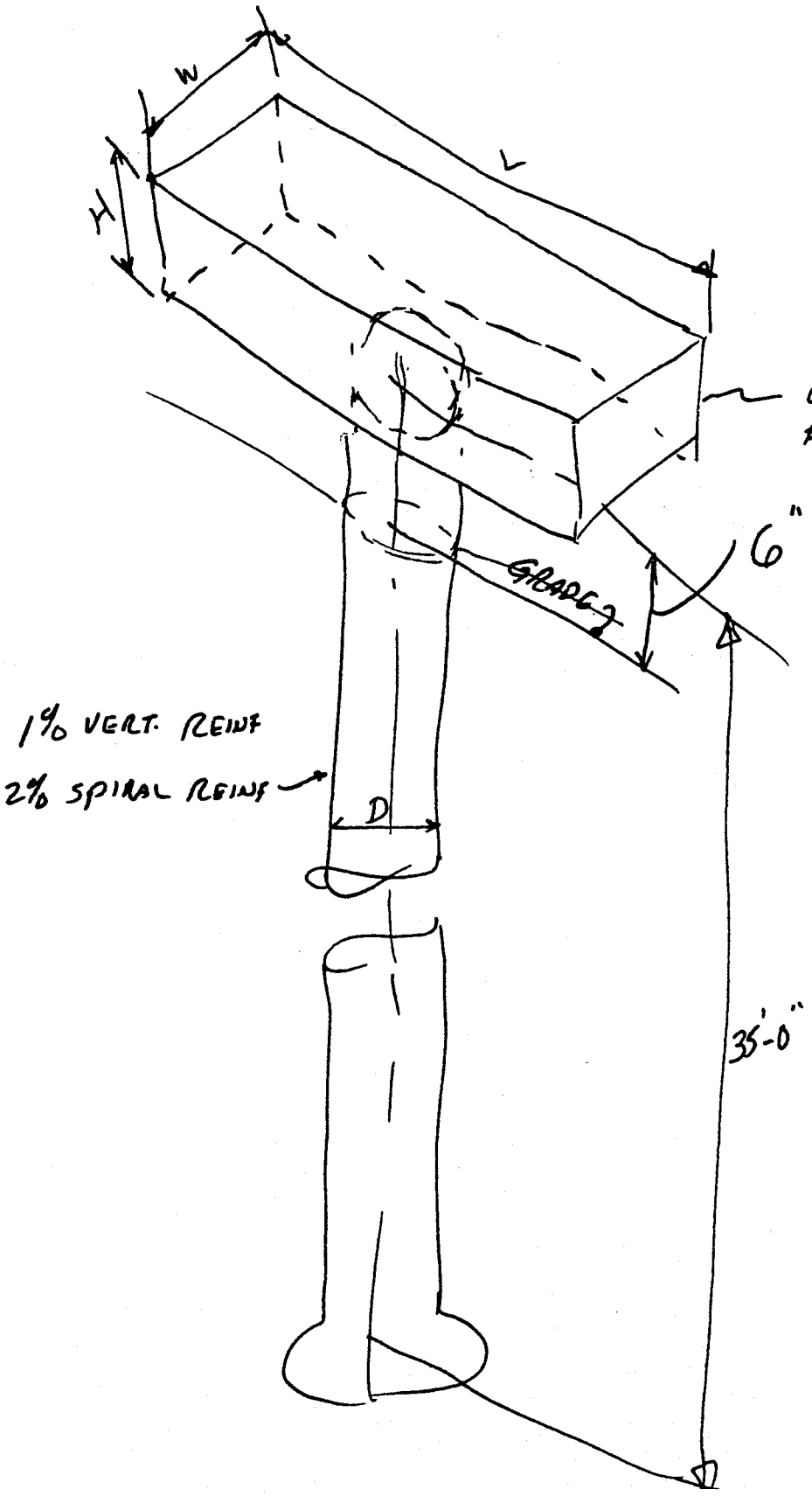

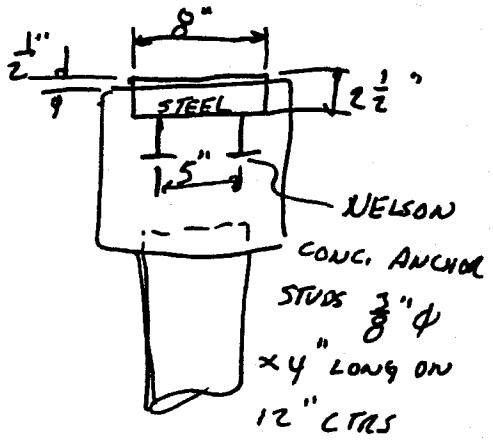

USE SPAULDITE INSULATING BOARD ($\frac{1}{8}$" THK) BETWEEN ALUMINUM & STEEL R.

STONE & WEBSTER ENGINEERING CORPORATION

CALCULATION SHEET

NOTED SEP 27 1983 A.D.Furia

Client MIT Location Est. No. J.O. No. 4190.02

Subject Interferometric Broad Band Gravitational Antenna (Installed Costs) Date By A.D. FURIA

Checked By

Based on Revised By

RECAP - SCHEME NO.1 - INSULATION
(Johns-Manville-Zeston w/Aluminum Jacket)

Insulation Thickness											
12" ø Tube											
6"	$33.80/LF	×	32,790	=	$1,108,300	$60.30/LF	×	32,790	=	$1,977,200	
9"	52.90/LF	×	32,790	=	1,734,600	91.00/LF	×	32,790	=	2,983,900	
12"	74.70/LF	×	32,790	=	2,449,400	125.00/LF	×	32,790	=	4,098,800	
24" ø Tube											
6"	$102.00/LF	×	32,790	=	$3,344,600	$147.90/LF	×	32,790	=	$4,849,600	
9"	153.30/LF	×	32,790	=	5,026,700	225.20/LF	×	32,790	=	7,384,300	
12"	208.50/LF	×	32,790	=	6,836,700	302.40/LF	×	32,790	=	9,915,700	
36" ø Tube											
6"											
9"											
12"											
48" ø Tube											
6"											
9"											
12"											

▲ 5010.1D

STONE & WEBSTER ENGINEERING CORPORATION

Preliminary

CALCULATION SHEET

Item

NOTED SEP 27 1983 A.D.Furia

Client MIT | Location | Est. No. | J.O. No. 14190.02

Subject PIPE INSULATION | Date | By A.D. Furia

Johns-Manville (ZESTON) | Checked | By

Based on $/LF | Revised | By

	THICKNESS 6"	9"	12"
12" Ø			
Material	$ 13.50	$ 22.15	$ 31.80
Labor	7.30 ~~25.10~~	11.95 ~~41.15~~	17.20 ~~59.10~~
Total	$ ~~38.60~~ $ 20.80	$ ~~63.30~~ $ 34.10	$ ~~90.90~~ $ 49.00
Aluminum Waterproof Jacket - 0.016"			
Material	$ 4.00	$ 5.80	$ 7.90
Labor	9.00	13.00	17.80
Total	$ 13.00	$ 18.80	$ 25.70
	33.80 $ ~~51.60~~/LF	$ ~~52.90~~ ~~82.10~~/LF	$ ~~74.70~~ ~~116.60~~/LF
24" Ø			
Material	$ 24.40	$ 38.40	$ 54.15
Labor	13.20 ~~45.30~~	20.80 ~~71.30~~	29.25 ~~100.65~~
Total	$ ~~69.70~~ 37.60	$ ~~109.70~~ 59.20	$ ~~154.80~~ 83.40
Aluminum Waterproof Jacket - 0.016"			
Material	$ 7.00	$ 9.80	$ 12.80
Labor	15.70	22.00	28.80
Total	$ 22.70	$ 31.80	$ 41.60
	$ ~~92.40~~ 60.30/LF	$ ~~141.50~~ 91.00/LF	$ ~~196.40~~ 125.00/LF

Client MIT | Location | Est. No. | J.O. No. 14190.02

Subject PIPE INSULATION | Date | By A.D. Furia

Johns-Manville (ZESTON) | Checked | By

Based on $/LF | Revised | By

	THICKNESS 6"	9"	12"
36" Ø			
Material	$ 41.35	$65.05	$90.10
Labor	22.35 ~~76.85~~	35.15 ~~+20.85~~	48.70 ~~+67.40~~
Total	$ ~~+18.20~~ 63.70	$ ~~+85.90~~ 100.20	$ ~~257.50~~ 138.80
Aluminum Waterproof Jacket - 0.016"			
Material	$ 11.80	$ 16.35	$ 21.45
Labor	26.50	36.75	48.25
Total	$ 38.30	$ 53.10	$ 69.70
	$ 102.00/LF	$ 153.30/LF	$ 208.50/LF
48" Ø			
Material	$ 59.35	$ 96.00	$ 131.10
Labor	32.05	51.90	70.90
Total	$ 91.40	$ 147.90	$ 202.00
Aluminum Waterproof Jacket - 0.016"			
Material	$ 17.40	23.80	30.90
Labor	39.10	53.50	69.50
Total	$ 56.50	$ 77.30	$ 100.40
	$ 147.90/LF	$ 225.20/LF	$ 302.40/LF

NOTED SEP 27 1983 A.D.Furia

Client MIT Location Est. No. J.O. No. 14190.02

Subject Pipe Insulation Date By A.D. Furia

Checked By

Based on Revised By

Industrial Insulation & Packing Products Co.
60 Lansdowne St.
Cambridge, MA

324-8251 (Malden - New Number)

Ed Burquhart

Johns-Manville (Zeston) 36" W x (See Thickness Below)
↳ Similar To Fiberglass

MATERIAL

1" Thick	1½" Thick	2"	3"
43 LF/Roll	35 LF/Roll	26 LF/Roll	17½ LF/Roll
$.87/SF	$.91 SF	$1.14/SF	$1.73/SF

Aluminum Waterproof Jacket, w/Vapor Barrier
- and 0.016" Thick

Plain or Corrugated - Same Price

36" x 100 LF --- $94.17/Roll

$.314/SF

Scheme I (Above Ground)

	6" Thick	9" Thick	12" Thick
12" ∅ 24" ∅ 36" ∅ 48" ∅ } Alum. Pipe	(See Sheet 16. for Recap)		

▲ 5010.1D STONE & WEBSTER ENGINEERING CORPORATION

Preliminary

Item

NOTED SEP 27 1983 A.D. FURIA CALCULATION SHEET

Client MIT Location Est. No. J.O. No. 14190.02

Subject Interferometric Broad Band Gravitational Antenna Date 9/20/83 By A.D. Furia

Checked By

Based on Electrical Work In Antenna Area Revised By

12-16-82 Estimate (Scheme 1, 2 & 3) * Escalation ↓

** $7,877,150 ÷ 41.1 Miles = $191,660 × 1.04923 =

$201,095 × 6.21 Miles =

$1,248,800

Mine

12-16-82 Estimate --- $ 7,877,150

Poles, Hdwre & Assoc. Materials < 938,650 >

$ 6,938,500 ÷ 41.1 Miles

= $168,820 × 1.04923

= $177,130 × 6.21 Miles

= $1,099,980

Use → $1,100,000

TOTAL LOAD

Antenna 2,500 KVA

Building Area 750 KVA

Total Load 3,250 KVA

Use → 3,750 KVA

(115 KV Transmission Line To Site)

** Cable
Terminations
Hangers - Uni-strut or Cable Trays
Pad Mtd. Transformers
Disconnect Switches
MCC
Feeders
Control & Instrumentation
Allowance.

* Escalation @ 6½%/Yr.
9 Months - 3 Days

9.1 × .00541 = .04923

▲ 5010.1D

STONE & WEBSTER ENGINEERING CORPORATION

CALCULATION SHEET

Preliminary

Item

NOTED SEP 27 1983 A.D.Furia

Client MIT | Location | Est. No. | J.O. No. 14190.02

Subject Interferometric Broad Band Gravitational Antenna | Date | By A.P. FURIA

Checked | By

Based on SCHEME 2 | Revised | By

Clear & Grade

12' x 1' = 12 SF/LF x $.35/SF = $4.20/LF

*Backfill (4' of Cover Over Above Ground Culvert)

Purchased Backfill - Select Structural Fill

7 CY/LF x $6.50/CY = $45.50/LF

Use ↓ $46.00/LF

* Incl. Compaction & Soil Stabilization

$ 50.20 x 32,790 LF = $1,646,100 ✓

ARMCO Corrugated Steel Pipe Arch - Galvanized & Coated - 20' Sections - Hugger-Type Joints (Bar & Strap Connector w/O-Ring Gaskets)

137" Span — 87" Rise

11'-5" — 7'-3"

Bob Clayman
ARMCO Inc.
Construction Div.
Malboro, MA
485-1323
} 9/20/83

$155 Delivered (1,000 Mile Radius of Ohio Plant)
25 Installation → 20' sections
$180.00/LF Delv. & Installed

↓ Scheme 2 & 3

Use Multi-Plate Pipe Arch (Galvanized - 10 GA (0.138"))

$160 Delivered
50 Installation
$210.00/LS Delv. & Installed ✓ (11'-5" Span, 7'-3" Rise)

*$210.00/LF x 32,790 LF = $6,885,900 ✓

*(Incl. Tee Sections)

▲ 5010.1D

STONE & WEBSTER ENGINEERING CORPORATION

Preliminary

CALCULATION SHEET

Item

NOTED SEP 27 1983 A.D.Furia

Client MIT Location Est. No. J.O. No. 4190.02

Subject Interferometric Broad Band Gravitational Antenna Date By A.D. FURIA

Based on SCHEME 3 Checked By

Revised By

Sloping Side Trench (Avoids Using Sheeting)

Excavation

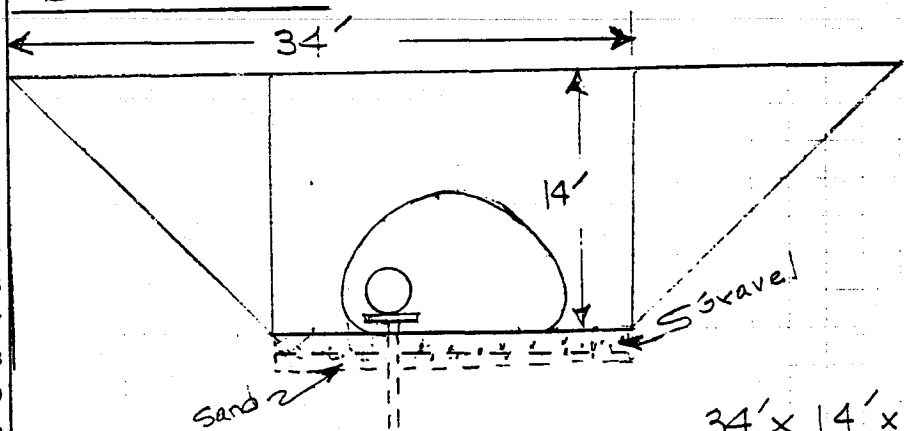

34' x 14' x 1' = 17.6 CY/LF

x $2.50/CY = $44.00/LF

Back-fill

14.6 CY/LF x 1.50/CY = 21.90/LF

Gravel Bedding

20' x 1' x 1' = .741 CY/LF

x $6.50/CY = $4.80/LF

Sand Bedding

20' x 1' x 1' = .741 CY/LF

x $7.30/CY = $5.40/LF

$76.10/LF

$76.00/LF x 32,790LF = $2,492,000 ✓

Use → $76.00/LF

▲ 5010.1D

STONE & WEBSTER ENGINEERING CORPORATION

CALCULATION SHEET

Page No. 53.1

Preliminary

Item

NOTED OCT 3 1983

Client MIT Location

Subject Interferometric Broad Band Gravitational Antenna SCHEME 4 MINE

Est. No. J.O. No. 14190.02

Date A.D.Furia By A.D.Furia

Checked By

Based on Revised By

SUMMARY - SCHEME NO.4 (MINE)

Tube Size	$/Km Tunneling 10'x 12'	Tunnel Ventilation	Electrical Antenna Run	Supports	Total Cost/Km	Total Cost 10 Km of Tunneling	Fixed Cost Independent of Length	Total Cost 10 Km of Tunneling + Fixed
12"Ø	$656,000	$46,000	$88,000	$73,970	($863,970)	$8,639,700	+ $6,610,000 =	$15,249,700
	902,000			↓	($1,109,970)	11,099,700		17,709,700
24"Ø	656,000			83,590	($873,590)	8,735,900		15,345,900
	902,000			↓	($1,119,590)	11,195,900		17,805,900
36"Ø	656,000			63,340	($853,340)	8,533,400		15,143,400
	902,000			↓	($1,099,340)	10,993,400		17,603,400
48"Ø	656,000			77,620	($867,620)	8,676,200		15,286,200
	902,000			↓	($1,113,620)	11,136,200		17,746,200

* Total Cost 8 Km of Tunneling + Fixed

12"Ø	656,000			73,970	($863,970)	8,639,700		13,521,760
	902,000			↓	($1,109,970)	11,099,700		15,489,760
24"Ø	656,000			83,590	($873,590)	8,735,900		13,598,120
	902,000			↓	($1,119,590)	11,195,900		15,566,720
36"Ø	656,000			63,340	($853,340)	8,533,400		13,436,720
	902,000			↓	($1,099,340)	10,993,400		15,404,720
48"Ø	656,000			77,620	($867,620)	8,676,200		13,550,960
	902,000			↓	($1,113,620)	11,136,200		15,518,960

* Based on 1 Km of Existing Tunnel/Leg ( ) = Range - Low ~ High

▲ 5010.1D

STONE & WEBSTER ENGINEERING CORPORATION

Preliminary

CALCULATION SHEET

Item

NOTED SEP 27 1983 A.D.Furia

Client MIT Location Est. No. J.O. No. 14190.02

Subject Interferometric Broad Band Gravitational Antenna (Installed Costs) Date By A.D. Furia

Checked By

Based on Revised By

RECAP - SCHEME NO. 4 SUPPORTS

(Footing in Mine)

Tube Size	Concrete	Steel	Rock Excavation	Subtotal	No. of Supports	Total
12" ∅	# 615	# 150	# 50	# 815	× 724	= # 590,060
24" ∅	920	220	75	1,215	× 592	= 719,280
36" ∅	1,230	300	100	1,630	× 330	= 537,900
48" ∅	1,535	370	125	2,030	× 330	= 669,900

✓ Total Pipe Assemblies Supports

✓ Fixed 17,640 132,000 = 739,700

✓ Sliding 17,640 99000 = 835,920

Total # 24,500 73,920 = 633,380

81,840 = 776,240

NOTED SEP 27 1983 A.D.Furia

Client MIT Location Est. No. J.O. No. 14190.02

Subject Interferometric Broad Band Gravitational Antenna Date By A.D. Furia

Checked By

Based on Revised By

Footing in Mine (See Attached Sketch)

*Concrete (Incl. Allow. for Forms & Reinforcing (& 3/8" ø Studs x 4" L)

Tube Size	*Concrete CY/Footing		Unit Price #/CY	Total
12" ø	1.364	x	#450	#615.00
24 ø	2.047	x	"	#920.00
36 ø	2.728	x	"	#1,230.00
48 ø	3.411	x	"	#1,535.00

Steel Plate - 2½" Th. 8"W - 68 #/LF

12" ø	8"W x 24"L	= 136 LBS x #1.10/LB	= #150.00
24" ø	8"W x 36"L	= 204 LBS x 1.10/LB	= 220.00
36" ø	8"W x 48"L	= 272 LBS x 1.10/LB	= 300.00
48" ø	8"W x 60"L	= 340 LBS x 1.10/LB	= 370.00

Rock Excavation

12" ø	.415 CY	x	120.00/CY	=	#50.00
24" ø	.622 CY	x	"	=	75.00
36" ø	.854 CY	x	"	=	100.00
48" ø	1.037 CY	x	"	=	125.00

▲ 5010.1D

STONE & WEBSTER ENGINEERING CORPORATION

CALCULATION SHEET

Preliminary

Item

NOTED SEP 27 1983 A.D.Furia

Client MIT Location Est. No. J.O. No. 14190.02

Subject Interferometric Broad Band Gravitational Antenna Date By A.D. Furia

Checked By

Based on Revised By

Recap

Tube Size	Concrete	Steel Plate	Rock Excavation		Total	Use
12" ∅ (24")	$615	150	50	=	$815	$820.
24" ∅ (36")	920	220	75	=	$1,215	$1,220
36" ∅ (48")	1,230	300	100	=	$1,630	$1,630
48" ∅ (60")	1,535	370	125	=	$2,030	$2,030

$/Footing (Mine)

▲ 5010.1D

STONE & WEBSTER ENGINEERING CORPORATION

CALCULATION SHEET

Preliminary

Item

NOTED SEP 27 1983 A.D.Furia

Client MIT Location Est. No. J.O. No.

Subject Date By

Checked By

Based on FOOTING IN MINE Revised By

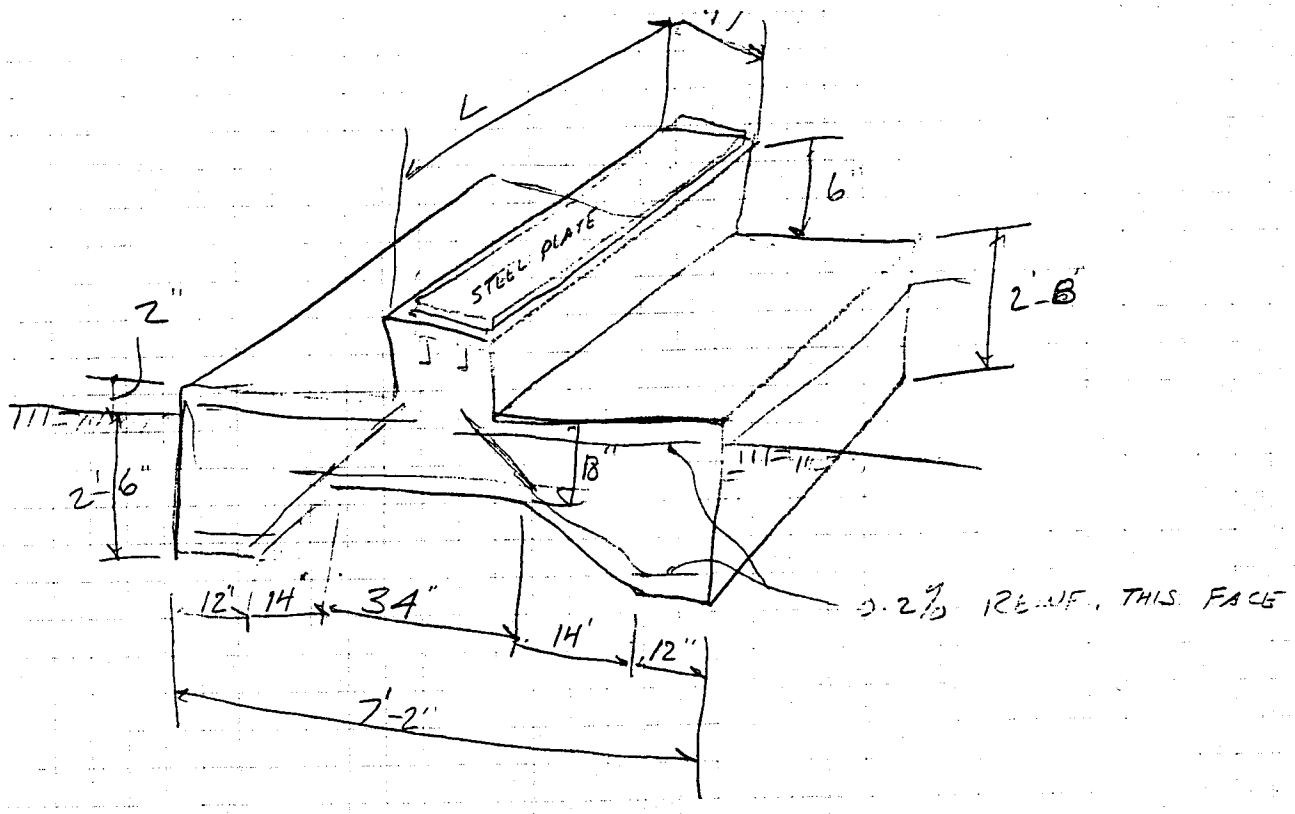

TUBE	L	W
12"	24"	12"
24	36"	12"
36	48"	12"
48	60"	12"

▲ 5010.65

CALCULATION IDENTIFICATION NUMBER				
J.O. OR W.O. NO.	DIVISION & GROUP	CALCULATION NO.	OPTIONAL TASK CODE	PAGE 1/2
14190.02	GEOTECH	G-B-1		

Rock Properties for Antenna Supports in Mine

Max. Down Load = 7000 lb
Max. Lateral load = 5000 lb for 48 in dia pipe. } Ry. R. Deluca 9/19/83

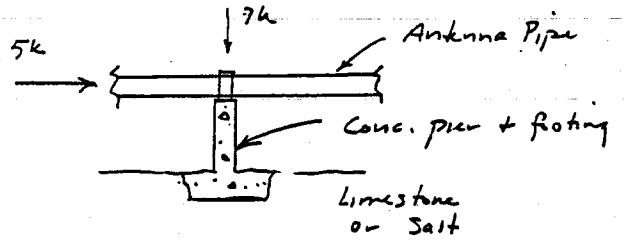

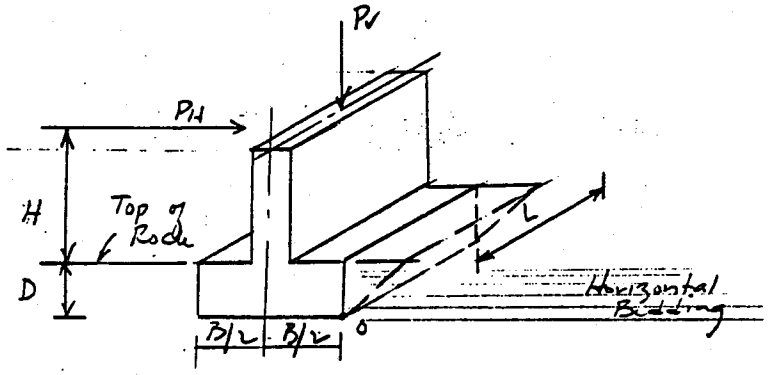

Require F.S. against overturning of 1.5

$$F.S. = \frac{\Sigma^1 \text{ Resisting Moment}}{\Sigma^1 \text{ Driving Moment}} = 1.5$$

Resisting Moment = $(P_V + \text{Wt pier} + \text{Wt Footing})\ B/2$

Driving Moment = $(P_H)(H+D)$

Require F.S. against sliding of 2.0

$$F.S. = \frac{\Sigma^1 \text{ Resisting Forces}}{\Sigma^1 \text{ Driving Forces}} = 2.0$$

Resisting Forces are base friction + passive force of rock wedge

Limestone

Base Friction = $(P_V + \text{Wt Pier} + \text{Wt Footing}) \tan \phi$
$\tan \phi = 0.70$ for concrete on clean sound rock
Ry (NAVFAC DM-7, Table 10-1, 1971)

∴ Base Friction = $0.7\ (P_V + \text{Wt Pier} + \text{Wt. Footing})$

STONE & WEBSTER ENGINEERING CORPORATION

CALCULATION SHEET

▲ 5010.65

CALCULATION IDENTIFICATION NUMBER				
J.O. OR W.O. NO.	DIVISION & GROUP	CALCULATION NO.	OPTIONAL TASK CODE	PAGE 2/2
14190.02				

Limestone

Passive Force = $\frac{1}{2} \gamma D^2 K_p L$

Assume angle of internal friction across bedding = 45°

$K_p = \frac{1+\sin\phi}{1-\sin\phi} = \frac{1.707}{0.293} = 5.83$

$\gamma = 160$ pcf $= 0.160$ kcf for limestone

Passive Force = $(.5)(.160)(D^2)(5.83)L$ kips

$= 4.66 D^2 L$ kips

Salt

Salt doesn't exhibit creep behavior at stress differences below about 1000 psi. Thus, for magnitude of horizontal loads expected, salt will behave as an elastic material.

Assume $\phi = 40°$ across bedding

$\gamma = 130$ lb/cuft $= 0.13$ kcf

Base Friction = 0.7 (Pv + Wt Pier + Wt Footing)

Passive Force = $(0.5)(.130)(D^2)\left(\frac{1+\sin 40°}{1-\sin 40°}\right) L$

$= (0.5)(.130)(D^2)(4.60)(L)$

$= 2.99 D^2 L$

$\sim 3 D^2 L$

INTEROFFICE CORRESPONDENCE

42.

TO: R. Deluca	LOCATION 245/09	SUBJECT / REFERENCE / J.O. NO. 14190.02 GWA tunnel
FROM: L M Tyrala	LOCATION 245/12	

MESSAGE:—

For the GWA subsurface excavations, use the following numbers:

→ 10' x 12' passage (3.0m x 3.7m): $200. to $275./ft ($656. to $902./meter)

20' x 20' passage (6.1m x 6.1m): $300. to $375./ft ($984. to $1,230./meter)

for end station vaults figure = $80,000 - $100,000 each

For the mines under consideration, use the following lump sums:

Randolph Mine: $8,667,000
Cleveland Mine: $7,480,000
Nash Draw Mine: removed from consideration
Jonathan Mine: $10,356,500
Mullins Mine: $10,540,000
Barbarton Mine: $6,325,400

9/22/83 — DATE

L M Tyrala — SIGNATURE

8613 — TELEPHONE

REPLY:

The excavations, noted above, are to extend all mines to two arms with a 5.0 km length of each passage. The costs include drilling, blasting, mucking, and removal and disposal of rock. The passages are unlined, no steel, timber, or shotcrete, but allowed for some rock bolting. The history of these mines (10-35 years) has indicated very good to excellent rock stability. These estimates includes excavation of the two end-station vaults. The attached work sheets give details for each operation.

DATE — SIGNATURE — TELEPHONE

▲ 040.13B

▲5010.65

CALCULATION IDENTIFICATION NUMBER				
J.O. OR W.O. NO. 14190.02-	DIVISION & GROUP	CALCULATION NO.	OPTIONAL TASK CODE	PAGE 1/2

NOTED SEP 22 1983 L.TYRALA

For GWA Tunnel Study

for siting in the Randolph Mine, Kansas City, Missouri (limestone mine)

given : $10.-/ton for limestone
$5.-/CY for shale
one : 1.4 km. passage
1.6 km. passage

need : - two 5.6 km passage plus two end station vaults
- have to excavate 7.0 kms.

equipment : single boom Jay drill jumbo
one 980 loader
one 20T tandem IMCO truck

for GWA tunnel, figure 20'×20' passage opening :
(opening dimensions for mining equipment) 400 sq ft area or 400 CF / lin. foot advance

ls = 160 lbs/CF = 400 CF × 160 lbs/CF ÷ 2000

= 32. tons / LF at $10.-/T

= $320 / LF +15% cont.

= $368./LF or $1207./meter ($1,207,000/km.)

for vaults, figure 91,000 CF × 160 lbs/CF ÷ 2000

= 7280 tons at $10.-/ton = $72,500/vault

plus ramp cut at 135'×20'×20'×.5 × 160 lbs/CF ÷ 2000

= 2,160 ton.

9440 tons rock excavation per vault

at $10./ton = $94,400 +15% = $108,600

say $109,000 / vault

STONE & WEBSTER ENGINEERING CORPORATION

CALCULATION SHEET

▲5010.65

CALCULATION IDENTIFICATION NUMBER				PAGE 2/2
J.O. OR W.O. NO.	DIVISION & GROUP	CALCULATION NO.	OPTIONAL TASK CODE	

20. GWA tunnel needs 7.0 km of passage at $1,207,000/km

= $8,449,000

plus two vaults at $109,000/vault

total cost for passage extension plus two vaults

$ 8,667,000 — excavation only

NOTES OF TELEPHONE CONVERSATION

J.O.No. FP 1499.01

Call Date 9/21/83 3:35 Incoming ____ Outgoing ✓

Between D. Hudson Midwest of Mining Corp

Kansas City of Randolph Mine (limestone)

and J. Tysdale of Stone & Webster.

SUBJECT GWA Tunnel

SUMMARY

For mucking of shale floor figure $5.-/c.y.

For mine development work, figure $5.-/ton

in area of full face advance. - 25' high x 40' wide

Drilling with single boom jbj w/ hydraulics,

980 loaders into 20T tandem dump trucks

to 6" crusher at entrance. For less than

full face advance, i.e., single passage

extended development, figure ~$10.-/ton

for limestone removal.

▲5010.65

CALCULATION IDENTIFICATION NUMBER				
J.O. OR W.O. NO. 19190.02	DIVISION & GROUP Geotech 5000	CALCULATION NO.	OPTIONAL TASK CODE	PAGE 1/2

Cleveland Mine Underground Costs
International Salt Co., Cleveland, Ohio (Salt mine)

NOTED SEP 22 1983 L.TYRALA

given by Int. Salt: 135 lbs/CF for wgt conversion
$12.-/T for development mining cost
vertical access

Equipment: ~~Jeep~~ • twin boom Fletcher drill jumbo w/2¼" augers
• 2 - 1¾ CY LHD's

Advancement of development face ~10'/day (one shift)

standard passage size for mining operation:

20' × 40' × 1' = 800 CF × 135 ~~CF~~ lbs/CF ÷ 2000#/T

= 54 T/lin ft advance at 12.-/LF

= $ 648./LF + 15% cont = $745.-/LF

passage opening for GWA study:

18' × 20' × 1' (opening size for mining equipment) = 360 CF × 135 lbs/CF ÷ 2000 lbs/T

= 24.3 T/LF at $12.-/T

= 291.60/LF + 15% cont =

= $335.-/LF =

= $1099.-/~~LF~~ lin meter say $1,100/~~LF~~ L meter

= $1,100,000/kilometer of passage

Vault opening per GWA

35' high × 40' wide × 65' long = 91,000 CF × 135 lbs/CF ÷ 2000 lbs/T

= 6,142 T ~~at 12/T~~ per vault

plus ramp cut 15% grade =

= 135' × 20' × 20' × .5 × 135 lbs/CF ÷ 2000

= 1,522 T

= 7,964 T at $12./T

= $95,568/vault + 15% cont = $100,000/vault

STONE & WEBSTER ENGINEERING CORPORATION

CALCULATION SHEET

▲ 5010.65

CALCULATION IDENTIFICATION NUMBER				
J.O. OR W.O. NO.	DIVISION & GROUP	CALCULATION NO.	OPTIONAL TASK CODE	PAGE 2/2
14190-02				

GWA tunnel needs two 5.0 km passages. Cleveland mine has two 1.7 km passage. Need to excavate an additional 6.6 km

so, 6.6 km × $1,100,000 / km = $7,260,000

plus two vaults at $110,000 / vault = $220,000

Total cost is $ 7,260,000
220,000
$ 7,480,000 —— for excavation only.

NOTES OF TELEPHONE CONVERSATION

J.O.No. 14190.02

Call Date 9/21/83 11:10 Incoming ____ Outgoing ✓

Between Lou Bush of Cleveland Mine (Salt)

Cleveland Ohio of 216/651-7200

and L. Tyrala of Stone & Webster.

SUBJECT GWA tunnel

SUMMARY

Use $12.-/ston for passage development cost (they take the salt.). They would make a passage 20'×40' at a rate of 10'/day. Equipment is a twin boom Fletcher w/2¼" augers, blasting w/ ~~ammonium~~ ammonium nitrate and caps, and haulage with LHD's. Figure salt at 135 lbs/CF. All miners drill & blast with Joy 6" undercutter. Shaft size can accomodate 9'6"×9'0"×30' and <10,000 ~~lbs~~ lbs, but can add counterweights (at a surcharge) to carry extra weight. Passage can probably be extended to the east at going salt value rate.

9/23/83

AM - Mr. Bush felt that, based upon their experience, if the use of diesel equipment was minimal, the single passage with brattice and ventilation flex tubing. If the end-station are only occupied intermittently, a vertical escape route ~~would~~ or parallel passage wouldn't be required.

PM - It is possible that Ohio would receive a parallel passage to be driven.

STONE & WEBSTER ENGINEERING CORPORATION

CALCULATION SHEET

▲ 5010.65

CALCULATION IDENTIFICATION NUMBER				
J.O. OR W.O. NO. 14190.02	DIVISION & GROUP	CALCULATION NO.	OPTIONAL TASK CODE	PAGE ____

Jonathan Mine (limestone) Zanesville, Ohio
horizontal access

NOTED SEP 22 1983 LTYRALA

for 20'×20' passage:

400 CF of rock per foot of advance. Limestone at 160 lbs/CF

= (400 CF)(160 lbs/CF)/ 2000 lbs/ton

= 32 tons/ft at $10.-/ton for mine development cost

= $320.-/ft +15% cont.

= $368.-/ft or $1,207.-/meter ($1,207,000/km.)

for vaults (35'×40'×65') figure 9,440 tons of rock per vault excavation at $10.-/ton +15% cont
= $109,000/vault

so. figure excavation of additional 8.4 kms for both passages

$1,207,000/km × 8.4 km = $10,138,800

plus two vaults $109,000/vault × 2 = $218,000

~~total cost~~ total cost $10,356,800

STONE & WEBSTER ENGINEERING CORPORATION

CALCULATION SHEET

▲ 5010.65

CALCULATION IDENTIFICATION NUMBER				
J.O. OR W.O. NO. 14190-02	DIVISION & GROUP	CALCULATION NO.	OPTIONAL TASK CODE	PAGE ____

NOTED SEP 22 1983 L.TYRALA

Mullins Mine (limestone)
Mt. Vernon, Kentucky

horizontal access

for 20' x 20' passage:

$368.-/ft or $1,207.-/meter ($1,207,000/km)

(see Jonathan calcs)

for vaults: $109,000/vault

so, figure excavation of additional 8.8 km for both passages

8.8 km x $1,207,000 = $ 10,622,000

plus two vaults

2 x $109,000 $ 218,000

Total $ 10,840,000

▲5010.65

CALCULATION IDENTIFICATION NUMBER				
J.O. OR W.O. NO. 14190.02	DIVISION & GROUP	CALCULATION NO.	OPTIONAL TASK CODE	PAGE ____

Barberton Mine

NOTED SEP 22 1983 LTYRALA

Akron, Ohio vertical access

10' × 12' opening : estimated cost of $210.-/ft or $689/meter ($689,000/km)

vaults : ~~Total of~~ $200,000 (est)/vault

so, 8.6 km of additional passage at $689,000/km

= $5,925,400

plus two vaults at $200,000/vault

$400,000

Total $6,325,400

NOTED SEP 27 1983 A.D.Furia

Client MIT Location Est. No. J.O. No. 14190.02

Subject Interferometric Broad Band Gravitational Antenna Date By A.V. Furia

Checked By

Based on Revised By

Ventilation - Mine

Ductwork - Flexible, Vinyl Coated Spring Steel

18" ∅ --- $12.00/LF x 32,790 = $393,480

Fans - Surface-Reversible -- 60,000

Fans - Booster-Mine -- 120,000

Heating Coils - Electric & Controls -- 80,000

653,480

AFI 66,520

Total - Ventilation - Mine $720,000

▲ 5010.1D STONE & WEBSTER ENGINEERING CORPORATION Preliminary

CALCULATION SHEET NOTED SEP 27 1983 Item A.D.Furia

SECTION 9

Client MIT Location Est. No. J.O. No. 4190.02

Subject Interferometric Broad Band Gravitational Antenna Date By A.D. Furia

Checked By

Based on Fixed Costs Revised By

SCHEME NO. 1, 2 & 3

(Above Ground - W & W/O Windwall)

Support Facility Trailers & Potable Water Storage	---	# 112,100
End Station Buildings 3 @ # 269,000	---	807,000
Electrical - Sub Station, Switchgear, Power Distribution @ 13.8 KV. Tie To Unit Substation & Switchgear	---	1,831,500
Cable Run To End Stations	---	250,000
Transmission Line 115 KV (8 Miles)	---	680,000
Tie To Exist. 115 KV T/L	---	950,000
		3,711,500
Cooling System	---	250,000
Total Fixed Costs - Schemes 1-3	#	4,880,600

SCHEME NO. 4
(Mine)

Support Facility Trailers & Potable Water Storage (Above Ground)	---	# 112,100
End Station Vaults - Foundations, Cranes, etc. excl. Excavating Vault 3 @ # 408,800	---	1,226,400
Excavating Vaults (3)	---	330,000

Client MIT | Location | Est. No. | J.O. No. 14190.02

Subject Interferometric Broad Band Gravitational Antenna | Date | By A.D. Furia

Based on Fixed Costs | Checked | By | Revised | By

SCHEME NO. 4 (Cont.)
(Mine)

Electrical - Substation, Switchgear, Power Distribution @ 13.8 KV Tie To Unit Substation & Switchgear ---	1,831,500		
Transmission Line 115 KV (8 Miles) ---	680,000		
Cable Run To End Stations --	220,000		
Tie To Exist. 115 KV T/L --	950,000		
Tie From Surface To Antenna Array in Mine ---	650,000	4,331,500	
Cooling System ---		350,000	
Ventilation (End Stations)		260,000	
Total Fixed Costs - Scheme 4			$ 6610,000

NOTED SEP 27 1983 A.D.Furia

Client MIT Location Est. No. J.O. No. 4190.02

Subject Interferometric Broad Band Gravitational Antenna Date By A.D. Furia

Checked By

Based on Revised By

C. Computer & Control Trailer

20'x 8' = $6,500

(Incl. A/C, Lighting & Outlets)

V. & E. Office Trailers (2)

32'x 8' = $9,300 x 2 = $18,600

(Incl. A/C, Lighting & Outlets)
(Desks, Chairs, Reference Table & Filing Cabinets)

F. Recreation & Cafeteria

10'x 36' = $14,500

(Incl. Electric Range - 6 Burner w/Oven, Range Hood, Refrigerator/Freezer (18 CF), Hot Water Heater (30 Gal. Capacity) Electric, Stainless Steel Sink, Serving Cabinets, Chairs, Sofa & Dining Tables.)

G. & H. Living Quarters Trailers (2)

4-Man Sleeper, 10'x20'
$7,500 x 2 = $15,000

(Incl. Air-conditioner (12,000 BTU, Heat & Cool)

4 - Single Beds
4 - Metal Lockers
4 - Chairs, Folding Steel

$54,600

K. Potable Water Storage Tank, 3,000 Gal. Capacity (Insulated) (Skid Mounted) = 7,500

(Incl. Piping, Fittings & Valves to Tie-in to Trailers.

B. Central Maintenance Facility Building 40'-60'x 20'H = 50,000

$112,100

Client MIT Location Est. No. J.O. No. 14190.02

Subject Interferometric Broad Band Gravitational Antenna (Above Ground Antenna (Scheme 1 & 2) Date By A.V. Furia

Based on Checked By

Revised By

J. End Station Building

Pre-Engineered Steel Building - Insulated Siding
40'-0" x 62'-0" x 34'-0" High

20' x 20' Rolling Steel Door

Building * 2,480 SF x $26.50/SF	=	$ 65,720
Rolling Steel Door - 20' x 20'	=	1,900

* $/SF Incl. Wall & Roof Insulation, Doors & Windows & Allow. for Interior Partitions & Flooring

Foundation for End Building

Building Foundation & Experiment Housing Foundation

Excavation	1,000 CY x	$ 2.50/CY =	$ 2,500
Backfill	150 CY x	1.50/CY =	230

Concrete (Incl. Allow. for Forms & Reinf.

Laser Housing Area	240 CY		
Machine Shop Area	80 CY		
	320 CY x	$ 350/CY =	112,000

Building Services - Mechanical & Electrical

Heating & Ventilating	2,480 SF x	3.50 =	8,680
Plumbing		x 3.00 =	7,440
Fire Protection		x 1.20 =	2,980
Electrical - Lighting & Power		x 5.00 =	12,400

Crane - 12 Ton Capacity Bridge, Crane - Pendant Operated	= 52,000
Holding Tank - Floor Drain Run-Off	= 3,500
	269,350
Use →	$ 269,000

▲ 5010.1D

STONE & WEBSTER ENGINEERING CORPORATION

Preliminary

CALCULATION SHEET NOTED SEP 27 1983 A.D.Furia

Client MIT Location Est. No. J.O. No. 14190.02

Subject Interferometric Broad Band Gravitational Antenna Date By A.D. Furia

Based on (Above Ground Antenna Checked By

Revised By

Scheme No. 1 & 2

Concrete

Experiment Housing Area

Slab 40′ x 44′ x 2′ = 130.4 CY

Walls 8′ x 40′ x .6667 = 7.9 CY
8′ x 40′ x .6667 = 7.9 CY
8′ x 44′ x .6667 = 8.7 CY
8′ x 44′ x .6667 = 8.7 CY

Experiment Foundation 8′ x 8′ x 5′ = 12.0 CY

Machine Shop Area

Slab 18′ x 40′ x 1′ = 26.7 CY

Walls 18′ x 8′ x 1′ = 5.3 CY
18′ x 8′ x 1′ = 5.3 CY
8′ x 40′ x 1′ = 11.8 CY

Floor Slab

Machine Shop Area
18′ x 40′ x 1′ = 26.7 CY

Experiment Housing Area
40′ x 44′ x 1′ = 65.2 CY

316.6 CY

Excavation

42′ x 64′ x 10′ = 996 CY Say 1,000 CY

Backfill

150 CY

Client MIT | Location | Est. No. | J.O. No. 14190.02

Subject Interferometric Broad Band Gravitational Antenna (Below Ground Antenna) | Date | By A.D. Furia

Checked | By

Based on | Revised | By

(Scheme 3)

J.

End Station Building

Pre-Engineered Steel Building - Insulated Siding
40'-0" x 62'-0" x 24'-0" High

20'-0" x 20'-0" Rolling Steel Door

Building *	2,480 SF	x $21.50/SF =	$ 53,320
Rolling Steel Door ~ 20'x20'		=	1,900

* $/SF Incl. Wall & Roof Insulation, Doors & Windows & Allow. for Interior Partitions & Flooring.

Foundation for End Building

Building Foundation & Experiment Housing Foundation

Excavation	2,400 CY	x $2.50/CY =	$ 6,000
Backfill	300 CY	x 1.50/CY =	450

Concrete (Incl. Allow. for Forms & Reinf.)

Experiment Housing Area 295 CY
Machine Shop Area 115 CY

410 CY x $350/CY = 143,500

Building Services - Mechanical & Electrical

Heating & Ventilating	2,480 SF	x 3.00	=	$ 7,440
Plumbing		x 2.50	=	6,200
Fire Protection		x 1.20	=	2,980
Electrical - Lighting & Power		x 4.50	=	11,160

Crane ~ 12 Ton Capacity Bridge Crane - Pendant Operated 52,000

Holding Tank - Floor Drain Run-Off 3,200

288,150

(Use Scheme 2 Figures) Use → $ 288,000

NOTED SEP 27 1983 A.D.Furia

Client MIT Location Est. No. J.O. No. 14190.02

Subject Interferometric Broad Band Gravitational Antenna Date By A.D. Furia

Checked By

Based on End Station Building Revised By

Scheme No. 3

Concrete

Experiment Housing Area

Slab 40′ x 44′ x 2′ = 130.4 CY

Walls
21′ x 40′ x .6667 = 20.7 CY
21′ x 40′ x .6667 = 20.7 CY
21′ x 44′ x .6667 = 22.8 CY
21′ x 44′ x .6667 = 22.8 CY

Machine Shop Area

Slab 18′ x 40′ x 1′ = 26.7 CY

Walls
18′ x 21′ x 1′ = 14.0 CY
18′ x 21′ x 1′ = 14.0 CY
21′ x 40′ x 1′ = 31.1 CY

Experiment Foundation 8′x8′x5′ = 12.0 CY

Floor Slab

Machine Shop Area
18′ x 40 x 1′ = 26.7 CY

Experiment Housing Area
40′x44′x1′ = 65.2 CY

395.1 CY

Excavation

42′ x 64′ x 24′ = 2,390 CY Say 2,400 CY

Backfill 300 CY

STONE & WEBSTER ENGINEERING CORPORATION

CALCULATION SHEET

NOTED SEP 27 1983 A.D.Furia

Client MIT | Location | Est. No. | J.O. No. 14190,02

Subject Interferometric Broad Band Gravitational Antenna | Date | By A.D.Furia

~~Based on~~ Trailer Area – Transmission Line & Tie | Checked | By | Revised | By

Sub Station at Site - - - -		$226,000
Outdoor 13.8 KV Switchgear - -		314,700
Outdoor Unit Substation - - -		152,300
Power Distribution - - -		1,096,200
13.8 KV Tie To Unit Substation & Switchgear - - -		12,300
Pads for Transf. & Swgr. - Substation - - -		30,000
		$1,831,500
Transmission Line 115 KV ($85,000/Mile) X 8 Miles	=	680,000
Tie To Exist. 115 KV T/L	=	950,000
	$	3,461,500 ✓
Electrical Work (8 Miles) - Antenna Area ($156,100/Mile)		1,248,800
	$	4,710,300

▲ 5010.1D

STONE & WEBSTER ENGINEERING CORPORATION

CALCULATION SHEET

Preliminary

Item

NOTED SEP 27 1983 A.D.Furia

Client MIT Location Est. No. J.O. No. 4190.02

Subject Interferometric Broad Band Gravitational Antenna Date By A.D. FURIA

Checked By

Based on Revised By

Stockade Type Wood Fence (Wind Barrier)

Creosoted Boards (8 Lbs./CF) (2"x 6" Board)

8' High

Material --	$ 29.00
Labor --	7.00
Total	$ 36.00/LF

$ 72.00/LF x 32 808 = $ 2,362,205

x 2 = $ 72.00/LF

Cooling System

3" - Sch. 40 Carbon Steel Pipe (Buried - 3' Cover) - Wrapped & Coated Supply & Return	13,150 LF x $ 15.00/LF = $ 197,250
1½" Insulation on Above Ground Piping	400 LF x $ 12.00/LF = 4,800
1 - Chiller 350,000 BTU Capacity (30 Tons)	= 15,000
1 - Circ. Water Pump 15 HP, 100 GPM	= 3,500
	$ 220,550
Housing - Cooling System	6,500
	$ 227,050
AFI	22,950
	$ 250,000

TABLE 9.10 - FIXED COST INDEPENDENT OF LENGTH (10^3 #)

Scheme No.	Support Buildings #	End Stations #	Cooling System #	Ventilation #	Transmission Line ~8 Miles & Line To Tunnel #	Power Distrib. #	Line Tie-In #	Wiring To Vaults #	Total Fixed Cost #
1.	112	807	250	—	680	1,831	950	250	4,880 ✓
2.	112	807	250	—	680	1,831	950	250	4,880
3.	112	864	250	—	680	1,831	950	250	4,937
								Use 2 →	4,940 ✓
4.	112	1,560	350	260	1,330	1,831	950	220	6,613
								Use 2 →	6,610 ✓

▲ 5010.1D

STONE & WEBSTER ENGINEERING CORPORATION

CALCULATION SHEET

Page No. _____
Preliminary _____
Item _____

NOTED OCT 3 1983 A.D.Furia

Client MIT | Location | Est. No. | J.O. No. 14190.02

Subject Interferometric Broad Band Gravitational Antenna | Date | By A.D. Furia

Based on TABLE 8.11 | Checked | By | Revised | By

TABLE 9.11 - COSTS DEPENDENT ON LENGTH ($/Km)

Scheme No. & Tube Size		Clearing & Grading #	Trenching, Bedding & Backfill #	Tunneling 10'x12' #	Ventil. Tunnel #	Supports #	Insulation Tube. (Based on 6") #	Housing #	Beam Electrical #	Total Per Km $
1	12"	10	—	—	—	122	111	—	100	= 343
	24"	100	—	—	—	104	198	—	100	= 412
	36"	100	—	—	—	156	334	—	100	= 600
	48"	10	—	—	—	259	485	—	100	= 854
2	12"	14	—	—	—	76	—	689	151	= 1,030
	24"	14	—	—	—	78	—	689	151	= 1,032
	36"	14	—	—	—	56	—	689	151	= 1,010
	48"	14	—	—	—	66	—	689	151	= 1,020
3	12"	28	249	—	—	76	—	689	—	= 1,142
	24"	28	249	—	—	78	—	689	—	= 1,144
	36"	28	249	—	—	56	—	689	—	= 1,122
	48"	28	249	—	—	66	—	689	—	= 1,132
4 (Mine)	12"	—	—	656	46	74	—	—	88	= 864
	24"	—	—	656	46	84	—	—	88	= 874
	36"	—	—	656	46	63	—	—	88	= 853
	48"	—	—	656	46	78	—	—	88	= 868
	12"	—	—	902	46	74	—	—	88	= 1,110
	24"	—	—	902	46	84	—	—	88	= 1,120
	36"	—	—	902	46	63	—	—	88	= 1,099
	48"	—	—	902	46	78	—	—	88	= 1,114

STONE & WEBSTER ENGINEERING CORPORATION

Preliminary

CALCULATION SHEET

Item

NOTED OCT 3 1983 A.D.Furia

Client MIT | Location | Est. No. | J.O. No. 14190.02

Subject Interferometric Broad Band Gravitational Antenna | Date | By A.T. Furia

Based on TABLE 8.12 | Revised | By

( ) = Range Low High

TOTAL COSTS
ARM LENGTH ~ 5 Km

Scheme No.	Tube Size	Fixed #	Total Variable Costs K#	Total M#
1	12"	4,880	3,430	8.3
	24"	4,880	4,120	9.0
	36"	4,880	6,000	10.9
	48"	4,880	8,540	13.4
2	12"	4,880	10,300	15.2
	24"	4,880	10,320	15.2
	36"	4,880	10,100	15.0
	48"	4,880	10,200	15.1
3	12"	4,940	11,420	16.4
	24"	4,940	11,440	16.4
	36"	4,940	11,220	16.2
	48"	4,940	11,320	16.3
4 (Mine)	12"	6,610	(6,912 8,880)	(13.5 15.5)
	24"	6,610	(6,992 8,960)	(13.6 15.6)
	36"	6,610	(6,824 8,792)	(13.4 15.4)
	48"	6,610	(6,944 8,912)	(13.6 15.5)
	12"	6,610	(8,640 11,100)	(15.2 17.7)
	24"	6,610	(8,740 11,200)	(15.3 17.8)
	36"	6,610	(8,530 10,990)	(15.1 17.6)
	48"	6,610	(8,680 11,140)	(15.3 17.7)

8 Km of Tunneling

10 Km of Tunneling

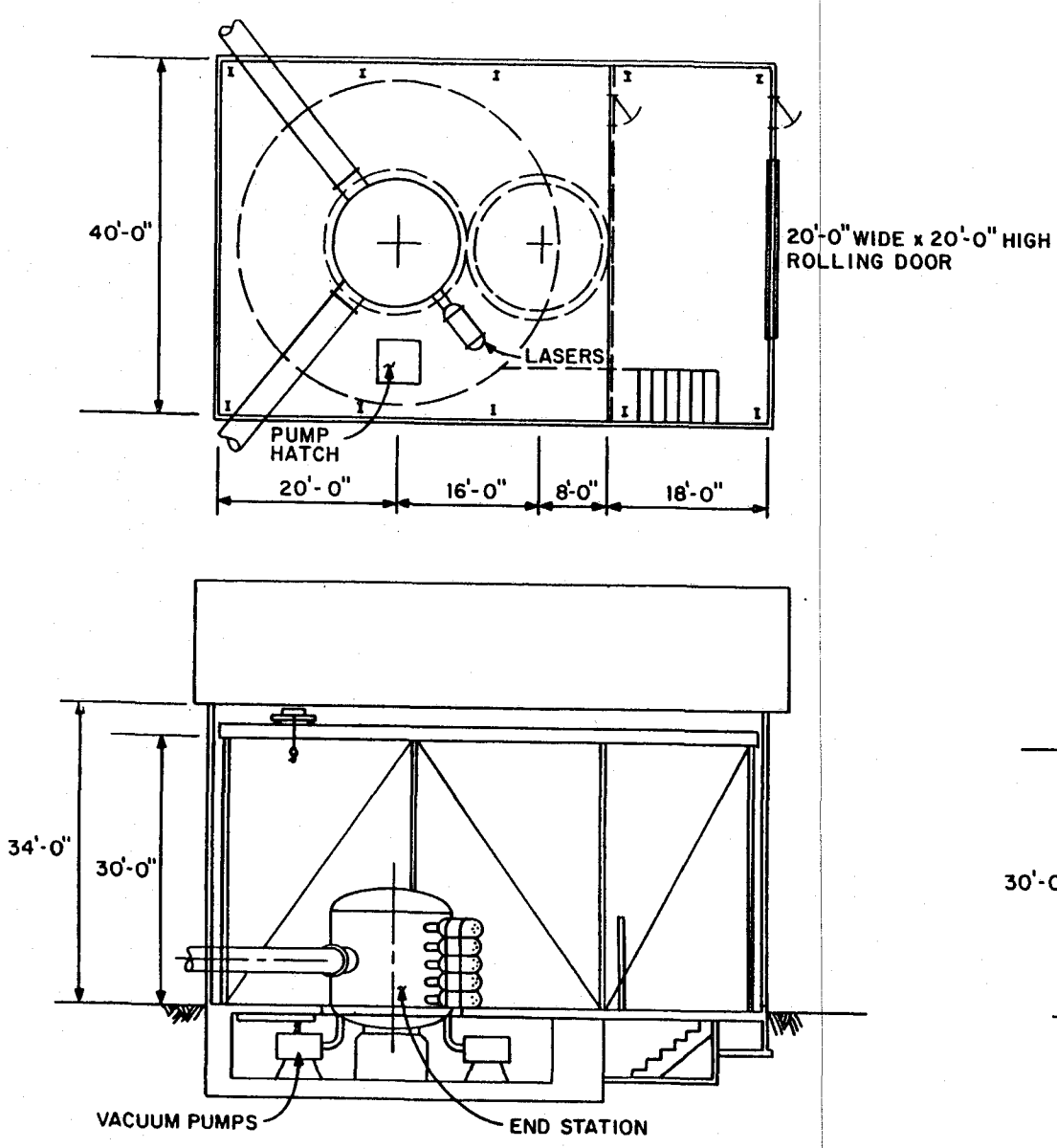

FIGURE 6.201
END STATION BUILDING FOR
SCHEMES 1 & 2

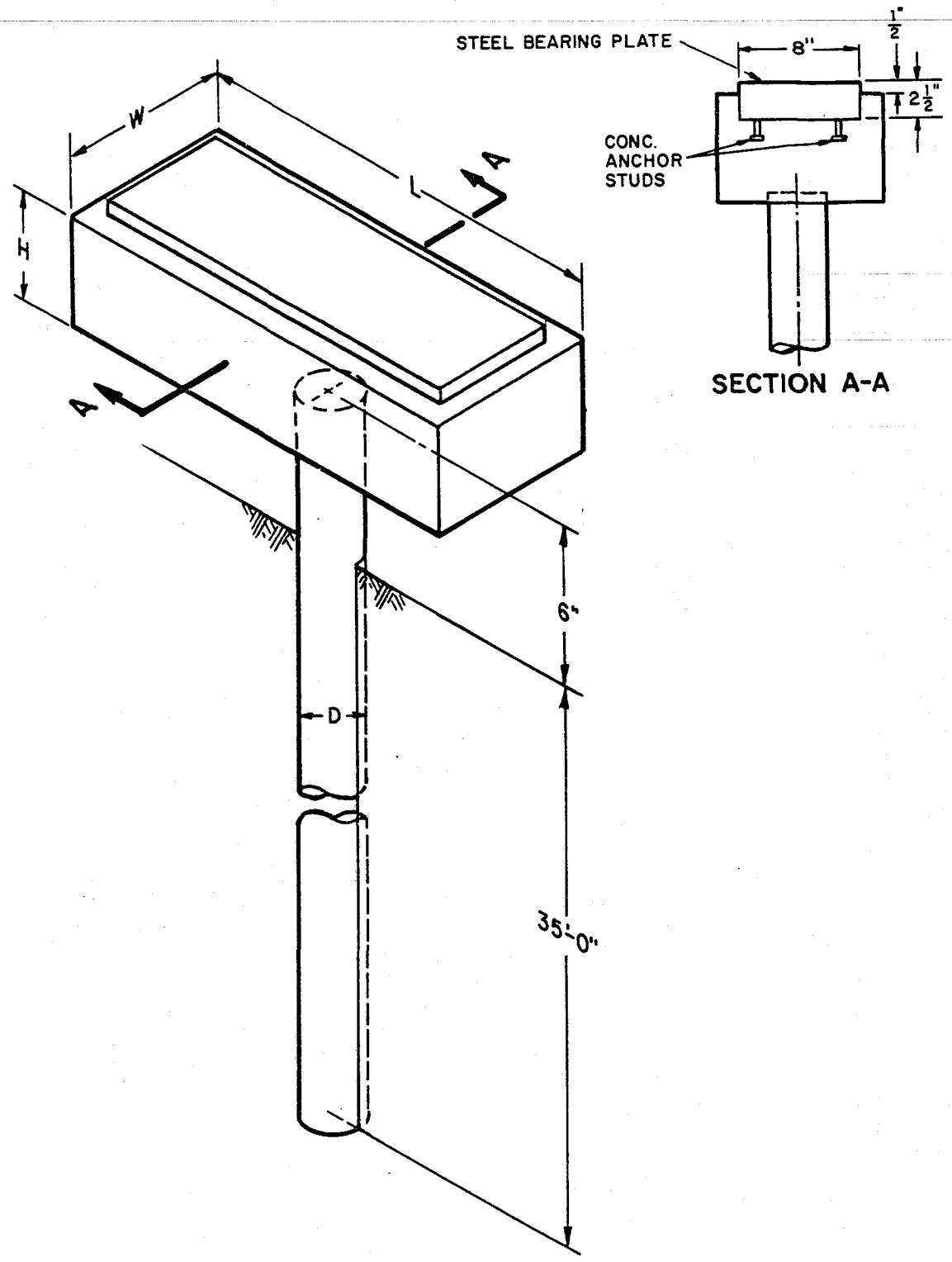

FIGURE 6.203
TYPICAL REINFORCED CONCRETE PILE
& CAP FOR FIXED & SLIDING SUPPORT

The design study which is described in this volume has had two major aspects: consideration of the physical nature of the performance limits of a large gravitational wave antenna system, and the conceptual engineering design of a complete system which could attain a high sensitivity for a reasonable cost. The scientific issues, such as sensitivity and the antenna noise sources, have been discussed in the sections I through V and in the appendices of the report written by MIT in consultation with the CalTech group. The conceptual design of the high capital cost parts of the system (which involve for the most part only well-known technology) is described in the sections written by the industrial consultants (section VI on the vacuum system by Arthur D. Little, Inc., and Sections VII and VIII on the siting and installation by Stone and Webster Engineering Co.).

In this final section of the report we describe the estimated total cost of a gravitational wave antenna system. At a minimum, such a system includes two large antennas, since detection of burst events or stochastic backgrounds is impossible with only one antenna. Preferably these two antennas should be separated by distances of continental scale. Thus, to arrive at a total system cost we must multiply the cost of a single antenna by a factor nearly equal to two. (The factor would be exactly two if there were no ways to share costs between the two installations.)

For discussion purposes, the system costs can be divided into capital costs and operating costs. Operating costs include the salaries of the scientific and technical staff,

in addition to maintenance costs and the costs of consumables such as power and water. Capital costs consist of the costs of the vacuum system and the installation, detailed in the sections written by the industrial consultants, and also the costs of the scientific apparatus, estimated below. The funding schedule for the project can be derived by spreading the capital costs over the construction period, then adding the appropriate operating cost for each year of construction, instrument start-up, or scientific operation.

Throughout the work of the industrial consultants, the arm length of the interferometer was left unspecified within the range of 1 to 10 km, and the vacuum tube diameter was allowed to be anywhere from 12 to 48 inches. To arrive at a final estimated cost for the system, we are required to specify these dimensions of the apparatus. In making this decision, there is no unarguably right answer, although there are some wrong ones. The main reasons for this are the trade-offs that must be made between performance, risks and cost.

Three principles have guided our choices.

1) The antenna should not be so small that the fundamental limits of performance can not be attained with realistic estimates of technical capability. The question of system noise as a function of antenna length was addressed in detail in the discussion of the noise budget, section V. There it is shown that in order to reach a regime where the system performance is independent of arm length (the shot-noise limit), the length must be greater than some minimum, which is itself a function of frequency, circulating light power and the

assumption made regarding the suppression of the effect of stochastic forces. If performance at 1 kHz is the issue, noise within a factor of three of the shot noise limit of present laser intensities could be attained, in principle, with arms 500 meters long. However, the advent of increased circulating light powers would not improve the antenna sensitivity at 1 kHz in a 500 meter system, since the stochastic forces would dominate the noise budget with the present assumptions concerning our ability to reduce their effects. Reduction in risk and planning for the future argues for longer antenna length even at 1 kHz. At 100 Hz or below, where the electromagnetically coupled antenna is most promising, the noise is still decreasing nearly as the inverse first power of the length even at a length of 5 km.

2) The scale of the system should be large enough so that further improvement of the performance by a significant factor requires cost increments by a substantial factor. This means simply that it is unwise to build a system so small that the total cost is dominated by the fixed costs instead of by the variable (length-dependent) costs. As the discussion of the installation and vacuum system, sections VI and VIII, show, antenna lengths of several kilometers satisfy this condition.

3) Within reason no choice in external parameters of the present antenna design should preclude future internal design changes which, with advances in technology, will substantially improve performance. Examples of such planning are the following. The vacuum system is designed for operation at

10^{-6} mmHg but no elements in it preclude operation at 10^{-8} mmHg. The diameter of the vacuum tube should be large enough to allow future operation of multiple interferometers within the same tube or the implementation of the scheme to interchange beams in a search for preiodic sources as proposed by Drever. In the long run a generous decision on the tube diameter will certainly pay off.

With these guiding principles in mind, we have chosen to propose two antennas each with 5Km arms using vacuum tubes of 48 inch diameter. The proposed construction technique is to bury the pipes below ground surrounded by a cover, option 3 of the Stone and Webster Engineering Study.

The decision to choose 48" diameter tubes is not mandated by the needs of a first generation design but follows guiding principle number three and furthermore appears prudent in considering the costs. In a 5 Km antenna the difference in overall costs in going from the minimum usable diameter of 24" to 48" is a 15% increment in capital costs of the system giving a factor of 4 increase in beam area and considerably more safety in alignment sensitivity and the effects of light scattering.

The most controversial decision is to use a cover. Several arguments are involved in this decision. First, the study of mine sites, which would not need a cover, is not at present sufficiently definitive in costing and in determining mine site availability and tunneling accesibility to be a strong candidate for a realistic proposal. This will be studied

further, but present best estimates indicate no large savings will result by operating in a mine. Second, although about $14M is tied up in the cover, it is the price paid to respond in a responsible manner to a set of eventualities that must be considered. Once having made the decision to bury the pipe which is driven by considerations of thermal stability, wind induced noise, apparatus safety and environmental impact; the cover may appear unnecessary. The utility companies regularly bury gas pipes in shallow trenches backfilled with soil, however they do not have to worry about small leaks, the possible need to thermally outgas or to maintain tube alignment nor do they require as closely spaced pumping stations as are needed in the antenna. All these factors argue for a cover.

COST ESTIMATES FOR THE PROJECT

CAPITAL COSTS

Costs Independent of Antenna Length/Antenna

Vacuum System

3 end stations and pumps	870K
Isolation valves	280K

Construction

Support buildings	112K
End station buildings	864K
Cooling system	250K
Transmission line to site	680K
Power sub station on site	1831K
Power line tie in	950K
Wiring to antenna	250K

Instrumentation

Lasers	300K
Optical components	500K
Vibration isolation system	400K
Machining costs	500K
On site control computer and data storage	100K
General laboratory instrumentation	500K
Total length independent costs per antenna	8390K

Capital Costs Linear in Antenna Length

Vacuum System

48" tubing, valves, bellows, alignment jigs, welding, ion pumps, roughing pumps	885/km

Construction

Clearing & grading	28K/km
Trenching, backfill, bedding	249K/km
Supports	66K/km
Housing	689K/km

Construction (continued)	
Electrical wiring	100K/km
Subtotal cost/km	2020K/km
Subtotal cost 2 x 5km	20200 K
Subtotal capital cost/antenna	$28.59M
Subtotal capital cost for 2 antennas Assume 1.9 factor for shared facilities such as cleaning station, alignment jigs, welding equipment etc.	$54.30M
ADDITIONAL COSTS COMMON TO BOTH ANTENNAS	
Data Analysis Center - Central computer, array processor, display equipment, large scale data storage equipment	600K
Engineering - Estimated at 1% of construction costs	~~500K~~ 3-10%
Total additional fixed cost	900K
Total cost two antennas	$55.~~2~~4M
RECURRING COSTS	
Operations Costs at Both Antennas/Year	
Maintenance	80K/yr.
Power	130K/yr.
Travel - 10 persons /100 days/yr. $40/day/person $400 airfare/10 trips/yr. (MISTAKE → ~~400K~~ 40%)	~~85K/yr.~~
Subtotal operations cost/yr.	2~~9~~5K/yr.
Personnel Costs ~~at Both~~ Institutions/Year	
3 faculty/institution	50K/yr.
4 research physicists/institution	120K/yr.
4 graduate students/institution	60K/yr.
2 electronic instrumentation technical support staff/institution	70K/yr.
1 mechanical instrumentation technical support staff/institution	35K/yr.

Personnel Costs (continued)

1 optical instrumentation technical support staff/institution	35K/yr.
1 computer programmer/institution	30K/yr.
1 project manager/administrator/ institution	40K/yr.
Total personnel salaries and wages/inst./yr.	440K
Employee benefits and overhead S & W x 1.25/institution/yr.	550K
Subtotal cost per institution	990K
Total cost both institutions	$1.98M/yr.
Estimated Costs/Year at Both Institutions For Development Work Toward Antenna Improvements	400K/yr.
Estimated Material and Services Costs	
At both institutions	200K/yr.
Total estimated recurring costs/year	$2.9M/yr.

APPENDIX A

ACOUSTIC AND ELECTROMAGNETICALLY COUPLED ANTENNAE IN THE NAIVE QUANTUM LIMIT

Acoustic antennae are now operating at noise levels two orders of magnitude in amplitude and correspondingly four orders of magnitude in power above the naive quantum limit. The limit is set by a straightforward application of quantum mechanics to the interaction of the transducer and associated amplifier with the acoustic resonator. The opinion held by some working in the quantum theory of measurement is that in principle the naive quantum limit need not impose a firm limit to the detection of gravitational radiation by acoustic resonators (or electromagnetically coupled antennae). Transducer schemes have been proposed which could circumvent the naive quantum limit (quantum nondemolition systems), however they appear difficult to implement and the gain in sensitivity over the naive quantum limit is unfortunately a strong inverse function of the power losses in these schemes. It is in our opinion a fair assumption that even if the naive quantum limit is not a limit it will be difficult to make much progress to get below it. For the sake of the ensuing calculations, we assume that the naive quantum limit is a real limit.

Present day prototype interferometric antennae have not yet approached the present performance of acoustic antennae. Therefore it may seem silly at this stage to contemplate their quantum limited performance. However, in discussing the ultimate idealized performance of either system, the quantum limit is a hard boundary, and in principle

getting to it is a matter of technical improvement.

The result of this section is that the ratio of the quantum noise limited strain sensitivity of an idealized electromagnetically coupled antenna to that of an idealized acoustically coupled antenna of the same mass is close to the ratio of the velocity of sound in the acoustic antenna to the velocity of light, a factor of the order of 10^5. The quantum limit of a 1 ton acoustic antenna is of the order of a few times 10^{-23} strain/$Hz^{\frac{1}{2}}$, while the quantum limit of an interferometric antenna with 1 ton end masses and of optimal length is a few times 10^{-28} strain/$Hz^{\frac{1}{2}}$. A perusal of the section of this report on the noise sources in the electromagnetic antenna indicates that attaining such a sensitivity would pose a formidable technic challenge . At 1 KHz,but not at lower frequencies,the light power required is beyo reason. However, it is worth noting that a long baseline electromagnetically coupled antenna using present day engineering practice will perform close to an order of ma nitude better in amplitude sensitivity than the quantum limited acoustic antenna and furthermore there is about a factor 10^4 margin before one hits the fundamental limi

Naive Quantum Limit of an Idealized Acoustic Antenna

The treatment follows the presentation given by Weiss in Sources of Gravitational Radiation , L. Smarr, Editor, Cambridge Univ. Press, 1979. The gravitational wave tidal force density acting on the acoustic antenna of mass m and length ℓ is given by

$$F_g^2(f) = \left(\frac{m\ell\omega^2 h(f)}{2}\right)^2 \qquad (1)$$

where h(f) is the gravitational wave strain amplitude density and ω the frequency. The motion transducer attached to the acoustic antenna is described by the matrix

$$\begin{pmatrix} F \\ \phi \end{pmatrix} = \begin{pmatrix} Z_{11} & Z_{12} \\ Z_{21} & Z_{22} \end{pmatrix} \begin{pmatrix} u \\ I \end{pmatrix} \qquad |Z_{12}| = |Z_{21}| \quad \text{reciprocity} \qquad (2)$$

where F is the force exerted by the transducer on the antenna, u the velocity of the antenna motions at the transducer, I the current running through and ϕ the voltage across the transducer.

A useful quantity defining the transducer is the ratio of the electromagnetic energy stored in the transducer to the mechanical energy stored in the acoustic resonator. This is given by

$$\beta = \frac{|Z_{21}|^2}{|Z_{22}|} \, m\omega \qquad (3)$$

Another useful quantity is the position sensitivity of the transducer

$$\alpha = |Z_{21}|\omega \quad \text{volts/cm} \qquad (4)$$

The noise in the amplifier that follows the transducer is characterized by a series voltage noise generator $e_n^2(f)$, and a shunt current noise generator, $i_n^2(f)$. When the transducer is matched to the amplifier, the noise power from these two noise generators become equal.

Z_{22}, the transducer electrical impedence, should be $e_n(f)/i_n(f)$. Under these circumstances the noise in the amplifier, if it is quantum limited, (limited by spontaneous emission at the input,) is given by

$$e_n(f)i_n(f) = \frac{\hbar\omega}{\ell n 2} \tag{5}$$

The amplifier noise sets the displacement noise density to

$$x^2(f) = \frac{2|Z_{22}|e_n(f)i_n(f)}{\alpha^2} \quad \frac{2\hbar}{m\beta\ell n 2\omega^2} \tag{6}$$

and the shunt current noise generator drives the acoustic resonator through the transducer with a back reaction force density given by

$$F_{br}^2(f) = \frac{\beta\hbar\omega^2 m}{\ell n 2} \tag{7}$$

The gravitational strain sensitivity limit is derived from the condition that the gravitational tidal force density should have a larger effect than the stochastic force densities and the displacement noise density

$$F_{grav}^2(f) \geq F_{br}^2(f) + \frac{\hat{x}^2(f)}{|T(\omega)|^2} + F_{th}^2(f) \tag{8}$$

where $|T(\omega)|$ is the magnitude of the acoustic resonator displacement to force transfer function given by

$$|T(\omega)|^2 = \frac{1}{m^2[(\omega^2-\omega_o^2)^2 + \frac{(\omega\omega_o)^2}{Q}]} \tag{9}$$

$F_{th}^2(f)$ is the thermal Nyquist force given by

$$F_{th}^2(f) = \frac{4kTm\omega_o}{Q} \qquad (10)$$

Q is the quality factor of the resonator and ω_o its resonance frequency in the observed mode.

The limiting gravitational strain amplitude densities are for three frequency regimes.

$$h(f) \quad \frac{2}{\ell\omega}\left(\frac{\hbar}{\ell n 2 m}\right)^{\frac{1}{2}} \rightarrow \begin{cases} \left[\beta + \frac{2}{\beta}\left(\frac{\omega_o}{\omega}\right)^4 + \frac{4kT\ell n 2}{h\omega_o Q}\right]^{\frac{1}{2}} & \omega<\omega_o \\ \left[\beta + \frac{2}{\beta Q^2} + \frac{4kT\ell n 2}{h\omega_o Q}\right]^{\frac{1}{2}} & \omega=\omega_o \\ \left[\beta + \frac{2}{\beta} + \frac{4kT\ell n 2}{h\omega_o Q}\right] & \omega>\omega_o \end{cases} \qquad (11)$$

Except for the case directly on resonance, it is best to make the transducer coupling as strong as possible $\beta \sim 1$. The thermal noise term is then negligible. On resonance the best value for β is approximately $\sim 1/Q$ if the thermal noise can be made small enough.

The first factor of Eq. 11 may be reformulated since the length of the resonator and its resonance frequency are related by the sound speed c_s as

$$\ell = \frac{\pi c_s}{\omega} \qquad (12)$$

The quantum limit of the general case, near resonance, is then given as

$$h(f) \geq \frac{2}{\pi c_s} \left(\frac{\hbar}{m\ell n2}\right)^{\frac{1}{2}} \qquad (13)$$

which corresponds to $h(f) \sim 3.8 \times 10^{-23}$ strain/$Hz^{\frac{1}{2}}$ for a $m = 10^6$ grams made of aluminum for which $c_s = 6.4 \times 10^5$ cm/sec. The directly on resonance case, useful for periodic sources with a very well defined frequency, could be better by a factor of $1/\sqrt{Q}$ if the thermal noise could be eliminated by cooling to a temperature $T < \frac{\omega_o}{k} \sim 6 \times 10^{-8}$ °K at 1KHz.

Naive Quantum Limit of an Electromagnetically Coupled Antenna

The reasoning is analogous to the acoustic antenna case. The strain spectral density when limited only by the photon counting statistics is given by

$$h^2(f) = \left(\frac{1}{8\pi c t_{st}}\right)^2 \left(\frac{hc\lambda}{\eta P}\right) \qquad (14)$$

The uncorrelated photon recoil fluctuation force on the masses plays the same role as the back reaction force in the acoustic antenna. The strain spectral density due to this force is

$$h^2(f) = 8\left(\frac{ct_{st}}{\ell^2 m\omega^2}\right)^2 \left(\frac{hP}{\lambda c}\right) \qquad (15)$$

where m is the mass of one antenna mass. The gravitational strain spectral density must be larger than the sum of 14 and 15

$$h_g^2(f) > \left(\frac{1}{8\pi c t_{st}}\right)^2 \left(\frac{hc\lambda}{\eta P}\right) + 8\left(\frac{ct_{st}}{\ell^2 m\omega^2}\right)^2 \left(\frac{hP}{\lambda c}\right) \qquad (16)$$

The minimum occurs when the two terms of Eq. 16 are equal. Setting a condition on the light power, P_{opt}, given by,

$$P_{opt} = \frac{\lambda c m \ell^2 \omega^2}{\sqrt{2}\ 16\pi\eta^{\frac{1}{2}}(ct_{st})^2} \tag{17}$$

For this power the amplitude spectral density is given by

$$h(f) > \frac{1}{\ell\omega}\left(\frac{\hbar}{\sqrt{2}\eta^{\frac{1}{2}}m}\right)^{\frac{1}{2}} \tag{18}$$

If the gravity antenna length is optimized,

$$\ell = \pi c/\omega$$

h(f) becomes

$$h(f) > \frac{1}{\pi c}\left(\frac{\hbar}{2\eta^{\frac{1}{2}}m}\right)^{\frac{1}{2}} \tag{19}$$

The parameters for an antenna optimized at 1KHz are not realistic. The optimum antenna would have a length of 150 km and with an end mass of 10^6 gm, the limiting $h(f) \sim 3\times10^{-28}$ strain/$Hz^{\frac{1}{2}}$. The circulating optical power required in the antenna, if $\lambda \sim 5\times10^{-5}$cm, is 8×10^{10} watts!

The figure shows the optimum optical power required and the strain amplitude spectral density at this power for a quantum limited 5km long antenna in which the storage time is maintained at 1/f. The antenna end masses are 10^6 gms. At mid frequencies ~100 Hz, the quantum limit could be reached in second generation improvements of such a system.

Quantum limited performance of a 5 km antenna

with $t_{stor} = 1/f$

$m = 10^6$ grams

$\lambda = 5 \times 10^{-5}$ cm

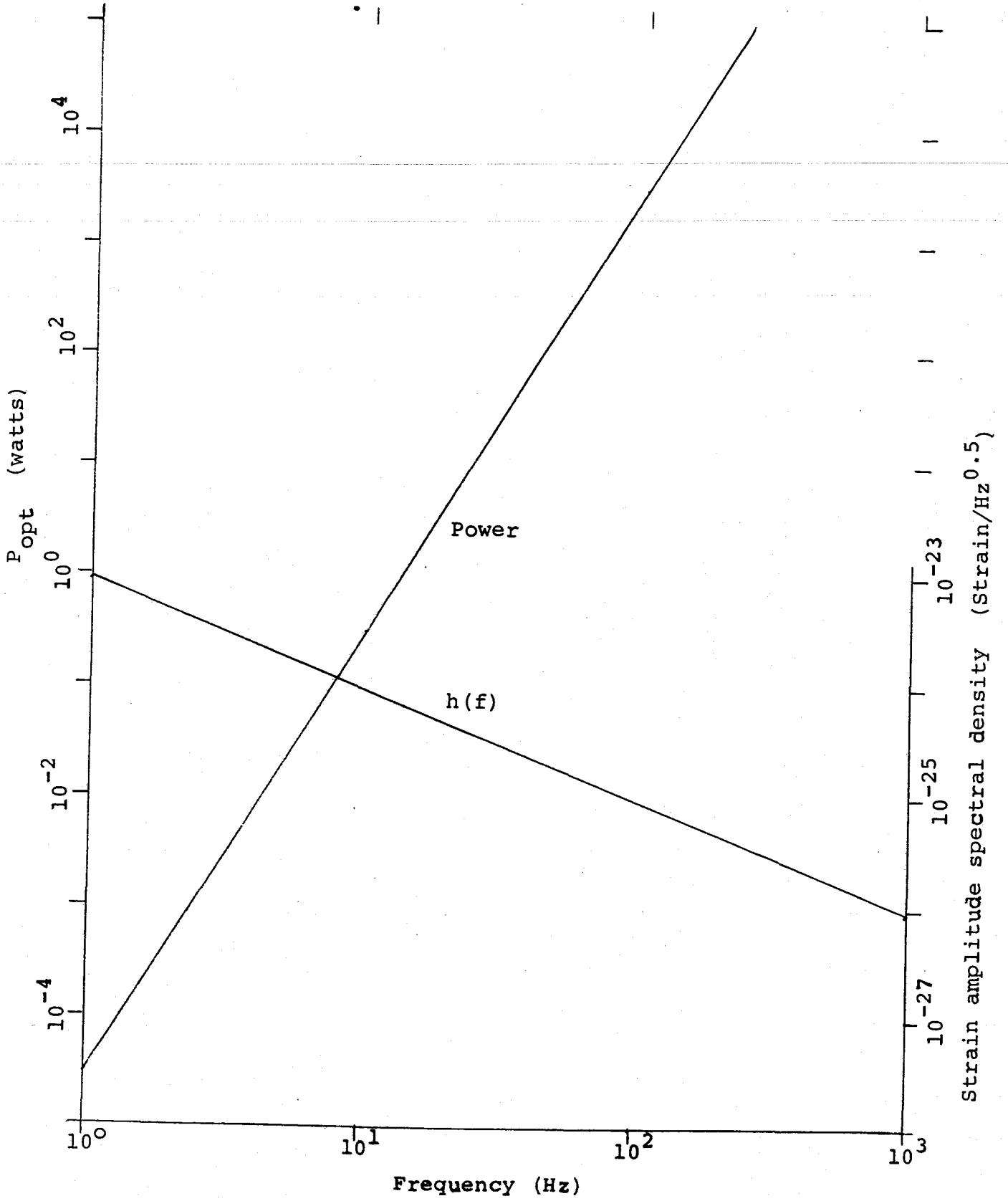

APPENDIX B

Why a Fiber Optic Antenna Will Not Suffice

When one compares the cost of the large evacuated enclosure that is required for an optical interferometer gravity wave antenna with the cost of the fiber optic links that now are used routinely for communication tasks, it seems possible that the fabrication costs, and, to some extent, the operational cost also, might be reduced significantly if single mode optical fibers could be used as the interferometer arms of the antenna. We have studied this superficially attractive alternative at some length.

We conclude that there are several compelling arguments why a fiber optic system will not function adequately as a gravity wave antenna. The arguments will be evaluated in this section.

In summary, there are three major intrinsic problems:

A. The power handling capability of single mode optical fibers is limited by intensity damage. Presently available fibers would limit the power to a level that is some 100 times lower than that required for successful operation of the antenna. In principle, this restriction could be ameliorated by increasing the diameter of the core, or by using multiple fibers.

B. The power handling capability is limited even more severely by nonlinear effects caused by stimulated Raman and Brillouin scattering processes. The power level that can be handled in a long, low loss, single mode, fiber is at least 10^5 times lower than the required power level. It is not clear that there is an available solution to this intrinsic problem.

C. The thermal noise occasioned by length and index of refraction fluctuations in a single mode optical fiber at room temperature typically is $\sim 10^8$ larger in amplitude than our total allowable system noise, and cooling the fiber to liquid helium temperature only would reduce this thermal noise by a factor of 10. Again, it is not clear that there is an available solution to this intrinsic problem.

In addition to the preceding intrinsic problems, optical fibers are susceptible to external influences such as mechanical strain, temperature gradients, and magnetic fields. The effect of these external driving forces would be significant at the noise levels of interest in a gravity wave antenna. In principle, the extrinsic effects probably could be attenuated to acceptable levels by careful engineering, but the cost of supporting optical fibers without mechanical strain in a temperature stabilized and magnetically shielded environment would largely negate the cost saving originally postulated for the fiber optic antenna, and thus would defeat the purpose.

Limitation due to damage threshold of optical fibers.

The radius of the core of a conventional single mode optical fiber is about equal to the wavelength of the light that is to be transmitted and, because of this small size, a modest propagating power can create an internal power density that is sufficient to cause physical damage to the fiber.

A typical power density damage threshold for available fibers is

$I_{max} \sim 10^8$ w/cm^2

Thus, for a fiber with a core radius about equal to the wavelength of the green light that is preferred in a laser interferometer, that is about 5000A°, physical damage will be significant for an injected light power P of about 1 watt.

As shown elsewhere in this report, the laser power needed to achieve a satisfactory signal/noise ratio in a gravity wave antenna is about 100 watts. So the damage threshold problem, alone, immediately precludes the use of conventional optical fibers as the interferometer arms of the antenna.

Limitation due to nonlinear scattering processes

Stimulated Raman and Brillouin scattering processes limit the power handling capability of optical fibers even more severely than does the physical damage threshold.

Raman scattering is a parametric photon conversion process that converts some of the energy supplied by the laser to a lower frequency.

At large power densities in a long, low loss, fiber the pump wave will leave a large enough time dependent polarization along the length of the fiber that the process can have parametric gain, resulting in both forward and backward propagation of a new wave at a frequency lower than that of the pump.

Using a criterion that the amplitude of the converted wave should everywhere be less than the amplitude of the pump, Smith shows that a

good approximation to the maximum allowable input power is given by

$$P_{max} \sim 16\ A\ \alpha/\gamma_R$$

where A is the fiber cross sectional area (cm^2)

α is the fiber attenuation constant (cm^{-1})

γ_R is the Raman conversion gain coefficient

$\sim 5 \times 10^{-11}$ cm/w for amorphous glasses.

So, using $A = 7 \times 10^{-9}$ cm^2, and assuming an attenuation constant of 10^{-5} (4.3 db/km), the maximum allowable input power that avoids nonlinear effects caused by stimulated Raman scattering is 20 mw.

Stimulated Brillouin scattering is an elastooptic process. The electric fields associated with the forward travelling injected wave cause a spatial variation in the refractive index of the fiber, with an acoustic wavelength along the fiber equal to the wavelength of the injected light in the medium. The result is to form a diffraction grating which moves along the fiber at the velocity of sound in the medium. Interaction of the injected wave with this moving diffraction grating gives rise to a reflected backward travelling wave. This conversion process, also, can have parametric gain.

Using the criterion that the backward wave power should not exceed the input pump power at the injection face of the fiber, Smith shows that the maximum allowable input power is given approximately by

$$P_{max} \sim 21\ A\ \alpha\ /\ \gamma_B$$

where γ_B is the Brillouin gain coefficient

$\sim 3\ 10^{-9}$ cm/w

So, for the same fiber considered earlier, the maximum allowable input power that avoids nonlinear effects caused by stimulated Brillouin scattering is about 1 mw.

Comparing this limitation with the 100 watts that is needed to achieve an adequate signal to noise ratio in the laser interferometer, it is clear that fiber optics would be a candidate only if there is a major advance in the technology. Such an advance cannot be predicted at this time.

Intrinsic thermal noise in an optical fiber.

Thermal noise directly causes fluctuations in both the length and the density of the fiber, and, due to elastooptic coupling in the material, indirectly causes fluctuations in the refraction indices.

To evaluate the effect of thermal noise, we assume a one dimensional system, estimate the number of modes per frequency interval and obtain the thermal energy per unit length. We then calculate the length change per mode and show that the mode spacing is so close that it is reasonable to treat the problem as a continuum calculation to obtain an equivalent spectral density of displacement noise given by

$$X^2(f) = \frac{kT}{2\rho c_s A f^2} \text{ cm}^2/\text{Hz}$$

where k is Boltzmann's constant = 1.38×10^{-16} ergs/°K

T is temperature (deg K)

ρ is the density of the fiber material ~ 2 g/cm^3

c_s is the velocity of sound in the medium $\sim 5 \times 10^5$ cm/s

A is the cross sectional area of the fiber $\sim 10^{-8}$ cm^2

f is the signal frequency (Hz)

For a typical single mode fiber at visible wavelengths and room temperature, this yields

$$x(f) \sim \frac{10^{-6} \text{cm/Hz}^{\frac{1}{2}}}{f}$$

At a 1 kHz signal frequency and a 10 km antenna length, the strain noise is

$$h(f) = \frac{X(f)}{\ell} \sim 10^{-15} \text{strain/Hz}^{\frac{1}{2}}$$

REFERENCES

R.G. Smith, Optical Power Handling Capacity of Low Loss Optical Fibers as Determined by Stimulated Raman and Brillouin Scattering, App. Optics, 11, 2489 (1972)